Studies on the Mechanism of Action of Selectively Cytotoxic Glycosylated Polyketides

By

Benjamin Joshua Reisman

Dissertation

Submitted to the Faculty of the

Graduate School of Vanderbilt University

in partial fulfillment of the requirements

for the degree of

DOCTOR OF PHILOSOPHY

In

Chemical and Physical Biology

May 31, 2021

Nashville, Tennessee

Approved:
Jeffrey C. Rathmell, PhD (chair)
Brian O. Bachmann, PhD
Jonathan M. Irish, PhD
Lawrence J. Marnett, PhD
Vito Quaranta, MD

DEDICATION

To my parents, Jon and Juliana Reisman

ACKNOWLEDGEMENTS

First and foremost, I would like to thank my advisor, Dr. Brian Bachmann for his mentorship and support over the last 4.5 years. When I initially joined the lab, I planned to mostly work on methods development and discovery, but over time my project evolved to become more hypothesis driven which necessitated learning many new techniques and establishing new collaborations. I am truly grateful for Brian's encouragement to follow the science wherever it led and support for trying new things outside of our lab's expertise.

I would also like to thank my other faculty mentors, formal and informal, who taught me to how to science, including Dr. Brent Ferrell, Dr. Jonathan Irish, and my committee members Dr. Rathmell, Marnett, and Quaranta. It was a truly valuable experience to work with Brent as he transitioned from fellow, to instructor, to a junior faculty member with his own laboratory. Though I was never formally a member of the lab, I am grateful for all the time Brent spent discussing my project each week, inviting me to take part in journal club and lab outings, and allowing me to join him in his clinic – I could not have asked for better mentor on how to be a physician-scientist. I am also grateful to Dr. Jonathan Irish for his co-mentorship on the discovery project during the first part of my PhD, our lively scientific discussions, and for the opportunity to co-teach a cytometry course in London, UK.

I would also like to acknowledge my early career mentors who's mentorship started me down the road to this point including my Northwestern University faculty mentors SonBinh Nguyen, Chad Mirkin, and Luis Amaral, as well as my graduate student mentors Archana Krovi, Charles Machan, Alex Spokoyny, Pratik Randeria, and João Moreira.

I would also like to acknowledge the Vanderbilt Medical Scientist Training Program (MSTP) leadership team who created a wonderful and supportive environment to train as a physician-scientist, and my MSTP classmates whose friendship has made these past seven years fly by. I am also grateful for the financial support to myself and my laboratory provided by the NIH and Vanderbilt University.

I would like to extend a special acknowledgement to the individual collaborators who made the work described in the subsequent chapters possible. For the work described in Chapters 2 and 3, I am grateful for the contributions of Hui Guo and his mentor John Rubinstein on the

TABLE OF CONTENTS

LIST OF TABLES

LIST OF FIGURES

LIST OF SPECTRA

CHAPTER 1 – INTRODUCTION

1.1 The Search for "Magic Bullets" – Selectively Cytotoxic Chemotherapeutics

1.1.1 Paul Ehrlich and the 'magic bullet' concept

One of the organizing principles of modern pharmacology is the need to develop selectively cytotoxic therapeutics. This paradigm is particularly important for the development of antimicrobial and anticancer therapies which must selectively eliminate pathologic cells such as bacteria, fungi, viruses, or the hosts own cancerous cells, while sparing the hosts' healthy cells. This work is focused on understanding the mechanism of action of selectively cytotoxic natural products and methods for finding new compounds which exhibit selective cytotoxicity. In order to place this work in context, it is necessary to consider how the concept of selective cytotoxicity has evolved since its inception and the role of selectively cytotoxic compounds in modern medicine.

The idea of searching for selectively cytotoxic therapeutics originates from the work of Paul Ehrlich, a physician-scientist who practiced in Germany at the turn of the 20th century. Ehrlich began his scientific career in histology, the microscopic study of biological specimens mounted on glass slides. As a medical student, he was fascinated by the staining patterns of synthetic aniline dyes which he was the first to apply to the study of histological specimens in his doctoral thesis "*Beiträge zur Theorie und Praxis der Histologischen Färbung"* (Contributions to the Theory and Practice of Histological Staining, Thesis, Leipzig University, 1878). Among the landmark results of his thesis was the description of a new type of cell, the mast cell, which was notable for its granules which stained brightly with his aniline dyes ([1]). Ehrlich's key observation was that certain dyes exhibit an affinity for certain cells and even substructures within the cell. Ehrlich's work established the basis of the idea that the effects of a compound on

a biological system depends on the interplay between its chemical structure and the specific cell type it is applied to (2), a concept which forms the basis of modern pharmacology, chemical biology, and histology.

As Ehrlich continued his work on histological stains, he realized that if a chemical can stain a particular cell or structure in a cell, that indicates it has a special affinity for that cell or structure – an affinity which could be leveraged therapeutically. From these observations, Ehrlich developed the concept of a 'magic bullet,' a therapeutic that is able to seek out the particular cells or structures that cause disease while sparing other cells that are not involved. This led him to begin testing synthetic dyes as chemical therapeutics or 'chemotherapy,' a word first coined by Ehrlich (3), in the search for antibiotic agents. This work, in arguably one of the first organized 'lead optimization' efforts, led to the discovery of the first antibiotic, *Salvarsan (Figure 1.1),* as a treatment for syphilis (4).
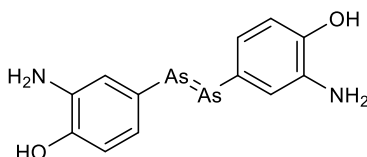
Figure 1.1. Structure of Salvarsan

Though Ehrlich laid the foundation for 'chemotherapy' the development of chemotherapies to address cancer would have to wait till after the second world war. The development of safe, effective, cancer therapeutics poses a unique challenge when compared to the development of antimicrobial agents. Whereas an antibiotic or antifungal agent must selectively target structures present in bacterial or fungal cells but not the host (cell walls, ribosomes, etc.), in the case of cancer, the diseased cell are derived from the host and share the

hosts' genetic code. This is the principal challenge of discovering and developing selectively cytotoxic agents to address cancer – finding a therapeutic index between healthy and diseased cells.

1.1.1 Methotrexate – the first cancer chemotherapy

The concept behind the first effective cancer chemotherapy originated from the study of normal cells, specifically hematopoietic cells. In the 1920s, George Minot discovered a group of 'pernicious' anemias which were caused not by iron deficiency, but by a lack of a critical micronutrient, vitamin B_{12}. For his discovery that pernicious anemia could be cured by replacing the missing vitamin B_{12} using liver extracts, Minot (along with Murphy and White) was awarded the 1934 Nobel prize in physiology or medicine. Around the same time, Lucy Wills discovered a similar group of anemias in malnourished patients that did not respond to B_{12} replacement, but rather to marmite yeast extract. The missing 'Wills factor' present in marmite was later discovered to be folic acid (folate).

Guided by Minot and Wills work on nutritional anemias, in the late 1940s Sidney Farber, a student of Minot, embarked on the search for effective chemotherapies to treat childhood acute lymphoblastic leukemia (ALL). Reasoning that folate was able to restore normal hematopoiesis in patients with pernicious anemia, Farber first attempted to treat his patients using folate supplementation with disastrous results. Instead of suppressing their leukemia, the additional folate accelerated the pace of their disease. If leukemia was a disease of hematopoiesis in overdrive, Farber reasoned that perhaps the cure lay in reproducing the state of folate deficiency which Wills had observed in her patients using an 'anti-folate.' In collaboration with a chemist named Yellapragada Subbarao, Farber began testing folic acid analogs as potential chemotherapies. (In addition to his work on anti-folates, Subbarao is best known for his co-

discovery of adenosine triphosphate – ATP.) In late 1947, Farber treated his first patient with a new folate analog developed by Subbarao, aminopterin, with remarkable results. When examined under the microscope, the patients' marrow, which had previously been crowded with malignant leukemia blasts, appeared normal. For the first time, a complete remission had been achieved using chemotherapy. An improved analog of aminopterin, methotrexate, is still used in the treatment of childhood ALL today.

Farber's work on folate and anti-folates was not guided by biochemical knowledge of the role of folate or by an understanding of its target, but rather by empirical evidence that blood cells were dependent on folate for survival. Later work on the mechanism of action of antifolates led to the discovery of one of their key targets, dihydrofolate reductase (DHFR), and the development of antifolates which selectively inhibit the bacterial enzyme – trimethoprim. DHFR is responsible for converting folic acid into dihydrofolate and subsequently into tetrahydrofolate, which is key intermediate in *de novo* purine biosynthesis and one-carbon metabolism (Figure 1.2). By inhibiting DHFR, methotrexate, inhibits the synthesis of purines, which are necessary to synthesize DNA in rapidly dividing cancer cells. The therapeutic index of methotrexate is thought to arise, in part, due to the difference in demand for purines in cancer cells compared to non-cancerous cells. As DHFR is present in both cancerous and non-cancerous cells, antifolates do not necessarily selectively traffic to cancer cells, but instead achieve their selectivity by the cancer cells' functional dependency on tetrahydrofolate for continued growth and survival. During the next half-century of cancer research, the pharmacopoeia of anticancer agents would continue to expand with new 'cytotoxic' chemotherapies which achieve their narrow selectivity by targeting functional dependencies of cancer – principally DNA synthesis, DNA repair, and cell division. Methotrexate and aminopterin were the founding members of the class of 'anti-

metabolites' which target metabolism to inhibit growth. Though this class would continue to grow by the addition of nucleoside analogs which inhibit DNA synthesis, the following decades in cancer drug discovery were largely devoid of therapeutics that target primary metabolism itself.
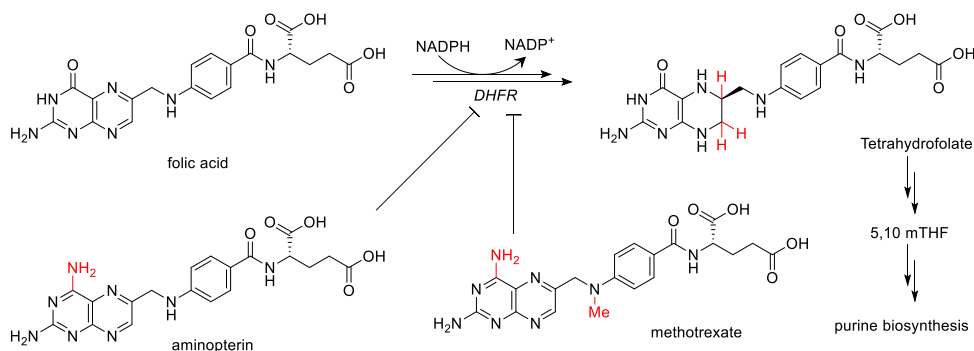
Figure 1.2. Folate metabolism and its inhibition in cancer therapy

Folic acid is converted to tetrahydrofolate (THF) by dihydrofolate reductase (DHFR) which is used a precursor in purine biosynthesis and one-carbon metabolism. Aminopterin and methotrexate are synthetic inhibitors of DHFR.

1.1.2 Imatinib, the first small molecule 'targeted' agent

The following section cites by the book "The Philadelphia Chromosome" by Jessica Wapner, 2013 (5).

One of the remarkable features of the development of cancer therapy over the 20th century is that many of most significant therapeutic advances arose in the absence of an understanding of their molecular mechanism or an understanding of the molecular basis of cancer itself. It was not till the molecular biology revolution of the 1960s and 70s that cancer researchers began to identify the molecular drivers of cancer – the features which separate healthy cells from cancer cells. This work is best summarized in a series of reviews by Hanahan and Weinberg which organize the findings of 20th century cancer biology into the so-called 'The

5

Hallmarks of Cancer ([6]),' published in 2000, and "Hallmarks of cancer: the next generation ([7])."
In these reviews, Hanahan and Weinberg outlined six 'hallmarks,' two 'emerging hallmarks,'
and two 'enabling characteristics' which can help organize our thinking about selectively
cytotoxic therapeutics.
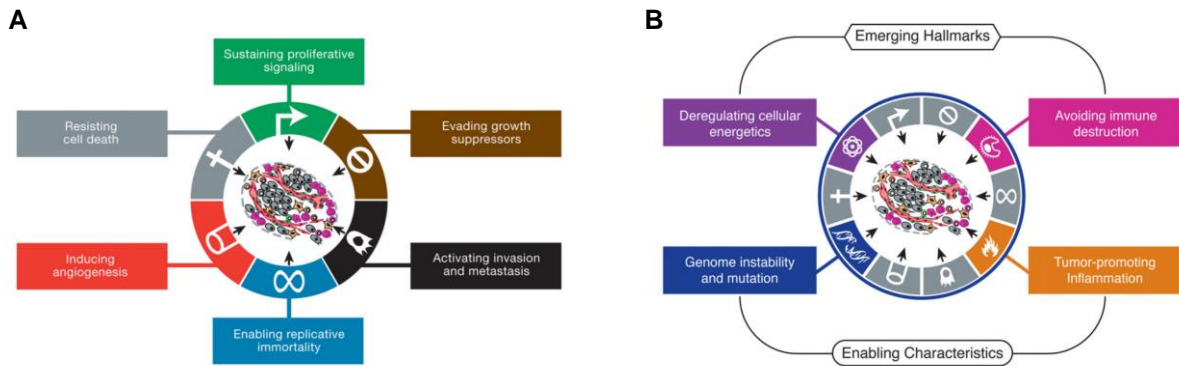
Figure 1.3. The Hallmarks of Cancer

The hallmarks of cancer as organized by Hanahan and Weinberg in their **A,** 2000 and **B,** 2011
review on cancer biology.

Healthy cells rely on extrinsic factors to signal when to begin growing and dividing.
These signals are transmitted from the cell surface to the nucleus by kinases, enzymes which
phosphorylate other proteins using ATP as a source of high-energy phosphate. In cancer, these
kinases can become dysregulated such that they signal the cell to divide in the absence of outside
signals. Theses autonomous, cancer-driving proteins and their genes are known as "oncogenes,"
a concept most associated with the Robert Weinberg, who is credited with discovering the first
human oncogene, *Ras*. In addition to oncogenes, Weinberg also discovered genes such as *Rb*
which act to suppress cell growth and can cause cancer if lost – tumor suppressors. These two
concepts 'oncogenes' and 'tumor suppressors' form the basis of two of Hanahan and Weinberg's
Hallmarks: 'sustaining proliferative signaling' and 'evading growth suppressors.'

Chronic Myeloid Leukemia (CML) is unique among cancers in that [in most cases] it is driven by only one of Hanahan and Weinberg's hallmarks: sustained proliferative signaling driven by the BCR-Abl kinase. The discovery of the molecular underpinnings of CML began with David Hungerford's 1959 observation that cells from patients with CML had an abnormally short chromosome 22, a feature he named the 'Philadelphia chromosome.' This discovery was followed-up by Janet Rowley in 1972 who, applying the newly developed technique of chromosome banding using Giemsa stain, observed that the missing piece of chromosome 22 had moved to chromosome 9, what is known as a reciprocal translocation denoted t(9,22). Rowley went on to discover other recurrent translocations in cancer including the t(15,17) translocation seen in promyelocytic leukemia which will be revisited.

In parallel to Hungerford and Rowley's cytogenetic studies on CML scientists in the laboratories of Harold Varmus, Michael Bishop (Varmus and Bishop shared the 1989 Nobel Prize for physiology or medicine for their discovery of proto-oncogenes), and David Baltimore were working to understand viral oncogenes that cause cancer in mice. Owen Witte, at the time a post-doc in David Baltimore's lab, together with David Rosenberg discovered the cancer-causing effects of the mouse Abelson virus were driven by the Abl kinase. Whereas all previously discovered kinases added phosphates to the amino acids serine or threonine, Abl added phosphate to tyrosine, a tyrosine kinase. In 1983, Witte, having established his own laboratory, discovered that antibodies against Abl reacted strongly with cells from a patient with CML, the first link between a tyrosine kinase and a human cancer. The first connection between the Abl kinase and Rowley's t(9,22) was made by John Groffen, a post-doc at the National Cancer Institute (NCI) who used probes designed against the mouse *Abl* gene to search for its human paralog, which he eventually located on chromosome 9. When he went on to apply his probes to

chromosomes from patients with CML he discovered that while one localized to chromosome 9, the other localized to chromosome 22, the two chromosomes involved in Rowley's translocation. As they studied the region of chromosome 22 involved in the CML translocation, they realized the same region was altered in every patient. They called this region the 'breakpoint cluster region' or *bcr*, and the fusion product Bcr/Abl. In 1984, Witte went on to show that K562 cells, a CML cell line which could be grown in the laboratory, possessed a constitutively active kinase, and two years later Baltimore's group identified the constitutively active kinase in K562 cells as the fusion product of *bcr/abl* genes.

The work of Witte and Baltimore established that the Bcr/Abl kinase present in patients with CML was the result t(9,22), but not necessarily that the Bcr/Abl kinase was the *cause* of CML. In the late 1980s, George Daley, then a post-doc in Baltimore's laboratory, filled in this final piece of the puzzle. In his first series of experiments, Daley demonstrated that the Bcr/Abl kinase was capable of 'transforming' non-cancerous cells – allowing them to grow in the absence of exogenous signals. BaF3 cells are a mouse pro-B cell line which are dependent on the cytokine IL-3 for survival – the absence of IL-3 they stop growing and undergo apoptosis. Daley showed that by when the Bcr/Abl kinase was introduced to BaF3 cells using a retrovirus, the cells became transformed – they continued to grow when IL-3 was withdrawn (8). The final proof came two years later when Daley used a similar retroviral system to introduce the Bcr/Abl kinase into mouse bone-marrow cells which he then transplanted into a new mouse. The second mouse then developed a leukemia that resembled human CML, establishing that the Bcr/Abl kinase encoded by the t(9,22) translocation was the cause of CML (9).

While the discovery of the Philadelphia chromosome was useful for diagnosing patients with CML, oncologists were not yet able to use this finding to guide therapy. Though the

connection between Bcr/Abl and CML had not solidified quiet yet, in the 1980s, the swiss

pharmaceutical company Ciba-Geigy established a program to develop kinase inhibitors to target

dysregulated signaling in cancer, one of the first programs designed to address a specific

molecular target. Around the same time, Brian Druker, a physician-scientists at Dana Farber

cancer center had developed an antibody for detecting phosphotyrosine. A collaborator was

established between Druker and Ciba-Geigy to screen for tyrosine kinase inhibitors using

Druker's antibody. One of the first kinase inhibitors discovered in 1986 was the natural product

staurosporine, produced by *Streptomyces staurosporeus*. Though a potent inhibitor of kinases,

staurosporine acted non-specifically inhibiting all kinases. What was needed was a compound

that selectively inhibited a single kinase. Ciba-Geigy's kinase program eventually yielded the

lead compound CGP-57148B, an inhibitor of the Abl kinase, which Druker, now at OHSU,

tested in CML samples cultured *ex vivo* and found that they eliminated the Bcr/Abl positive cells

while sparing normal, Bcr/Abl negative cells. Ciba-Geigy eventually became the pharmaceutical

company Novartis, CGP-57148B was renamed, first as STI-571, then imatinib, and finally as

Gleevac, the first targeted small molecule therapy (Figure 1.4).
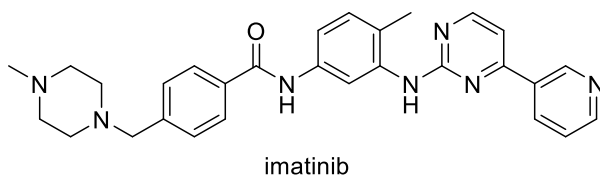
imatinib

Figure 1.4. Structure of imatinib

Though this dissertation does not focus on kinase inhibitors or molecularly targeted

therapies in general, the story of CML, Bcr/Abl, and imatinib is key for understanding the

current paradigm of cancer drug development and the concept of selective cytotoxicity. Many of

tools used to study the molecular drivers of CML will also return as players in the story of

apoptolidin and ammocidin. In many ways, the success of *imatinib* inspired many of the modern-

day efforts to target cancer with small molecules. CML is a cancer caused by a mutation, which

causes abnormal signaling, which can be interrupted by a small molecule, which stops the cancer

in its tracks. This paradigm can also be applied to other cancers such as melanoma (BRAF,

MEK), lung cancer (EGFR, ALK), acute myeloid leukemia (FLT3), myelofibrosis (JAK), where

it improved outcomes for many patients in the form of extended survival, though none has been

as successful as a curative monotherapy as imatinib (Figure 1.5).
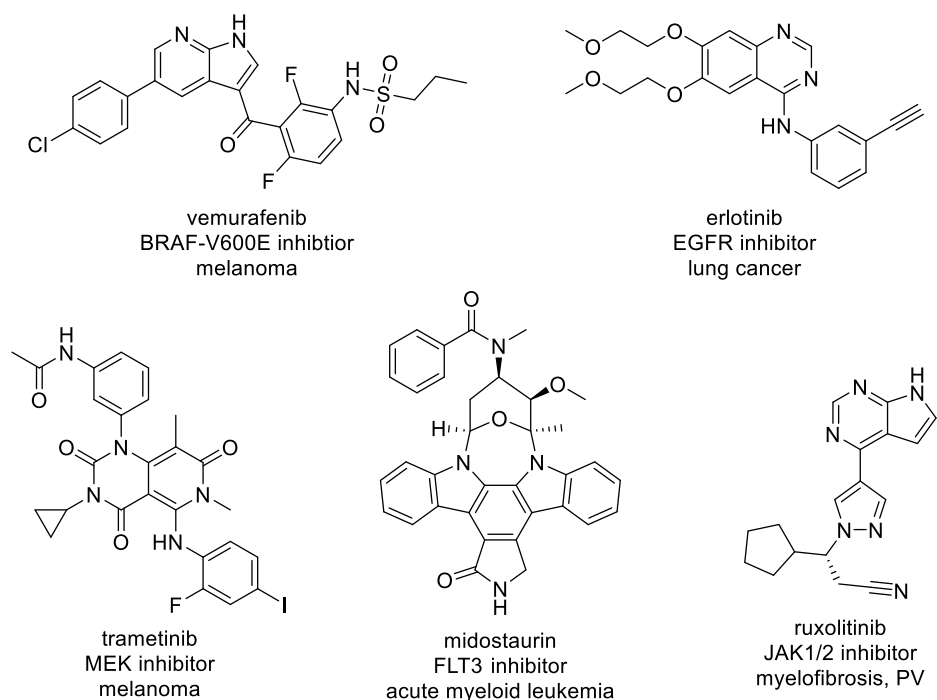
Figure 1.5. Structures of small-molecule targeted therapies

Labels include drug name, molecular target, and therapeutic indication.

One of the other major success stories of targeted cancer therapy is the discovery of ATRA as a treatment of acute promyelocytic leukemia (APL). Like CML, APL is defined by a balanced translocation t(15,17), which joins the promyelocytic leukemia protein gene (PML) on chromosome 15 to the retinoic acid receptor (RARα) on chromosome 17. The RARα protein is a nuclear receptor involved with activating genes required for myeloid differentiation. When joined to PML in promyelocytic leukemia, it is no-longer able to carry out this function, resulting in a block in differentiation and an accumulation of immature promyelocytes, which manifests clinically as leukemia. This molecular defect can be corrected by treating patients with all-trans retinoic acid (ATRA), which overcomes the blockade and allows cells to resume normal differentiation. Whereas before ATRA, APL was a rapidly fatal disease, the advent of ATRA therapy and combinations of ATRA with arsenic trioxide (ATRA-ITO) have transformed APL into a highly curable cancer with a good long-term prognosis. Though on some levels the story of APL and ATRA mirrors that of CML and imatinib, the two stories differ in one important way – in the case of ATRA the discovery of the targeted therapy preceded the discovery of the molecular defect. The differentiation inducing effects of retinoic acid derivatives were discovered in the early 1980s by Zhen-Yi Wang and Zhu Chen, who observed that ATRA could induce differentiation in cultured cells, and then in patients ([10], [11]) in 1988. Though the t(15,17) translocation was known, the identification of the role of RARα and PML as the fusion partners did not come till 1990 ([12-14]), and the connection between PMR-RARα and ATRA was not made until 1996 ([15]).

1.1.3 Venetoclax – Inhibitors of BCL-2 targeting functional cancer dependencies

As a final example of targeted cancer therapy, we turn to the story of BCL-2. Revisiting Hanahan and Weinberg's hallmarks – while Bcr/Abl is the prototypical oncogene, BCL-2 is the

prototypical anti-apoptotic factor. The *BCL2* gene was first cloned by Tsujimoto from cells derived from a patient with B-cell ALL and found to be disrupted in patients with follicular lymphoma, which led him to named it Bcl2 for "B-cell lymphoma ([16])." *BCL2* was the founding member of the entire BCL-2 protein family, including anti-apoptotic factors: BCL-2, BCL-XL, MCL-1 and others; and pro-apoptotic factors: BAX, BAK, BAD, BIM, and others. The BCL-2 family of proteins contain one or more Bcl-2 homology (BH) domains, denoted BH1, BH2, BH3, and BH4. The pro-apoptotic members of the family contain the BH3 domain which is necessary to promote oligomerization and initiate the series of changes leading to the release of cytochrome C, activation of caspases, and ultimately cell death. The anti-apoptotic factors, BCL-2, BCL-XL, and MCL-1 contain a BH3 binding grove which binds to and sequesters the BH3 motif of the proapoptotic factors and prevents their oligomerization. Thus, over-expression of BCL-2 family members suppress apoptosis in cells which would otherwise undergo controlled cell death, overriding tumor suppressors and promoting chemoresistance.

Though BCL-2 was discovered in the context of a translocation, subsequent studies noted that BCL-2 family members were overexpress in many cancers, particularly hematological malignancies, in the absence of any mutations ([17]). This dependency is thus distinct from the examples described previously in that a proto-oncogene has not been mutated to become an oncogene, but rather the overexpression of a protein has created a state of 'functional dependency' which could theoretically be targeted. Anthony Letai's group was the first to demonstrate that BCL-2 overexpression could be targeted therapeutically. As BCL-2 family overexpression sequestered the BH3 domains of the pro-apoptotic factors, one strategy for overcoming this state was by providing a decoy BH3 mimetic which could fill the BH3 binding groves and allow the pro-apoptotic factors to predominate and initiate apoptosis. Using a panel

of short peptide BH3 mimetics, Letai demonstrated each BCL-2 family member recognized different BH3 domains and that BH3 mimetics could be used to trigger apoptosis ([18](#)). He proposed that in addition to the cell states "alive" and "dead," cells could exist in a state which he referred to as "primed for death." This 'primed' state was unique to malignant cells, opening a therapeutic window where malignant cells could be selectively targeted.

While BH3 mimetic peptides provided a proof of concept for targeting BCL-2 overexpression in hematologic malignancies, unmodified peptides cannot cross cell membranes and therefore are not viable drugs or chemical probes suitable for use in live cells. Multiple academic and industry groups undertook efforts to develop small-molecule BH3 mimetics which had favorable bioavailability profiles. Though this dissertation is primarily on small molecules discovered via phenotypic screening, the development of small molecule inhibitors of BCL-2 was a notable triumph of rational, targeted-based, drug design. Stephen Fesik, then at the pharmaceutical company Abbot Labs (now AbbVie) and currently a faculty member at Vanderbilt University, led a team that developed the first small molecule inhibitors of BCL-2 using a new technique "SAR by NMR" also known as fragment-based drug discovery ([19](#)).

The first generation BCL-2 family inhibitor, ABT-737 had high affinity to BCL-2 and BCL-XL, and proved to be a useful chemical probe for studying apoptosis, though poor oral bioavailability limited its therapeutic potential ([20](#)). The second generation BCL-2/BCL-XL inhibitor, ABT-263 (navitoclax), had favorable oral bioavailability and advanced into the clinical trials where it showed efficacy as a first line treatment for chronic lymphocytic leukemia (CLL). However, the dose limiting toxicity of navitoclax proved to be thrombocytopenia (low platelets), which was later found to be due to on-target inhibition of BCL-XL ([21](#), [22](#)). This led to the development of the monoselective BCL2 inhibitor ABT-199 (venetoclax), which entered clinical

13

trials as a monotherapy for CLL. The remarkable efficacy of venetoclax as a monotherapy in

CLL in phase II trials prompted its approval as a 'breakthrough therapy' in 2015 while other

trials in myeloid disease continued.
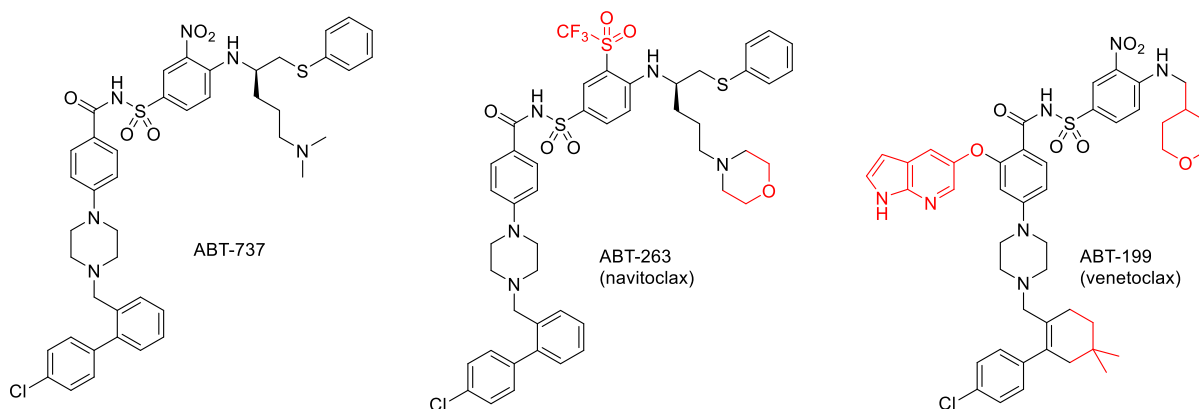
Figure 1.6. Small molecule BCL-2 family inhibitors.

In acute myeloid leukemia (AML), initial trials with venetoclax monotherapy showed

modest responses, but combination therapy with the hypomethylating agent 5-azacytadine (Aza)

proved highly effective (23, 24). Recent studies by Craig Jordan's group suggest that the synergy

between venetoclax and azacytidine (Ven-Aza) is due to inhibition of oxidative phosphorylation

in leukemic stem cells. This hypothesis will be addressed further in chapter 3. The remarkable

efficacy of Ven-Aza in AML led to its approval as a first line treatment for AML in 2020.

This dissertation primarily considers antitumor activity in the context of acute myeloid

leukemia (AML). At the outset of this project in 2016, the introduction would have noted that

despite decades of research on the pathogenesis of AML, no new agents have been approved for

clinical use since the 1970s and that treatment regimens (anthracyclines + cytarabine, 7+3) have

remain essentially unchanged for 40+ years. Fortunately, the therapeutic landscape for AML has

changed dramatically since this project began, with the approval of liposomal formulations of

doxorubicin and cytarabine (Vyxeos), the FLT3 kinase inhibitors midostaurin and gilteritinib for patients with FLT3 inhibitors, the IDH2 inhibitors enasidenib for patients with IDH2 mutations, and venetoclax + azacytidine. Whereas previously patients were treated with intravenous cytotoxic therapies which also suppressed normal hematopoiesis, necessitating months long hospital stays while the hematopoietic system recovered, many patients are now eligible for oral therapies which can be administered in the outpatient setting. Despite these advances, AML remains a challenging disease to treat for patients and physicians alike. While these novel therapies are able to induce remissions in many patients and extend median survival, none have proven curative. For young, fit, patients, the first line therapy with the greatest potential of a long-term cure remains cytotoxic chemotherapy to induce remission followed by allogeneic hematopoietic stem cell transplant (aHSCT) ([25](#)). Thus, the need for new therapeutic options for AML remains great.

1.2 A Brief History of Studies on Oxidative Phosphorylation, its Role in Disease, and Inhibitors of the Mitochondrial ATP Synthase

This section cites the book 'Searching for a Mechanism – a History of Cell Bioenergetics' by John N. Preeble ([26](#)).

Oxidative phosphorylation (OXPHOS) is the process by which cells generate chemical energy in the form of ATP using the electron transport chain located in the mitochondria. The oxidative part of OXPHOS refers to the oxidation of NADH and FAD_2 by the electron transport chain complexes I-III, culminating in the reduction of molecular oxygen to water by Cytochrome C oxidase (complex IV). The phosphorylation part of OXPHOS refers to addition of inorganic phosphate (Pi) to ADP by ATP synthase to generate ATP, which serves as a high energy phosphate donor for various cellular processes. OXPHOS can be contrasted with the substrate

level phosphate used during glycolysis, in which a high energy phosphate is transferred from a substrate (i.e. 1,3-BPG or PEP) to ADP to from ATP. The enzymes which use high energy phosphate to append phosphates are known as kinases, while ATP synthase is in a unique class of enzymes which are able to utilize 'low-energy' inorganic phosphate.

The history of cellular metabolism and bioenergetics is full of fascinating stories which form the basis of the modern discipline of biochemistry. Similarly, the connections between cellular metabolism and cancer are numerous and provides insights into many existing and emerging cancer therapies. For the purposes of this introduction, I will primarily address the history of ATP synthase, inhibitors of ATP synthase, and the role of OXPHOS in carcinogenesis.

The first scientist to use the term 'oxidative phosphorylation' was the Spanish biochemistry Severo Ochoa,[1] a student of Meyerhoff, who studied bioenergetics in the 1940s, following up on earlier results of Vladimir Belitzer at the University of Moscow. Belitzer was the first to rigorously study the phenomenon that would become known as OXPHOS by simultaneously measuring oxygen consumption and phosphorylation, expressed as the P/O ratio[2]. Using preparations derived from animal muscle, he measured P/O ratios between 2 and 3.5, far higher than the rate of phosphorylation provided by glycolysis. Importantly, he noted that unlike in glycolysis, where metabolism was "unconditionally" (obligatorily) linked to phosphorylation, in oxidative phosphorylation the processes of oxidation and phosphorylation were conditionally linked – that is, they were coupled together but could also be uncoupled. Ochoa also experimented with measuring P/O ratios obtaining an average value of 3.0 for the complete

---

[1] Ochoa went on to discover the enzyme polynucleotide phosphorylase (PNPase), work for which he was awarded the 1959 Nobel Prize in physiology or medicine for this discovery of enzymes which synthesize RNA, though the role of PNPase in RNA synthesis was later overturned.

[2] Note that P/O is expressed as the number of phosphorylation events per *atom* of oxygen, O_2 contains two oxygen atoms.

16

oxidation of pyruvate with a range of 2.3-4.0. The curious aspect of this result is that the P/O

ratio of OXPHOS did not appear to be an integer as one would expect with a conventional

chemical reaction.

One of the key tools that early biochemists used to dissect OXPHOS was inhibitors and

uncouplers of the various steps of OXPHOS. For example, antimycin A (Figure 1.7) was

observed to inhibit OXPHOS and its site of action was determined to lay between cytochrome *b*

and *c*. Edward Slater, a former student of Ochoa, noted that 2,4-dihydrophenol (2,4-DNP)

inhibited phosphorylation, but not oxidation, but also not substrate level phosphorylation. This

led him to propose a chemical theory of oxidative phosphorylation in which oxidation generates

a high energy phosphate intermediate '~C' which is used to activate phosphate so that it can be

added to ADP. Britton Chance also led a laboratory studying oxidative phosphorylation and

discovered that oxidative phosphorylation was reversible – while oxidation could drive ATP

synthesis, ATP hydrolysis could drive reduction, specifically the reduction of NAD by electrons

from succinate, in coupled, but not uncoupled, mitochondria. Thus, the search for the

phosphorylating enzyme was also a search for an ATPase.
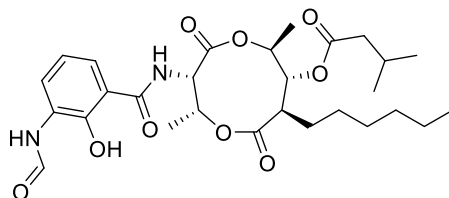
Figure 1.7. Structure of antimycin A, complex III inhibitor

The task of isolating, characterizing, and reconstituting, the ATPase responsible for

phosphorylation fell to Efraim Racker, who used classical biochemistry techniques to separate

mitochondria into various fractions which could be purified or combined with each other to

reproduce the reactions of OXPHOS. Using such an approach, he identified a soluble

mitochondrial fraction, F_1, which exhibited ATPase activity and, when added to mitochondrial membrane fractions, could restore oxidative phosphorylation ([27], [28]).

Around this time, Lardy and colleagues were experimenting with a novel antibiotic, oligomycin, named as such due to its toxicity in a relatively small (oligo = few) range of pathogens ([29], [30]). They observed that oligomycin inhibits both the ATPase activity and the Pi exchange reactions of mitochondria ([31]), and thus it followed that the phosphorylating enzyme must be oligomycin sensitive. Racker's F_1 ATPase, however, was not oligomycin sensitive, prompting a successful search for the missing, membrane bound factor which restores oligomycin sensitivity to the ATPase, named F_O ([32]). This is not to be confused with the Oligomycin sensitivity conferral protein (OSCP) which lies elsewhere in the ATP synthase complex. Around this time, Humerto Fernandez-Moran, an electron microscopy expert at Massachusetts General Hospital, first examined mitochondrial membranes under the electron microscope and noted small 80-90 Å particles dotting the inner membrane of the mitochondria. Racker and Kagawa went on to show that these particles were the F_1 ATPase isolated earlier in his research ([33]). Later studies showed that submitochondrial particles containing F_O were permeable to protons, but this permeability could be eliminated by the addition of F_1 or oligomycin. This led investigators to conclude that the F_O subunit was a proton channel.
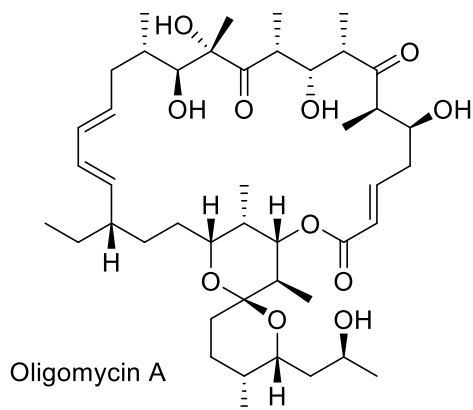
Figure 1.8. Structure of oligomycin A

Thus, the modern model of ATP synthase began to come into focus during the late 1960s and 1970s. ATP synthase is composed of two subcomplexes, the F_O and F_1 subunits. The F_O subunit contains the oligomycin binding site and forms a proton channel, while the F_1 subunit is a soluble ATPase. Together, they form the functional ATP synthase, though in intact mitochondria a number of additional smaller subunits help organize individual ATP synthases into dimers and higher order oligomers which give the mitochondria cristae their shape. Slater's chemical theory of oxidative phosphorylation was eventually overturned by Paul Mitchell's chemo-osmotic theory, in which the oxidation reactions of complex I-IV create a proton gradient between the inner membrane space and the mitochondrial matrix which is used by ATP synthase (complex V) to synthesize ATP from ADP and Pi. The molecular workings of ATP synthase came into more precise focus with Paul Walker crystal structure of bovine F_1 ATPase ([34]). Previously, Walker had determined the sequence and stoichiometry of the bovine F_1 ATPase, finding that it contained 5 distinct subunits α, β, γ, δ, ε, in 3:3:1:1:1 stoichiometry ([35]) with a total molecular weight of ~ 370 kDa. Walker's structure revealed that the α and β subunit were arranged like six orange slices with six nucleotide binding sites at the interface each set of α/β

19

subunits. The γ subunit formed a central stalk composed of two alpha helices which ran through the center of the α/β hexamer and, with the help of the δ and ε subunits, connected the F_1 and F_O portions of the ATP synthase ([36]).

While the α and β units each have nucleotide binding sites, only the nucleotide binding sites located on the β subunits participate in catalysis. Walker's structure showed the three different β subunits in three different conformations with different nucleotides bound at each site, a tight conformation with ATP bound (β_{TP}), and loose conformation with ADP bound (β_{DP}), and an empty confirmation with no nucleotide bound (β_E) ([37]). As the central stalk (γ, δ, ε) rotates, it interacts with the C-terminal domain of the β subunit to open and close the catalytic site and drive the synthesis of ATP from ADP and phosphate. The principal subunits of the F_O subunit are the c-ring and the 'a' subunit. The c-ring is a homomeric ring of 8-17 helices which span the membrane and contain a critical glutamine (Glu59 in the yeast enzyme) which shuttles protons from one side of the membrane to the other ([36]). The A subunit (encoded by MT-ATP6, not to be confused with the α subunit), forms two half channels that allow protons to move from one side of the membrane to Glu69, but no further. In order for the proton to complete its transversal across the membrane, the c-ring must turn ~360 degrees to access the second half-channel. Oligomycin, binds to the Glu69 to prevent proton transit across the c-ring and thus inhibit the ATP synthase ([37]).

As discussed previously, ATP synthase can utilize the proton gradient to drive ATP synthesis as well as hydrolyze ATP to pump protons. V-type ATPases work by a similar mechanism and are used by cells to acidify various organelles. In most *in vitro* context, ATP synthase is assayed as an ATPase ([38]), as assays which measure ATP synthesis require intact membranes and a proton motive force which are difficult ([39-42]) to maintain *in vitro*. Under

'normal' circumstances ATP synthase is thought to function in the forward direction, though the exceptions provide insights to interplay between various mitochondrial proteins. In yeast (*S. cerevisiae*), partial or complete loss of the mitochondrial genome results in colonies that grow slowly on fermentable media (glucose) and do not grow at all on non-fermentable media (galactose). Since the mitochondrial genome encodes critical components of complexes I, III, IV, and V, these petite (ρ_0) yeast are not able to generate a proton motive force via the ETC, but perhaps surprisingly, they do retain a mitochondrial membrane potential. Mutations which prevent the formation of petite colonies include loss of the adenine nucleotide translocase (ANT) ([43](#)) as well as ATP synthase ([44](#)). It is tempting to speculate that ATP synthase is functioning in reverse, pumping protons across the membrane via the F_O subunit, but these mutants lack the mitochondrially encoded subunits of F_O which form the proton half-channels and are oligomycin insensitive ([43](#)). Instead, mitochondrial membrane potential is maintained by the F_1 ATPase and ANT, with the ANT exchanging the ATP (with four negative charges) for ADP (with three negative charges) and the F_1 ATPase hydrolyzing ATP into ADP + Pi, thus maintaining the membrane potential. While we normally think of ATP generation as the critical function of ATP synthase, the petite phenomenon demonstrates that the other roles of a functional ATP synthase – sustaining the membrane potential, maintaining flux through the ETC, etc… – can be just as important.

1.2.1 <u>Intrinsic ATP synthase inhibitors</u>

The petite phenomenon is not unique to yeast. M1 [classical] macrophages exhibit high glycolysis and an impaired TCA cycle which they use to generate reactive oxygen species (ROS) ([45](#)). Like petite yeast, M1 macrophages maintain their mitochondrial membrane potential via the ANT and ATPase activity of F_1 ([46](#)). The same mechanism is thought to maintain the

21

mitochondrial membrane potential in cancer cells utilizing glycolysis for ATP ([47](#)). Outside of these special circumstances, uncontrolled hydrolysis of ATP would impair cell fitness and thus life has evolved various mechanisms for inhibiting ATP synthase. In eukaryotic cells, this role is filled by the ATP synthase inhibitory factor (IF1, gene: *ATP5IF1*). In actively respiring mitochondria the pumping of protons out of the mitochondrial matrix imparts a slightly basic pH (~8.5) to the mitochondrial matrix while the addition of uncouplers eliminates the proton gradient and restores a pH of ~7.5. At pH 8.5, the inhibitory factor oligomerizes into a form not compatible with ATP synthase binding, while at pH 7.5 the C-terminal His49 is protonated, preventing oligomerization and allowing the otherwise disordered N-terminal domain to bind to and inhibit ATP synthase ([48](#)). Intrinsic inhibitory mechanisms are also present in bacterial and plant ATP synthases. In bacteria, the ε subunit adopts adopt two confirmations based on the binding of ATP, with high ATP concentrations favoring a conformation in which ATP synthase can either synthesize or hydrolyze ATP, while low ATP concentrations favor a conformation where ATP synthase can only synthesize ATP ([49](#)). This ATP dependent confirmational change has been utilized to create fluorescent sensors of ATP using a recombinant ε subunit ([50](#)). In plants, the inhibitory mechanism is based on the redox controlled disulfide bond form between two cystines present in the chloroplast γ subunit ([51](#)). When exposed to light, the light reactions of photosynthesis generate electron donors which keep the disulfide reduced whereas periods of prolonged darkness allow the disulfide bonds to form and for ATP synthase to be 'locked-up' for the night ([51](#)).

Thus far we have discussed two 'classes' of ATP synthase inhibitors: oligomycin family macrolides which block proton transit through the F_O subunit and the native inhibitory factors which prevent ATP hydrolysis under low membrane potential settings. During the late 20th

century two additional classes of ATP synthase inhibitors were discovered which target the F_1 portion of ATP synthase: the aurovertin family polyketides and the efrapeptin family of cationic non-ribosomal synthesized (NRPS) peptides.

The aurovertin family of ATP synthase inhibitors were discovered in a screen for toxic compounds when injected (*as a crude extract*) into naïve mice ([52](#)). Baldwin noted the pattern of toxicity was similar to that observed by Lardy for oligomycin, and so aurovertin was evaluated in the context of OXPHOS and found to inhibit NADH oxidation, which could be reversed by the addition of an uncoupler, consistent with ATP synthase inhibition. Aurovertin is a fluorescent polyketide produced by *Calcarisporium arbuscula* which exhibits enhanced fluorescent upon binding to ATP synthase ([53](#)). Unlike other ATP synthase inhibitors, aurovertin is able to bind the isolated β subunit, separate from the α and γ subunits ([54](#), [55](#)). Walker determined the crystal structure of aurovertin bound to bovine F_1 ATPase by crystal soaking with inhibitor. In Walker's crystal structure aurovertin is bound at both $β_E$ and $β_{TP}$ at a cleft between the nucleotide binding pocket and the C-terminal domain, and is thought to inhibit ATP synthesis by blocking opening and closing of the C-terminal domain ([56](#)). Citreoviridin is a non-fluorescent biosynthetically related polyketide which also inhibits ATP synthase, thought there is some evidence that they bind to non-identical sites on ATP synthase ([57](#)). Interestingly, introduction of the β-Arg398His mutation which confers resistance to aurovertin in *E. coli* does not confer resistance to nematodes which are infected with the producing organism or exposed to aurovertin, suggesting its ecological target may not be ATP synthase ([58](#)).
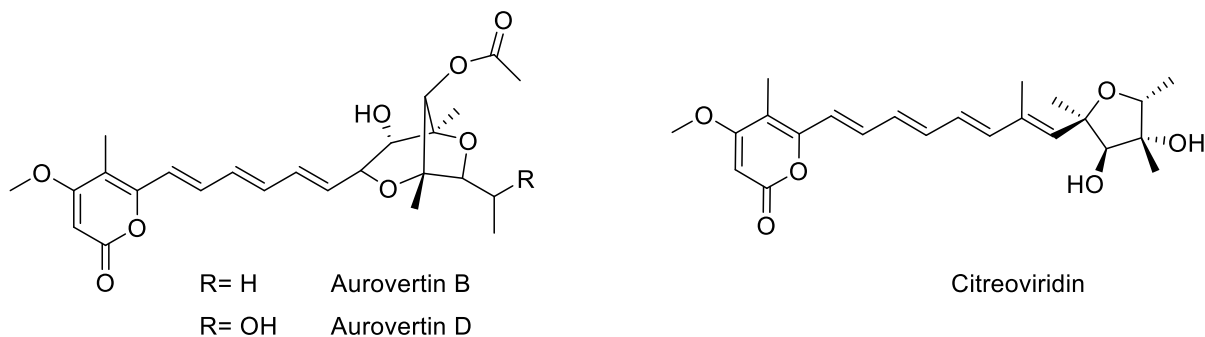
Figure 1.9. Aurovertins and related ATP synthase inhibitors

The efrapeptin family of ATP synthase inhibitors are produced *Tolypocladium sp.* and are peptidic inhibitors of ATP synthase. Efrapeptin (also known as A23871 or efrastatin) was originally isolated by scientists at Eli Lilly & Co (59) and identified as an F_1 ATPase inhibitor by Lardy and colleagues (60). Kinetic studies on efrapeptin revealed that it acted as a competitive inhibitor of ATP synthase with respect to ADP and phosphate, but an uncompetitive inhibitor of the F_1 ATPase with respect to ATP (61), which helped provide early insights into the unique mechanism of ATP synthase (62). The complete structure of efrapeptins D and F was determined by Jon Clardy in 1991 (63). Though peptides are usually thought to be cell impermeable, as non-ribosomally synthesize peptides the efrapeptins have unique features which allow them to access the mitochondria including an 'N-terminal' acetyl group, an unusual 'C-terminal' blocking group which imparts a net positive charge to the peptide, and the gem-dimethyl amino acid *o*-aminoisobutyric acid. Krasnoff and Gupta carried out extensive ecological studies on *Tolypocladium* strains for efrapeptin production which are useful for identifying producing strains (64, 65). Walker determined the co-crystal structure of bovine F_1 ATPase bound to efrapeptin, revealing a unique binding site deep inside the ATP synthase below the 'catch-1'

contact with extensive interactions between β_E and γ which prevent conversion of β_E to the

nucleotide binding confirmation ([66](#)).
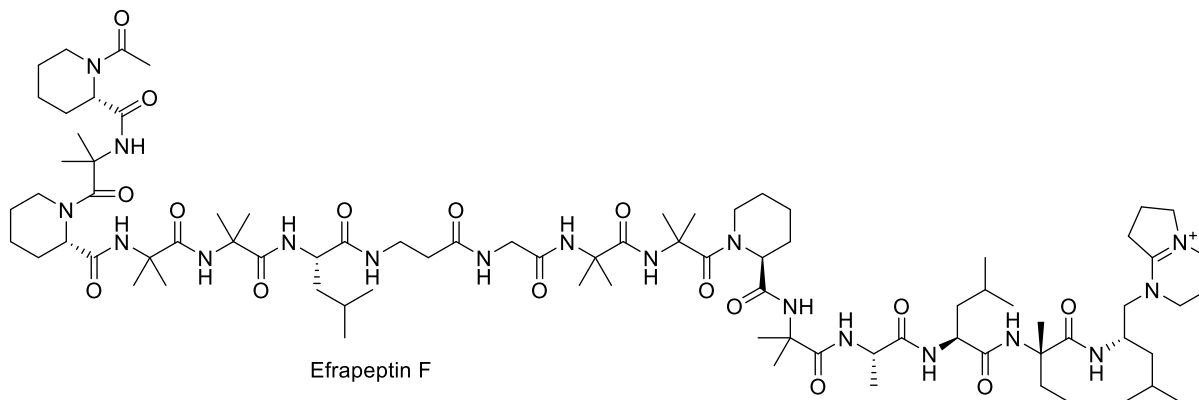
Efrapeptin F

Figure 1.10. Structure of Efrapeptin F

To summarize, ATP synthase inhibitors can be classified as F_O or F_1 inhibitors, with

oligomycin and related macrolides being the prototypical F_O inhibitors widely used as tool

compounds for those studying OXPHOS. The inhibitors of the F_1 ATPase are diverse and

include that intrinsic inhibitory factors and the fungal natural products related to aurovertin and

efrapeptin. From this literature, Walker proposed that there are four inhibitory sites in the F_1

ATPase – the active site, which can be inhibited with nucleoside analogs (AMP-PNP), and the

three allosteric binding sites for aurovertin, efrapapetin, and inhibitory factor ([67](#)). Of note,

neither aurovertin or efrapeptin are commercially available, and so both were reisolated from

their producing organisms in Chapter 2.

1.2.2 OXPHOS as a therapeutic target in cancer

Dysregulated cellular energetics is one of Hanahan and Weinberg's hallmarks of cancer.

The early models of cancer bioenergetics were heavily influenced by the work of Otto Warburg

and his 'Warburg hypothesis ([68]).' Warburg observed that cancer cells metabolize glucose to lactate in the presence of adequate oxygen, a phenomenon known as aerobic glycolysis. In Warburg's original formulation of his hypothesis, he proposed that mitochondrial dysfunction led to cancer, though in modern discussions on 'Warburg metabolism' the direction of causality is reversed – cancer cells generally make excess lactate. A simplified formulation of Warburg metabolism might be that cancer cells obtain their ATP from fermentation of glycolysis to lactate rather than OXPHOS, though recent studies have shown that this is not necessarily the case ([69]). First cancer is not a homogenous disease in regard to metabolism; some cancers, like renal cell carcinoma, are highly glycolytic while others, such as myeloid malignancies, appear to rely more on OXPHOS. Second, glycolysis and OXPHOS are not mutually exclusive and cells can use different carbon sources such as glutamate, amino acids, and fatty acids as sources of energy ([70]). Third, OXPHOS has an important role in cellular metabolism outside of generation of ATP as flux through the TCA cycle generates various metabolic intermediates which are essential for cell growth and homeostasis ([69], [71], [72]). In the past decade, there is increasing recognition that OXPHOS is a potentially targetable dependency of cancer cell metabolism that can be addressed therapeutically ([73-76]). Evidence supporting OXPHOS inhibition as a therapeutic strategy in cancer a summary of previous efforts to target OXPHOS in cancer will be more thoroughly addressed in Chapter 3.

1.3 Defining Mechanism, Chemical Probes, and Drugs

Chemical biology is the study of biological systems using chemical tools – making (or finding) chemicals and putting them into cells. The field of chemical biology is closely aligned with medicinal chemistry and pharmacology, disciplines which are dedicated to developing chemicals to address challenges in human health – drugs. Though the disciplines are closely

aligned, they differ slightly in their goals and scope of study – chemical probes vs. drugs – and therefore it useful to consider what separates a bioactive compound, from a chemical probe, from a drug. For a compound that falls in any of these categories, scientists are often interested in determining the 'mechanism of action' of a compound in a biological system. Whereas compounds, chemical probes, and drugs can be classified by generally agreed upon definitions, the term 'mechanism of action' can mean different things to different people. As this dissertation is focused on determining the mechanism of action of a class of compounds, it is useful to consider the components which define a 'mechanism of action' and how we wish to define it here.

1.3.1 Mechanism of action

The mechanism of action of a drug is usually described in terms of biological pathway diagrams such as Figure 1.2 with a flat arrow indicating which component of the pathway is inhibited by the compound. Though these diagrams appear simple, the evidence required to confidently draw such a diagram is often nuanced. Taking the example of a phenotypic screening program for a DNA damage inducer, the initial arrowhead may point to DNA and indicate 'damage.' In this case, it is important to consider how DNA damage is defined, in Chapter 6 we defined DNA damage as activation of γH2AX which is more precisely part of the DNA damage response ([77](77)). Though markers like γH2AX may be easier to measure than damaged DNA, there may be factors (cell cycle, replication stress, etc..) which influence the connection between DNA damage and γH2AX which may confound the interpretation of these data. Similar issues arise for defining apoptosis which can be assayed via Caspase activation, DNA fragmentation, Annexin V exposure, PARP cleavage or other markers. In the case of natural products discovery, these 'rough' assessments of mechanism may be the only assays completed at the time a structure is

solved and published, leading investigators to name compounds like "*apopto*lidin" based on their ability to induce *apopto*sis.

As investigations into a compounds mechanism of action continue, scientists seek to narrow these definitions to focus on specific proteins or targets – instead of causing DNA damage, a definition may focus on the specific type of DNA damage (alkylation, intercalation, etc…), its effects on the cell (p53, γH2AX, etc…) or how it is repaired by the cell. Often times, these descriptions will focus on a specific 'target' which is thought to be responsible for the effects. In the case of target-based screening efforts, these specific molecular targets form the foundation of their mechanism. Evidence supporting the assignment of a specific target may take the form of phenocopying a genetic knockout, rescue by genetic overexpression, evidence of target engagement *in vivo* or *in vitro* in the form of inhibition or binding assays, or identification of resistance mechanisms. Some of this evidence can support that a molecule binds to its putative target, but it cannot necessarily exclude that additional targets are either involved or entirely responsible for its effects.

The challenge of assigning the 'mechanistic target' of a compound vs. a bystander target requires excluding all other possible targets. One of the most troublesome examples of where these target identification and validation efforts can fall short is the case of pan-assay interference compounds or PAINS (78-81). The classic example of this class of compounds is curcumin – a polyphenol present in turmeric for which many molecular 'targets' have been proposed (Figure 1.11). Though curcumin may cause a desirable effect in cell culture and may inhibit an enzyme *in vitro*, it also hits many other targets and therefore one cannot exclude that one of these other targets may be responsible for its observed activity. Much effort over the last decade in drug screening has been dedicated to 'triaging' such non-specific activity which would

otherwise consume limited research effort. It should be noted that the presence of secondary or alternative targets does not necessarily preclude a well-defined mechanism as a compound may have different targets in different settings. One of the most prominent example of such a mechanism is the immunomodulatory imide drug (IMiDs) such as lenalidomide, a thalidomide derivative, which can target different proteins for degradation in different settings ([82], [83]).
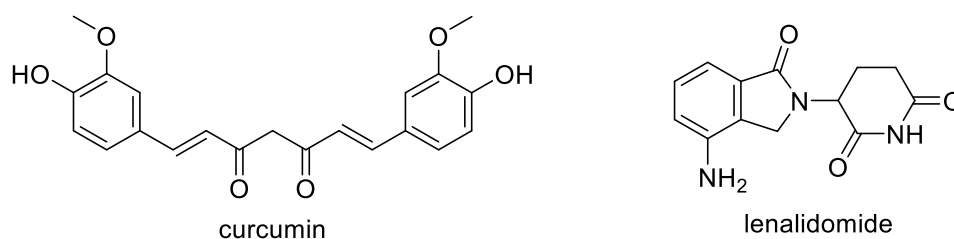
Figure 1.11. Structures of compounds with multiple targets

Thus far, we have discussed the challenge of defining a 'mechanism of action' in a reductionist model – aiming to dissect the biological system into smaller and smaller pieces to permit a more precise definition of mechanism. A full understanding of a compounds mechanism can also include ever more general understandings of its effects to understand the 'systems-biology' of a phenotype. Schreiber's work on tacrolimus ([84]) and trapoxin ([85]) may have identified their molecular targets as calcineurin and histone deacetylases (HDACs), but his mechanism did not explain why inhibition of calcineurin inhibits the activity of T-cells to prevent organ rejection or how histone acetylation modulates transcription and cellular differentiation. Even in the case of antibiotics whose mechanisms are thought to be well understood (cell-wall biosynthesis, ribosome, etc…), our understanding of how these inhibitors actually cause cell death is still evolving ([86]). Though a systems level understanding of how modulation of a target induces its observed effects on cells may take decades, one of the major

contributions of chemical biology to biology at large is the provision of well validated probe

compounds to biologists studying these pathways.

1.3.2 Chemical probes vs drugs

To delineate between chemical probes and drugs, we turn to Arrowsmith et al.'s

commentary "The promise and peril of chemical probes (87)." At the most basic level, chemical

probes are compounds use for research purposes to study biological systems while drugs are

compounds used to treat human disease. Though there are compounds which can be considered

both chemical probes and drugs, the demands of application are unique.

DRUGS
Must be safe
and effective

PROBES
Ask a specific
biological question

- May have undefined MoA
- IP restrictions; limited availability
- Must have human bioavailability
- High bar for physicochemical (guidelines for MW, lipophilicity, etc.) and pharmaceutic properties (stability, reasonable and economic synthesis, defined crystallization form, etc.)

- Defined MoA is required
- Needs selectivity
- Freely available (both the physical compound itself and activity data)
- Drug-like properties, such as bioavailability, not necessarily required
- Value is markedly enhanced by use of structurally related inactive and structurally unrelated active compounds

Figure 1.12. Definitions of Drugs and Chemical Probes from Arrowsmith et al., 2015

As alluded to above, chemical probes are used to study specific biological pathways,

therefore one of the principal considerations is validating that they act specifically on their

putative targets or if they act non-specifically, the scope of their non-specific activity is well

defined. For better or worse, the demand from biology for chemical probes often exceeds

chemical biology's ability to generate and validate such probes. This has led the literature and

30

supplier catalogs to fill with poorly validated probes, or in some case, probes with documented

contradictory evidence that they act on additional targets or do not act on their putative target at

all. The Target 2035 initiative is an ambitious attempt to address this gap by creating validated

chemical probes for all ~20,000 proteins in the human proteome by 2035 (88). In the meantime,

it is important to carefully scrutinize the evidence supporting the validation of chemical probes

before using them to address specific biological questions.

Whether a compound can be considered a drug or not is determined by regulatory

agencies, in the United States – the food and drug administration (FDA), who ascertains whether

a compound is both safe and effective. A drug does not necessarily need to function through a

defined mechanism of action to be approved, though a mechanistic understanding can be very

helpful to guide medicinal chemistry optimization, toxicity assessments, and pharmacodynamic

markers. Many widely used drugs entered the pharmacopeia before the development of

molecular biology and were thus approved without knowledge of their molecular mechanism.

Examples included non-steroidal anti-inflammatory drugs (NSAIDs), metformin, and cardiac

glycosides. In cancer therapy, there is emerging evidence that some drugs, such as

anthracyclines, which were thought to act via a defined mechanism, may actually gain some of

their therapeutic activity via 'off-target' effects (89, 90).

One recent example highlighting the difference between chemical probes and drugs was

Lin et al.'s 2019 study with the provocative title "Off-target toxicity is a common mechanism of

action of cancer drugs undergoing clinical trials (91)." Lin et al. studied drugs which had entered

clinical trials that were 'designed' to address putative cancer dependencies. In particular, they

focused on drugs which lacked known mutations on their target which conferred resistance to the

drug, which they proposed at the 'gold standard' of mechanism of action validation. Using

CRISPR-Cas9, they knocked out each of the putative targets and found that cancer cells were not, in fact, dependent on those targets. Though each drug's putative target had been genetically ablated, many remained active in cellular assay, suggesting that their efficacy derived from an 'off-target' effect. In one case, they were able to identify the 'true' target of a putative PBK inhibitor, OTS964, as CDK11 by sequencing cells that had evolved spontaneous resistance to OTS964 by passage in increasing doses of the drug. To validate the putative target, they used CRISPR-Cas9 to knock-in the identified resistance mutation, demonstrating that introduction of a resistant variant was sufficient to eliminate OTS964s activity.

This example is illustrative of the challenge of defining mechanism of action, chemical probes, and drugs. Lin's study does not refute that OTS964 is a PBK inhibitor; the evidence from the original studies on OTS964 demonstrates that it does inhibit PBK (92). The study also does not refute that OTS964 is a clinically useful drug or that its evaluation in clinical trials was unwarranted. Rather, it demonstrates that OTS964 achieves its anti-cancer efficacy via inhibition of CDK11. It is tempting to revise the catalog page for OTS946 to reflect is mechanism as PBK and CDK11 inhibition, though its lack of specificity arguably disqualifies it from classification as a chemical probe. Arrowsmith et al. highlight similar issues with dorsomorphin (87), which has been suggested to act as both an AMPK inhibitor (93), an BMP signaling inhibitor (94), and a AKT/mTOR inhibitor independent of its AMPK activity (95).

To summarize, chemical probes are research tools whose principal requirement is that they act through a defined mechanism of action while drugs are compounds use to treat human disease which have been demonstrated to be safe and effective. Though not required, a detailed understanding of a drug's mechanism of action is useful for, guiding medical chemistry optimization and biological applications, assessing on and off target activity, and anticipating

toxicity. The concept of a mechanism of action can different things to different investigators and at different stages in a compound's development.

For the purposes of this dissertation, we will consider three categories of evidence which can be used to define a proposed mechanism of action [adapted from the framework proposed by Scholes et al. for small molecule degraders (96)]:

1. Assessment of induced cellular phenotypes and effects consistent with known signaling pathways. (e.g. measurements of kinase substrate phosphorylation, DNA damage, apoptosis, etc.…)
2. Evidence of direct target engagement *in vivo* and/or *in vitro*. (e.g. chemoproteomics, cryoEM/crystal structure, *in vitro* binding assessment using interferometry, *in vitro* enzymatic assays, etc.…)
3. Evidence of genetic dependencies. (e.g. CRIPSR screens, identification of resistance mutations, etc.…).

All three categories of evidence – induced phenotypes, target engagement, and genetic dependencies – are required to confidently define a compound's mechanism of action.

1.4 Selectively Cytotoxic 20-membered Glycomacrolides and Efforts to Understand their Mechanism

As discussed above, one of the major discoveries of late 20th century cancer biology was the discovery of oncogenes and proto-oncogenes. Though cancer cell lines were available by the 1960s and 1970s, they were derived from spontaneous cancers from humans or rodents that could be grown *ex vivo*. The discovery of oncogenes, recombinant DNA technology, and the phenomenon of 'transformation,' allowed researchers to create molecularly defined models of cancer that could be studied in the laboratory. Importantly, these new cell lines were 'isogeneic' – each transformed cell line had a corresponding non-transformed 'parental line' that it could serve as a control. While Baltimore, Varmus, and colleagues, were using these models to study

the molecular drivers of cancer, these isogeneic transformation models also provided ripe opportunity to search for selectively cytotoxic anticancer compounds.

In the 1990s, a group led by Haruo Seto at the university of Tokyo undertook just such an effort. Instead of screening for compounds which that were cytotoxic to cancer cells, or screening for compounds which inhibited the activity oncogenes *in vitro*, they searched for compounds which were toxic towards oncogene transformed cells but not their untransformed parental lines ([97]). Specifically, they screened for compounds which selectively induce apoptosis in E1A/E1B transformed rat fibroblasts and glial cells, but not the parental cell line.

The E1A protein and gene are derived from human adenoviruses – the most studied version being the E1A gene encoded by the type Ad5 adenovirus[3]. In humans, adenoviruses are a frequent cause of the common cold rather than cancer, but in cell culture models they are capable of introducing transformation. As alluded to in the discussion of the Abelson virus and Bcr/abl, viral oncogenes often encode homologs of human proto-oncogenes which makes them useful models of cancer. Specifically, the E1A gene product acts as a negative regulator of the Rb protein which controls cell cycle entry; when E1A binds to Rb, it removes this repression and induces the cell to enter the cell cycle in the absence of normal growth signals – transformation (Figure 1.13). Normally, this abnormal cell cycle entry would be recognized by the anti-apoptotic factor MCL-1 or by the tumor suppressor p53, each of which are capable of initiating apoptosis. The pro-apoptotic effects of E1A transformation are countered by the anti-apoptotic effects of the E1B gene which encodes two proteins E1B-19k and E1B-55k. E1B-19k is a homolog of the BCL-2 family protein MCL-1 whose overexpression can block apoptosis, while

---

[3] The Ad5 adenoviral vector was used in the Johnson & Johnson Covid-19 vaccine.

E1B-55k acts as an inhibitor of p53. For successful transformation, both E1A, E1B-19k and

E1B-55k must be present.
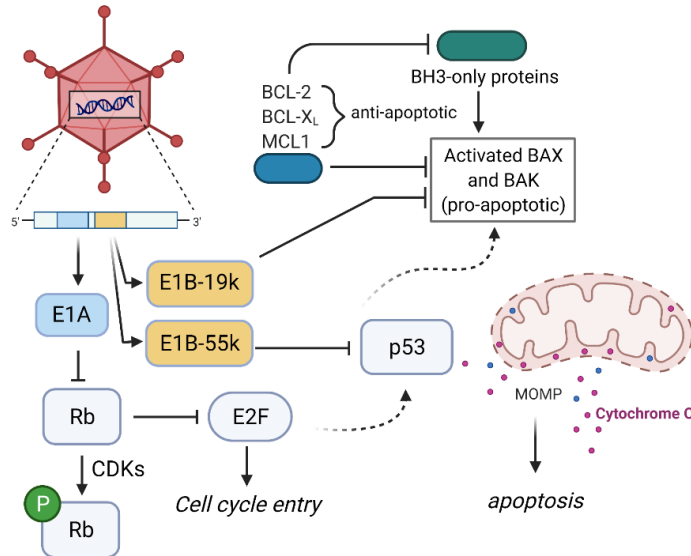
Figure 1.13. Oncogenic Transformation by E1A/E1B oncogenes

1.4.1 The apoptolidins

In their program for screening for selectively cytotoxic anticancer cancer compounds, the

Seto group generated isogeneic rat cell lines which were transformed with E1A alone, or E1A in

combination with E1B-19k and/or E1B-55k. Among the compounds identified using this

screening system was apoptolidin (apoptolidin A), produced by the actinomycete strain

Nocardiopsis sp. FU-40 (98). After 24 hrs of treatment with 1 μg/mL apoptolidin (~ 1 μM), E1A

transformed rat fibroblasts were observed to exhibit features consistent with apoptosis –

condensed chromatin, fragmented nuclei, and fragmented DNA. Interestingly, apoptolidin was

also able to induce apoptosis in rat fibroblasts transformed with E1B-19k and or E1B-55k, the

factors which normally protected E1A/E1B transformed cells from apoptosis. This was true in

both rat glial cells, as well as the 3Y1 rat fibroblast cell line. No cytotoxicity was observed in the

parental lines, or in 3Y1 cells transformed with various other oncogenes, including H-*ras*, v-*src*, or SV40 large T-antigen ([98](#)).

Seto and colleagues went on to determine the structure of apoptolidin by NMR ([99](#)). Apoptolidin is classified as a polyketide, and more specifically a macrolide, with its C19 hydroxyl joined to the C1 carboxylic acid by an ester linkage. A hemiketal is formed by the linkage between C21 and C25. Beyond the polyketide core, apoptolidin A is decorated with three sugars, 6-deoxy-4-*O*-methyl-L-glucose at the C9 position and a disaccharide (D-oleandrose and L-olivomycose) appended to the C27 position. Using NOESY correlations, Seto proposed the stereochemistry at each position, which was later confirmed by KC Nicoleau's total synthesis of apoptolidin ([100](#)). Apoptolidin A was later joined by apoptolidins B ([101](#)), C ([101](#)), D ([102](#)), E ([103](#)), and F ([103](#)), which were found as minor products of FU-40 by Paul Wender's group. Bachmann and Sulkowski identified apoptolidin G ([104](#)), which is formed by UV-light induced isomerization of the C2-C3 double bond, as well as apoptolidin H which was produced by *Nocardiopsis sp* FU-40 ΔGT2 (knockout of the GT2 glycosyltransferase) ([105](#)). More recently, Taifo Mahmud's group at Oregon State University discovered succinylated apoptolidins produced by an alternative producer *Amycolatopsis sp.* ICBB 8242 ([106](#)), which can also be detected in in extracts of *Nocardiopsis sp.* FU-40. In the course of their studies on Apoptolidin, both Sulikowski ([107](#)) and Wender (in collaboration with Seto) ([108](#)) also identified a ring-expanded form of apoptolidin, which they named 'isoapoptolidin,' which results from a ring expansion from C19 to C20. Apoptolidin and isoapoptolidin were found to exist in equilibrium with one-another, with complete equilibration in ~30 hrs.
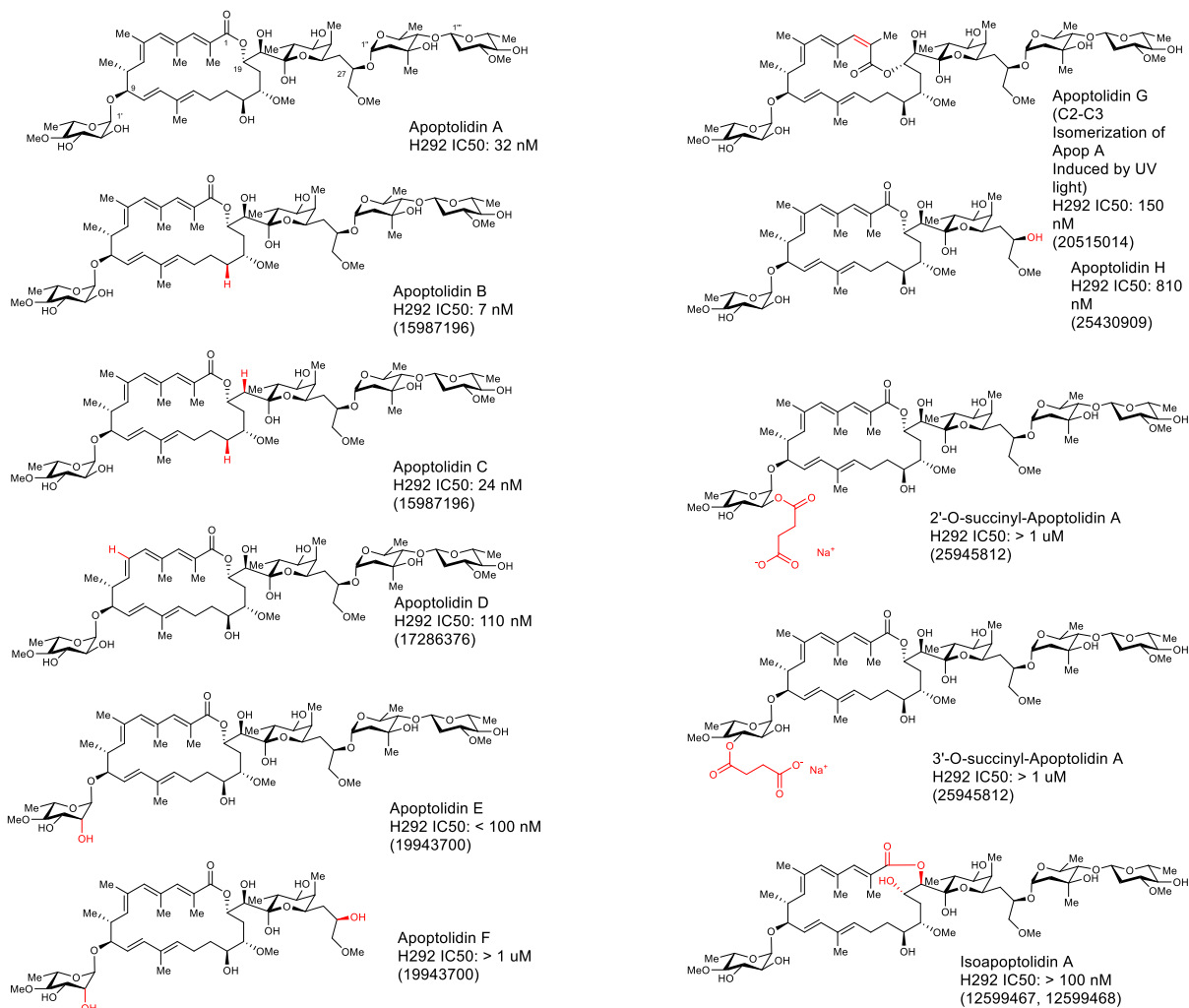
Figure 1.14. Structures of naturally occurring apoptolidins

1.4.2 The ammocidins

In addition to the apoptolidins, two other groups of selectively cytotoxic 20-membered glycomacrolides have been identified – the ammocidins and the amycolatopsins. The ammocidin were discovered by Hayakawa's group[4] at the University of Tokyo in collaboration with Seto

---

[4] Hayakawa was the first author on the apoptolidin A papers

and the Japanese pharmaceutical company Ajinomoto Co ([109](#)). The ammocidin producer, *Saccharothrix sp.* AJ9571 (AJ = Ajinomoto) was originally isolated from the Tottori sand dunes in Japan by Takauki Kaijura ([110](#)). The name ammocidin originates from the word "ammos" meaning 'sand' in Greek ([110](#)). As was the case for the apoptolidins, ammocidin A was discovered in a screen for compounds which selectively induce apoptosis in transformed cells while sparing healthy cells. Instead of using E1A transformed rat fibroblasts, Murakami *et al.* conducted their screen in BaF3 cells which were transformed using H-Ras-G12V, a constitutively active form of H-Ras. This system is very similar to the one used by Daley and Baltimore to demonstrate that Bcr/Abl was a bona-fide oncogene. In their initial studies on the bioactivity of ammocidin Murakami et al. also noted the induction of apoptosis in the HRasG12v transformed cells, with growth suppression, but no apoptosis in the parental line which was grown in the presence of IL-3. In addition to cytotoxicity assessments, Murakami also examined the signaling downstream of Ras including ERK and S6K, and found that phosphorylation of both was suppressed by treatment with ammocidin A ([109](#)).
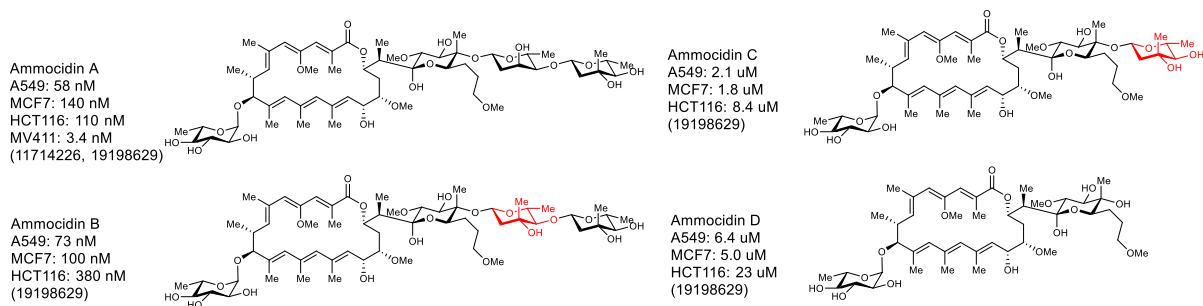
Figure 1.15. Structures of the Ammocidins

The structure of ammocidin A resembles apoptolidin A in many ways – both compounds are polyketides with a 20-membered macrolide core, a hemiacetal, and three sugars, with one

38

being a 6-deoxyglucose at C9 (111). There are several notable differences between the two compounds. Unlike apoptolidin, ammocidin has a methyl group at C20 rather than a hydroxyl, which prevents it from isomerizing into an iso-apoptolidin like molecule. The disaccharide is attached at C24 rather than C27, and the two sugars are switched with the branched olivomycose attached to β-digitoxoside rather than directly to the polyketide. At the C9 position, ammocidin lacks an O-methyl at the C4' position, while at the hydroxyl at C16 is thought to have the opposite stereochemistry relative to apoptolidin (112), though this assignment has not been confirmed. Beyond ammocidin A, Murakami and colleagues went on to describe three additional ammocidins B, C, and D (113) (Figure 1.15).

1.4.3 The amycolatopsins

The amycolatopsins were identified by RJ Capon's group at the University of Queensland, Australia (114). The producing strain *Amycolatopsis sp.* MST-108494, was isolated from soil samples collected near Port Augusta, Australia, and the active extract identified in a screen for compounds with activity against mycobacteria. The amycolatopsins appear to share features of both ammocidin and apoptolidin, with a similar scaffold to ammocidin A, but with the addition of the C4' OMe found in apoptolidin. Unlike apoptolidin or ammocidin, amycolatopsins A and C have a hydroxyl appended to the C6 methyl group, which they postulates is important in determining its activity against mycobacteria (114).
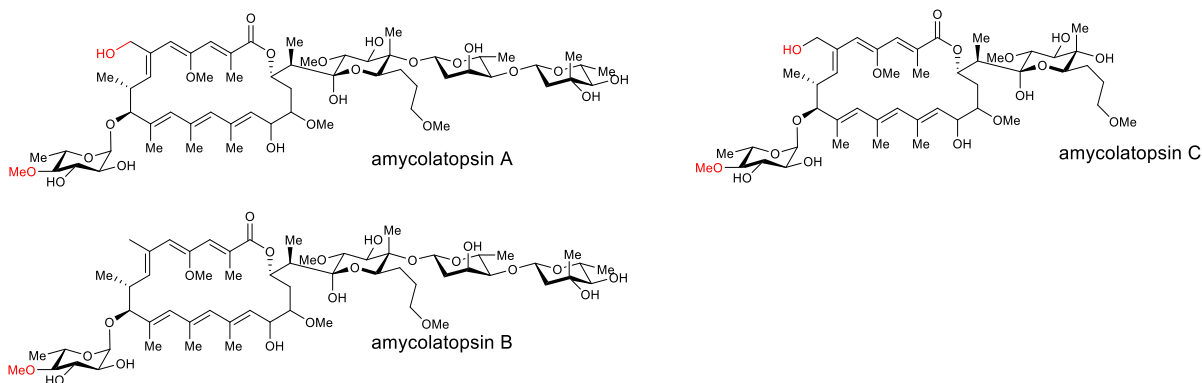
Figure 1.16. Structures of the Amycolatopsins

1.4.4 Khosla's Studies on the Mechanism of Action of the Apoptolidins

The remarkable selective cytotoxicity of the apoptolidins towards oncogene transformed cells prompted a search for their molecular target. The first to undertake this challenge was the Khosla Group at Stanford University, led by first author A Salomon ([115]). Initially, Salomon *et al.* examined whether apoptolidin induced apoptosis in a p53 dependent or independent manner using isogeneic cell lines. They observed that the EC_{50} of apoptolidin did not change in the p53 wt or p53 -/- cells, from which they concluded that apoptolidin induced apoptosis in a p53 independent manner ([115]). Next they examined whether apoptosis was dependent on BCL-2 expression using isogenic cell lines, finding that BCL-2 overexpression prevented apoptolidin induced apoptosis and concluding that apoptolidin acted upon a mitochondrial associated target ([115]).

In order to narrow the search for the apoptolidin target, Salomon submitted apoptolidin to the National Cancer Institutes (NCI) NCI-60 screening program, which assesses growth inhibition and cytotoxicity across 60 different cell lines ([116]). As tens of thousands of compounds have been screened across the same 60 cell lines, compounds with similar selectivity

profiles can be grouped together and one may hypothesize that they act via a similar mechanism. Using such an approach, Salomon proposed that apoptolidin could be grouped together with cytovaricin, ossamyicin, and oligomycin – inhibitors of the mitochondrial F_OF_1 ATP synthase. As evidence supporting a common grouping of these four inhibitors, Salomon observed that all four could be classified as macrolides and therefore shared a common SAR and binding mode – on the F_O portion of the ATP synthase ([115](#), [117](#), [118](#)). To confirm that apoptolidin was acting as an ATP synthase inhibitor, Salomon *et al.* evaluated its ability to inhibit the ATPase activity of isolated yeast mitochondrial and observed that it did act as an ATPase inhibitor with a K_i of 5 μM.

Salomon and Kohsla's efforts to dissect the mechanism of action contributed much to our early understanding of the mechanism of action of the apoptolidins, coming just three years after the discovery of apoptolidin. As shall be addressed in chapter 2, their conjecture that apoptolidin is an ATP synthase inhibitor proved to be correct. However, with 20+ years of hindsight, it is evident that some of their conclusions regarding the apoptolidins were premature. The title of Salomon's 2021 PNAS paper was: "Apoptolidin, a selective cytotoxic agent, is an inhibitor of F_0F_1-ATPase." On close examination, this tile makes two statements about apoptolidin: 1. Apoptolidin is a selective cytotoxic agent; and 2. Apoptolidin is an inhibitor of the F_OF_1-ATPase. It is tempting to connect these two statements – to conclude that apoptolidin's selective cytotoxicity is due to its activity against the F_OF_1-ATPase, however, this conclusion could not be made at the time. The gap between these two findings is raised the question as to whether the selective cytotoxicity of apoptolidin was due to its activity against ATP synthase or whether ATP synthase inhibition is an off-target effect and its true *mechanistic* target lay elsewhere.

Salomon and Khosla attempted to bridge this gap with their structural comparison of apoptolidin to other known ATP synthase inhibitors. As discussed in the previous section, the mechanism of action of oligomycin against the F_O portion of ATP synthase was well understood. If apoptolidin acted in the same manner as oligomycin, then one could reasonably conclude that apoptolidin achieved its selective cytotoxicity via inhibition of ATP synthase. Salmon noted that truncated analogs of apoptolidin, lacking the disaccharide, exhibited reduced activity 5 μM → 10 μM against the yeast enzyme *in vitro,* and 100 nM → 10 μM against sensitivity LYas cells (117). From this data, they concluded that the disaccharide was dispensable for activity against the ATP synthase, but was important for transport to the mitochondria. Focusing their comparison on the macrolide core of apoptolidin and oligomycin, Salomon proposed that the partially reduced 20-membered macrolide ring of apoptolidin was sufficiently similar to the partially reduced 26-membered macrolide ring of oligomycin to conclude that they could be classified together.

1.4.5 SAR Studies on the apoptolidin family glycomacrolides

Note that there are many more studies than are summarized here on the SAR of apoptolidins using fragments of apoptolidin derived by total synthesis. Much effort has been dedicated by multiple groups towards the total synthesis of apoptolidin and apoptolidin analogs, however pure synthetic studies are not the focus of this thesis. For excellent summaries on synthetic efforts to access apoptolidins see (100, 119-123).

Salomon's work focused on the mechanism of action of 'apoptolidin', rather than 'apoptolidin A,' as his work took place before the discovery other apoptolidin family members. As apoptolidin analogs were discovered by fermentation, semi-synthesis, and genetic engineering, many were assayed in the context of both selective cytotoxicity and ATP synthase inhibition. The study of how a compounds structure influences its bioactivity is known as

structure-activity-relationship (SAR) studies. By deliberately modifying a compound at one or more positions (or taking advantage of nature's modifications), one can infer the relative contribution of each chemical feature to their biological activity. If a modification greatly reduces the activity of a compound that position is likely important for its interaction with the target. Alternatively, if a modification does not greatly influence a compounds bioactivity that position is likely not involved with binding to its target and may be a good site to attach a probe functionality or to modify the pharmacological properties of a compound.

Examining the SAR of the naturally occurring apoptolidins, one of the striking features is that most analogs have similar low-mid nanomolar activity, despite addition or removal of various hydroxyl or methyl groups. Using apoptolidin A as a starting point, apoptolidin B, lacking the C16 hydroxyl, is ~3 fold more potent, while apoptolidin D, lacking the C6 methyl group is ~3 fold less potent – suggesting that the C6 and C16 are important positions for apoptolidin's interaction with its target. Apoptolidins F and H, lacking the C27 disaccharide are significantly less active (> 10 fold) than apoptolidin A, indicating the disaccharide is also important. This is further supported by comparing the activity of ammocidin D to ammocidin A, which also exhibits a large drop in activity with loss of the disaccharide. A similarly substantial drop in activity is noted for isoapoptolidin compared to apoptolidin, though these assays are confounded by the conversion of isoapoptolidin to apoptolidin under normal cell culture conditions. Nonetheless this suggests that the 20-membered macrolide is an important feature of bioactive apoptolidins whereas 21-membered isoapoptolidin is not active. The succinylated apoptolidins are also notable for their lack of activity again purified ATPase. As the addition of a succinyl group imparts a negative charge to apoptolidin, if the target of apoptolidin were in the mitochondria a drop in activity is not entirely surprising, as respiring mitochondria have a net

43

negative charge which increases their affinity for positively charged compounds whereas negatively charged metabolites must be actively transported or shuttled into the mitochondria as neutral intermediates.

Paul Wender's group set-out to characterize the SAR of the apoptolidins via a semi-synthetic approach – using naturally occurring apoptolidins as a starting point for making new synthetic analogs. In his first paper on the SAR of the apoptolidins, Wender and Jankowski set out to 'scan' each of the hydroxyl groups adding a methyl, acyl, or benzyl group at each position, using a protecting group strategy ([124]). The results of their studies are summarized in Figure 1.17. Consistent with the SAR of the naturally occurring apoptolidins, the change in EC_{50} for the various analogs are relatively small (under a factor of 10). The most notable change is seen with acylation of C16 which results in a nearly 10-fold loss of activity. Acylation or benzoylation of the C2' or C3' positions approximately doubled the potency of apoptolidin A, and though this effect is small it is consistent with the results reported in Chapter 3.

compound	Gi$_{50}$ (µM) (Ad12-3Y1)	Gi$_{50}$ (µM) (3Y1)	IC$_{50}$ (µM) ATPase
1 apoptolidin A	0.0065	1	0.7
2 C2'-OBz	0.0036	1	0.3
3 C4'''-OAc, C23-OAc	0.0095	0.5	0.4
4 C4'''-OAc	0.0098	1	0.8
5 C16-OAc	0.56	1	0.8
6 C3'-OAc	0.0027	1	0.4
7 C20-OAc	0.011	1	1.1
8 C20-OMe	0.012	1	2.8
9 C21-OMe	0.016	1	2.3
10 isoapoptolidin	0.009	1	17
11 macrolide, C20-OH	5.4	7	13
12 macrolide, C20-OMe	1.4	5	16
13 macrolide, C20-OBz	2.4	16	32
14 δ-lactone	12	12	190
15 Diels-Alder adduct	3.2	5	2.1
16 oligomycin	0.0002	3.3	1

apoptolidin A

δ-lactone

macrolide

Diels-Alder adduct

Adj. R² = 0.46

Figure 1.17. Wender's SAR studies on Semi-synthetic apoptolidins

Wender continued his studies on the SAR of the apoptolidins and published his expanded results in 2006, including derivatives based off the apoptolidin macrolide core, the disaccharide and δ-lactone alone, and a Diels-Alder adduct formed by addition at C10-C13. With these compounds in hand, Wender was able to correlate their activity *in vivo* (against E1A transformed rat fibroblast) against their activity *in vitro* (against yeast ATPase). Though these results appear to show a correlation against *in vivo* and *in vitro, o*ne of the most striking features of this plot is the change in scale between the two assays nearly – each compound is nearly 100-fold less potent *in vitro* then *in vivo*. Kohsla and Salomon observed the same discrepancy and postulated that the basic pH (~8.5) of the ATPase assay may have influenced their activity – though the mitochondrial matrix is similarly basic. In addition to the change in the magnitude of activity between the two assays, Wender noted that compound the C16-OAc analog and Diels-Alder adduct lost cellular activity but largely retained their *in vitro* activity. These discrepancies led

45

Wender to conclude that "Inhibition of ATP hydrolysis mediated by mitochondrial F_0F_1-ATPase isolated from yeast is not sufficient to predict the potency and in some cases relative activity order of new compounds in a cell-based assay." He further went on to question where a "more relevant secondary biological target of apoptolidin exists that gives rise to its observed cellular effects."

1.4.6 Wender's apoptolidin photoaffinity probes

The following two decades of research on the apoptolidins following their discovery were focused on determining whether apoptolidin could be considered part of the 'oligomycin family' of F_O ATP synthase inhibitors and whether there were additional and/or alternative targets of apoptolidin that could account for its selective cytotoxicity. The classic approach to identifying the targets of bioactive molecules is to design a probe compound which can be followed to 'fish out' the molecular target from the complex milieu of the cell – a process called 'target identification' or 'Target ID'. The earliest iterations of this approach utilized radioactive analogs of the compounds that would stick to their target and provide a signal that could be tracked in the process of purifying the target. A more modern approach is to design an 'affinity' probe of the molecule that can be affixed to a solid support which can be used one of two ways. In one approach, the probe molecule is attached to the solid support and cell lysates are passed across the support where the target molecule will stick to the support while non-target molecules can be washed away. The target protein is then 'eluted' by cleaving the probe from the resin or by incubating the resin with an excess of the parent molecule which competes with the probe and allows the target protein to elute from the resin. Such an approach was taken by the Schreiber group in their studies on FK506/Tacrolimus(125, 126) and Trapoxin (85).

Alternatively, the probe molecule can be designed to be applied directly to live cells where it can interact with its targets as a bifunctional probe. One end of the probe is designed to mimic the interactions of the parent compound, while the other end of the probe has an affinity handle such as biotin which allows for enrichment. For compounds which act as covalent inhibitors, the probe chemically attaches to the target protein. For compounds which act as non-covalent inhibitors, photo-affinity moieties can be added to the probe to facilitate covalent attachment after target binding. Once the probe is covalently attached, the cells are lysed, and the tagged lysates are applied to an affinity resin which recognizes the affinity handle functionality of the probe, i.e., biotin-streptavidin. The non-attached proteins can then be washed away, followed by cleavage of displacement of the affinity handle from the solid support, allowing the enriched targets to be identified.

The first known attempt to identify the apoptolidin target via affinity enrichment was pursued by Jankowski, a student of Paul Wender, however the results were never published outside of Jankowski's thesis ([127]). Jankowski attached various photo-affinity groups to apoptolidin A obtained by fermentation, targeting the C9 sugar which is both most reactive to acylation and was thought to be outside the pharmacophore (see discussion of SAR). Unfortunately, Jankowski's photoaffinity probes were not active in live cells, precluding their use to label apoptolidin targets *in situ*. Undeterred, Jankowski applied his probes to cell lysates from sensitive cell lines (MCF-7 and H292) and searched for specific protein bands. In order to delineate specific from non-specific bands, Jankowski treated cells with or without un-modified apoptolidin in 'competition experiments.' If the interaction between the probe and target was specific, the interaction should be outcompeted by an excess of the parent compound. Unfortunately, no such specific interactions could be identified using the biotin photoaffinity

probes together with excess apoptolidin. Jankowski did note that at least one band was competed by excess (50 μM) oligomycin, which led him to the conclusion that apoptolidin, or one of its isomers, shares a binding site with the target of oligomycin.
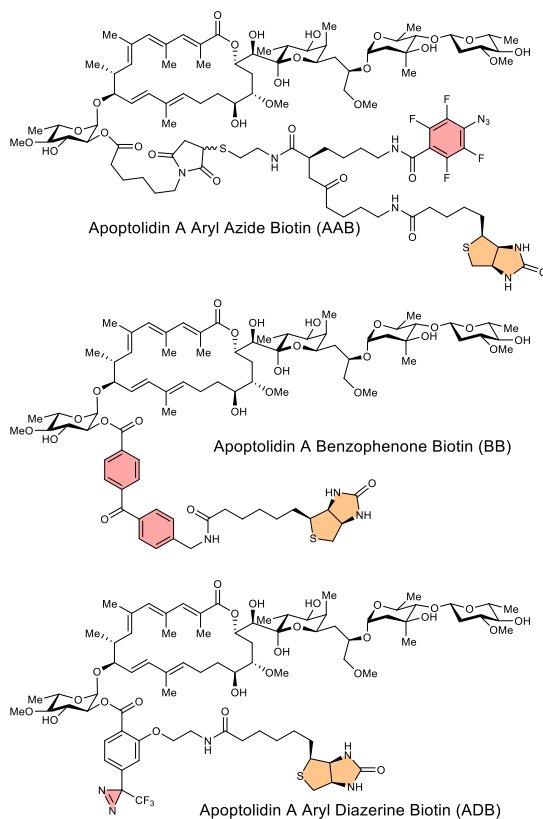
Figure 1.18. Jankowski's Apoptolidin Photoaffinity Probes from Jankowski, 2004.
Photo-reactive group highlighted in red, affinity tag (biotin) highlighted in orange.

1.4.7 Sulikowski's 'clickable' apoptolidin probes

One of the drawbacks of Wender and Jankowski's approach was that their photoaffinity probes were not active in cells, casting doubt on whether they are still able to bind to their apoptolidin target. To circumvent this challenge, Deguire and Sulikowski, in collaboration with the Bachmann group, designed a series of 'clickable' probe derivatives of apoptolidin A which

retained activity in live cells. Like Jankowski, Deguire chose the C9 sugar as his site for modification. The major difference between Deguire and Jankowski's approach is that Deguire split his affinity tag into two smaller parts, a minimal alkyl azide which was attached to the C9 sugar, and a larger alkyne 'tag' portion consisting of a fluorophore or biotin which could be azide using 'click chemistry.' Click chemistry is a form of 'bio-orthogonal' labeling – bio-orthogonal indicating that these functionalities do not [ordinarily] occur in nature. In the presence of a copper catalyst an azide reacts with an alkyne via an azide-alkyne Huisgen cycloaddition. This reaction occurs with exceptionally high yield and proceeds at room temperature in aqueous buffers, making it very well suited for studying biological molecules such as protein and nucleic acids ([128]).

Where Jankowski's probes did not specifically label structures in the cell or suppress their proliferation, Deguire's did both. Using a Cy3 apoptolidin probe, Deguire was able to visualize localization of the probe to the mitochondria, the location of ATP synthase ([129]). However, cyanine probes such as Cy3 are also known to localize to the mitochondria on their own, which led to the conclusion that mitochondrial localization of the apoptolidin probes did not greatly affect their antiproliferative effects, supporting, but not proving, that the mechanistic target of apoptolidin lay in the mitochondria. The Sulikowski group went on to utilize Deguire apoptolidin A and H Cy3 probes to study their uptake in healthy (PBMC) and malignant cells ([130]). Notably, the cancer cell lines (A549, U87, LN229, SW620) exhibited higher uptake of apoptolidin A and H than healthy PBMCs. Uptake of apoptolidin A Cy3 and apoptolidin H Cy3 were broadly similar.
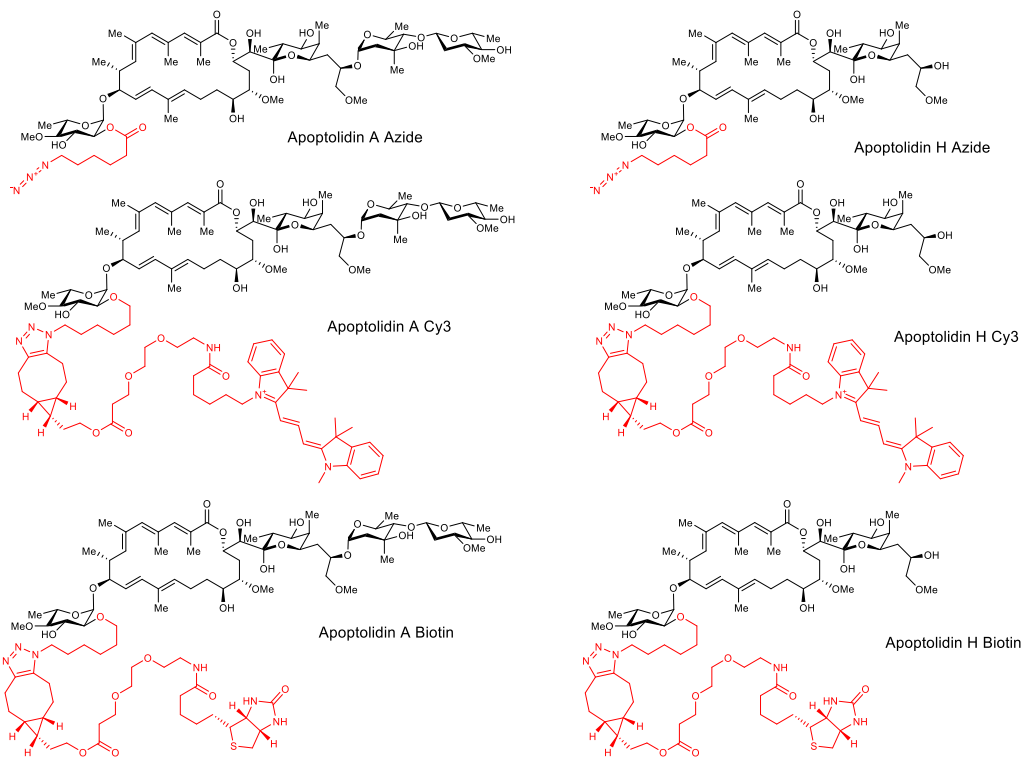
Figure 1.19. Deguire's Apoptolidin A and H probes

1.5 Statement of Dissertation

The central challenge of developing safe and effective cancer therapeutics is obtaining selective cytotoxicity towards cancer cells while sparing healthy cells. Early efforts to find selectively cytotoxic therapeutics provided the first proof that cancer could be treated and even cured used chemicals – chemotherapy. The last half-century of research in cancer biology has provided many insights into the molecular events which initiate and sustain cancer and targeted therapies developed using those insights have revolutionized the treatment of many cancers. However, these targeted therapies have fallen short for many cancers, particularly acute myeloid leukemia where most patients are still treated with a cytotoxic regimen developed in the 1970s. Natural products have proven a valuable source of anticancer compounds and studies on the

mechanism of action of natural products have provided insights into cancer dependencies which were not easily accessible by genetic tools alone.

This dissertation attempts to address these gaps in cancer therapy by determining the mechanism of action of a group of selectively cytotoxic anticancer natural products produced by actinobacteria. In Chapter 2, I summarize our efforts to identify the mechanism of action of the apoptolidin family of glycosylated macrolides including identification of their molecular target as the F_1 portion of ATP synthase using chemoproteomics, identification of their precise binding site using CryoEM (work done in collaboration with Hui Guo and John Rubinstein at the University of Toronto), identification of resistance mechanisms which provide conclusive target validation, and preliminary *in vivo* studies demonstrating their efficacy in a mouse model of human leukemia (in collaboration with Haley Ramsey and Michael Savona at VUMC). In Chapter 3, I report our progress towards the translational development of apoptolidin family glycomacrolides to address cancer including patient selection and development of optimized analogs. In Chapter 4, I summarize our progress towards identification of the mechanism of action of the ciromicin family of selectively cytotoxic glycosylated marcolactams which are produced by the same strain that makes the apoptolidins.

In addition to determining the mechanism of action of known selectively cytotoxic natural products, part of my dissertation work focused on methods to enable the discovery of new anticancer compounds with a focus on high-content screening platforms which provide clues to a compounds' mechanism of action prior to isolation. In Chapter 5 I report the development of a software package, *DebarcodeR*, which enables automated analysis of fluorescent cell barcoded flow cytometry data and permits rapid, reproducible, high-content screening of hundreds of chemical perturbations in cell lines or primary cells. In Chapter 6, I

demonstrate the application of fluorescent cell barcoding with an early version of DebarcodeR to

screen a library of synthetic acylphloroglucinol scaffolds (SASs) synthesized by Jonathan Boyce

and Jonathan Porco at Boston University – an approach we call 'Multiplexed Activity Profiling."

1.6 References

1.   I. Buchwalow, W. Boecker, M. Tiemann, The contribution of Paul Ehrlich to histochemistry: a tribute on the occasion of the centenary of his death. *Virchows Arch* **466**, 111-116 (2015).
2.   K. Strebhardt, A. Ullrich, Paul Ehrlich's magic bullet concept: 100 years of progress. *Nat Rev Cancer* **8**, 473-480 (2008).
3.   V. T. DeVita, Jr., E. Chu, A history of cancer chemotherapy. *Cancer Res* **68**, 8643-8653 (2008).
4.   K. J. Williams, The introduction of 'chemotherapy' using arsphenamine - the first magic bullet. *J R Soc Med* **102**, 343-348 (2009).
5.   J. Wapner, *The Philadelphia Chromosome: A Mutant Gene and the Quest to Cure Cancer at the Genetic Level*. (The Experiment, 2013).
6.   D. Hanahan, R. A. Weinberg, The hallmarks of cancer. *Cell* **100**, 57-70 (2000).
7.   D. Hanahan, R. A. Weinberg, Hallmarks of cancer: the next generation. *Cell* **144**, 646-674 (2011).
8.   G. Q. Daley, D. Baltimore, Transformation of an interleukin 3-dependent hematopoietic cell line by the chronic myelogenous leukemia-specific P210bcr/abl protein. *Proc Natl Acad Sci U S A* **85**, 9312-9316 (1988).
9.   G. Q. Daley, R. A. Van Etten, D. Baltimore, Induction of chronic myelogenous leukemia in mice by the P210bcr/abl gene of the Philadelphia chromosome. *Science* **247**, 824-830 (1990).
10.   Z. Y. Wang, Z. Chen, Acute promyelocytic leukemia: from highly fatal to highly curable. *Blood* **111**, 2505-2515 (2008).
11.   M. E. Huang *et al.*, Use of all-trans retinoic acid in the treatment of acute promyelocytic leukemia. *Blood* **72**, 567-572 (1988).
12.   H. de The, C. Chomienne, M. Lanotte, L. Degos, A. Dejean, The t(15;17) translocation of acute promyelocytic leukaemia fuses the retinoic acid receptor alpha gene to a novel transcribed locus. *Nature* **347**, 558-561 (1990).
13.   M. Alcalay *et al.*, Translocation breakpoint of acute promyelocytic leukemia lies within the retinoic acid receptor alpha locus. *Proc Natl Acad Sci U S A* **88**, 1977-1981 (1991).
14.   J. Borrow, A. D. Goddard, D. Sheer, E. Solomon, Molecular analysis of acute promyelocytic leukemia breakpoint cluster region on chromosome 17. *Science* **249**, 1577-1580 (1990).
15.   J. V. Raelson *et al.*, The PML/RAR alpha oncoprotein is a direct molecular target of retinoic acid in acute promyelocytic leukemia cells. *Blood* **88**, 2826-2832 (1996).
16.   Y. Tsujimoto, J. Cossman, E. Jaffe, C. M. Croce, Involvement of the bcl-2 gene in human follicular lymphoma. *Science* **228**, 1440-1443 (1985).
17.   S. Kitada, I. M. Pedersen, A. D. Schimmer, J. C. Reed, Dysregulation of apoptosis genes in hematopoietic malignancies. *Oncogene* **21**, 3459-3474 (2002).

18.   A. Letai *et al.*, Distinct BH3 domains either sensitize or activate mitochondrial apoptosis, serving as prototype cancer therapeutics. *Cancer Cell* **2**, 183-192 (2002).
19.   S. B. Shuker, P. J. Hajduk, R. P. Meadows, S. W. Fesik, Discovering high-affinity ligands for proteins: SAR by NMR. *Science* **274**, 1531-1534 (1996).
20.   T. Oltersdorf *et al.*, An inhibitor of Bcl-2 family proteins induces regression of solid tumours. *Nature* **435**, 677-681 (2005).
21.   K. D. Mason *et al.*, Programmed anuclear cell death delimits platelet life span. *Cell* **128**, 1173-1186 (2007).
22.   H. Zhang *et al.*, Bcl-2 family proteins are essential for platelet survival. *Cell Death Differ* **14**, 943-951 (2007).
23.   C. D. DiNardo, M. Y. Konopleva, A venetoclax bench-to-bedside story. *Nature Cancer* **2**, 3-5 (2021).
24.   C. D. DiNardo *et al.*, Safety and preliminary efficacy of venetoclax with decitabine or azacitidine in elderly patients with previously untreated acute myeloid leukaemia: a non-randomised, open-label, phase 1b study. *Lancet Oncol* **19**, 216-228 (2018).
25.   C. D. Dinardo, A. H. Wei, How I treat acute myeloid leukemia in the era of new drugs. *Blood* **135**, 85-96 (2020).
26.   J. N. Prebble, *Searching for a Mechanism: A History of Cell Bioenergetics*. (Oxford University Press, 2018).
27.   M. E. Pullman, H. S. Penefsky, A. Datta, E. Racker, Partial resolution of the enzymes catalyzing oxidative phosphorylation. I. Purification and properties of soluble dinitrophenol-stimulated adenosine triphosphatase. *J Biol Chem* **235**, 3322-3329 (1960).
28.   H. S. Penefsky, M. E. Pullman, A. Datta, E. Racker, Partial resolution of the enzymes catalyzing oxidative phosphorylation II. Participation of a soluble adenosine triphosphatase in oxidative phosphorylation. *J Biol Chem* **235**, 3330-3336 (1960).
29.   R. M. Smith, University of Wisconsin--Madison, (1953).
30.   R. M. Smith, W. H. Peterson, C. E. Mc, Oligomycin, a new antifungal antibiotic. *Antibiot Chemother (Northfield)* **4**, 962-970 (1954).
31.   H. A. Lardy, D. Johnson, W. C. McMurray, Antibiotics as tools for metabolic studies. I. A survey of toxic antibiotics in respiratory, phosphorylative and glycolytic systems. *Archives of Biochemistry and Biophysics* **78**, 587-597 (1958).
32.   Y. Kagawa, E. Racker, Partial resolution of the enzymes catalyzing oxidative phosphorylation. 8. Properties of a factor conferring oligomycin sensitivity on mitochondrial adenosine triphosphatase. *J Biol Chem* **241**, 2461-2466 (1966).
33.   Y. Kagawa, E. Racker, Partial resolution of the enzymes catalyzing oxidative phosphorylation. IX. Reconstruction of oligomycin-sensitive adenosine triphosphatase. *J Biol Chem* **241**, 2467-2474 (1966).
34.   J. P. Abrahams, A. G. Leslie, R. Lutter, J. E. Walker, Structure at 2.8 A resolution of F1-ATPase from bovine heart mitochondria. *Nature* **370**, 621-628 (1994).
35.   J. E. Walker *et al.*, Primary structure and subunit stoichiometry of F1-ATPase from bovine mitochondria. *J Mol Biol* **184**, 677-701 (1985).
36.   W. Kuhlbrandt, Structure and Mechanisms of F-Type ATP Synthases. *Annu Rev Biochem* **88**, 515-549 (2019).
37.   J. Symersky, D. Osowski, D. E. Walters, D. M. Mueller, Oligomycin frames a common drug-binding site in the ATP synthase. *Proc Natl Acad Sci U S A* **109**, 13961-13965 (2012).

38.	M. E. Pullman, in *Oxidation and Phosphorylation*. (Academic Press, 1967), vol. 10, pp. 57-60.

39.	R. E. Beyer, in *Oxidation and Phosphorylation*. (Academic Press, 1967), vol. 10, pp. 186-194.

40.	G. Schatz, H. S. Penefsky, E. Racker, Partial Resolution of the Enzymes Catalyzing Oxidative Phosphorylation: XIV. INTERACTION OF PURIFIED MITOCHONDRIAL ADENOSINE TRIPHOSPHATASE FROM BAKERS' YEAST WITH SUBMITOCHONDRIAL PARTICLES FROM BEEF HEART. *J Biol Chem* **242**, 2552-2560 (1967).

41.	P. L. Pedersen *et al.*, in *Methods in Cell Biology Volume 20*. (Academic Press, 1978), vol. 20, pp. 411-481.

42.	M. Galkin, R. Venard, J. Vaillier, J. Velours, F. Haraux, Functional transitions of F0F1-ATPase mediated by the inhibitory peptide IF1 in yeast coupled submitochondrial particles. *Eur J Biochem* **271**, 1963-1970 (2004).

43.	D. J. Kominsky, M. P. Brownson, D. L. Updike, P. E. Thorsness, Genetic and biochemical basis for viability of yeast lacking mitochondrial genomes. *Genetics* **162**, 1595-1604 (2002).

44.	X. J. Chen, G. Clark-Walker, α and β subunits of F 1-ATPase are required for survival of petite mutants in Saccharomyces cerevisiae. *Molecular and General Genetics MGG* **262**, 898-908 (1999).

45.	M. M. Mehta, S. E. Weinberg, N. S. Chandel, Mitochondrial control of immunity: beyond ATP. *Nat Rev Immunol* **17**, 608-620 (2017).

46.	A. Garedew, S. O. Henderson, S. Moncada, Activated macrophages utilize glycolytic ATP to maintain mitochondrial membrane potential and prevent apoptotic cell death. *Cell Death Differ* **17**, 1540-1550 (2010).

47.	A. Chevrollier *et al.*, ANT2 isoform required for cancer cell glycolysis. *J Bioenerg Biomembr* **37**, 307-316 (2005).

48.	J. Garcia-Bermudez, J. M. Cuezva, The ATPase Inhibitory Factor 1 (IF1): A master regulator of energy metabolism and of cell survival. *Biochim Biophys Acta* **1857**, 1167-1182 (2016).

49.	H. Guo, T. Suzuki, J. L. Rubinstein, Structure of a bacterial ATP synthase. *Elife* **8**, (2019).

50.	H. Imamura *et al.*, Visualization of ATP levels inside single living cells with fluorescence resonance energy transfer-based genetically encoded indicators. *Proc Natl Acad Sci U S A* **106**, 15651-15656 (2009).

51.	A. Hahn, J. Vonck, D. J. Mills, T. Meier, W. Kuhlbrandt, Structure, mechanism, and regulation of the chloroplast ATP synthase. *Science* **360**, eaat4318 (2018).

52.	C. Baldwin, Biological and chemical properties of aurovertin, a metabolic product of Calcarisporium abuscula. *Lloydia* **27**, 88-95 (1964).

53.	R. M. Bertina, Waarland : "Gerja", Waarland (1972).

54.	M. G. Douglas, Y. Koh, M. E. Dockter, G. Schatz, Aurovertin binds to the beta subunit of yeast mitochondrial ATPase. *J Biol Chem* **252**, 8333-8335 (1977).

55.	G. J. Verschoor, P. R. van der Sluis, E. C. Slater, The binding of aurovertin to isolated beta subunit of F1 (mitochondrial ATPase). Stoicheiometry of beta subunit in F1. *Biochim Biophys Acta* **462**, 438-449 (1977).

56. M. J. van Raaij, J. P. Abrahams, A. G. Leslie, J. E. Walker, The structure of bovine F1-ATPase complexed with the antibiotic inhibitor aurovertin B. *Proc Natl Acad Sci U S A* **93**, 6913-6917 (1996).

57. E. M. Gause, M. A. Buck, M. G. Douglas, Binding of citreoviridin to the beta subunit of the yeast F1-ATPase. *J Biol Chem* **256**, 557-559 (1981).

58. Y.-l. Wang *et al.*, Yellow pigment aurovertins mediate interactions between the pathogenic fungus Pochonia chlamydosporia and its nematode host. *J Agr Food Chem* **63**, 6577-6587 (2015).

59. C. G. Jackson, P. E. Linnett, R. B. Beechey, P. J. Henderson, Purification and preliminary structural analysis of the efrapeptins, a group of antibiotics that inhibit the mitochondrial adenosine triphosphatase [proceedings]. *Biochemical Society transactions* **7**, 224-226 (1979).

60. H. Lardy, P. Reed, C. Lin, in *Federation proceedings*. (1975), vol. 34, pp. 1707-1710.

61. R. L. Cross, W. E. Kohlbrenner, The mode of inhibition of oxidative phosphorylation by efrapeptin (A23871). Evidence for an alternating site mechanism for ATP synthesis. *J Biol Chem* **253**, 4865-4873 (1978).

62. W. E. Kohlbrenner, R. L. Cross, The mode of inhibition of oxidative phosphorylation by efrapeptin (A23871): measurement of substrate effects on rates of inactivation by a tight-binding inhibitor. *Arch Biochem Biophys* **198**, 598-607 (1979).

63. S. Gupta *et al.*, Structures of the efrapeptins: potent inhibitors of mitochondrial ATPase from the fungus Tolypocladium niveum. *J Am Chem Soc* **113**, 707-709 (2002).

64. S. B. Krasnoff, S. Gupta, Identification and directed biosynthesis of efrapeptins in the fungusTolypocladium geodes gams (Deuteromycotina: Hyphomycetes). *J Chem Ecol* **17**, 1953-1962 (1991).

65. S. B. Krasnoff, S. Gupta, Efrapeptin production by Tolypocladium fungi (Deuteromycotina: Hyphomycetes): Intra-and interspecific variation. *Journal of Chemical Ecology* **18**, 1727 (1992).

66. J. P. Abrahams *et al.*, The structure of bovine F1-ATPase complexed with the peptide antibiotic efrapeptin. *Proc Natl Acad Sci U S A* **93**, 9420-9424 (1996).

67. J. R. Gledhill, J. E. Walker, Inhibitors of the catalytic domain of mitochondrial ATP synthase. *Biochemical Society transactions* **34**, 989-992 (2006).

68. O. Warburg, The Metabolism of Carcinoma Cells. *The Journal of Cancer Research* **9**, 148-163 (1925).

69. R. J. DeBerardinis, N. S. Chandel, We need to talk about the Warburg effect. *Nat Metab* **2**, 127-129 (2020).

70. B. I. Reinfeld *et al.*, Cell-programmed nutrient partitioning in the tumour microenvironment. *Nature*, (2021).

71. I. Martinez-Reyes *et al.*, Mitochondrial ubiquinol oxidation is necessary for tumour growth. *Nature* **585**, 288-292 (2020).

72. K. Vasan, M. Werner, N. S. Chandel, Mitochondrial Metabolism as a Target for Cancer Therapy. *Cell Metab* **32**, 341-352 (2020).

73. J. R. Molina *et al.*, An inhibitor of oxidative phosphorylation exploits cancer vulnerability. *Nat Med* **24**, 1036-1046 (2018).

74. T. M. Ashton, W. G. McKenna, L. A. Kunz-Schughart, G. S. Higgins, Oxidative Phosphorylation as an Emerging Target in Cancer Therapy. *Clin Cancer Res* **24**, 2482-2490 (2018).

75.   V. Sica, J. M. Bravo-San Pedro, G. Stoll, G. Kroemer, Oxidative phosphorylation as a potential therapeutic target for cancer therapy. *Int J Cancer* **146**, 10-17 (2020).
76.   Y. Xu, D. Xue, A. Bankhead, 3rd, N. Neamati, Why All the Fuss about Oxidative Phosphorylation (OXPHOS)? *J Med Chem* **63**, 14276-14307 (2020).
77.   E. P. Rogakou, W. Nieves-Neira, C. Boon, Y. Pommier, W. M. Bonner, Initiation of DNA fragmentation during apoptosis induces phosphorylation of H2AX histone at serine 139. *J Biol Chem* **275**, 9390-9395 (2000).
78.   J. B. Baell, G. A. Holloway, New substructure filters for removal of pan assay interference compounds (PAINS) from screening libraries and for their exclusion in bioassays. *J Med Chem* **53**, 2719-2740 (2010).
79.   J. L. Dahlin *et al.*, PAINS in the assay: chemical mechanisms of assay interference and promiscuous enzymatic inhibition observed during a sulfhydryl-scavenging HTS. *J Med Chem* **58**, 2091-2113 (2015).
80.   J. L. Dahlin, M. A. Walters, How to Triage PAINS-Full Research. *Assay Drug Dev Technol* **14**, 168-174 (2016).
81.   J. Blagg, P. Workman, Choose and Use Your Chemical Probe Wisely to Explore Cancer Biology. *Cancer Cell* **32**, 9-25 (2017).
82.   K. A. Donovan *et al.*, Thalidomide promotes degradation of SALL4, a transcription factor implicated in Duane Radial Ray syndrome. *Elife* **7**, (2018).
83.   J. Kronke *et al.*, Lenalidomide causes selective degradation of IKZF1 and IKZF3 in multiple myeloma cells. *Science* **343**, 301-305 (2014).
84.   M. W. Harding, A. Galat, D. E. Uehling, S. L. Schreiber, A receptor for the immuno-suppressant FK 506 is a cis–trans peptidyl-prolyl isomerase. *Nature* **341**, 758-760 (1989).
85.   J. Taunton, C. A. Hassig, S. L. Schreiber, A mammalian histone deacetylase related to the yeast transcriptional regulator Rpd3p. *Science* **272**, 408-411 (1996).
86.   F. Baquero, B. R. Levin, Proximate and ultimate causes of the bactericidal action of antibiotics. *Nat Rev Microbiol* **19**, 123-132 (2021).
87.   C. H. Arrowsmith *et al.*, The promise and peril of chemical probes. *Nat Chem Biol* **11**, 536-541 (2015).
88.   A. J. Carter *et al.*, Target 2035: probing the human proteome. *Drug Discov Today* **24**, 2111-2115 (2019).
89.   A. Rabbani, R. M. Finn, J. Ausio, The anthracycline antibiotics: antitumor drugs that alter chromatin structure. *Bioessays* **27**, 50-56 (2005).
90.   B. Pang *et al.*, Drug-induced histone eviction from open chromatin contributes to the chemotherapeutic effects of doxorubicin. *Nat Commun* **4**, 1908 (2013).
91.   A. Lin *et al.*, Off-target toxicity is a common mechanism of action of cancer drugs undergoing clinical trials. *Sci Transl Med* **11**, eaaw8412 (2019).
92.   Y. Matsuo *et al.*, TOPK inhibitor induces complete tumor regression in xenograft models of human cancer through inhibition of cytokinesis. *Sci Transl Med* **6**, 259ra145 (2014).
93.   G. Zhou *et al.*, Role of AMP-activated protein kinase in mechanism of metformin action. *The Journal of clinical investigation* **108**, 1167-1174 (2001).
94.   P. B. Yu *et al.*, Dorsomorphin inhibits BMP signals required for embryogenesis and iron metabolism. *Nat Chem Biol* **4**, 33-41 (2008).
95.   L. Vucicevic *et al.*, Compound C induces protective autophagy in cancer cells through AMPK inhibition-independent blockade of Akt/mTOR pathway. *Autophagy* **7**, 40-50 (2011).

96.   N. S. Scholes, C. Mayor-Ruiz, G. E. Winter, Identification and selectivity profiling of small-molecule degraders via multi-omics approaches. *Cell Chem Biol*, (2021).

97.   Y. Hayakawa *et al.*, Studies on new antitumor antibiotics, leptofuranins A, B, C and D.I. Taxonomy, fermentation, isolation and biological activities. *J Antibiot (Tokyo)* **49**, 974-979 (1996).

98.   J. W. Kim, H. Adachi, K. Shin-ya, Y. Hayakawa, H. Seto, Apoptolidin, a new apoptosis inducer in transformed cells from Nocardiopsis sp. *J Antibiot (Tokyo)* **50**, 628-630 (1997).

99.   Y. Hayakawa *et al.*, Structure of Apoptolidin, a Specific Apoptosis Inducer in Transformed Cells. *J Am Chem Soc* **120**, 3524-3525 (1998).

100.   K. C. Nicolaou *et al.*, Total synthesis of apoptolidin: completion of the synthesis and analogue synthesis and evaluation. *J Am Chem Soc* **125**, 15443-15454 (2003).

101.   P. A. Wender *et al.*, Correlation of F0F1-ATPase inhibition and antiproliferative activity of apoptolidin analogues. *Org Lett* **8**, 589-592 (2006).

102.   P. A. Wender, K. E. Longcore, Isolation, structure determination, and anti-cancer activity of apoptolidin D. *Org Lett* **9**, 691-694 (2007).

103.   P. A. Wender, K. E. Longcore, Apoptolidins E and F, new glycosylated macrolactones isolated from Nocardiopsis sp. *Org Lett* **11**, 5474-5477 (2009).

104.   B. O. Bachmann *et al.*, Light-induced isomerization of apoptolidin a leads to inversion of C2-C3 double bond geometry. *Org Lett* **12**, 2944-2947 (2010).

105.   Y. Du *et al.*, Biosynthesis of the Apoptolidins in Nocardiopsis sp. FU 40. *Tetrahedron* **67**, 6568-6575 (2011).

106.   Y. Sheng *et al.*, Succinylated Apoptolidins from Amycolatopsis sp. ICBB 8242. *Org Lett* **17**, 2526-2529 (2015).

107.   J. D. Pennington, H. J. Williams, A. R. Salomon, G. A. Sulikowski, Toward a stable apoptolidin derivative: identification of isoapoptolidin and selective deglycosylation of apoptolidin. *Org Lett* **4**, 3823-3825 (2002).

108.   P. A. Wender, A. V. Gulledge, O. D. Jankowski, H. Seto, Isoapoptolidin: structure and activity of the ring-expanded isomer of apoptolidin. *Org Lett* **4**, 3819-3822 (2002).

109.   R. Murakami *et al.*, Ammocidin, a new apoptosis inducer in Ras-dependent cells from Saccharothrix sp. I. Production, isolation and biological activity. *J Antibiot (Tokyo)* **54**, 710-713 (2001).

110.   R. Murakami, T. Kajiura*, B. J. Reisman, B. O. Bachmann, Eds. (2021).

111.   R. Murakami *et al.*, Ammocidin, a new apoptosis inducer in ras-dependent cells from Saccharothrix sp. II. Physico-chemical properties and structure elucidation. *J Antibiot (Tokyo)* **54**, 714-717 (2001).

112.   S. T. Chau, Y. Hayakawa, G. A. Sulikowski, 18O assisted analysis of a gamma,delta-epoxyketone cyclization: synthesis of the C16-C28 fragment of ammocidin D. *Org Lett* **13**, 756-759 (2011).

113.   R. Murakami *et al.*, Ammocidins B, C and D, new cytotoxic 20-membered macrolides from Saccharothrix sp. AJ9571. *J Antibiot (Tokyo)* **62**, 123-127 (2009).

114.   Z. G. Khalil *et al.*, Amycolatopsins A-C: antimycobacterial glycosylated polyketide macrolides from the Australian soil *Amycolatopsis* sp. MST-108494. *J Antibiot (Tokyo)* **70**, 1097-1103 (2017).

115.   A. R. Salomon, D. W. Voehringer, L. A. Herzenberg, C. Khosla, Apoptolidin, a selective cytotoxic agent, is an inhibitor of F_0F_1-ATPase. *Chem Biol* **8**, 71-80 (2001).

116. J. N. Weinstein, Spotlight on molecular profiling: "Integromic" analysis of the NCI-60 cancer cell lines. *Mol Cancer Ther* **5**, 2601-2605 (2006).
117. A. R. Salomon, Y. Zhang, H. Seto, C. Khosla, Structure-activity relationships within a family of selectively cytotoxic macrolide natural products. *Org Lett* **3**, 57-59 (2001).
118. A. R. Salomon, D. W. Voehringer, L. A. Herzenberg, C. Khosla, Understanding and exploiting the mechanistic basis for selectivity of polyketide inhibitors of F(0)F(1)-ATPase. *Proc Natl Acad Sci U S A* **97**, 14766-14771 (2000).
119. V. P. Ghidu *et al.*, Synthesis and evaluation of the cytotoxicity of apoptolidinones A and D. *J Org Chem* **73**, 4949-4955 (2008).
120. M. T. Crimmins, H. S. Christie, A. Long, K. Chaudhary, Total synthesis of apoptolidin A. *Org Lett* **11**, 831-834 (2009).
121. J. Wang, Vanderbilt University, Nashville, TN (2009).
122. K. E. Longcore, Stanford, Palo Alto, California (2010).
123. S. Deguire, Vanderbilt University, Nashville, TN (2013).
124. P. A. Wender, O. D. Jankowski, E. A. Tabet, H. Seto, Toward a structure-activity relationship for apoptolidin: selective functionalization of the hydroxyl group array. *Org Lett* **5**, 487-490 (2003).
125. J. Liu *et al.*, Calcineurin is a common target of cyclophilin-cyclosporin A and FKBP-FK506 complexes. *Cell* **66**, 807-815 (1991).
126. E. J. Brown *et al.*, A mammalian protein targeted by G1-arresting rapamycin-receptor complex. *Nature* **369**, 756-758 (1994).
127. O. D. Jankowski, Stanford University, Palo Alto, Ca (2004).
128. A. L. MacKinnon, J. Taunton, Target Identification by Diazirine Photo-Cross-Linking and Click Chemistry. *Current Protocols in Chemical Biology* **1**, 55-73 (2009).
129. S. M. DeGuire *et al.*, Fluorescent probes of the apoptolidins and their utility in cellular localization studies. *Angew Chem, Int Ed* **54**, 961-964 (2015).
130. K. M. Chong *et al.*, The use of fluorescently-tagged apoptolidins in cellular uptake and response studies. *J Antibiot (Tokyo)* **69**, 327-330 (2016).

CHAPTER 2 – STUDIES ON THE MECHANISM OF ACTION OF APOPTOLIDIN FAMILY OF GLYCOSYLATED MACROLIDES

2.1 Introduction

The development of effective cancer therapeutics is constrained by the need to identify targets and drugs that selectively eliminate cancer cells with limited toxicity to healthy cells. One approach to addressing this challenge is to identify functional dependencies that are unique to cancer; even if these 'essential' targets may be present in all cells, the unique demands of cancer cells create vulnerabilities that can be leveraged therapeutically ([131](#)). Alterations in bioenergetics have long been recognized as a hallmark of cancer ([7](#), [69](#), [132](#)), with Warburg's observation that many cancer cells convert glucose to lactate in the presence of adequate oxygen for aerobic metabolism. Although Warburg metabolism predominates in some cancers, there is increasing recognition that many cancers and subsets of cancer cells are dependent on mitochondrial oxidative phosphorylation (OXPHOS) to serve both bioenergetic and biosynthetic needs ([71](#), [76](#), [133](#)). Notably, OXPHOS dependence appears to be a recurrent vulnerability of cancer stem cells (CSCs) and leukemia stem cells (LSCs), which are often responsible for treatment failure ([134-137](#)). Despite these vulnerabilities, outside of a small group of genetically defined tumor subsets ([138](#)), therapeutics designed for metabolic targets in cancer have largely fallen short of their great promise.

The apoptolidin family of glycosylated macrolides (glycomacrolides) was discovered in a series of phenotypic screens for compounds that induce apoptosis selectively in oncogene-transformed cells. Apoptolidin A, produced by *Nocardiopsis* sp., was discovered to selectively induce apoptosis in E1A transformed rat fibroblasts ([98](#), [99](#)), while ammocidin A, a structurally related glycomacrolide produced by *Saccharothrix* sp., was discovered in a screen for compounds that selectively induce apoptosis in HRas-G12V transformed BaF3 cells ([109](#), [111](#)).

59

When evaluated in the NCI-60 screening program, apoptolidin A was noted to be among the top 0.1% most cell line selective cytotoxic agents tested at that time, and early studies of its mechanism of action suggested that it targets ATP synthase, a mitochondrial membrane protein complex involved in oxidative phosphorylation ([115]). These findings prompted multiple groups to develop new analogs via fermentation ([102-105], [113], [114]), semi-synthesis ([101], [124]), and total synthesis ([112], [119], [120], [139]). Structure-activity relationship (SAR) studies of these analogs supported a role for OXPHOS inhibition at ATP synthase in the mechanism of apoptolidin family compounds, but subtle differences in the bioactivity of apoptolidins compared to other classical ATP synthase inhibitors such as oligomycin suggested a distinct biochemical target ([101], [140]). Given the remarkable selectivity of apoptolidin family compounds *ex vivo* and emerging evidence of the importance of OXPHOS in cancer, identification of the apoptolidin target could reveal new targetable dependencies in cancer metabolism. In this study, we applied photoaffinity probes of apoptolidin family macrolides and electron cryomicroscopy (cryoEM) to identify their specific target and binding site on the F_1, rather than F_O, subcomplex of ATP synthase. Resistance mutations uncovered by deep mutational scanning eliminated both binding and cytotoxicity, confirming the mechanistic role for ATP synthase in their selective cytotoxicity. Ammocidin A was able to suppress leukemia development in mouse xenografts demonstrating that ATP synthase can be effectively targeted in OXPHOS dependent cancers.

2.2 Results

2.2.1 <u>Identification of the F$_1$ subcomplex of ATP synthase as the target of glycomacrolides</u>

The apoptolidin family of glycomacrolides, including apoptolidin A (**1**), apoptolidin H (**3**), and ammocidin A (**5**) all incorporate a 20-membered macrolide conjugated to three deoxy sugar units and are produced by taxonomically related actinobacteria. While superficially structurally similar, there are multiple differences in the functionality of the macrolide cores, decorating sugars, and in the positioning of glycosyl units. In order to identify the target of this family, we synthesized photoaffinity probe analogs of apoptolidin family macrolides (Figure 2.1A). The C9 2-deoxyglucose was selected as the site of modification as previous studies had demonstrated that it could tolerate modification with retention of nanomolar cytotoxicity ([129]). Apoptolidin A PA (**2**) incorporates a diazirine, which provides for *in situ* photoreactive crosslinking when exposed to UV-A light ([141]), as well as an alkyne, which allows for post-treatment ligation of fluorophores or affinity enrichment tags using click chemistry ([142]). The MV-4-11 acute myeloid leukemia cell line was selected as a primary model system for target identification based on its high sensitivity to apoptolidin family compounds. The activity of (**2**) was comparable to (**1**) with regards to both cytotoxicity (Figure 2.2A) and suppression of S6 [Ser235/236] phosphorylation (pS6 – Figure 2.2B), a marker of activation of the AMPK pathway which has been implicated in the mechanism of action of apoptolidin ([140]). When applied to adherent, apoptolidin sensitive, H292 cells and probed with rhodamine azide after fixation, (**2**) exhibited the expected mitochondrial localization (Figure 2.2C) consistent with previous studies using fluorescent live cell apoptolidin probes ([129]).
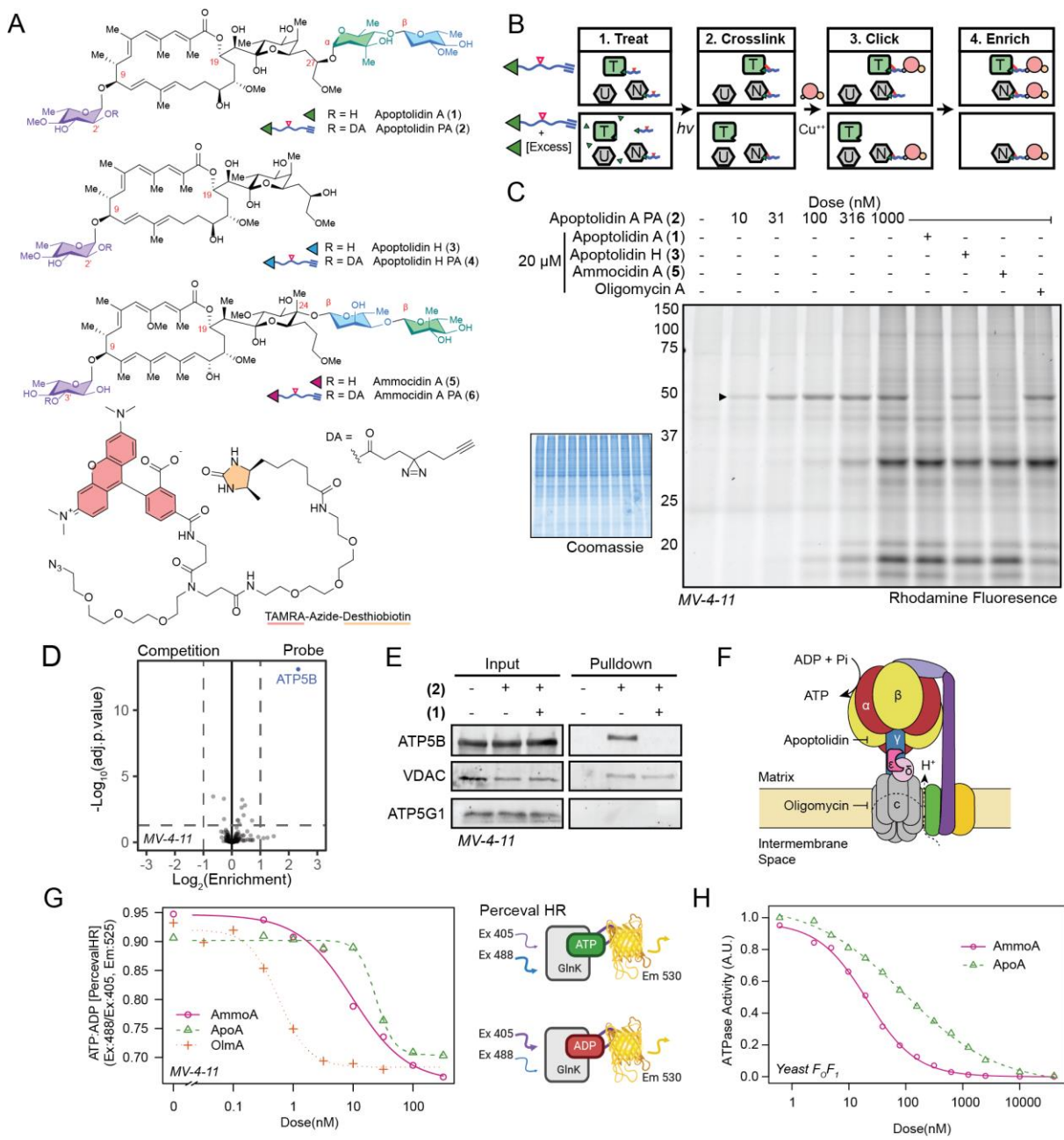
Figure 2.1. Identification of F₁ subcomplex of ATP synthase as the target of apoptolidin A.

A, Structures of natural products and probes used in this study with key differences between apoptolidin and ammocidin highlighted; **B,** Experimental design for target adduct visualization and identification studies for probe (top) and competition (bottom) reactions, *hv* = irradiation with 365 nM light, T = targets, N = non-specific targets, U = unbound proteins; **C,** In gel profiling of (**2**) targets after conjugation with TAMRA-azide-desthiobiotin and imaging of TAMRA dye fluorescence. Apoptolidin A and ammocidin A are observed to compete with adduction of a 50 kDa target in MV-4-11 cells that is not competed by oligomycin; **D,** Volcano plot of identified proteins from tandem mass tagged-multiplexed quantitative proteomics of **2** (probe) vs **1** + **2** (competition) treated MV-4-11 cells, adjusted p-values calculated using Limma; **E,** Validation of top target and non-specific proteomics hits by immunoblot of pulldowns showing specific enrichment of ATP synthase F1 β subunit (ATP5B), non-specific enrichment of VDAC, and no enrichment of ATP synthase c-ring, target of oligomycin (ATP5G1); **F,** Schematic depicting ATP synthase subunits and inhibitor binding sites; **G,** Quantification of ATP synthase inhibition *in vivo* by flow-cytometry using MV-4-11 cells expressing the ATP::ADP sensor Perceval-HR; **H,** Quantification of ATPase inhibition with purified yeast ATP synthase.
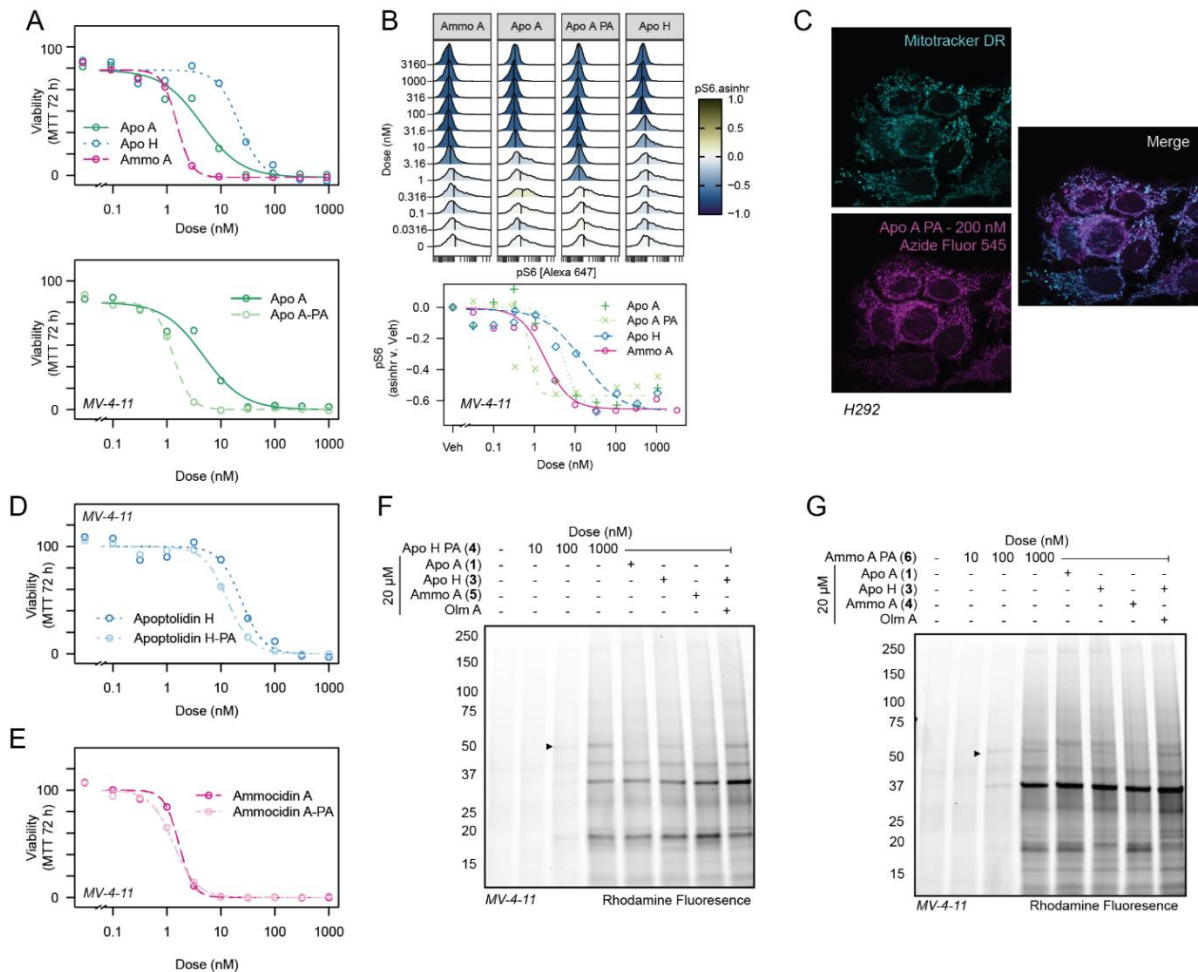
Figure 2.2. Validation of apoptolidin family photoaffinity probes

A, Assessment of cytotoxicity of apoptolidin family compounds (top) and photoaffinity probe (bottom) in MV-4-11 leukemia cells treated for 72 hrs assessed using MTT viability assay; **B,** Assessment of pS6 [Ser235/236] after 16 h treatment as a marker of AMPK activation in MV-4-11 cells by FCB barcoded flow cytometry; **C,** Confirmation of mitochondrial localization of (**2**) in H292 cells using confocal microscopy; **D,** Assessment of cytotoxicity of apoptolidin H PA at 72 hrs using MTT assay; **E**, assessment of cytotoxicity of Ammocidin A PA at 72 hrs using MTT assay; **F,** Gel-based profiling of apoptolidin H PA probe in MV-4-11 cells line; **G,** Gel-based profiling of ammocidin A PA probe targets in MV-4-11 cell line.

To identify apoptolidin family binding proteins, MV-4-11 cells were treated with DMSO, probe (**2**) alone, or (**2**) combined with various potential competitors (Figure 2.1B). Proteins were photocrosslinked prior to lysis and then conjugated via azide-alkyne *Huisgen* cycloaddition to a trifunctional TAMRA-azide-desthiobiotin (Figure 2.1A) reagent, which facilitated both gel-based fluorescent profiling and subsequent affinity enrichment. Gel-based profiling of (**2**) adducts (Figure 2.1C) revealed concentration-dependent labelling of a ~50 kDa target with an apparent EC_{50} of ~10 nM. Adduction of the 50 kDa target was eliminated by competition with excess apoptolidin A (**1**) as well as ammocidin A (**3**) suggestive of a shared putative binding site for the two glycomacrolides. Apoptolidin H (**3**), lacking the C-27 disaccharide and known to have reduced cytotoxicity relative to apoptolidin A ([105](#)), exhibited decreased competitive displacement of apoptolidin A PA (**2**). Furthermore, oligomycin did not exhibit any competition, suggesting that the 50 kDa target engaged by apoptolidins and ammocidin A was not the target of oligomycin, as previously proposed ([118](#)). To confirm similar adduction specificity across the family we synthesized photoaffinity probes apoptolidin H PA (**4**) and ammocidin A PA (**6**), which also retain cytotoxicity similar to the parent compounds (Figure 2.2D-E). Gel-based profiling of adducted proteins demonstrated the same 50 kDa band (Figure 2.2F, Figure 2.2G). Similar binding patterns were observed in additional cell lines (Figure 2.3) including HRasG12V transformed BaF3s and H292 lung cancer cells, similar to those used in previous studies on apoptolidin family glycomacrolides ([109](#), [124](#)). The trienoate and C21 hemiketal functional groups of apoptolidin A are potential electrophiles that could allow apoptolidin to act as a covalent inhibitor. However, irreversible binding to the 50 kDa target was dependent on both the diazirine and exposure to UV light, suggesting that covalent modification of the target does not play a role in target engagement in naturally occurring apoptolidin family macrolides (Figure

2.4B).
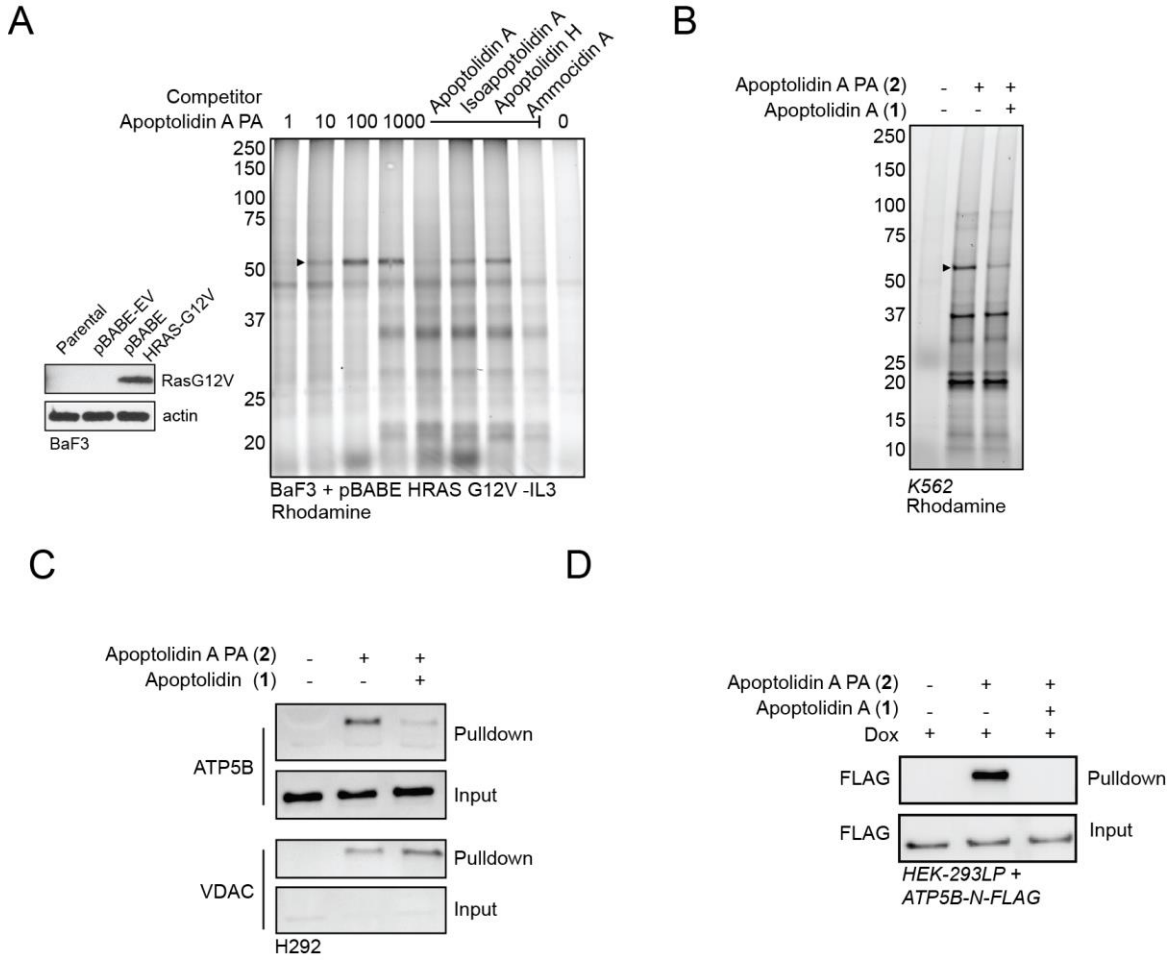
Figure 2.3. Validation of photoaffinity probes in additional cell lines

A, Gel-based profiling of (**2**) adducts in BaF3 cells transformed with HRAS-G12V, insert on left confirming overexpression of the mutant RAS by immunoblot; **B,** Gel-based profiling of (**2**) adducts in K562, chronic myeloid leukemia cell line; **C,** Confirmation of specific enrichment of ATP5B after streptavidin enrichment of in H292, lung cancer cell line, treated with (**2**); **D,** Confirmation of ATP5B binding by (**2**) in HEK293-LP cells expressing C-terminal FLAG-tagged ATP5B by immunoblot against FLAG epitope.
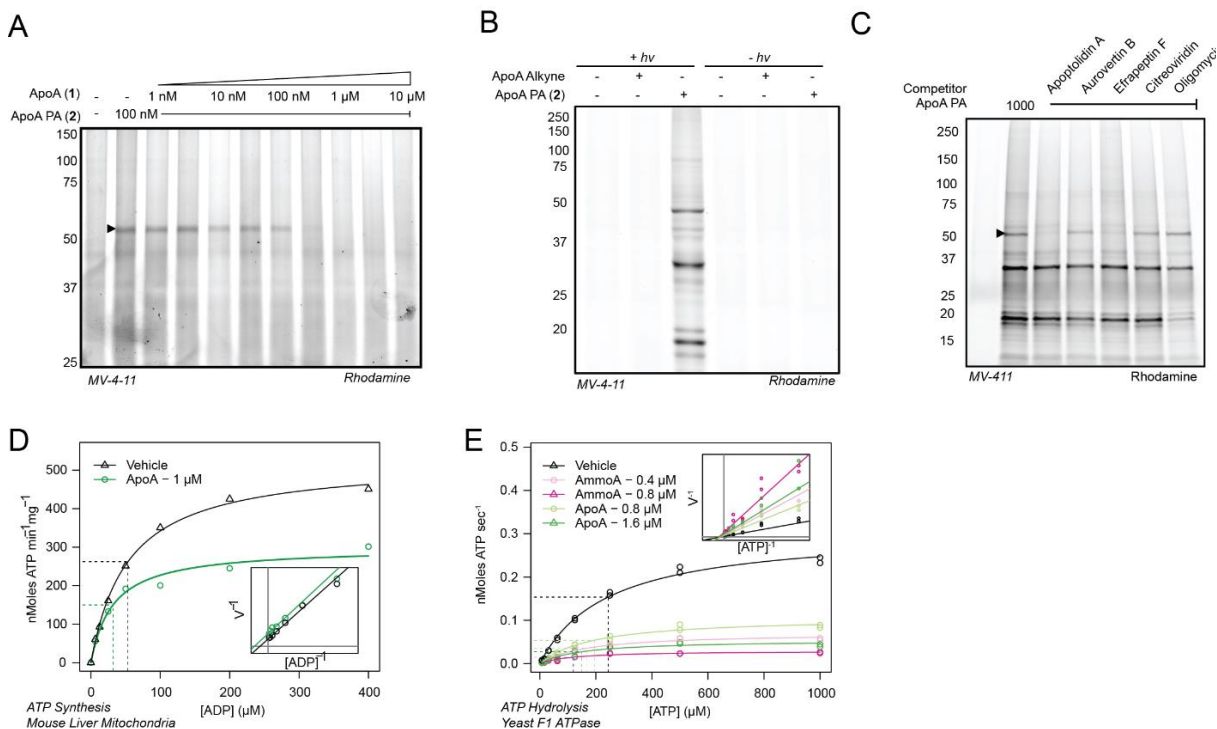
Figure 2.4. Analysis of apoptolidin A binding mode, photoaffinity labeling, and enzymatic assays

A, Gel-based analysis of apoptolidin A competition against (**2**) at a fixed concentration of 100 nM (**2**); **B,** Gel-based analysis of diazirine and UV light dependent labeling of (**2**) at 1 µM, suggestive of non-covalent binding in the absence of a photocrosslinker; **C,** Gel-based analysis of (**2**) binding to ATP5B (arrowhead) in the presence of known ATP synthase inhibitors; **D,** Analysis of ADP concentration dependence on inhibition of ATP synthesis by apoptolidin A in isolated mouse liver mitochondria using a HK/G6PDH coupled assay; **E,** Analysis of ATP concentration dependence on inhibition of ATP hydrolysis by (**1**) and (**3**) in isolated yeast F1 ATPase using a PK/LDH coupled assay.

67

To identify the putative targets of apoptolidin A in the MV-4-11 proteome, affinity enrichment was performed after *in situ* photocrosslinking of (**2**) with or without excess apoptolidin A (**1**). Subsequent to lysis and cycloaddition to TAMRA-azide-desthiobiotin, samples were affinity enriched using streptavidin resin and labeled for multiplexed mass

5   spectrometry quantification using isobaric tandem mass tags (TMT) as depicted in Figure 2.5. Quantitative proteomics on the enriched tagged samples revealed a single, highly enriched target relative to the competition control: ATP5B, the β subunit of ATP synthase (Figure 2.1D). ATP synthase is a ~600 kDa multiprotein complex responsible for converting the electrochemical proton gradient generated by the electron transport chain into chemical energy by the synthesis

10   of ATP from ADP and phosphate. ATP synthase is composed of two subcomplexes: the membrane-embedded F_O region, which contains the proton channel and is the target of oligomycin, and the soluble F_1 region, which contains the catalytic sites (Figure 2.1F). The F_1 subcomplex is composed of five distinct subunits with the stoichiometry $\alpha_3\beta_3\gamma\delta\epsilon$ and is largely conserved across the kingdoms of life (34). The three catalytic sites are located at the interfaces

15   of the α and β subunits with the catalytic residues localized to the β subunit, which is encoded by the gene *ATP5F1B* in humans. The three catalytic αβ sites are found in different conformations designated by their nucleotide content as $\alpha_{DP}\beta_{DP}$ (ADP-bound), $\alpha_{TP}\beta_{TP}$ (ATP-bound), $\alpha_E\beta_E$ (empty). During ATP synthesis, proton translocation through the F_O region induces rotation of the central rotor complex that drives ATP synthesis in the F_1 region (143). The enzyme can also

20   catalyze ATP hydrolysis (ATPase), which causes the rotor to reverse direction and pump protons from the matrix to the intermembrane space.
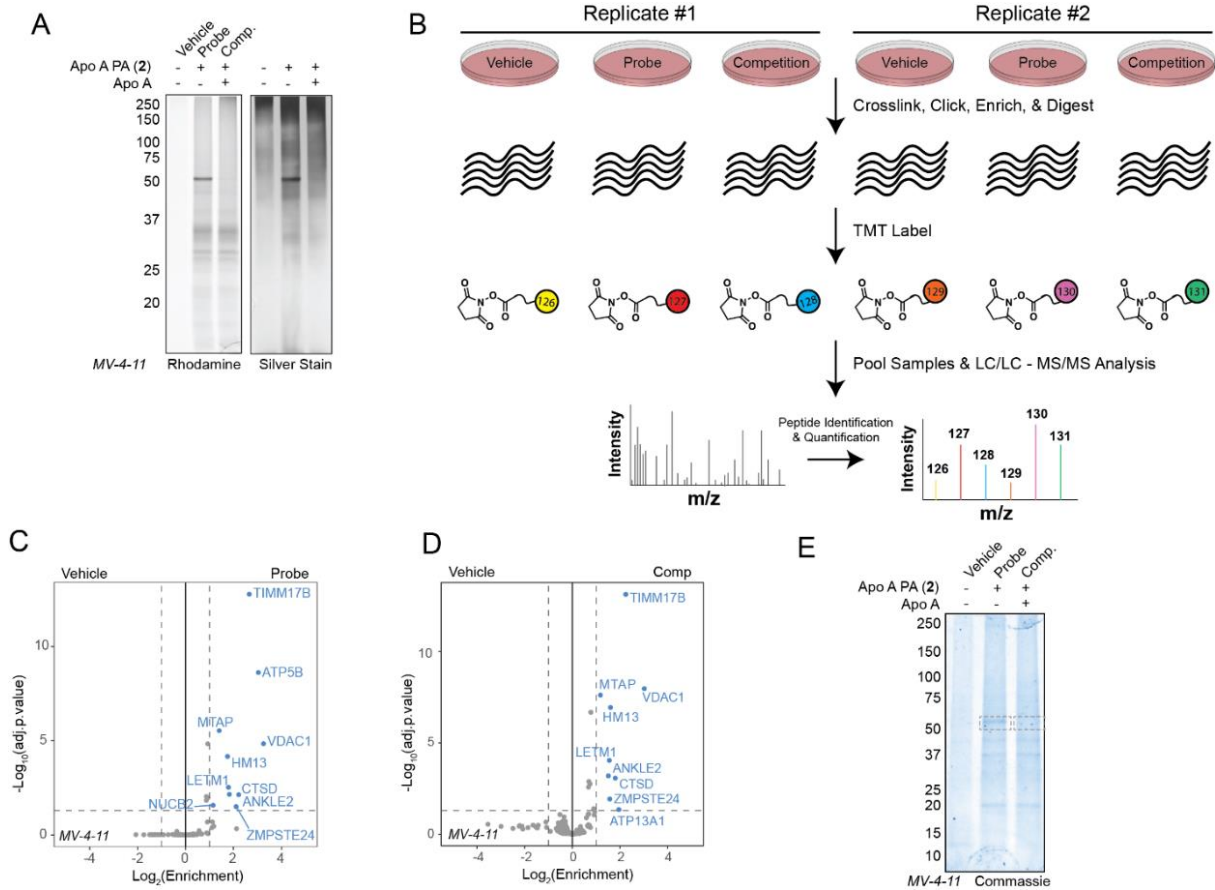
Figure 2.5. Identification of ATP5B as the target of apoptolidin A using comparative proteomics

A, Gel-based profiling of (**2**) targets in MV-4-11 with ± 1 μM ApoA PA, ± 20 μM ApoA after affinity enrichment using streptavidin resin prior to digestion and TMT labeling imaged by rhodamine fluorescence and after silver staining; **B,** schematic of the TMT multiplexing strategy for to combine vehicle, probe, and competition, conditions from two separate biological replicates **C,** Volcano plot of proteins significantly enriched in 'Probe' condition compared to 'Vehicle' analyzed by TMT-multiplexed MuDPIT proteomics; **D,** Volcano plot of proteins significantly enriched in 'Competition' condition compared to 'Vehicle' analyzed by TMT-multiplexed MuDPIT proteomics; **E,** Coomassie stained gel-based profiling of (**2**) targets in MV-4-11 cells – 50 kDa band from probe and competition conditions were cut and subjected to in-gel digestion.

Several non-specific adducts were enriched in the competition conditions compared to vehicle (Figure 2.5D). These include the mitochondrial membrane proteins VDAC and TIMM17B, as well as other membrane proteins, many of which are documented non-specific targets of alkyl diazirines ([144]). Immunoblotting confirmed the specific interaction of (**2**) with the β subunit of ATP synthase and nonspecific interactions with VDAC, and no interaction with ATP5G1, the c subunit in the F_O region that is target of oligomycin (Figure 2.1E). Several attempts were made to identify the adduction site of (**2**) on the β subunit using shotgun proteomics, but these were unsuccessful, likely due to the large size of the theoretical adduct. β subunit binding by (**2**) was also confirmed by direct in-gel digestion of Coomassie dye stained bands after affinity enrichment (Figure 2.5E). Finally, binding specificity to the β subunit was also confirmed in HEK-293 landing pad (HEK293-LP) cells expressing transgenic *ATP5F1B* with a C-terminal FLAG-tag (Figure 2.3D).

ATP synthase had been proposed as a target of apoptolidin family glycomacrolides based on similar cytotoxicity profiles to oligomycin in the NCI-60 screening program ([115]). Due to their common general classification as macrolides, apoptolidin and oligomycin were proposed to share a SAR model and both bind to the F_O region of ATP synthase ([117]). More recent studies questioned whether the ATP synthase F_O region is truly the mechanistic target of apoptolidin due to the discrepancy between *in vitro* (low μM) and *ex vivo* (low nM) activity ([101]) and different effects on cell signaling ([140]). These data demonstrate that apoptolidin and oligomycin act via distinct mechanisms at different binding sites on ATP synthase. Of note, apoptolidin and ammocidin represent the first known bacterial compounds to target the F_1 ATP synthase, as all previously described F_1 inhibitors are of fungal origin ([67]), while bacterial ATP synthase inhibitors such as oligomycin target the F_O region ([37]).

70

To evaluate whether apoptolidin was acting as an inhibitor of ATP synthase at the cytotoxic concentration, ATP synthesis was evaluated in MV-4-11 cells expressing the intracellular ADP/ATP reporter, Perceval HR (145). Treatment with apoptolidin A, ammocidin A, or oligomycin A elicited an increase in ADP/ATP ratio at concentrations comparable with their cytotoxicity (Figure 2.1G). *In vitro*, apoptolidin A and ammocidin A exhibited similar low nano-molar inhibition of ATPase activity by purified *Saccharomyces cerevisiae* ATP synthase (Figure 2.1H). Competition experiments with known F_1 binding inhibitors revealed uncompetitive binding with aurovertin and a lack of binding to the efrapeptin-bound conformation (Figure 2.4C). Kinetics studies in isolated mouse liver mitochondria and in yeast F_1 subcomplexes under non-saturating conditions revealed mixed inhibition (Figure 2.4D, E), consistent with an allosteric binding site distal to the catalytic sites at the interfaces of the α and β subunits.

Surprisingly, pre-treatment of cells with the uncoupling agents carbonyl cyanide *p*-trifluoromethoxyphenylhydrazone (FCCP) or 2,4-dinitrophenol (DNP) also eliminated adduction of (**2**) to the β subunit (Figure 2.6A). This observation suggested that either transport of (**2**) to the mitochondrial matrix was membrane potential dependent and/or the addition of uncouplers eliminated the apoptolidin binding site. Under uncoupled conditions, the decrease in mitochondrial matrix pH causes a conformational change in the inhibitory factor (ATPIF1, IF_1) that allows it to bind to the F1 subcomplex and inhibit the ATPase activity of ATP synthase (146). To test if IF_1 binding was interfering with apoptolidin binding, CRISPR/Cas9 was used to knock out *ATPIF1* in K562 leukemia cells (Figure 2.6B). In this setting, FCCP eliminated binding of (**2**) to the β subunit in the parental line, but not in cells with *ATP5IF1* knocked out (Figure 2.6C), suggesting that IF_1 prevents binding of apoptolidin to ATP synthase.

71
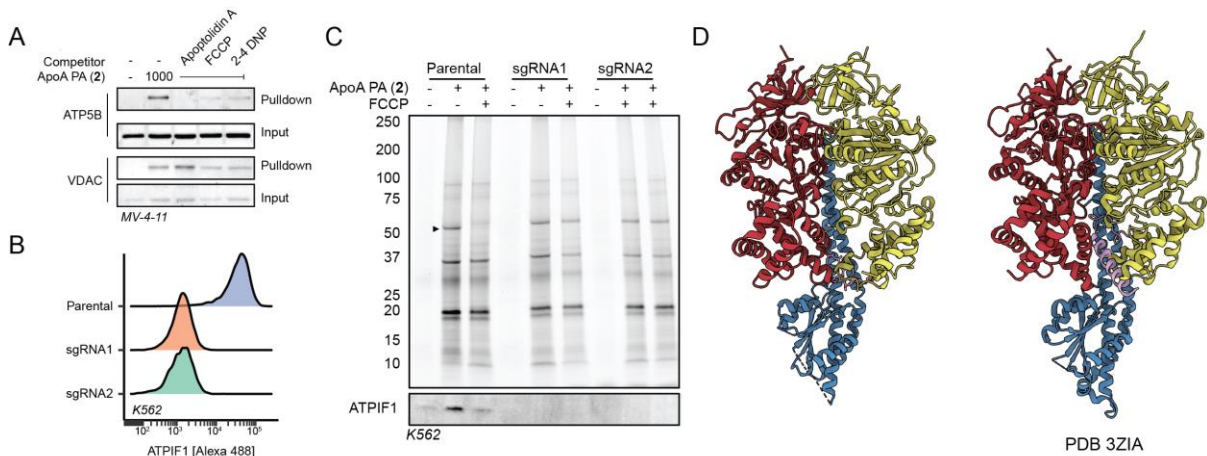
Figure 2.6. ATPIF1 prevents binding of apoptolidin A to ATP synthase under uncoupled conditions

A, Affinity enrichment and immunoblot of (**2**) (1 µM) adducts after pre-treatment with (**1**) (10 µM), FCCP (1 µM), or 2,4-DNP (1 µM) in MV-4-11 cells demonstrating loss of adduction in the presence of uncouplers; **B,** Confirmation of knockout of ATPIF1 using CRISPR/Cas9 in K562 cells via flow cytometry; **C,** Gel-based profiling (top) of (**2**) adducts parental K562 or two independent ATPIF1-KO clones in the presence or absence of FCCP (1 µM) ; **D,** Comparison of alpha/beta/gamma interface when bound to ammocidin (left) or ATPIF1 (right).

2.2.2 <u>Identification of the glycomacrolide binding site on ATP synthase via cryoEM</u>

The novel mode of inhibition of glycomacrolides revealed by photoaffinity labeling and enzymatic assays prompted a search for their binding site by structure studies of *S. cerevisiae* ATP synthase. CryoEM and image analysis yielded 3D maps of the ATP synthase bound to ammocidin A and apoptolidin A at 3.1 and 3.4 Å resolutions, respectively, allowing construction of atomic models for the complexes. In order to investigate conformational changes induced in ATP synthase upon inhibitor binding, we also determined a structure of the yeast ATP synthase without either inhibitor under otherwise identical conditions, and refined the F_1 region of the map to 4.2 Å resolution (Figure 2.7, Figure 2.8, Table 2.1).
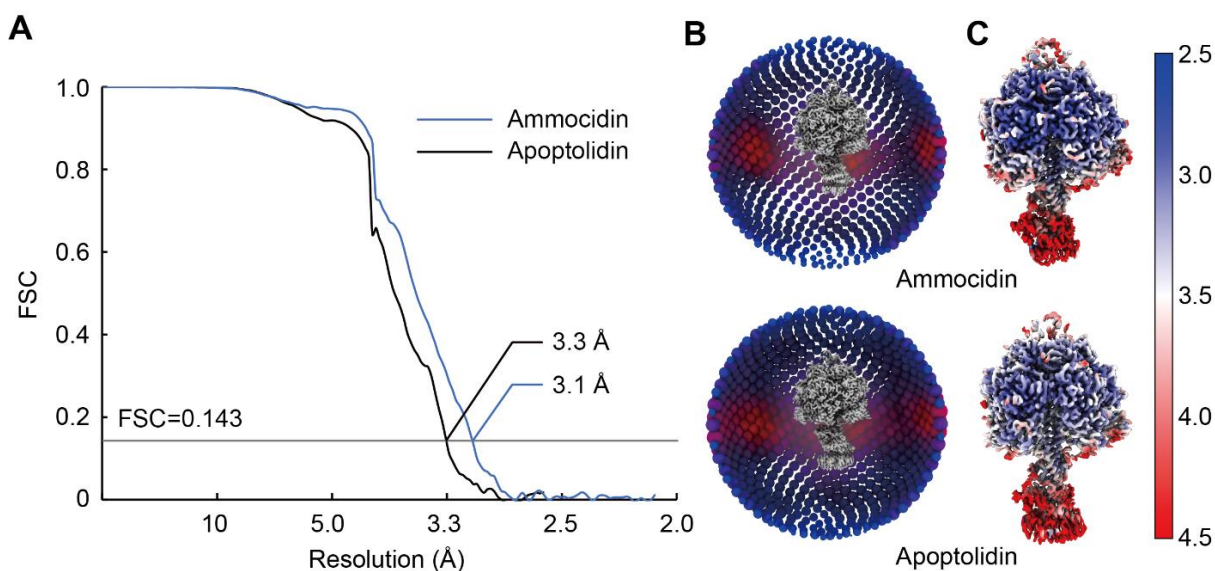
Figure 2.7. CryoEM map validation

Corrected Fourier shell correlation curves after gold-standard refinement **A,** local resolution maps **B,** and orientation distribution plots **C,** are shown for the maps of the F_1 regions of the ammocidin-bound, apoptolidin-bound, and inhibitor-free datasets.
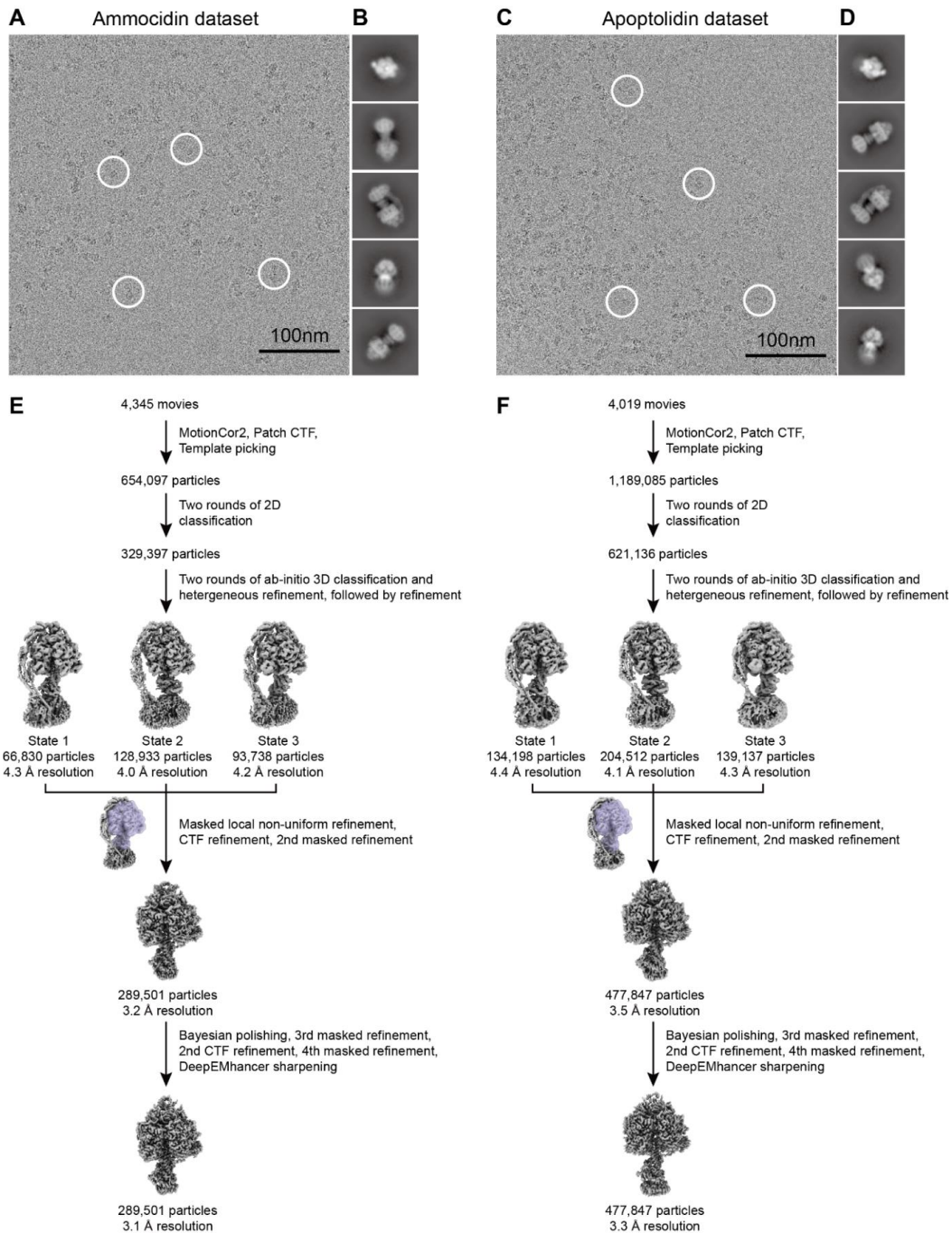
Figure 2.8. Workflow for cryoEM image analysis for ammocidin-bound and apoptolidin-bound yeast ATP synthase

Example micrographs (**A, C**), 2D class average images (**B, D**), and Workflow for obtaining maps of the F_1 regions (**E, F**) for ammocidin-bound, and apoptolidin-bound ATP synthases, respectively.

Table 2.1. CryoEM data collection, refinement, and validation statistics

	yF$_1$F$_O$ ammocidin (EMDB-23763) (PDB 7MD2)	yF$_1$F$_O$ apoptolidin (EMDB-23764) (PDB 7MD3)	yF$_1$F$_O$ (EMDB-23765)
Data collection and processing			
Magnification	75,000	75,000	25,000
Voltage (kV)	300	300	200
Electron exposure (e–/Å^2)	43	45	36
Defocus range (μm)	0.7-2.4	1.1-2.5	1.0-3.2
Movie pixel size (Å)	1.03	1.03	1.45
Final map pixel size (Å)	1.03	1.2875	1.45
Symmetry imposed	C1	C1	C1
Initial particle images (no.)	654,097	1,189,085	38,514
Final particle images (no.)	289,501	477,847	34,035
Map resolution (Å)	3.1	3.3	4.2
FSC threshold	0.143	0.143	0.143
Map resolution range (Å)	2.5-5.0	2.8-5.0	3.8-8.0
Refinement			
Initial model used (PDB code)	2XOK	2XOK	
Model resolution (Å)	3.1	3.5	
FSC threshold	0.5	0.5	
Model resolution range (Å)	330-3.1	330-3.5	
Map sharpening B factor (Å^2)	Sharpened locally	Sharpened locally	
Model composition			
Non-hydrogen atoms	23474	23031	
Protein residues	3115	3133	
Ligands	8	8	
B factors (Å^2)			
Protein	80.34	79.68	
Ligand	61.10	63.57	
R.m.s. deviations			
Bond lengths (Å)	0.008	0.006	
Bond angles (°)	0.739	0.692	
Validation			
MolProbity score	1.10	1.25	
Clashscore	3.08	3.80	
Poor rotamers (%)	0.25	0.26	

Density corresponding to the inhibitor is found in the catalytic F$_1$ region of ATP synthase (Figure 2.9A, pink density). Despite the presence of three-fold pseudosymmetry in the F$_1$ region, which provides three nearly-equivalent potential glycomacrolide binding sites, only a single inhibitor molecule was found to bind at the α$_{DP}$β$_{DP}$ interface. This binding site is formed mainly by subunits α$_{DP}$, β$_{DP}$, and γ, although neighboring β$_{TP}$ and α$_E$ subunits provide additional protein-inhibitor contacts (Figure 2.9B). Despite the functional differences in the aglycone, attachment site, and sequence of glycosylation between apoptolidin A and ammocidin A, both molecules

bind to ATP synthase in a strikingly similar manner (Figure 2.9B, green density) and for clarity

this discussion is focused on the higher-resolution ammocidin structure. The core macrolide is

buried deeply inside the binding pocket and interacts with multiple hydrophobic residues of

nearby subunits, while the head and tail sugar groups form fewer interactions with the protein

5   (Figure 2.9B, C). The structure indicates that introducing photoaffinity probes at the C-2'

position of the C-9 deoxysugar of apoptolidin, and the C-3' position of ammocidin (Figure 2.1A,

Figure 2.2D) is unlikely to interfere with drug binding, supporting the reliability of the

photoaffinity labeling experiments described above. Together, these observations indicate that

the high-affinity binding of ammocidin and apoptolidin to ATP synthase are achieved through

10   extensive interactions between the core macrolides and their hydrophobic binding site in the

enzyme (Figure 2.9C). Comparison of the inhibitor-free and inhibitor-bound structures shows

that inhibitor binding forces subunit β_{DP} to move outward to adopt a more "open" conformation

(Figure 2.9D, red arrows and Movie 1), while the conformation of the non-catalytic α_{DP} subunit

remains largely unchanged except for the residues in direct contact with the inhibitor. This

15   "open" conformation of β_{DP} is incompatible with nucleotide binding and explains why the only

natural substrate found in the inhibitor-bound structures is a phosphate ion at the β_{TP} subunit

(Figure 2.9E). In addition to making β_{DP} incapable of binding substrates, the inhibitors likely also

block the rotation of ATP synthase by interacting strongly with subunits α_{DP}, β_{DP}, and γ,

preventing the conformational changes needed for ATP hydrolysis and thereby inhibiting the

20   rotary catalytic mechanism of the enzyme (34).
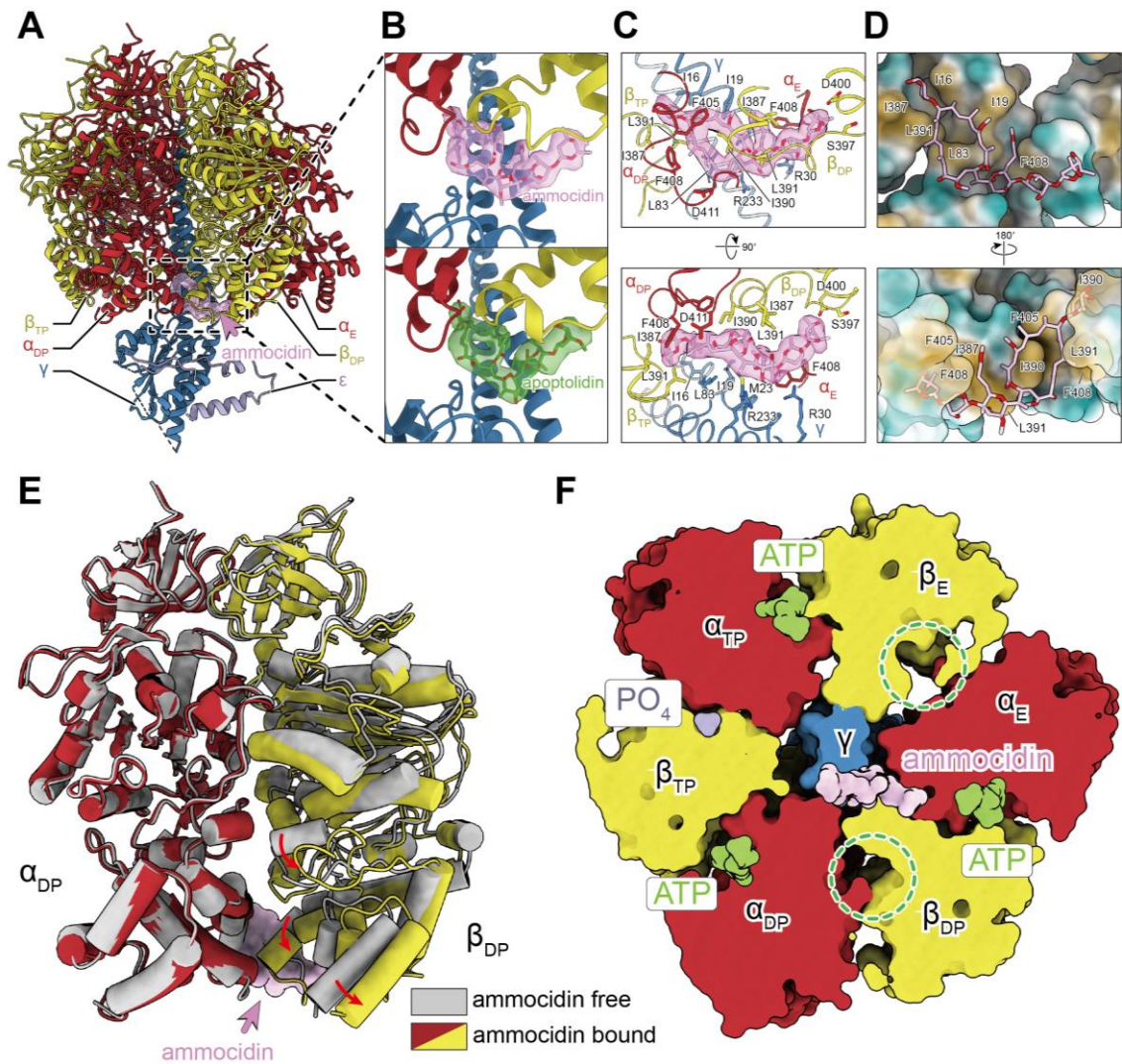
Figure 2.9. Structure of glycomacrolide bound yeast ATP synthase bound reveals a novel mode of inhibition.

A, Atomic model of the F_1 region of yeast ATP synthase bound to ammocidin, cryoEM density of ammocidin is shown in pink; **B,** Close-up view of the ammocidin (top) and apoptolidin (bottom) binding site; **C,** Ammocidin binding pocket is largely formed with hydrophobic residues (yellow surface); **D,** Ammocidin binding induces conformational change of β_{DP} subunit (red arrows) and forces it to adopt a more "open" conformation; **E,** Cross section through the F_1 region shows that β_{DP} does not bind to nucleotide (green circles) when bound to ammocidin.

2.2.3 Deep mutational scanning of glycomacrolide binding site reveals mutations that confer resistance to apoptolidin and ammocidin

Having determined that the F_1 region of ATP synthase is a target of apoptolidin A and ammocidin A, we next sought to determine whether binding to ATP synthase was essential for the cytotoxicity of apoptolidin by identifying one or more resistance mutations in the complex that prevent binding and cytotoxicity. Genomic analysis and multiple sequence alignment of ATP synthase genes from the apoptolidin producer *Nocardiopsis sp.* FU-40, revealed a substitution of phenylalanine at position ATP5B-L394 (Figure 2.10A) that we hypothesized would cause a clash that prevents binding. Introduction of ATP5B-L394F into MV-4-11 or K562 cell lines by CRISPR/Cas9 homology-directed repair (HDR) ([147](#)) revealed decreased sensitivity to ammocidin A, but unexpectedly increased sensitivity to apoptolidin A compared to the parental line (Figure 2.10D, E). Comparing the binding poses of apoptolidin A to ammocidin A, ATP5B-L394 interacts most closely with the cyclic hemiketal that exhibits large differences in binding pose to account for the differing attachments of the disaccharide at C24 vs C27 (Figure 2.10F). Although this substitution does not provide cross resistance against both macrolides, the diverging effects on sensitivity supports the binding mode identified by cryoEM of the yeast enzyme.
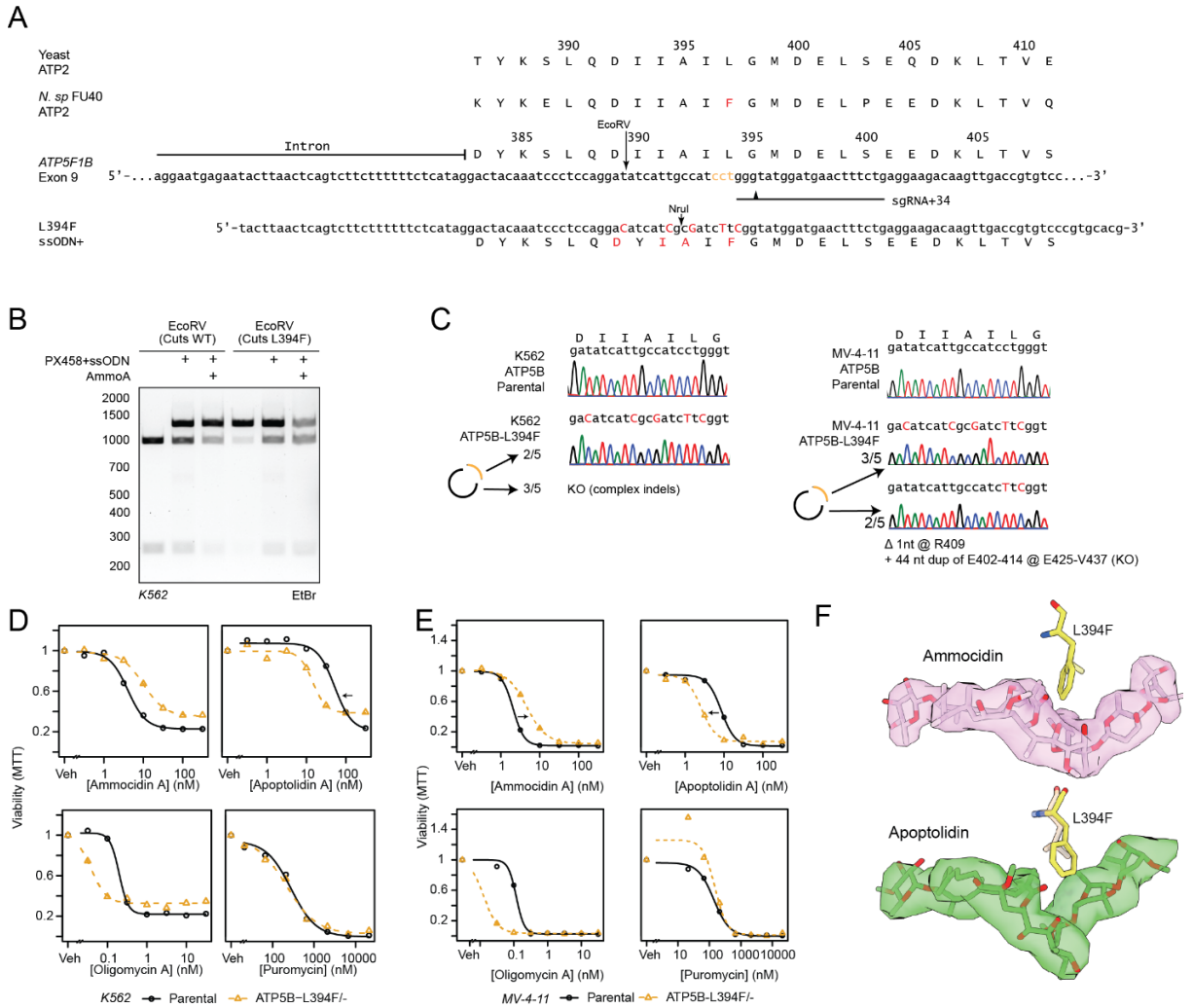
Figure 2.10. ATP5B-L394F mutation has opposing effects on apoptolidin and ammocidin sensitivity.

A, Multiple sequence alignment of ATP synthase β subunit C-terminal domain and CRISPR/Cas9 HDR editing strategy for human exon 9 and using plasmid (PX458) encoding sgRNA and Cas9 and ssODN repair template, PAM sites labeled in yellow, cut locations noted with arrowhead, edits noted in red, restriction sites noted; **B,** Restriction digest of *ATP5F1B* Exon 9/10 amplicons from parental K562s or PX458 + ssODN treated K562s treated with ammocidin A (150 nM x 5 d) showing loss of wildtype allele and retention of edited alleles with ammocidin treatment; **C,** Confirmation of introduction of ATP5B-L394F mutation and KO of wildtype ATP5B in K562s and MV-4-11 cells by Sanger sequencing; **D,** ATP5B-L394F sensitizes cells to apoptolidin A and provides some resistance against ammocidin in K562 and **E,** MV-4-11 cells as measured by MTT assay at 72 hrs; **F,** Modeling of the L394 (yeast L397) mutation on the ammocidin (top) and apoptolidin (bottom) structures showing proximity to the hemiketal.

In order to identify a mutation that confers complete resistance to both apoptolidin and ammocidin, a deep mutational scanning approach was taken, using the Bxb1 "landing pad" system (148) to conduct a pooled screen of all possible missense mutations in the binding site. Mutagenesis targets were identified by selecting all residues within 4.5 Å of apoptolidin or ammocidin in the atomic models, identifying 21 residues across the α (5), β (8), and γ (8) subunits (Figure 2.11A), and a mutant library containing all 420 point mutants of the three genes was generated using nicking mutagenesis (149) (Figure 2.12B).

After transfection of the mutant library and selection for cells that had undergone successful recombination, each pool of mutant-expressing cells was exposed to varying concentrations of apoptolidin A or ammocidin A (Figure 2.11B). Cells were cultured in galactose-containing media to enforce OXPHOS dependence and select against loss of function mutants. After two rounds of selection, resistant mutants were expanded, and the integrated variants were amplified by PCR and subjected to deep sequencing. Allelic enrichment was consistent across biological replicates and no enrichment was seen in cells passaged without inhibitors (Figure 2.12C). Comparison of the variant abundance in the plasmid library to the variant abundance in successfully integrated cells allows for inference of variant fitness in the absence of any treatment. Notably, ATP5B (β subunit) I393, L394, and E398, which all make close contacts with ammocidin in the atomic model of the inhibited ATP synthase, were enriched for wildtype alleles, suggesting that mutations at these positions result in a loss of fitness (Figure 2.12D).
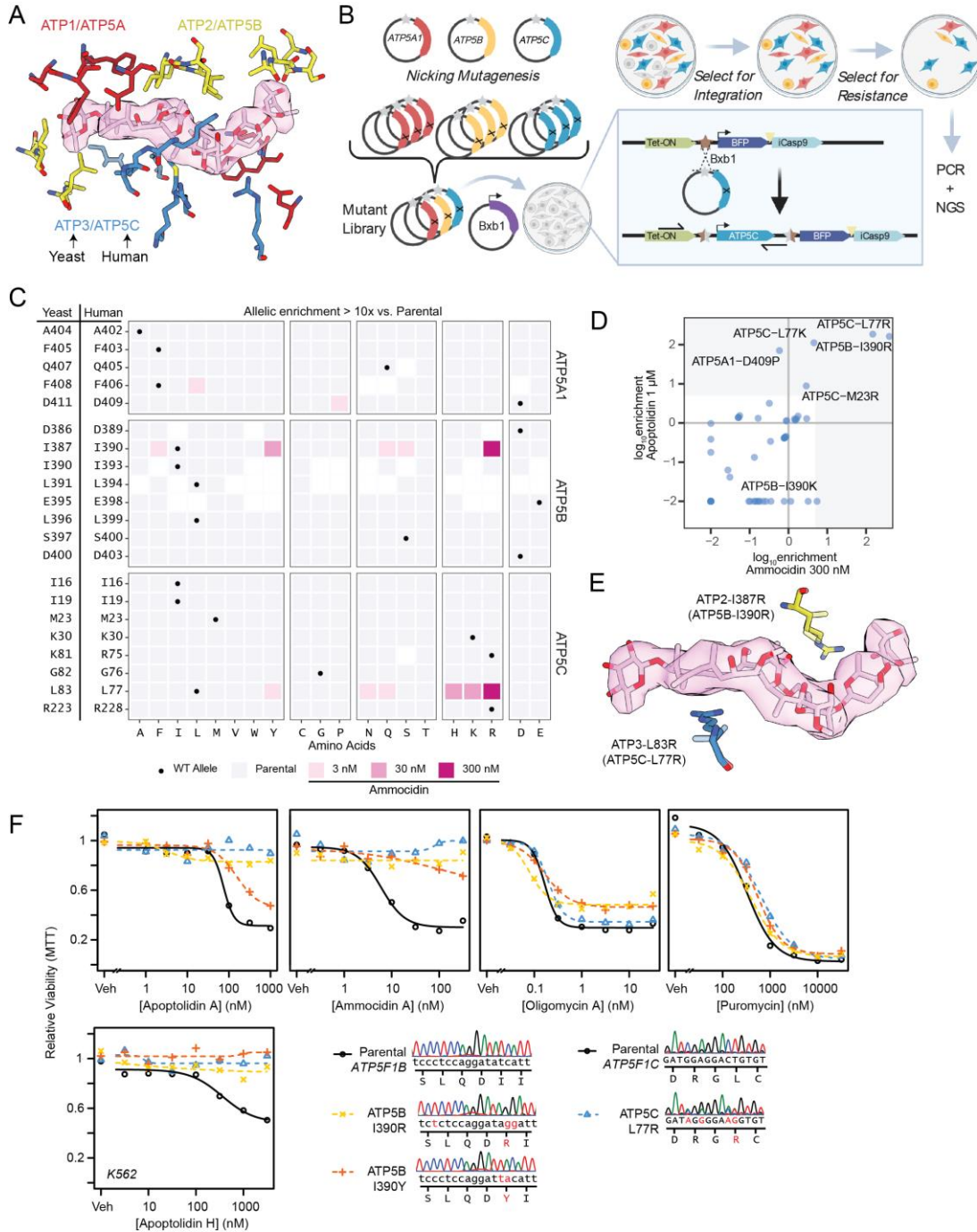
Figure 2.11. Deep Mutational Scanning of Ammocidin Binding Site on ATP Synthase

Figure 2.11: Deep Mutational Scanning of Ammocidin Binding Site on ATP Synthase

A, Selection of residues for mutagenesis on α (Yeast ATP1, Human ATP5A – red), β (Yeast ATP2, Human ATP5B – yellow), and γ (Yeast ATP3, Human ATP5C – blue) subunits within 4.5 Å of ammocidin or apoptolidin; **B,** Schematic of mutagenesis experiment, with pooled nicking mutagenesis on each gene, which were combined and transfected into landing pad expressing HEK-293 cells (HEK293-LP) with Bxb1 encoding plasmid (created with BioRender.com); **C,** Tile plot of enrichment after treatment, filled based on the highest dose at which >10-fold enrichment was observed based on sequencing counts (see Fig. S10); **D,** Comparison of mutation enrichment by 300 nM ammocidin A vs 1 μM apoptolidin A; **E,** Modeling of L83R and I387R mutations in the ammocidin cryoEM model (~ human residues in parenthesis); **F,** Comparison of drug sensitivity by MTT assay at 48 hrs between K562 Parental and K562 CRISPR/Cas9 knock-in resistant mutants demonstrating cross resistance to apoptolidin A and ammocidin A without an effect on sensitivity to oligomycin or puromycin (biological triplicates).
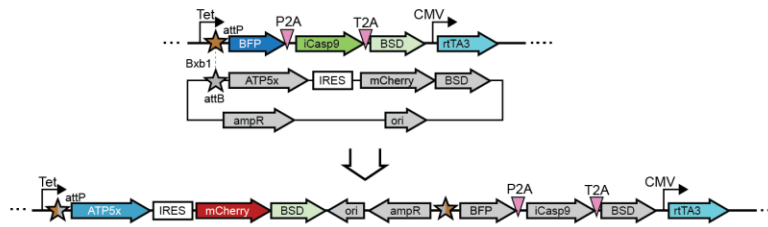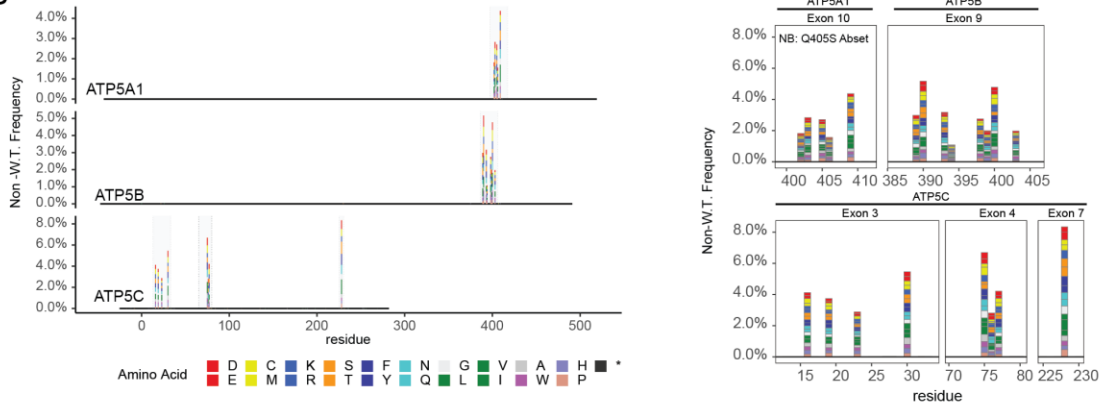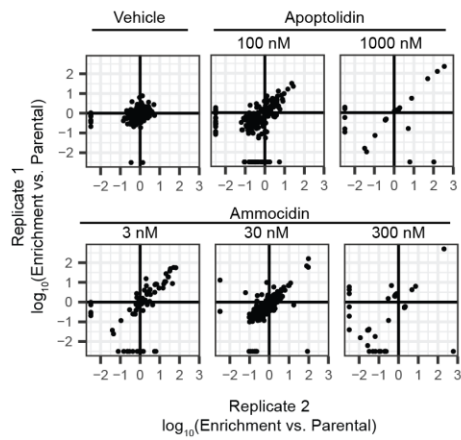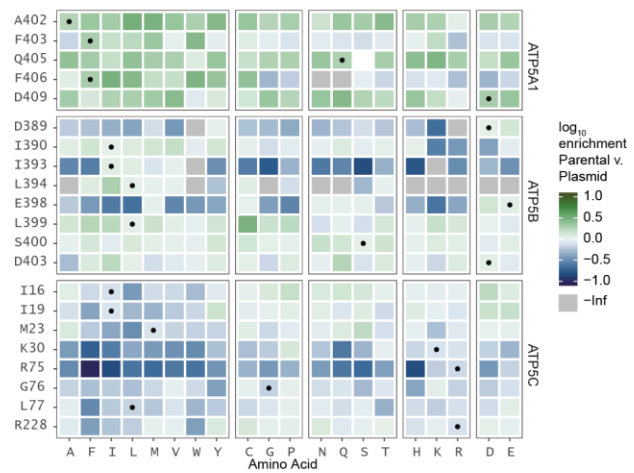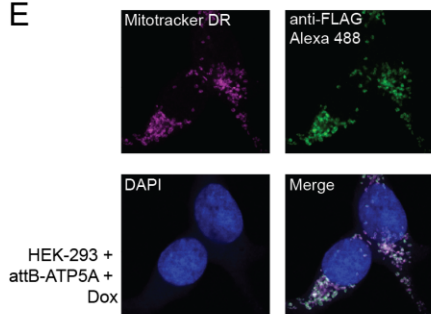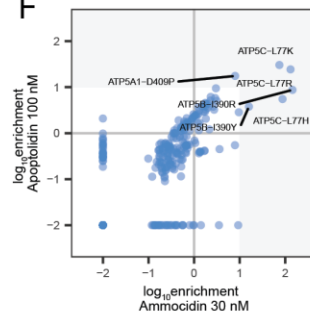
Figure 2.12. Deep Mutational Scanning of Ammocidin Binding Site on ATP Synthase (continued)

A, Illustration of the Bxb1 landing pad system consisting of an *attP* containing landing pad
integrated at a single site in the genome and an *attB* transfer plasmid containing the variant gene
of interest (ATP5x), colored genes are expressed in the presence of doxycycline, adapted from
([148]); **B,** Validation of ATP synthase variant library after nicking mutagenesis showing the
frequency of non-wildtype variants at each position, with residue 1 corresponding to the first
residue of the mature peptide; **C,** assessment of reproducibility between biological replicates
showing consistent enrichment of resistance mutations, variants which were not observed were
set to -2.5; **D,** Comparison of variant frequencies that were observed after selection for
successful integration compared to the original library, variants which were observed in the
original library but not detected after integration were set to -Inf. Variants which exhibit negative
enrichment or complete loss are thought to exhibit decreased fitness relative to the WT alleles; **E,**
Confirmation of proper mitochondrial localization of the landing-pad expressed ATP5A by
immunofluorescence at 63x in HEK-293T landing pad cells; **F,** Comparison of variants enriched
by apoptolidin and ammocidin at medium dose (100 nM / 30 nM) demonstrating that apoptolidin
and ammocidin select for similar resistance mutations (see also Fig 3D for high dose).
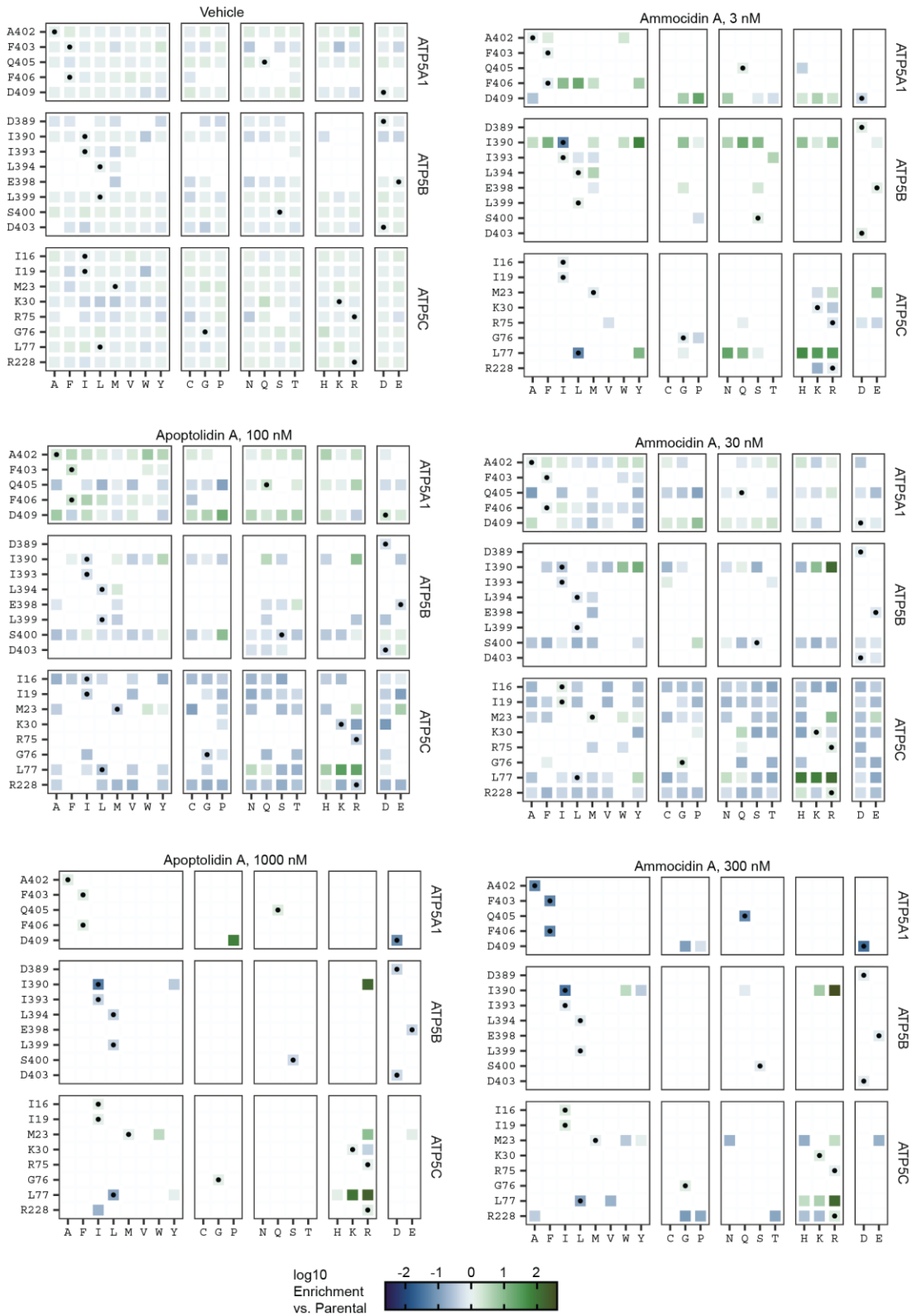
Figure 2.12. Apoptolidin and Ammocidin select for similar resistance mutations.

Tile maps of amino acid enrichment relative to the parental library at each position at each dose of ammocidin or apoptolidin. Vehicle treated cells were allowed to grow for one additional passage after selection. White squares indicate variants which were not detected (<100 counts) by deep sequencing. Circles represent WT alleles.

5   Comparing variant abundance between the parental cell line and those treated with ammocidin A revealed two key mutational hot-spots: ATP5B-I390 and ATP5C-L77. Mutations at these positions conferred varying degrees of resistance to both apoptolidin and ammocidin (Figure 2.11C, Figure 2.13), with positively charged residues exhibiting enrichment at the highest concentrations of ammocidin A and apoptolidin A (Figure 2.11D). Modeling these

10 substitutions in the atomic model suggests that introduction of arginine at these positions likely alters binding site electrostatics and disrupts the hydrophobic interactions necessary for binding (Figure 2.11E). Resistance was confirmed by expressing each mutation independently in 239LP cells (Figure 2.14A-C), as well as with CRISPR/Cas9 genome editing of the native alleles in K562 (Figure 2.11F) and MV-4-11 leukemia cell lines (Figure 2.14H). Consistent with the

15 results of the deep mutational scanning experiment, introduction of the ATP5B-I390R or ATP5C-L77R mutations conferred complete resistance to apoptolidin A and ammocidin A, while the ATP5B-I390Y variant raised the EC50s by 3 to 10-fold (Figure 2.11F). None of the mutations tested notably affected sensitivity to oligomycin or puromycin, reflecting retention of a functional electron transport chain. These data establish that ATP synthase is the sole

20 mechanistic target of apoptolidin family glycomacrolides; binding to the F_1 subcomplex of ATP synthase is necessary for the selective cytotoxicity of the family.
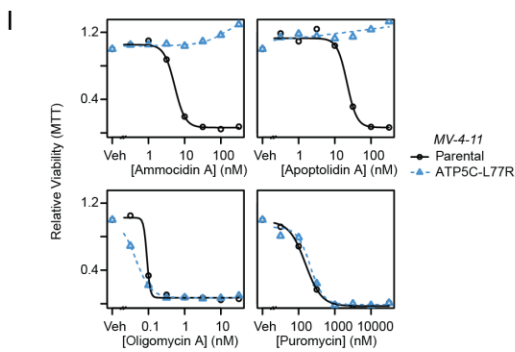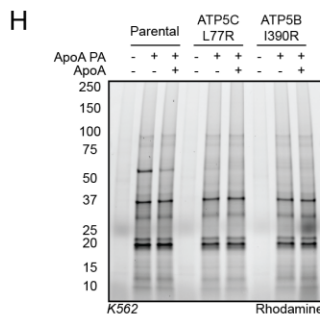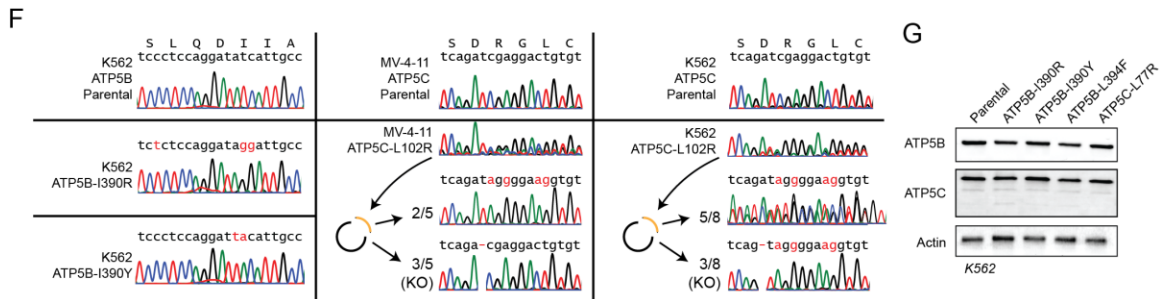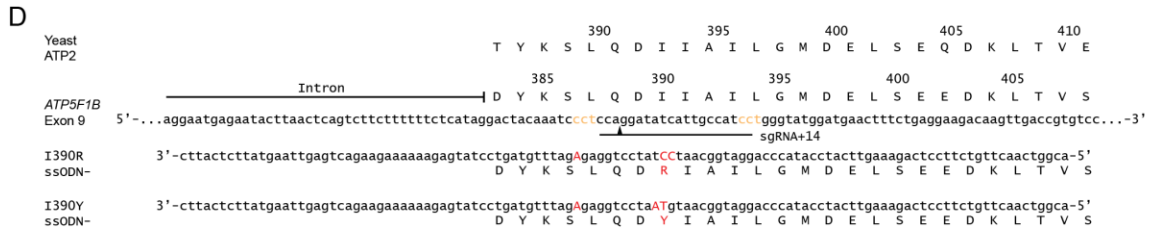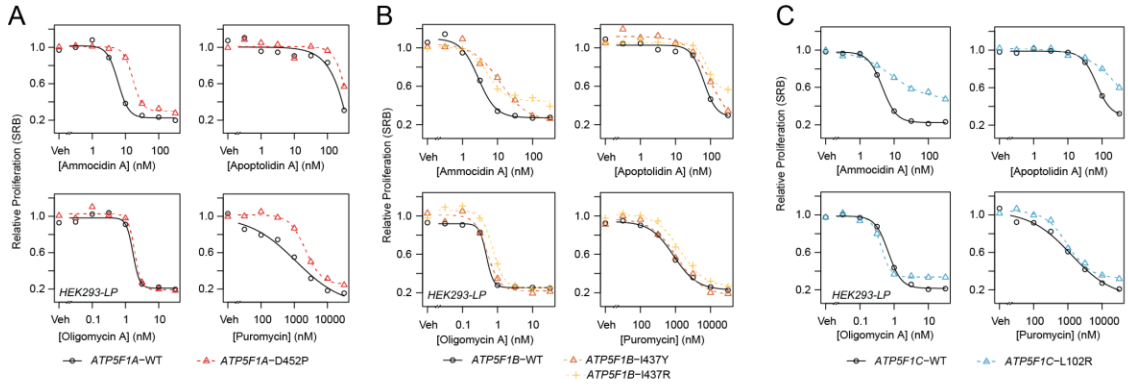
Figure 2.14. Validation of ATP synthase resistance mutations using CRISPR/Cas9 Genome Editing.

A, Validation of resistance mutations using transgenic mutant ATP synthase in HEK293LP cells at 72 hrs by SRB assay for mutations in the alpha; **B,** beta; and **C,** gamma subunits; **D,** CRISPR/Cas9 HDR editing strategy for ATP5B exon 9 and **E,** ATP5C exon 4 using plasmid (PX458) encoding sgRNA and Cas9 and ssODN repair template, PAM sites labeled in yellow, cut locations noted with arrowhead, edits noted in red; **F,** Confirmation of desired edits in single-cell clones by sanger sequencing of PCR amplicons and/or PCR cloning to resolve heterozygous edits; **G,** Confirmation of unchanged expression of ATP synthase genes in CRISPR/Cas9 edited clones by immunoblot; **H,** Gel-based profiling of (**2**) targets in K562s Parental or CRISPR/Cas9 edited cell lines showing loss of binding to ATP5B; **I,** Secondary validation of ATP5C-L77R mutant in CRISPR edited MV-4-11 cell line using MTT-assay at 48 hrs.

The binding modes of apoptolidin family macrolides revealed by cryoEM and deep

mutational scanning studies also help contextualize the previous studies on the SAR of

apoptolidin, which were notable in that no single modification was able to eliminate its activity

(101, 124). This observation is consistent with its binding site, which is dominated by

5   hydrophobic interactions each of which contributes a fractional amount to its nanomolar affinity.

The structure also provides clues to the role of the disaccharide that is key for its activity:

although loss of the disaccharide on apoptolidin H reduces its activity by >10 fold, it still retains

sub micro-molar activity *ex vivo*. Importantly, this residual activity is eliminated by introduction

of the apoptolidin resistance mutations ATP5B-I390R and ATP5C-L77R (Figure 2.11F),

10 suggestive of a shared binding mode of the macrolide core.

2.2.4 Ammocidin A inhibits leukemia growth *in vivo*

Although apoptolidin and ammocidin are distinguished by their ability to induce

apoptosis in transformed cells while sparing healthy cells, ATP synthase, the target of

apoptolidin, is ubiquitously expressed and considered 'essential' in non-cancerous cells. Though

15 the ATP synthase inhibitor oligomycin is widely used as a tool compound in cellular assays, its

lipophilicity and narrow therapeutic index render it poorly suited for *in vivo* applications (29).

These studies on older ATP synthase inhibitors prompted us to question whether inhibition of

ATP synthase by apoptolidin family glycomacrolides could be leveraged therapeutically and

whether a therapeutic index between cancerous cells and healthy cells exists. Ammocidin A was

20 selected as the lead compound for *in vivo* studies due to its serum stability, higher potency, and

the known proclivity of apoptolidin A to isomerize *in vivo* to isoapoptolidin A via ester

migration of C-20 (107, 108). Preliminary pharmacokinetic studies confirmed that ammocidin

injected intraperitoneally was bioavailable in blood (Figure 2.15A) and dose escalation studies

established ammocidin 0.1 mg/kg/day as the maximum tolerated dose, with minimal detectable

toxicity over 14 days.
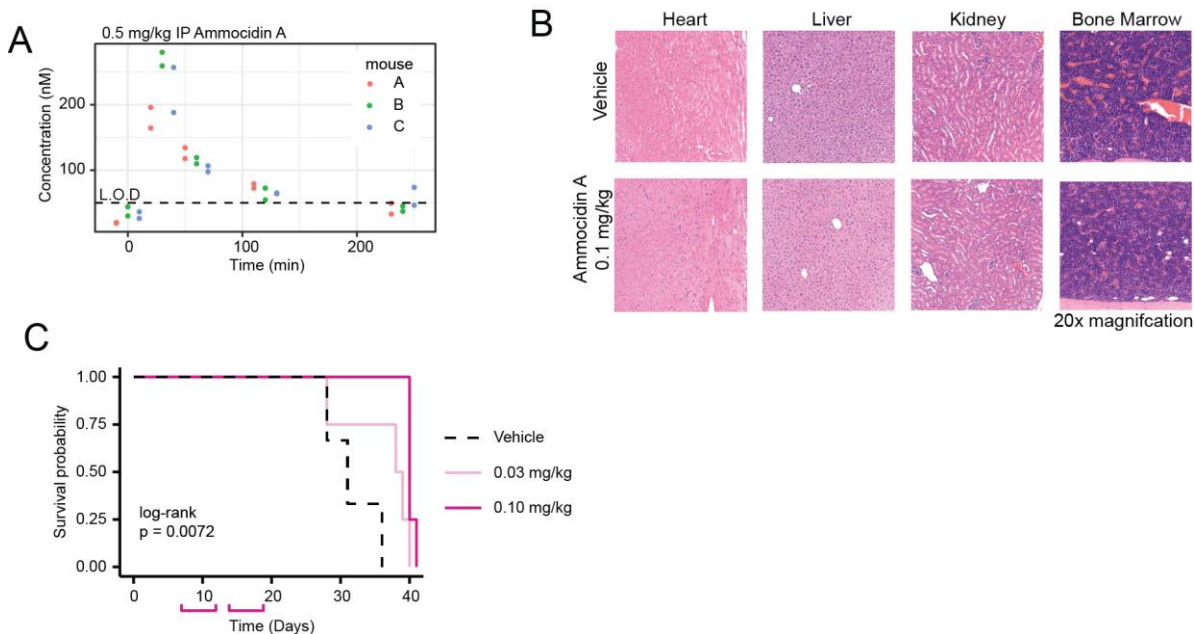
Figure 2.13. Evaluation of Ammocidin Dosing, Pharmacokinetics and Toxicity in NSGS Mice and efficacy in NSGS MV-4-11 Xenograft.

A, Preliminary (non-GLP) evaluation of PK profile of ammocidin A in NSGS mice with a single dose of Ammocidin A (technical duplicate); **B,** Gross histology of H&E sections from organs of NSGS mice 2 weeks after treatment with ammocidin A (0.1 mg/kg IP QD for 5 on, 2 off) revealing/reveal no tissue damage related toxicity **C,** Engrafted mice (n = 4 per group) were treated from day 7 to day 18 (pink brackets) and therapy was then held. Mouse survival was measured by Kaplan-Meier analysis (p-value calculated using log-rank test).

Based on the efficacy observed for ammocidin *in vitro*, we tested the compound as a

monotherapy in an *in vivo* model. Antileukemic efficacy was evaluated in a systemic murine

NSGS xenograft model (150) using MV-4-11 human leukemia cells. Engrafted mice were

treated with vehicle, 0.1 mg/kg or 0.03 mg/kg ammocidin A dosed daily, five days on, two days

off, for two weeks (Figure 2.16A). Weekly chimerism analyses were conducted, and the

percentage of MV-4-11 cells were quantified via flow cytometric analysis of murine peripheral

blood using anti-human CD45 (hCD45) and anti-human CD33 (hCD33) monoclonal antibodies.

At day 28, vehicle mice became moribund and all mice were sacrificed. Blood, bone marrow, and splenic tissues were harvested for chimerism analysis (150). Treatment with ammocidin resulted in dramatically decreased bone marrow leukemia burden in a dose-dependent manner in mice treated with 0.1 mg/kg ammocidin (B). A trend towards leukemia suppression was noted in

5 the spleen, however, this effect was not statistically significant. Leukemia burden was also assessed by immunohistochemistry for hCD45 in bone marrow, which similarly revealed dose-dependent leukemia suppression in ammocidin A treated mice (Figure 2.16C). The remarkable degree of efficacy seen for ammocidin A monotherapy in leukemia is consistent with recent studies that suggest that leukemia cells, and in particular therapy resistant leukemia stem cells

10 (LSCs), are exquisitely sensitive to OXPHOS inhibition (134, 151-153).
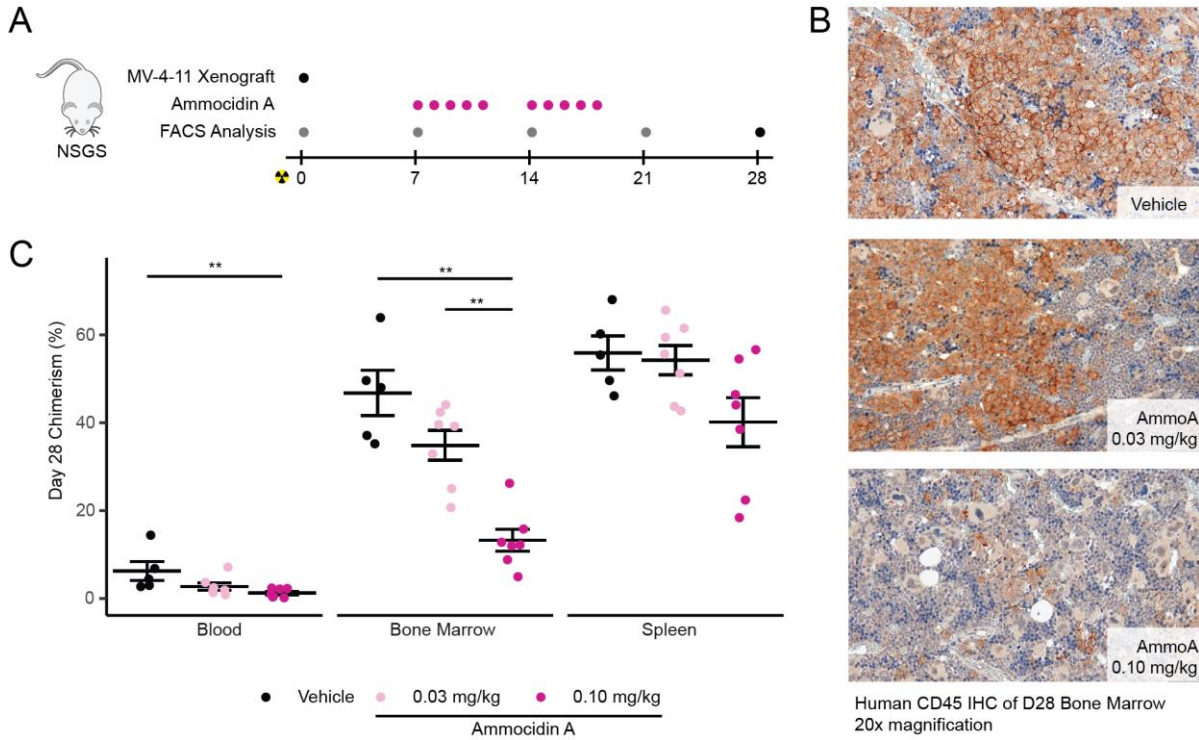
Figure 2.14. Ammocidin A inhibits leukemia growth *in vivo*.

A, Experimental scheme for xenograft experiments—grey dots indicate assessment of human MV-4-11 chimerism in blood only, pink dots on days of ammocidin dosing, and black dot for terminal analysis on day 28 (e.g. assessment of chimerism in the blood, marrow, and spleen); **B,** Immunohistochemistry against human CD45 in day 28 marrow showing dose dependent decrease in leukemia burden; **C,** Assessment of human MV-4-11 chimerism in the blood, bone marrow, and spleen at day 28; bars represent mean ± S.E.M for each group (n = 6 − 7 per group, ** = P < 0.01).

2.3 Discussion

Alterations in bioenergetics, including OXPHOS dependency, have long been recognized as a hallmark of cancer, however, efforts to target this vulnerability have been hampered by a dearth of metabolic inhibitors with sufficient selectivity and acceptable toxicity profiles (74). This unmet need is especially acute as many of the cancers that appear to be most vulnerable to OXPHOS inhibition are those for which few therapeutic options exist, including acute myeloid leukemia and glioblastoma. Previous efforts to target mitochondrial bioenergetics in leukemia include inhibitors of mitochondrial complex I (73, 151), complex III (71), and the mitochondrial

translation machinery responsible for synthesizing the mitochondrially encoded components of the electron transport chain (154). Outside of leukemia, therapeutic targeting of ATP synthase has previously been attempted in the context of autoimmune conditions with the OSCP binding benzodiazepine Bz-423 (155) which advanced to Phase II clinical trials, as well as the FDA

5   approved anti-tuberculosis agent bedaquiline which targets the mycobacterial ATP synthase (156). In addition to efforts to target the electron transport chain directly, recent studies have suggested that venetoclax, an inhibitor of BCL-2 recently approved for treating myeloid leukemias, targets LSCs by inhibiting OXPHOS (136, 137, 153). There is also evidence that OXPHOS inhibitors can be combined synergistically to increase the efficacy of venetoclax

10   therapy, suggesting a possible route for efficacious combination therapies with apoptolidin family glycomacrolides (154, 157, 158). This work demonstrates that apoptolidin family glycomacrolides are unique among all OXPHOS inhibitors currently in clinical development or any previously described ATP synthase inhibitors.

Chemical probes, particularly compounds derived from natural products discovered in

15   phenotypic screens (159), have contributed much to our understanding about the functional dependencies of cancer cells. Though tool compounds may modulate pathways and phenotypes in desirable ways, to be considered a chemical probe a compound must act selectively through a defined mechanism of action (87). In order for a compound to be considered a therapeutic candidate, it must be bioavailable, capable of modulating its target *in vivo,* and possess an

20   acceptable therapeutic index (87). Though ATP synthase was proposed as the target of apoptolidin based its cytotoxicity profile in the NCI-60 screen (115), a lack of target validation precluded its use as a chemical probe and apoptolidin's reduced stability precluded its development as a therapeutic agent. This work defines the mechanism of action of the entire

93

class of apoptolidin glycomacrolides including apoptolidin A and ammocidin A, combining

evidence from cellular target engagement, structural biology, and mutagenesis of the binding

site. The *in vivo* studies using ammocidin A represent the first application of this compound class

in vivo and demonstrate that ammocidin family compounds are bioavailable, well tolerated, and

5   efficacious at suppressing leukemia growth in human xenografts. Combined with the structural

insights and past work on the SAR of apoptolidin family compounds, this work establishes a path

towards the therapeutic development of apoptolidin family glycomacrolides to address OXPHOS

dependency in cancer and to study the reliance of cellular OXPHOS in human physiology and

disease.

10   **2.4 Materials and Methods**

2.4.1 Mammalian Cell Culture

MV-4-11, HEK-293T, and H-292 cells were purchased from the American Type Culture

Collection (ATCC, Manassas, VA). K562 cells were kindly provided by Dr. Gregor Neuert

respectively and were validated by STR profiling at the University of Arizona genetics core.

15   BaF3 cells were a kind gift of Dr. Christine Lovly, Vanderbilt University Medical Center. HEK-

293-LP cells were a kind gift of Kenneth Matreyek, Case Western Reserve University. Cell lines

were tested for mycoplasma contamination using the ATCC Universal Mycoplasma detection kit

before use. MV-4-11 and K562 cells were maintained with Gibco IMDM Glutamax media

supplemented with 10% FBS and 1% Pen/Strep. H292 cells were maintained with RPMI 1640

20   supplemented with 10% FBS and 1% Pen/Strep. HEK-293 cells were cultured in DMEM media,

10% FBS, 1% Pen/Strep, with glucose or supplemented with 10 mM galactose where indicated.

Cells grown with galactose media were grown in glucose free DMEM media supplemented with

10% FBS, 1% Pen/Strep, and 10 mM galactose. Cells were maintained at a density of 5×10^4- 1×10^6, except where single cells were isolated to generate clonal populations.

2.4.2 Molecular Biology

All plasmids were prepared using commercial MiniPrep kits (Qiagen, Hilden, Germany). All enzymes were obtained from New England Biolabs and used per the manufacturer's recommendations. PCR reactions were carried out using Q5 High-Fidelity Polymerase (New England Biolabs, Ipswich, MA) per the manufacturer's protocols. Primers were ordered from Genosys (Sigma-Aldirch, Burlington, MA) or Integrated DNA Technologies (Coralville, IA). Except where noted, genomic DNA was extracted using QuikExtract DNA reagent (Lucigen, Middleton, WI). Except where noted, non-viral plasmids were maintained in competent DH5-alpha *E. coli*, prepared by the Vanderbilt Molecular Cell Biology Resource (MCBR), lentiviral and retroviral plasmids were maintained in Stbl2 *E. coli* (ThermoFisher, Waltham, MA), and cloned plasmids were initially transformed into competent cells included with kits. Gibson assemblies were carried out using the NEB Gibson Assembly Cloning kit. Site Directed Mutagenesis was carried out using the QuikChange Lightning II cloning kit (Agilent, Santa Clara, CA). PCR cloning was carried out using the NEB PCR cloning kit. All Sanger sequencing was completed by Genewiz, Inc (South Plainfield, NJ).

2.4.3 Immunoblotting

Cell lysates were prepared using RIPA buffer (see lysis and click chemistry methods below) and run on SDS Tris-Glycine gels (Precast 4 - 20% Bio-Rad, or hand-casted 20%). Gels were transferred to low-background PVDF membranes using the BioRad TransBlot Turbo system and blocked with 5% milk powder in TBS + 0.1% Tween 20 (TBST) for 1 hr at room temperature. Primary antibodies were diluted at the indicated concentration (see supplement) in

5% BSA in TBST and incubated overnight at 4 °C. Membranes were washed for 5 min x 5 with TBST, and Starbright Blue 700 secondary antibody (Bio-Rad, Hercules, CA) for 1 hr at room temperature, followed by 5 x 5 min washes with TBST. Membranes were imaged using the ChemiDoc MP imaging system.

2.4.4 <u>Antibodies</u>

Target	Conjugate	Manufacturer	Clone/Catalog #
ATP5B	-	Proteintech	17247-1-AP
VDAC1	-	Cell Signaling Technology	4661
TIMM17B	-	Proteintech	11062-1-AP
FLAG®	-	Sigma Aldrich	M2
pS6[Ser235/236]	Alexa Fluor 647	Cell Signaling Technology	D57.2.2E
Human CD45	APC	Biolegend	2D1
Human CD33	PE-Cy7	Biolegend	P67.6
Murine CD45	PE	Biolegend	30-F11
ATP5G1		Abcam	EPR13908
Actin	Rhodamine	BioRad	12004163

2.4.5 <u>Photoaffinity Labeling</u>

Photoaffinity labeling was carried out essentially as described in Thomas JR, 2017 ([160]). Briefly, ~5 - 30M cells per condition were washed twice with OptiMEM media and resuspended in 1 mL of OptiMEM media in a 12 well plate. Each well was treated with vehicle (DMSO) or competitor as indicated for 1 hr at 37 °C followed by the addition of vehicle or photoaffinity probe for 1 hr at 37 °C. The samples there then irradiated with 365 nm light for 15 min on ice using a Stratalinker 2400 (Agilent). The samples were then washed twice with 1 mL of 1x PBS and then lysed as described below or flash frozen at -80 °C for later processing.

2.4.6 <u>Lysis and Click Reaction</u>

Samples were processed essential as described in Paxman et al, 2018 ([161](#)) with minor

modifications. Cell pellets were lysed in 100 μL of radioimmunoprecipitation assay buffer

(RIPA: 150 mM NaCl, 50 mM Tris pH 7.5, 1 % Triton X-100, 0.5% sodium deoxycholate, 0.1%

SDS). After lysis, the samples were centrifuged for 1 min at 28,000 g and the lysates transferred

to a fresh tube. Protein concentration was determined using the BCA assay (Pierce) and each

sample was adjusted to a concentration of 1 mg/mL. Each 100 - 1,000 μg click reaction was

carried out at the following final concentrations: 100 μM azide (as indicated: Azide Fluor 545 –

Sigma Aldrich OR TAMRA-Azide-Desthiobiotin – Broadpharm), 800 μM $CuSO_4$, 1.6 mM

BTTAA ligand (Click Chemistry Tools), and 5 mM sodium ascorbate. The azide was added

directly to the cell lysate while the $CuSO_4$, BTTA, and sodium ascorbate (fresh) were prepared

as a master mix and added to each tube. The samples were vortexed briefly and incubated at 37

°C for 1 hr. The proteins were precipitated using a methanol-chloroform precipitation using a

3:1:4 ratio of methanol, chloroform, and water. The pellet was washed once with 3:1

MeOH/CHCl$_3$, and once with methanol and dried briefly at room temp, taking care to avoid over

drying the pellet. Samples used for in-gel analysis were resuspended in 1 x loading buffer +

BME (Bio-rad), heated for 15 min at 37 °C followed by sonication for 15 min to aid

solubilization. The samples were boiled for 5 min at 95 °C, centrifuged at 20,800 g x 1 min, and

10 μg of protein was loaded into each lane. Samples used for affinity purification were processed

as described below.

2.4.7 <u>Affinity Enrichment</u>

Protein pellets functionalized with the TAMRA-Azide-Desthiobiotin (Click Chemistry

Tools, Scottsdale, AZ) were precipitated by methanol/chloroform as described above and

resuspended in 500 μL of 6M Urea + 25 mM ammonium bicarbonate, with 140 μL of 10% SDS

was added to aid resolubilization. 6 mL of 1 x PBS was added to each sample to lower the urea

concentration to < 0.5 M. 50 μL of high-capacity streptavidin beads (Pierce, Waltham, MA) were

washed three times with PBS, added to each sample, and incubated for 2 hrs at room temperature

on a rotator. Each sample was then loaded onto a 0.8 mL spin column (Pierce) in 500 μL

5   portions using a vacuum manifold. The beads were then washed with 4 x 500 μL volumes of 1%

SDS in PBS, 4 volumes of 4M Urea in PBS, 4 volumes of 1M sodium chloride, and 1 volume of

1% SDS in PBS. The bead slurry was then resuspended in 100 μL of 50 mM biotin, 1% SDS, in

PBS (pH 7.2), incubated at 37 °C for 10 minutes, agitated for 10 minutes, and then collected into

a fresh 1.5 mL Eppendorf tube via centrifugation at 5200 g x 3 min. The biotin elution was

10   repeated once with a second 100 μL volume of 50 mM biotin, 1% SDS in PBS. The two biotin

elution fractions were combined and precipitated with methanol/chloroform as described above

and resuspended in either 1 x loading buffer (if running a gel and silver staining) or in 0.1%

RapiGest SF (Waters Corp, Milford, MA) in 0.1 M HEPES pH 8.0 if proceeding to MudPIT

proteomics. Silver staining was carried out using the Pierce Silver Stain kit, per the

15   manufacturers protocols.

2.4.8 <u>TMT-Multiplexed Proteomics Sample Preparation</u>

      TMT samples were prepared as follows: RapiGest resuspended samples (in 50 μL) were

reduced by the addition of 0.5 μL 0.5 M TCEP (final concentration, 5 mM) for 30 min at room

temperature and cysteines alkylated using 1 μL 0.5 M iodoacetamide (final concentration, 10

20   mM) for 30 min at room temperature protected from light. Samples were digested by addition of

0.25 μg of sequencing grade trypsin dissolved in 50 mM acetic acid at 0.5 μg/mL (Promega)

overnight at 37 °C with vigorous shaking. Sample volume was adjusted to 60 μL with H_2O and

TMT labeling was carried out using the TMT sixplex isobaric label (Thermo Scientific) using

100 μg of reagent dissolved in 100% acetonitrile per sample and incubated at room temperature

for 1 hr. The labeling reaction was quenched with 4 μL of 10% w/v of ammonium bicarbonate

(final concentration of 0.4% w/v) at room temperature for 1 hr. Samples were then acidified with

formic acid (final conc 5% v/v) and concentrated *in vacuo* to ~1/6th of its original volume to

5   remove the acetonitrile and sample volume was adjusted to 600 μL with 0.1% formic acid.

Samples were then heated at 42 °C for 30 min to precipitate the RapiGest surfactant and

insoluble components were removed by centrifugation at 28,000 g x 30 min. Digested, TMT-

labeled samples were stored at -80 °C until analysis.

2.4.9 <u>In-gel Digest Proteomics Sample Preparation</u>

10   Gel bands were excised and washed three times with 25 mM ammonium bicarbonate in

1:1 acetonitrile/water, and then dried using a vacuum centrifuge. Proteins were reduced with the

addition of 10 mM DTT in 25 mM ammonium bicarbonate in 10% acetonitrile (v/v), and heating

at 56 ºC for 1 hr. Next, proteins were alkylated with 55 mM iodoacetamide at room temperature

for 45 minutes. Gel pieces were then rinsed with 25 mM ammonium bicarbonate is aqueous

15   solution, followed by 25 mM ammonium bicarbonate in 1:1 acetonitrile/water. Rinses were

repeated and gels pieces were dried using a vacuum centrifuge. Enough trypsin (12.5 ng/μL in 25

mM ammonium bicarbonate in aqueous solution) was added to cover the gel pieces and samples

were incubated on ice for 30 min. Excess trypsin solution was removed and 25 mM ammonium

bicarbonate in aqueous solution was added. Samples were then incubated at 37 ºC for 8 hrs.

20   After digestion, three volumes of water were added to the gel samples and they were vortexed

for 10 min, sonicated for 5 min, and the resulting supernatant was collected. Gel pieces then had

45% water/50% acetonitrile/5% formic acid (v/v/v) added and were vortexed for 10 min,

sonicated for 5 min, and the resulting supernatant was collected. The extraction with 45%

water/50% acetonitrile/5% formic acid (v/v/v) was repeated and supernatant was again collected. Samples were concentrated using a vacuum centrifuge and analyzed.

2.4.10 <u>Liquid Chromatography – Tandem Mass Spectrometry</u>

MudPIT microcolumns were prepared and peptide samples were directly loaded onto the columns using a high-pressure chamber. Samples were then desalted for 30 min with buffer A (95% water, 4.9% acetonitrile, 0.1% formic acid v/v/v). LC-MS/MS analysis was performed using a Q-Exactive HF (Thermo Fisher) mass spectrometer equipped with an Ultimate-3000 RSLCnano system (Thermo Fisher). MudPIT experiments were performed with 10 µL sequential injections of 0, 10, 30, 60, and 100% buffer C (500mM ammonium acetate in buffer A), followed by a final injection of 90% buffer C with 10% buffer B (99.9% acetonitrile, 0.1% formic acid v/v) and each step followed by a 130 minute gradient from 5% to 80% B with a flow rate of 300 nL/min on a 20 cm fused silica microcapillary column (ID 100 µm) ending with a laser-pulled tip filled with Aqua C18, 3 µm, 125 Å resin (Phenomenex). Electrospray ionization (ESI) was performed directly from the analytical column by applying a voltage of 2.0 V with an inlet capillary temperature of 275 °C. Data-dependent acquisition of mass spectra was carried out by performing a full scan from 300-1800 m/z with a resolution of 60,000. The top 15 peaks for each full scan were fragmented by HCD using normalized collision energy of 38, 0.7 m/z isolation window, 120 ms maximum injection time, at a resolution of 15,000 scanned from 100 to 1800 m/z and dynamic exclusion set to 60 s. Peptide identification and TMT-based protein quantification was carried out using Proteome Discoverer 2.3. MS/MS spectra were extracted from Thermo Xcalibur .raw file format and searched using SEQUEST against a Uniprot human proteome database (released 03/2014 and containing 20337 entries). The database was curated to remove redundant protein and splice-isoforms and supplemented with common biological MS

contaminants. Searches were carried out using a decoy database of reversed peptide sequences and the following parameters: 10 ppm peptide precursor tolerance, 0.02 Da fragment mass tolerance, minimum peptide length of 6 amino acids, trypsin cleavage with a maximum of two missed cleavages, dynamic methionine modification of 15.9949 Da (oxidation), static cysteine

5   modification of 57.0215 Da (carbamidomethylation), and static N-terminal and lysine modifications of 229.1629 Da (TMT sixplex).

2.4.11 Statistical Analysis of TMT Proteomics Data

Protein matches and TMT quantification were processed using a custom R script using the DEP pipeline ([162](#)). Briefly, raw TMT quantifications were normalized using the vsn

10   package ([163](#)). Differential enrichment was determined using limma ([164](#)). Enriched proteins were selected based on an adjusted p-value of 0.05 and log2 fold change of 2 (see Data S2). Plots were generated using ggplot2.

2.4.12 MTT Viability Assay

The MTT assay protocol was adapted from Deguire *et al. (*[129](#)*)*. Briefly, a 100 μL of

15   suspension cells at 100,000 per mL were added to wells of a microtiter plate precoated with 0.5 μL of test compound at 200x in DMSO and incubated for 48 - 72 hrs (as noted). MTT reagent was dissolved in fresh media at 1 mg/mL and 100 μL was added to each well to achieve a final concentration of 0.5 mg/mL and incubated for 2 hrs at 37 °C. Cells were centrifuged at 800 g x 5 min and decanted. MTT crystals were redissolved in 100 μL of DMSO, allowed to incubate for 5

20   min at RT, and read at 560 nM using a SpectraMax plus 384 plate reader (Molecular Devices, San Jose, CA). Absorbance values were normalized by background subtraction (wells without cells) and normalized such that vehicle treated cells had a viability of 1.0. IC_{50} curves were fit

101

using a custom R script using the DRC package ([165]) with a four-parameter log-logistic function.

2.4.13 Sulforhodamine B (SRB) Proliferation Assay

The SRB assay protocol was adapted from ([166]) to assess cytotoxicity in adherent cells (H292 and HEK-293). Cells were treated as above in the MTT assay in TC treated 96 well plates with 100 μL of media. After 48 – 72 hrs, cells were fixed by the gentle addition of 25 μL of cold 50% (w/v) trichloroacetic acid (TCA) and incubated at 4 °C for 1 h. Plates were then washed 4x by submersion in a basin of tap water and allowed to dry overnight. Cells were stained by the addition of 50 μL of 0.04% (w/v) SRB dissolved in 1% (v/v) acetic acid to each well and allowed to incubate at room temperature for 1 hr. The SRB solution was decanted and plates were washed with 4x 100 μL volumes of 1% (v/v) acetic acid and allowed to dry. The SRB reagent was redissolved by the addition of 10 mM Tris base (pH 10.5), allowed to incubate for 10 min, and absorbance was measured at 510 nM using a SpectraMax plus 384 plate reader (Molecular Devices, San Jose, CA). Absorbance values were normalized by background subtraction (wells without cells) and normalized such that vehicle treated cells had a viability of 1.0. IC_{50} curves were fit using a custom R script using the DRC package ([165]) with a four-parameter log-logistic function.

2.4.14 Immunofluorescence

Confocal fluorescence microscopy of cells was performed as follows. Coverslips, (22 mm diameter, 1.5H thickness) (Thorlabs) were washed with 1M HCl for 1 hrs at 55 °C, washed with DI water and 70% ethanol, and coated with poly-D-lysine (100 μg/mL in sterile water), and allowed dry. Adherent cells were plated on top of coverslips and grown till confluent. For imaging of apoptolidin A PA localization, cells were treated with 200 μM apoptolidin A PA for

1 h and photocrosslinked for 15 min as described under 'photoaffinity labeling'. Mitotracker Deep Red FM (Invitrogen) was added 30 min prior to the end of the experiment at a final concentration of 100 nM. Cells were washed 2x with PBS (containing Ca^{++} and Mg^{++}) and fixed with 1.6% PFA for 15 min. Apoptolidin A PA treated cells were permeabilized with ice cold

5   methanol for 20 min at -20 °C, while cells intended for immunofluorescence were permeabilized with 1% Triton X100 for 15 min. Cells were washed with 1% BSA in PBS twice, while cells intended for antibody staining were then blocked with 5% BSA in PBS. Azide Fluor 545 labeling was carried out as described under 'lysis and click reaction' with the azide concentration reduced to 100 μM, and samples were washed with 1% BSA in PBS after 1 hr at 37 °C. Samples for

10   immunofluorescence were stained for overnight with primary antibodies, washed 4x with 1% BSA in PBS, followed by 1 hr staining at room temperature with secondary antibodies (goat anti-mouse alexa 488 antibody, Invitrogen A-11008), followed by 4x washes with 1% BSA in PBS. Samples were stained briefly with DAPI (1 μg/mL) mounted on slides using ProLong Glass mountant (Invitrogen), allowed to set for 72 hrs and imaged using a Zeiss 880 Airyscan confocal

15   microscope.

2.4.15 <u>Yeast growth and ATP synthase purification</u>

ATP synthase was purified from yeast strain USY006 ([167](#)) bearing 6×His tags at the N-termini of the β subunits as described previously but with the following modifications ([168](#)). Yeast was cultured in an 11 L fermenter (New Brunswick Scientific) and the mitochondria were

20   prepared by breaking yeast cell wall by bead beating. All subsequent purification steps were performed at 4 °C. Mitochondria were washed with phosphate buffer (50 mM sodium phosphate, pH 9.0, 5 mM 6-aminocaproic acid, 5 mM benzamidine, 1 mM PMSF) for 30 min before being collected by centrifugation at 184,000 g for 30 min. Membranes were solubilized by

resuspending in buffer (50 mM Tris-HCl, pH 7.4, 10% [v/v] glycerol, 1% [w/w] dodecyl-β-D-maltoside [DDM, Anatrace], 5 mM 6-aminocaproic acid, 5 mM benzamidine, 1 mM PMSF) and mixed for 1 hour. Insoluble material was removed by centrifugation at 184,000 g for 30 min and the supernatant containing solubilized protein was collected. Imidazole was added to 40 mM and NaCl to 300 mM and the sample was loaded onto a HisTrap HP 5 mL column (MilliporeSigma, Burlington, MA) equilibrated with wash buffer (50 mM Tris-HCl, pH 7.4, 10% [v/v] glycerol, 0.05% [w/w], 40 mM imidazole, 300 mM NaCl, 5 mM 6-aminocaproic acid, 5 mM benzamidine, 1 mM PMSF). The column was washed with 5 column volumes of wash buffer and ATP synthase was eluted with the wash buffer containing 300 mM imidazole before being loaded to a Superose 6 increase column (MilliporeSigma) equilibrated with buffer (20 mM Tris-HCl, pH 7.4, 10% [v/v] glycerol, 0.05% [w/w], 100 mM NaCl, 5mM $MgCl_2$). Fractions containing ATP synthase were pooled and protein was concentrated to ~15 mg/ml prior to storage at -80 °C.

2.4.16 Yeast F_1-ATPase Preparation

Preparation of F1-ATPase followed the same protocol as intact ATP synthase preparation until the mitochondrial were pelleted after bead beating. Protocols were derived from Mueller, 2004 ([169](#)). Unless otherwise noted, all steps were done at 4 °C. Submitochondrial particles (SMPs) were prepared by resuspending mitochondria at 10 mg/mL in sonication buffer (SB - 0.25 M sucrose, 50 mM phosphate buffer, 5 mM 6-aminocaproic acid, 5 mM benzamidine, 1 mM PMSF, pH 7.5) with 1 mM EDTA and sonicated at 150W × 1 min in 5 s on 10 s off cycles, and centrifuged at 5000 g for 10 min. The supernatant containing SMPs was centrifuged at 100,000 g for 60 min at 4 °C. The pellet was washed twice with SB without EDTA, resuspended at 20 mg/mL, and warmed to room temperature. F1 ATPase was extracted from SMPs by the addition of 0.5 volumes of PBS saturated chloroform and vortexed for 30 s. ADP was added at a

final concentration of 2 mM and the phases were separated by centrifugation at 3000 g for 10 min at 15 °C. The aqueous layer was collected, methanol was added to a final concentration of 10% v/v, followed by the addition of Buffer D (10% MeOH, 1.2 M NaCl, 40% [w/v] glycerol, 0.25 M sucrose, 50 mM phosphate, 5 mM 6-aminocaproic acid, 5 mM benzamidine, pH 7.5).

5   The crude F1 preparation was loaded onto a 5mL HisTrap HP 5 mL column at 4 °C and washed with 300 mL of 97 % wash buffer (10% MeOH, 10% glycerol, 0.3M NaCl, 0.25 M sucrose, 50 mM phosphate, 5 mM 6-aminocaproic acid, 5 mM benzamidine, 1 mM PMSF, pH 7.5) + 3% elution buffer (wash buffer + 0.4 M imidazole). F1 ATPase was eluted with 100% wash buffer and the F1-containing fractions were pooled and concentrated to < 1 mL. F1 ATPase was further

10   purified by means of gel-filtration at room temperature with a Superdex 200 increase 10/300 GL column with SDX buffer (0.25 M sucrose, 0.2 M NaCl, 50 mM Tris, 1 mM EDTA, 1 mM ATP, 0.5 mM PMSF, pH 8.0) at 0.5 mL/min, the F1 containing fractions were pooled, and precipitated by the addition of saturated ammonium sulfate (70%), and stored at 4 °C.

2.4.17 CryoEM grids prepration

15   CryoEM grids of drug-free ATP synthase were prepared by removing glycerol from the sample with Zeba Spin Desalting Column (Thermo Fisher Scientific) immediately before freezing. Glycerol-free ATP synthase was then applied to home-made ([170](#)) holey-gold grids ([171](#), [172](#)) that had been glow discharged in air for 2 min. Grids were blotted with modified Vitrobot Mark III (Thermo Fisher Scientific) for 26 s with ~100% humidity at 4 °C before being

20   plunge frozen in a liquid ethane/propane mixture ([173](#)). Grids of ATP synthase with ammocidin and apoptolidin were prepared the same way except that ATP synthase was incubated with either 60 μM ammocidin or 20 μM apoptolidin for 1 hour and the glycerol removal step was performed with buffers containing the same concentrations of inhibitors.

2.4.18 <u>CryoEM Data collection</u>

CryoEM movies of yeast ATP synthase bound to ammocidin and apoptolidin were collected with a Titan Krios G3 electron microscope operated at 300 kV and equipped with a prototype Falcon 4 camera (Thermo Fisher Scientific). Automatic data collection was performed with *EPU* (Thermo Fisher Scientific). For the ammocidin dataset, 4345 movies each containing 30 fractions were collected at a nominal magnification of 75000×, corresponding to a calibrated pixel size of 1.03 Å. The total exposure and the camera exposure rate were ~45 e⁻/Å^2 and 5.0 e⁻/pix/s, respectively. The apoptolidin dataset, consisting of 4019 movies with 29 fractions each were collected at same magnification as the ammocidin dataset. The total exposure and the camera exposure rate for this dataset were ~43 e⁻/Å^2 and 4.8 e⁻/pix/s, respectively. The drug-free ATP synthase dataset was collected on a Tecnai F20 electron microscope (Thermo Fisher Scientific) operated at 200 kV and equipped with a K2 Summit camera (Gatan). A dataset consisting 190 movies each containing 30 fractions was manually collected at a nominal magnification of 25000×, corresponding to a calibrated pixel size of 1.45 Å. The total exposure and the camera exposure rate were ~36 e⁻/Å^2 and 5.0 e⁻/pix/s, respectively.

2.4.19 <u>Image analysis</u>

Image analysis was performed with *cryoSPARC v2* ([174](#)) except where noted. Movie frames were aligned with *MotionCor2 (*[175](#)*)* using a 7×7 grid and contrast transfer function (CTF) parameter were estimated in patches. Two templates displaying a sideview and an oblique view of ATP synthase for particle picking were generated with 2D classification of manually selected particles with a box size of 320×320. Template picking generated 654,097 particle images for the ammocidin dataset, 1,189,085 particle images for the apoptolidin dataset and 38,514 particle images for the drug-free dataset. After cleaning by 2D classification, 329,297,

621,136, and 34,035 particle images remained for the corresponding datasets. Ab initio 3D classification and heterogeneous refinement identified three classes for each dataset corresponding to the three main rotational states of ATP synthase. For each dataset, the maps of the three states were aligned based on the F_1 region and a masked local non-uniform refinement

5   (176) of the region was performed. For the high-resolution ammocidin and apoptolidin datasets, individual particle defocus parameters were estimated, and a second masked refinement was performed with updated CTF parameters. Image parameters were then converted to *Relion 3.0* *(177)* format with the *pyem* package (178) and individual particle motion was re-estimated with Bayesian Polishing (179). For the apoptolidin dataset, particle images were downscaled to a

10   pixel size of 1.2875 Å with *Relion 3.0*. The resulting particles were imported back to *cryoSPARC v2* and another round of masked non-uniform refinement of the F_1 region was performed. For the ammocidin and apoptolidin datasets, individual particle defocus was re-estimated, followed by a final round of masked refinement. The final maps of the ammocidin, apoptolidin, and drug-free dataset contain 289,501, 477,847 and 34,035 particle images and reached resolutions of 3.1 Å,

15   3.3 Å and 4.2 Å, respectively. The ammocidin and apoptolidin maps were locally sharpened with a *COSMIC2 (180)* implementation of *DeepEMhancer (181)*.

2.4.20 Atomic model building

To model the F_1 region of the ammocidin-bound structure, individual subunits of the F_1 region of a yeast ATP synthase crystal structure (2XOK) was fit rigidly into the ammocidin map

20   with *UCSF Chimera (182)*. The model was then manually adjusted in *Coot (183)* and *ISOLDE (184)* before being refined in *Phenix (185)*. The model of the apoptolidin bound structure was built in a similar manner, with the ammocidin model as the starting structure. To demonstrate the conformational change induced upon inhibitor binding, individual subunits of the same crystal

structure (2XOK) were fit into the drug-free map as rigid bodies to generate Figure 2D and Movie 1. Figures and supplementary movie were generated with *UCSF Chimera* and *USCF ChimeraX* ([186](#)).

2.4.21 Isolation of Mouse Liver Mitochondria

5   Mouse liver mitochondria were isolated essentially as described by Frezza et al.([187](#)) All steps were performed on ice. Freshly harvested mouse livers with the gallbladder removed were washed four times in mitochondrial isolation buffer (IB = 0.2 M sucrose, 10 mM Tris-MOPS, 1 mM EGTA/Tris, pH 7.4), weighed, and cut into small pieces with scissors. Liver pieces were resuspended in 2 volumes of IB, transferred to a 45 mL Potter-Elvehjem homogenizer, and

10   homogenized with four strokes of the pestle. The homogenate was diluted with an additional 3 volumes of IB, transferred to a 50 mL conical vial, and centrifuged at 600g x 10 min at 4 °C to pellet nuclei. The supernatant was transferred to a 50 mL Nalgene Oak Ridge Centrifuge Tube and centrifuged at 7000g x 10min at 4 °C in a Sorvall RC 2-B centrifuge equipped with an SA-600 rotor to pellet mitochondria. The mitochondrial pellet was resuspended in 5 volumes of IB

15   and centrifuged at 7000g x 10 min at 4 °C a second time to remove microsomes. The mitochondrial pellet was resuspended at 20 mg/mL as determined using a BCA assay (Pierce).

2.4.22 Enzyme Coupled ATP Synthesis Assay

      The ATP synthesis assay was adapted from assays described by Gouspillou ([188](#)) and Cross ([61](#)). The respiration buffer (RB) consisted of 240 mM mannitol, 100 mM KCl, 1mM

20   EGTA, 20 mM $MgCl_2$, 10 mM KH_2PO_4, and 0.1% (w/v) fatty acid free BSA (pH 7.2). 20 mM Succinate, pH 7.2 with KOH (S3674) was used as a substrate in all experiments. The assay readout consisted of 5 mM glucose, 2.5 U/ml hexokinase (Sigma H4502), 2.5 U/ml glucose-6-phosphate dehydrogenase (Sigma G8529), and 1.6 mM $NADP^+$(Sigma N8035). 20 µM P^1,P^5-

108

di(adenosine-5) pentaphosphate (AP5A) was used to inhibit adenylate kinase which could otherwise convert 2 ADP → AMP + ATP. The assay reagents were prepared at 2 × in RB and 100 μL was dispensed into each well of UV transparent 96 well plate. 50 μL of 4x succinate was then added, followed by 25 μL of 8x mitochondria. The plate was incubated at 25 °C for 5 min to allow the mitochondria to energize. The reaction was initiated by the addition of 25 μL of 8x ADP using a multichannel pipette to yield a total volume in the well of 200 μL. Absorbance was monitored at 340 nM using a SpectraMax Plus 384 plate reader (Molecular Devices) set at 25 °C.

2.4.23 Enzyme Coupled ATPase Assay for F_1 ATPase

The ATPase assay was adapted from Cross (61). The assay buffer consisted of 60 mM Tris-Acetate pH 7.8; 1 mM $MgCl_2$, 2.5 mM phosphoenolpyruvate; 1 mM KCN. The working solution was prepared at 2 × for a final concertation of 0.4 mM NADH; 3 U/mL of pyruvate kinase (PK) + 4.5 U/mL Lactate Dehydrogenase (LDH) [Sigma P0294]; ±10 μM carbonylcyanide p-trifluoromethoxyphenylhydrazone (FCCP). Unless otherwise specified, ATP was added as a 4x solution at 200 μM. Absorbance was monitored at 340 nm using a SpectraMax Plus 384 plate reader (Molecular Devices) set at 25 °C. 50 μL of enzyme was added to 100 μL of working solution and monitored for 2 min, 50 μL of ATP was then added for a final volume of 200 μL and absorbance was monitored over 10 minutes.

2.4.24 Enzyme Coupled ATPase Assay for ATP synthase

To measure the ATP hydrolysis activity of ATP synthase, enzyme-coupled ATPase activity assays (189) were performed in 96-well plates with 160 μL buffer (50 mM Tris-HCl pH 7.4, 150 mM NaCl, 10% [v/v] glycerol, 5 mM $MgCl_2$, 0.2 mM NADH, 2 mM ATP, 1 mM phosphoenol pyruvate, 3.2 units pyruvate kinase, 8 units lactate dehydrogenase, 0.05% [w/v] DDM, DMSO [v/v] 2%, 2 nM ATP synthase). NADH concentration was monitored at 24 °C

with a Synergy Neo2 Multi-Mode Assay Microplate Reader (BioTek) measuring absorbance at 340 nm. Inhibition with ammocidin and apoptolidin was determined by adding different concentrations of the inhibitors to assay mixture. Assays were performed in triplicates with two independently purified batches of yeast ATP synthase.

5   **2.4.25** Preparation of Lentivirus

H293T were maintained in high glucose DMEM supplemented with 10% FBS, without antibiotics at approximately 50 - 60% confluence on the day of transfection. The transfection mixture consistent of 1 μg lentiviral plasmid, 750 ng psPAX2 (Addgene #12260), and 250 ng of pMD2.G (Addgene #12259) using FuGENE 6 per manufacturers protocols. The cells were

10   incubated with plasmid for 16 hrs at which point the media was replaced with DMEM supplement with 10% FBS and 1% Pen/Strep. Viral supernatant was harvested at 24 hrs and 48 hrs and sterile filtered using 45 μM syringe filtered. Viral media was used immediately or frozen at -80 °C for later use.

2.4.26 Lentiviral Transduction

15   MV-4-11 were seeded into 6 well plates in 2 mL of media. 500 μL of viral supernatant was added to each well, along with 500 μL of 36 μg/mL DEAE-Dextran in DMEM + 10% FBS + 1% Pen/Strep, for a final DEAE-Dextran concentration of 6 μg/mL. Cells were allowed to incubate with virus for 48 hrs, at which point antibiotics were applied for selection or cells were single cell sorted to generate clones.

20   **2.4.27** Retroviral Production

Platinum-E (Plat-E) cells selected for 2 days in DMEM + 10% FBS + 10 μg/mL blasticidin + 1 μg/mL puromycin in 100 mm tissue culture treated dishes. Selection media was

replaced with DMEM + 10% FBS without antibiotics overnight. A transfection mix consisting of 500 μL OPTI-MEM + 30 μL FuGENE 6 was allowed to incubate for 5 min at room temperature. 10 μg of plasmid (pBABE-puro, Addgene #1764 or pBabe-puro Ras V12, Addgene #1768) was added to the FuGENE + OPTI-MEM, and allowed to incubate for 10 min. The media was

5   removed and replaced with fresh DMEM + 10% FBS + 1% PenStrep. Viral supernatant was harvested after 48 hrs, sterile filtered, and stored at -80 °C.

2.4.28 <u>Retroviral Transduction</u>

Retroviral transduction in BaF3s (gift of Dr. Christine Lovly) were conducted essentially as described in Gallant, 2015 ([190]). Cells were seeded at 50,000 /mL per well of a 6 well plate in

10   RPMI 1640 + 10% FBS + 1% PenStrep, supplemented with recombinant murine IL-3 (Gibco, PMC0035) at 1 μg/mL (BaF3). 1 mL of viral supernatant was added to each well along with polybrene in DMEM for a final polybrene concentration of 10 μg/mL. The cells were allowed to incubate with virus for 48 hrs, at which point the viral media was removed and replaced with RPMI 1640 + 10% FBS + 1% PenStrep + IL-3 + 2 μg/mL Puromycin.

15   **2.4.29** <u>ATP Synthase Mutant Library Preparation</u>

ATP synthase ORF clones were purchased from GenScript USA Inc (Piscataway, NJ, USA) [ATP5A1, NM001001937.1; ATP5B NM_001686.4; ATP5C NM_001001973.3], PCR amplified, and cloned into the NotI digested pAG490 ([191]) using Gibson assembly and were confirmed by Sanger sequencing using ag122 and ag123 primers (See Data S2). Mutagenic

20   primers were designed in three pools, one for each ORF, using the published primer design script, specifying a single codon for each of 20 amino acids without stop codons at a total of 21 positions (420 total variants), with 30 nt homology arms on both sides of the mutated codon (see Data S2 for primer sequences) ([192]). Primers were obtained as three separate 50 pm oPools from

Integrated DNA technologies (Coralville, IA, USA). Nicking mutagenesis was carried out exactly as described in Wrenbeck EE, 2016 (149), Supplementary Protocol 1, except for reversing the use of the Nt.BbvCI and Nb.BbvCI enzymes to degrade the proper strands. Primer ag123 was used to synthesize the complementary strand. The product of each mutagenesis reaction was transformed into XL1-Blue Electroporation-Competent Cells (Agilent Technologies, Santa Clara, CA, USA) and serial dilutions were plated to determine the total number of colonies. All colonies from the 25 cm x 25 cm LB plate were collected, and plasmid was purified by MiniPrep. The three pools were combined in a 5:8:8 ATP5A1:ATP5B:ATP5C ratio to reflect the number of variants present in each pool. A 'wildtype' pool was generated by combing the parental plasmids in the same 5:8:8 ratio for use as a negative control.

2.4.30 Mutant Library Transfection and Selection

HEK-293T landing pad cells (193) were maintained in glucose free DMEM (Gibco) supplemented with 10% heat inactivated FBS (Gibco), ±1% Pen/Strep, and 10 mM Galactose. On day -1, 500,000 cells with an 'empty' landing pad (LP-Neg) cells were plated into 6 well plates in antibiotic free media. On day 0, the cells were transfected with 1 μg of mutant library and 100 μg of *Bxb1* expressing plasmid (pCAG–NLS–HA–Bxb1; Addgene #51271, a gift from Pawel Pelczar) in triplicate. On day 1, the cells were replated into 60 mm TC dishes with antibiotic containing media and gene expression was induced with 1 μg/mL doxycycline. On day 3, cells were treated with 100 μg/mL Blasticidin S (Gibco) and 10 nM AP1903 (MedChemExpress) to select for cells which expressed the transgene and had undergone successful integration; selection was continued for 7 days. On day 10, HEK-293-integrated cells were plated into 6 well TC plates and treated with DMSO, apoptolidin A, ammocidin A at various concentrations (final DMSO concentration 0.25% v/v). Selective pressure was applied

112

for two rounds of 4 days of exposure to each compound, followed by 3 days for recovery in glycomacrolide free media. After selection, surviving cells were allowed to expand until confluent at which point genomic DNA was extracted using the Qiagen DNeasy Blood & Tissue Kit.

5 **2.4.31** <u>Amplicon Preparation and Sequencing</u>

The integrated ATP synthase genes were PCR amplified using primers designed to anneal to the landing pad (TRE3G_fwd) and plasmid IRES sequence (IRES_rev) using 5% of the genomic DNA as a template and Q5 polymerase (New England Biolabs - NEB) at 100 μL scale. The PCR product was purified using the Monarch PCR & DNA clean-up kit (NEB). All library

10 preparation and sequencing was carried out at the Vanderbilt Technologies for Advanced Genomics (VANTAGE) center. Sequencing libraries were prepared by tagmentation using the Nextera Flex library preparation kit (Illumina Inc. San Diego, CA, USA) using the manufacturers protocol. PE150 sequencing was carried out on the Novaseq 6000 platform at VATNAGE. Data are deposited in the gene expression omnibus (GEO), GSM5224467.

15 **2.4.32** <u>Analysis of Saturation Mutagenesis Experiments</u>

Demultiplexed reads were down-sampled to 5M paired reads using seqtk, aligned to the reference ORFs using bwa-mem (194) with a gap opening penalty of 100, and converted to BAM format using samtools. Variant frequency was determined using gatk version 4.1.8.1 (195). AnalyzeSaturationMutagenesis was used for each ORF. The resulting amino acid frequency

20 tables were analyzed using a custom R script with the tidy data deposited on GEO as a supplementary file. The log10 fold change for each amino acid was calculated by subtracting the log10 transformed frequency of each treated replicate to its parental frequency.

2.4.33 <u>Generation and Validation of CRISPR lines</u>

113

Isogenic mutants were generated using CRISPR-Cas9 gene editing as described in ([147](#)), using pSpCas9(BB)-2A-GFP (PX458), a gift from Feng Zhang (Addgene plasmid # 48138). Guide sequences (see supplement) were generated by annealing complementary oligonucleotides and golden-gate cloning with BbsI into PX458 and confirmed by sanger sequencing. 101-110 nt

5   ssODN HDR templates were ordered with 50 bp of homology on either side of the cut site. HDR templates were designed to eliminate the PAM sequence to prevent re-cutting and designed to incorporate one or more synonymous mutations to add or remove restriction sites to facilitate screening of clones. 200,000 cells were electroporated using the Neon Transfection system (ThermoFisher), with 500 ng of PX458 plasmid ± 10 pmol ssODN template. Single cells were

10   FACS sorted into U-bottom 96 well plates into conditioned media, selecting GFP+/PI- negative cells. Clones were expanded and genotyped by PCR of the targeted region, followed by restriction digest to identify edited clones. Successfully edited clones were further confirmed by PCR cloning and sanger sequencing of 6-8 colonies. ATPIF-1 K.O. lines were generated using PX458 without a donor template as described above. Individual clones were screened using

15   intracellular flow cytometry against ATPIF1.

2.4.34 *In vivo* Murine Modeling

All animal experiments were conducted in accordance to guidelines approved by the IACUC at Vanderbilt University Medical Center. Male NSGS [NOD-scid IL2Rgnull3Tg (hSCF/hGM-CSF/hIL3)] mice (The Jackson Laboratory), 6 - 8 weeks old were irradiated with

20   100 cGy microwave radiation. Twenty-four hours later, mice were transplanted with 1×10^6 MV-4-11 cells via tail vein injections in each irradiated mouse. Mice were randomized post xenograft transplantation into cages of 5. Prior to treatment, peripheral microchimerism was documented at week 1. Upon establishing microchimerism, mice were treated with either 0.1

mg/kg or 0.03 mg/kg ammocidin in saline or saline vehicle i.p. for 5 days on, 2 days off for 2 weeks. Murine CBC was analyzed from blood collected into EDTA tubes (Greiner Bio-One) and analyzed with a Hemavet (Drew Scientific) analysis system.

2.4.35 <u>Flow Cytometry</u>

5   For analysis of MV-4-11 cells expressing the Perceval HR reporter, cells were treated with compounds for 16 hrs in 96 well plates in 100 μL of media. Prior to analysis, propidium iodide was added at a final concentration of 300 ng/mL as a viability stain. Perceval-HR fluorescence was recorded on the YFP and AmCyan channels and intact, single, PI-negative cells were selected for analysis. ATP-ADP ratio was calculated by subtracting the asinh transformed

10   YFP and AmCyan intensities. Two independent clones were analyzed as biological replicates. Cells were analyzed using a 5-laser LSR instrument (Becton Dickinson).

For analysis of pS6 suppression and ATPIF1 expression, cells were analyzed using intracellular flow cytometry multiplexed using fluorescent cell barcoding. For pS6 suppression, cells were treated for 16 hrs with the indicated compound in 96 well plates, ATPIF1 expression

15   was measured in untreated cells. At the time of analysis, Alexa Fluor 700-NHS ester was added to each well as a viability stain (final 20 ng/mL) and allowed to incubate for 15 min, cells were fixed with 1.6% PFA for 10 min, and permeabilized with ice cold methanol for 30 min at -20 °C. Barcoding and staining was performed as described previously (196).

For analysis of mouse xenografts, red blood cells were lysed with EL Buffer on ice

20   (Qiagen), with remaining cells washed and resuspended in 1x PBS with 1% BSA and stained for 15 minutes with the following antibodies: human CD45-APC (Clone 2D1) (Biolegend), human CD33-PE-Cy7 (Clone P67.6) (Biolegend), murine CD45-PE (Clone 30-F11) (Biolegend) and

DAPI (Biolegend). Cells were washed and submitted for flow cytometric analysis using a 3-laser LSRII (Becton Dickinson).

2.4.36 Histology and Immunohistochemistry

Tissues were fixed in 4% paraformaldehyde for 48 hours and stored in 70% ethanol before being embedding in paraffin and sectioned at 5 µm. The bone tissue was decalcified prior to being embedded in paraffin. Sections were de-waxed in xylene and rehydrated in successive ethanol baths. Standard Mayer's Hematoxylin and Eosin (H&E) staining was performed. Antigen retrieval using a standard pH 6 sodium citrate buffer (BioGenex) was performed and sections were stained with Monoclonal Mouse Anti-Human CD45 (Dako, M0701, dilution 1:200) using the M.O.M. Kit (Vector).

2.4.37 Pharmacokinetic Studies

All animal experiments were conducted in accordance to guidelines approved by the IACUC at Vanderbilt University Medical Center. Pharmacokinetics of Ammocidin in NSGS male mice in biological triplicate were assessed in whole blood after dosing with ammocidin alone i.p. 0.5 mg/kg. Whole blood samples were collected up to in EDTA tubes for analysis of plasma. Blood plasma was mixed 1:1 with an internal standard solution consisting of 1 µM apoptolidin A in PBS. Metabolites were extracted with 200 µL of ethyl acetate, evaporated to dryness and resuspended in 100 µL of MeOH. Ammocidin A concentration was determined using LC-MS (Thermo TSQ Quantum Access Max) with technical duplicates on a 50 x 1.8mm C18 column, isocratic 60/40 H2O/Acetonitrile + 10 mM ammonium acetate at 250 µL/min in ESI+ mode monitoring ammocidin A (1139.7 → 208.8, CE 19 V, RT = 1.00 min) and apoptolidin A (1146.68 → 805.46, CE 19 V, RT = 1.66 min).

2.4.38 Isolation of Apoptolidin A, Apoptolidin H, Ammocidin A

116

Similar methods were used to obtain all three compounds by using different producing

strains. Apoptolidin A was obtained by cultivation of wild-type *Nocardiopsis sp.* FU-40.

Apoptolidin H was obtained by cultivation of *Nocardiopsis sp.* FU-40 in which *ApoGT2* was

replaced with an apramycin resistance cassette as previously described (105). Ammocidin A was

5   obtained by cultivation of *Saccharothrix sp.* AJ9571 provided by Ajinomoto Co., Inc (Kawasaki,

Japan). Each organism was plated on Bennett's agar (0.1% yeast extract, 0.1% beef extract, 0.2%

N-Z Amine Type A, 1.0% dextrose, 2.0% agar, pH 7.0) and incubated at 30 °C for 3 - 7 days

until sporulation. FU-40 ΔGT2 was grown on plates containing Bennet's media with the addition

of apramycin, 80 μg/mL. The seed culture was initiated using spores scraped from the solid

10   culture into 250 mL Erlenmeyer flasks containing 50 mL of seed medium (1.0% soluble starch,

1.0% molasses (Plantation Blackstrap, Unsulfured), 1.0% peptone, 1.0% beef extract, pH 7.0),

and incubated for 7 days at 30 °C while shaking at 220 RPM. Production cultures were carried

out in multiple 250 mL Erlenmeyer flasks containing 50 mL of production media (2.0% glycerol,

1.0% molasses, 0.5% casamino acids, 0.1% peptone, 0.4% calcium carbonate, pH 7.2) and

15   incubated at 30 °C for 7 days while shaking at 220 RPM.

Apoptolidin A, apoptolidin H, and ammocidin A were purified using similar methods and

differed only in the specific fractions collected according to their retention times. After 7 days of

fermentation, the mycelia were separated from the culture broth by centrifugation at 3000 g x 30

min. The culture broth was extracted 3x with 1 volume of ethyl acetate and the combined organic

20   layers were washed with brine, dried with Na_2SO_4 and concentrated *in vacuo*. The crude extracts

were then subjected to chromatography with LH-20 resin using methanol as the mobile phase

and the glycomacrolide containing fractions were identified by thin-layer-chromatography and

pooled. The LH-20 fractions were then subjected to reverse phase HPLC using a Waters

117

XBridge Prep C18 19 x 150 mm column with a 20-minute gradient from 70% A / 30% B to 20% A / 80% B, (Buffer A: 95% water, 5% acetonitrile, 10 mM ammonium acetate; Buffer B: 5% water, 95% acetonitrile, 10 mM ammonium acetate). Apoptolidin A – RT: 9.5 min, Apoptolidin H – RT: 8.0 min, Ammocidin A – RT 9.0 min. Fractions containing pure compounds were

5   lyophilized using a Genevac HT-6 to yield white solids. Purity of each compound was confirmed by NMR (H^1 and HSQC) and HPLC/MS.

2.4.39 <u>Isolation of Aurovertins B, D</u>

Aurovertin was obtained by cultivation of *Calcarisporium arbuscula,* NRRL-3705, obtained from the ARS Culture Collection, Peoria, IL, using the approach described by Baldwin

10   (52). Spores of NRRL-3705 were plated on modified Czapek agar (3.0% sucrose, 0.5% corn steep solids, 0.1% KH_2PO_4, 0.05% $MgSO_4$, 0.05% KCl, 0.01% $FeSO_4$) and incubated at 24 °C for 10 days. The production cultures were inoculated from a single colony of fungal mycelia into Roux bottles containing 70 mL of Baldwin production medium (3.0% Dextrose, 1.0% peptone, 0.5% NaCl, 0.5% dried corn steep, 0.5% yeast extract, 0.3% beef extract, pH 6.0) and incubated

15   at room temperature for 14 days in the dark.

The fungal mycelia were separated from the broth by centrifugation and extracted with 250 mL of acetone for 2 hrs. The acetone was concentrated *in vacuo,* until only water remained. The aqueous layer was extracted 3 x with $CHCl_3$, the organic layer was washed with brine, and dried with Na_2SO_4 and concentrated to ~5 mL. The desired product was precipitated by the

20   addition of pentane, filtered over Celite, and redissolved in methanol. The resulting semi-purified extract was then subjected to reverse phase HPLC using a Waters XBridge Prep C18 19 x 150 mm column with the following gradient at 10 mL /min : 0 min – 75 % A / 25 % B; 20 min – 60 % A/40 % B; 25 min – 60 % A/40 % B , 27 min – 5 %A/95 % B, 39 min – 5 % A/95 % B

(Buffer A: 95 % water, 5 % acetonitrile, 10 mM ammonium acetate; Buffer B: 5% water, 95% acetonitrile, 10 mM ammonium acetate). Aurovertin D – RT: 15 min; Aurovertin B – RT: 30 min. Fractions containing pure compounds were lyophilized using a Genevac HT-6 to yield yellow solids. Purity of each compound was confirmed by NMR (H^1 and HSQC) and HPLC/MS.

2.4.40 Isolation of Efrapeptins

Efrapeptins were obtained by cultivation of *Tolypocladium cyclindrosporium,* ARSEF 962 (ATCC 42438) obtained from the American Type Tissue Culture Collection (ATCC, Manassas, VA). ARSEF 962 was plated on Sabouraud agar + yeast extract (4.0 % peptone, 1.0 % peptone, 1.0 %, 2.0 % agar, 1.0 % yeast extract, pH 5.6) and incubated at room temperature for 14 days. Production cultures were inoculated into 250 mL flasks containing 100 mL of Czapek Dox + peptone media (3.0% sucrose, 0.3 % $NaNO_3$, 0.1 % KH_2PO_4, 0.05 % $MgSO_4$, 0.05 % KCl, 0.01 % $FeSO_4$, 0.5 % peptone, pH 5.6) (64). The fungal mycelia were separated from the broth by centrifugation and discarded. The broth was extracted 3x with dichloromethane, washed with brine, and dried with Na_2SO_4. The crude extract was concentrated *in vacuuo,* resuspended in 1 mL of methanol, and subjected to size exclusion chromatography using methanol as the mobile phase. The efrapeptin containing fractions were combined and subjected to reverse phase HPLC using a Waters XBridge Prep C18 19 x 150 mm column with the following gradient at 10 mL /min: 0 min – 70 % A / 30 % B; 20 min – 20 % A/80 %B (Buffer A: 95% water, 5 % acetonitrile, 10 mM ammonium acetate; Buffer B: 5% water, 95% acetonitrile, 10 mM ammonium acetate). Efrapeptin E – RT 16.8 min; efrapeptin F – RT 17.7 min. Fractions containing pure compounds were lyophilized using a Genevac HT-6 to yield white solids. Purity of each compound was confirmed by NMR (H^1 and HSQC) and HPLC/MS.

2.4.41 Synthesis of Apoptolidin A PA (**2**)

Photoaffinity probes were synthesized using reaction conditions adapted from Deguire, 2015 ([129](#)). To a solution of 3-(3-(but-3-yn-1-yl)-3H-diazirin-3-yl)propanoic acid (4.5 mg, 0.027 mmol, Enamine, Kyiv, Ukraine) in dichloromethane (4.0 mL) on ice, was added bromo-tris-pyrrolidinophosphonium hexafluorophosphate (PyBrop, 13.3 mg, 0.28 mmol) and

5   diisopropylethyl amine (DIPEA, 31 μL, 0.177 mmol). The resulting solution was stirred at 0 °C for 10 min. Apoptolidin A (20 mg 0.018 mmol) was added, followed by a crystal of 4-dimethylaminopyridine (DMAP). The resulting solution was warmed to room temperature overnight (16 h). The reaction was monitored by TLC (90:10 $CHCl_3$:MeOH) and quenched with 100 μL of MeOH and then concentrated. The resulting residue was diluted in EtOAc (20 mL)

10   and washed with 1 M HCL (5 mL). The aqueous layer was extracted twice with EtOAC (2 x 10 mL). The organic extracts were combined and washed with $NaHCO_3$ (5 mL) and brine (5 mL), dried with anhydrous sodium sulfate and concentrated *in vacuo*. The resulting residue was dissolved in 800 μL of MeOH and purified by reversed phase HPLC using a Waters XBridge Prep C18 19 x 150 mm column, with a 15-minute gradient from 32 % to 85 % acetonitrile in

15   water, with 25 mM ammonium bicarbonate. The fractions containing the desired product (rt = 11 min) were combined and lyophilized to afford (**2**) as a white solid (1.9 mg, 8% isolated yield). HRMS (ESI-TOF MS) m/z 1299.6973 $(M+Na)^+$ calculated, 1299.7023 observed (3.4 ppm). Regiochemistry of addition was confirmed by multidimensional NMR (see Table 2.2, Spectrum 2.1, Spectrum 2.2).

20

2.4.42 Synthesis of Apoptolidin H PA (**4**)

Apoptolidin H PA was synthesized using identical reaction conditions and work-up as used for (**2**), with Apoptolidin H (14.9 mg 0.018 mmol) The resulting residue was dissolved in

800 µL of MeOH and purified by reversed phase HPLC using a Waters XBridge Prep C18 19 x 150 mm column, with a 20-minute gradient from 32% to 77% acetonitrile in water, with 25 mM ammonium bicarbonate. The fractions containing the desired product (rt = 14 min) were combined and lyophilized to afford (**4**) as a white solid (2.4 mg, 13% isolated yield). HRMS (ESI-TOF MS) m/z 1011.5394 (M+Na)+ calculated, 1011.5405 observed (1.1 ppm). Regiochemistry of addition was confirmed by multidimensional NMR (see Table 2.3, Spectrum 2.3, Spectrum 2.4).

2.4.43 Synthesis of Ammocidin A PA (**6**)

Ammocidin A PA was synthesized using identical reaction conditions and work-up as used for (**2**), with Ammocidin A (21 mg 0.018 mmol) The resulting residue was dissolved in 800 µL of MeOH and purified by reversed phase HPLC using a Waters XBridge Prep C18 19 x 150 mm column, with a 20-minute gradient from 32% to 77% acetonitrile in water, with 25 mM ammonium bicarbonate. The fractions containing the desired product (rt = 16 min) were combined and lyophilized to afford (**6**) as a white solid (0.6 mg, 2.5% isolated yield). HRMS (ESI-TOF MS) m/z 1287.6854 (M+Na)$^+$ calculated 1287.6866, observed (0.9 ppm). Regiochemistry of addition was confirmed by multidimensional NMR (see Table 2.4, Spectrum 2.5, Spectrum 2.6).
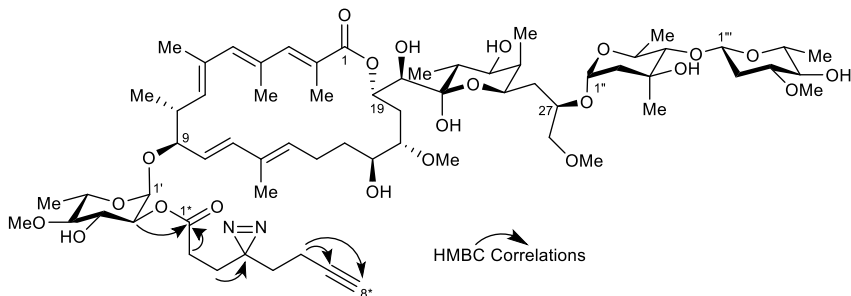
Table 2.2. NMR validation of Apoptolidin A PA (2)

	Apoptolidin A PA-Alkyne (2)				
Position	δ_C	δ_H	Position	δ_C	δ_H
1	172.3		1'	93.2	4.98
2	123.5		2'	75	4.56
3	149	7.38	3'	72.1	3.9
4	132.9		4'	87.1	2.81
5	146.8	6.19	5'	67.9	3.77
6	133.4		6'	18.1	1.28
7	142.5	5.21	4'-OMe	61	3.59
8	38.9	2.68			
9	84.1	3.83	1"	99.3	4.94
10	125.2	5.12	2"	45.4	1.92, 1.8
11	140.9	6.14	3"	72.7	
12	134.3		4"	85.6	3.35
13	133.5	5.63	5"	67.1	3.67
14	24.3	2.45, 2.05	6"	18.7	1.25
15	36.3	1.5, 1.42	3"-Me	22.4	1.32
16	74.4	3.41			
17	83.5	2.76	1'''	101.6	4.83
18	38	2.16, 1.74	2'''	36.8	2.45, 1.27
19	72.2	5.3	3'''	81.8	3.18
20	75.1	3.53	4'''	76.9	2.97
21	101		5'''	73.1	3.22
22	36.1	2.05	6'''	18.2	1.28
23	73.5	3.71	3'''-OMe	57	3.42
24	40.5	1.73			
25	69.2	3.95	1*	173.1	
26	36.7	1.58, 1.46	2*	28.8	2.25, 2.16
27	76.6	3.44	3*	28.7	1.82, 1.75
28	76.4	3.32	4*	78.8	
2-Me	13.9	2.1	5*	33.2	1.62
4-Me	17.7	2.19	6*	13.6	2.04
6-Me	16.3	1.94	7*	83.4	
8-Me	18.3	1.14	8*	70.2	2.28
12-Me	12	1.66			
22-Me	11.9	1.03			
24-Me	5	0.9			
17-OMe	61	3.37			
28-OMe	59.1	3.27			

Data recorded in CD₃OD at 600 Hz
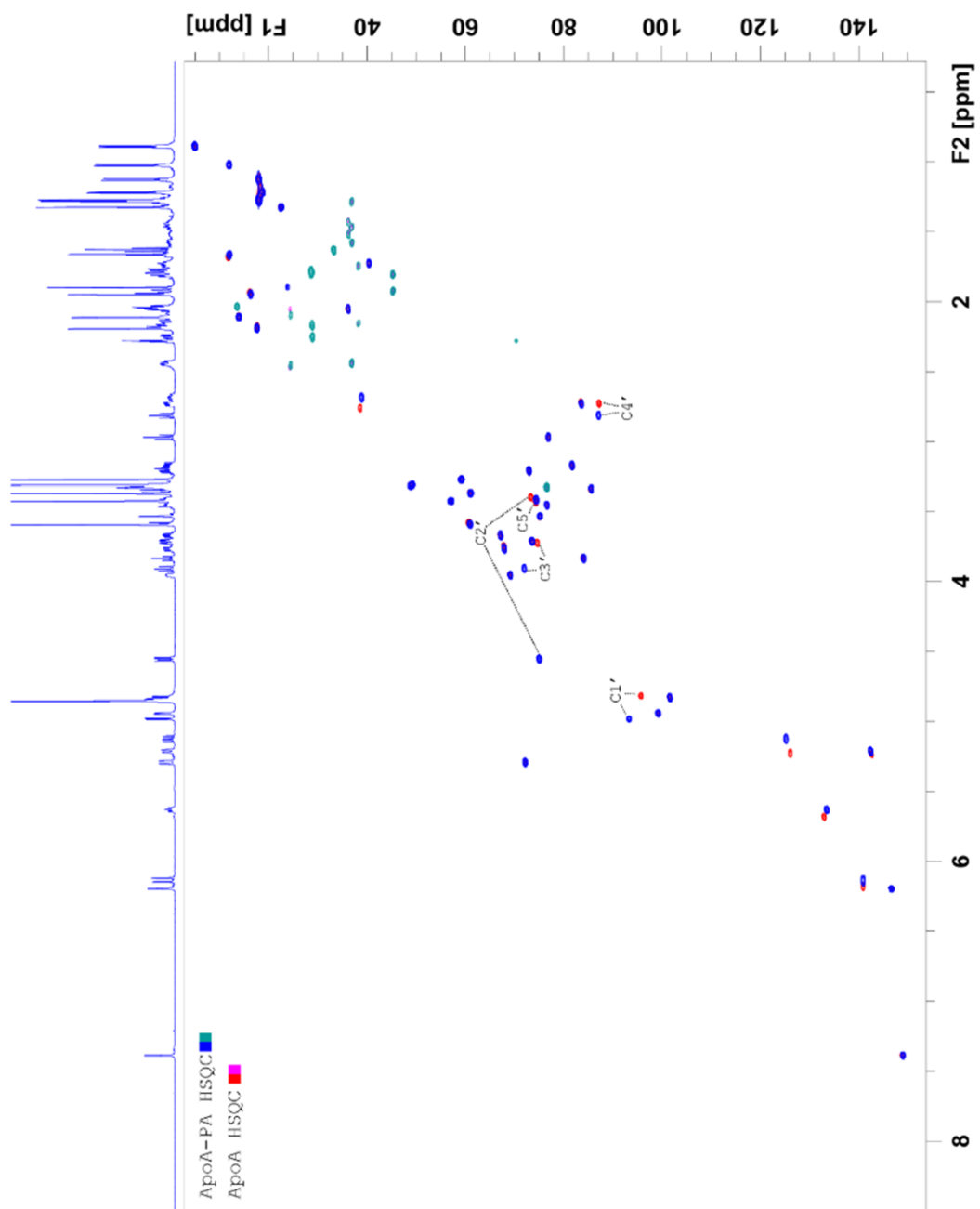
Spectrum 2.1. HSQC spectrum of Apoptolidin A PA (2) in MeOD at 600 MHz

Overlaid on HSQC spectrum of Apoptolidin A in MeOD (red/pink)
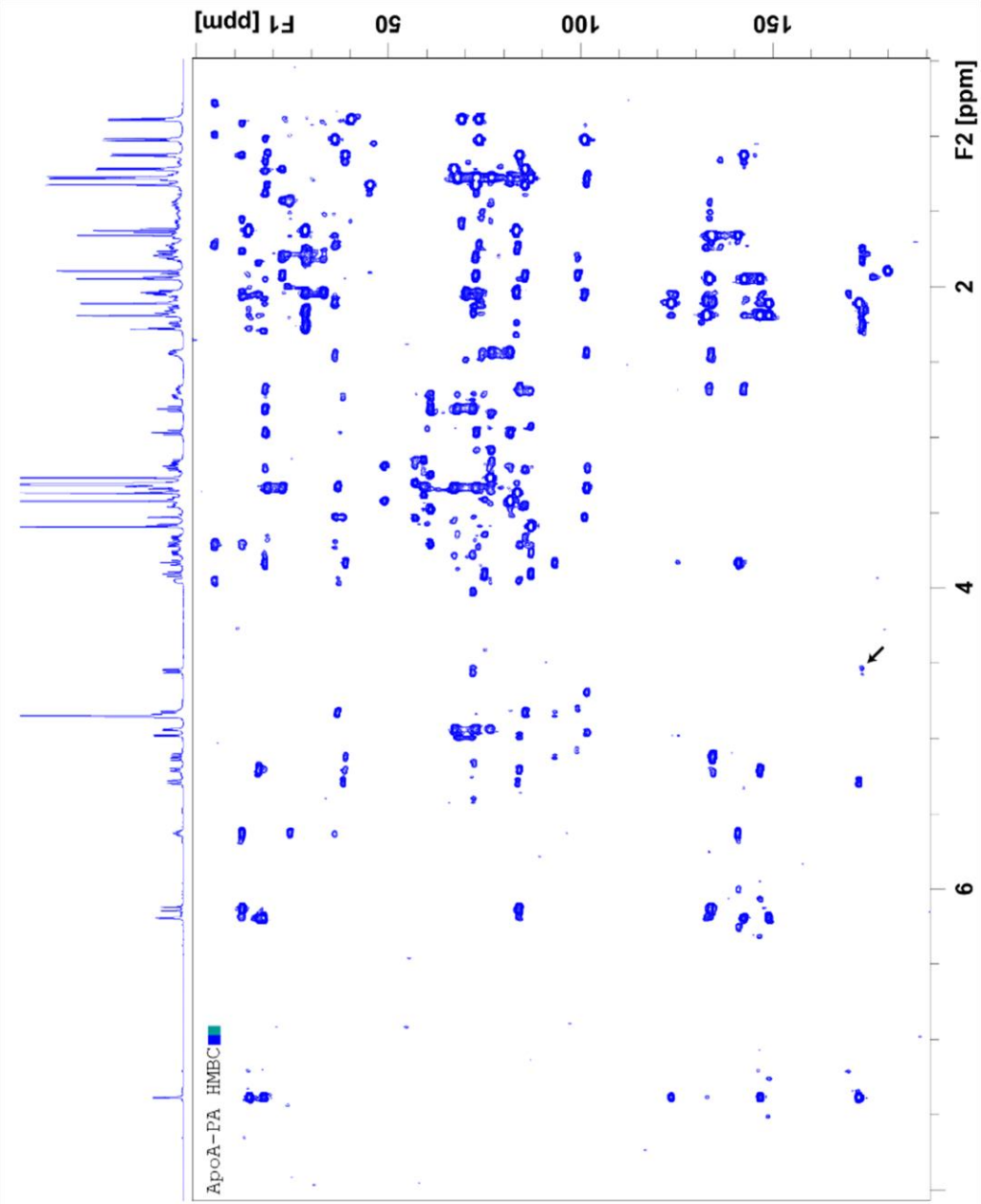
Spectrum 2.2. HMBC spectrum of Apoptolidin A PA (2) in MeOD at 600 MHz

Arrow denotes correlation from C2' to carbonyl of alkyl diazerine

Table 2.3. NMR validation of Apoptolidin H PA (4)

HMBC Correlations
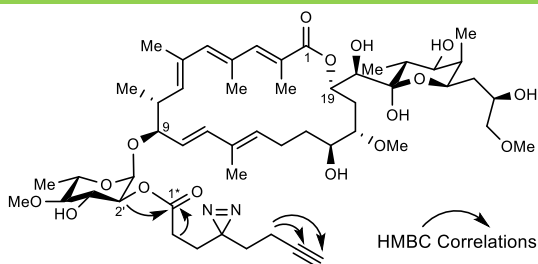
	Apoptolidin H PA-Alkyne (4)					
Position	δC	δH	Position	δC	δH	
1	172.6		1'	93.3	4.98	
2	123.8		2'	75	4.55	
3	148.7	7.36	3'	72	3.91	
4	133.5		4'	87	2.81	
5	146.7	6.19	5'	67.9	3.77	
6	133.3		6'	17.7	1.29	
7	142.5	5.22	4'-OMe	60.9	3.59	
8	38.7	2.76				
9	84	3.83				
10	126.1	5.22				
11	141	6.17				
12	134.8					
13	133	5.68				
14	24.3	2.47, 2.06				
15	36.2	1.52, 1.41				
16	74.5	3.43				
17	83.5	2.73				
18	38.2	2.15, 1.75				
19	72	5.31				
20	75.1	3.54				
21	101					
22	36.1	2.04				
23	73.5	3.75				
24	40.5	1.76				
25	68.9	4.09	1*	173.2		
26	38.1	1.58, 1.29	2*	28.8	2.26, 2.17	
27	67.9	3.55	3*	28.3	1.87, 1.75	
28	78.5	3.19	4*	73.1		
2-Me	14	2.11	5*	33.2	1.63	
4-Me	17.5	2.21	6*	13.7	2.03	
6-Me	16.1	1.92	7*	83.1		
8-Me	18.1	1.14	8*	70.3	2.28	
12-Me	11.8	1.67				
22-Me	12.1	1.02				
24-Me	5.1	0.89				
17-OMe	61.4	3.36				
28-OMe	59.3	3.29				

Data recorded in CD3OD at 600 Hz

125
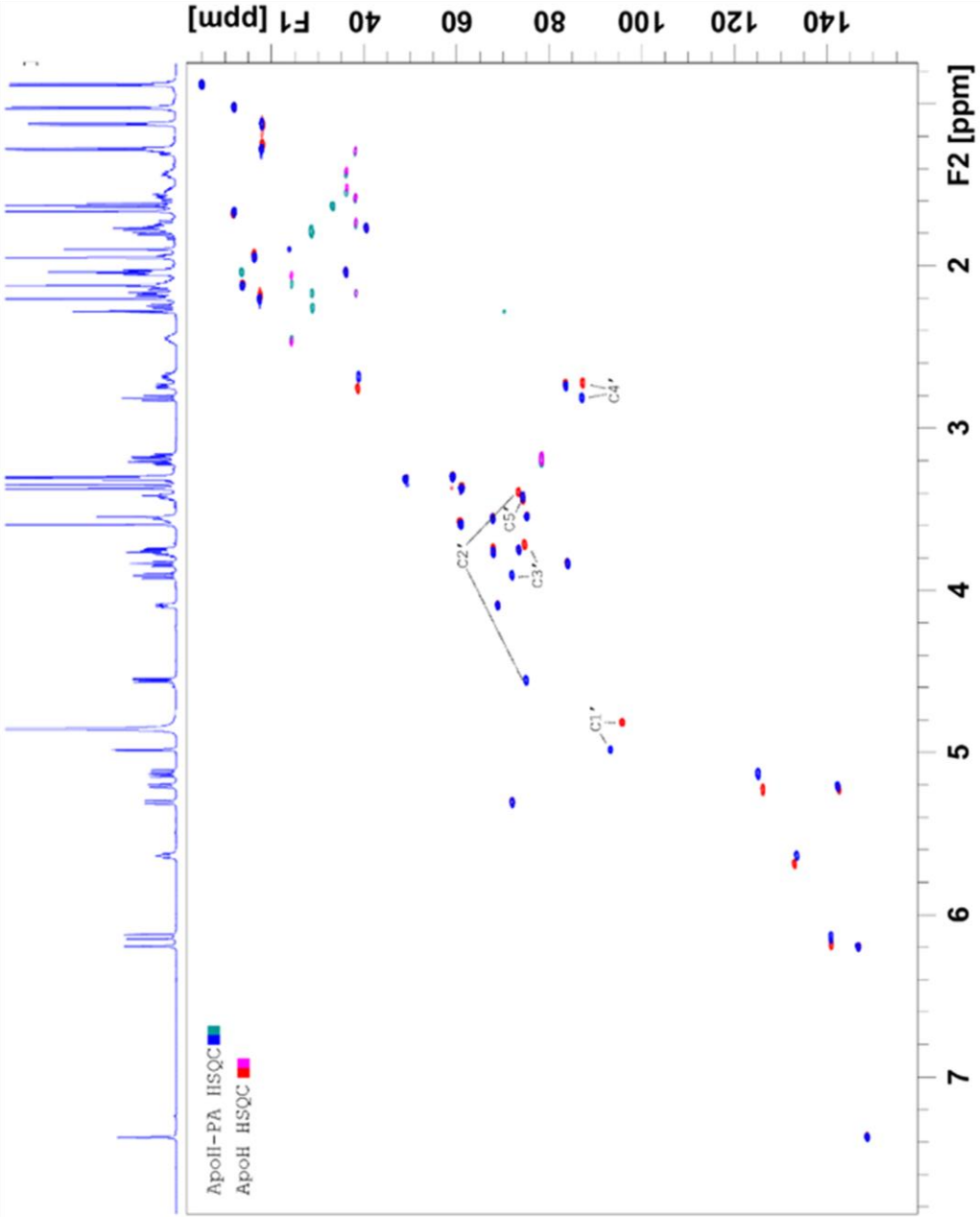
Spectrum 2.3. HSQC spectrum of Apoptolidin H PA (4) in MeOD at 600 MHz

Overlaid on HSQC spectrum of Apoptolidin H in MeOD (red/pink)

126
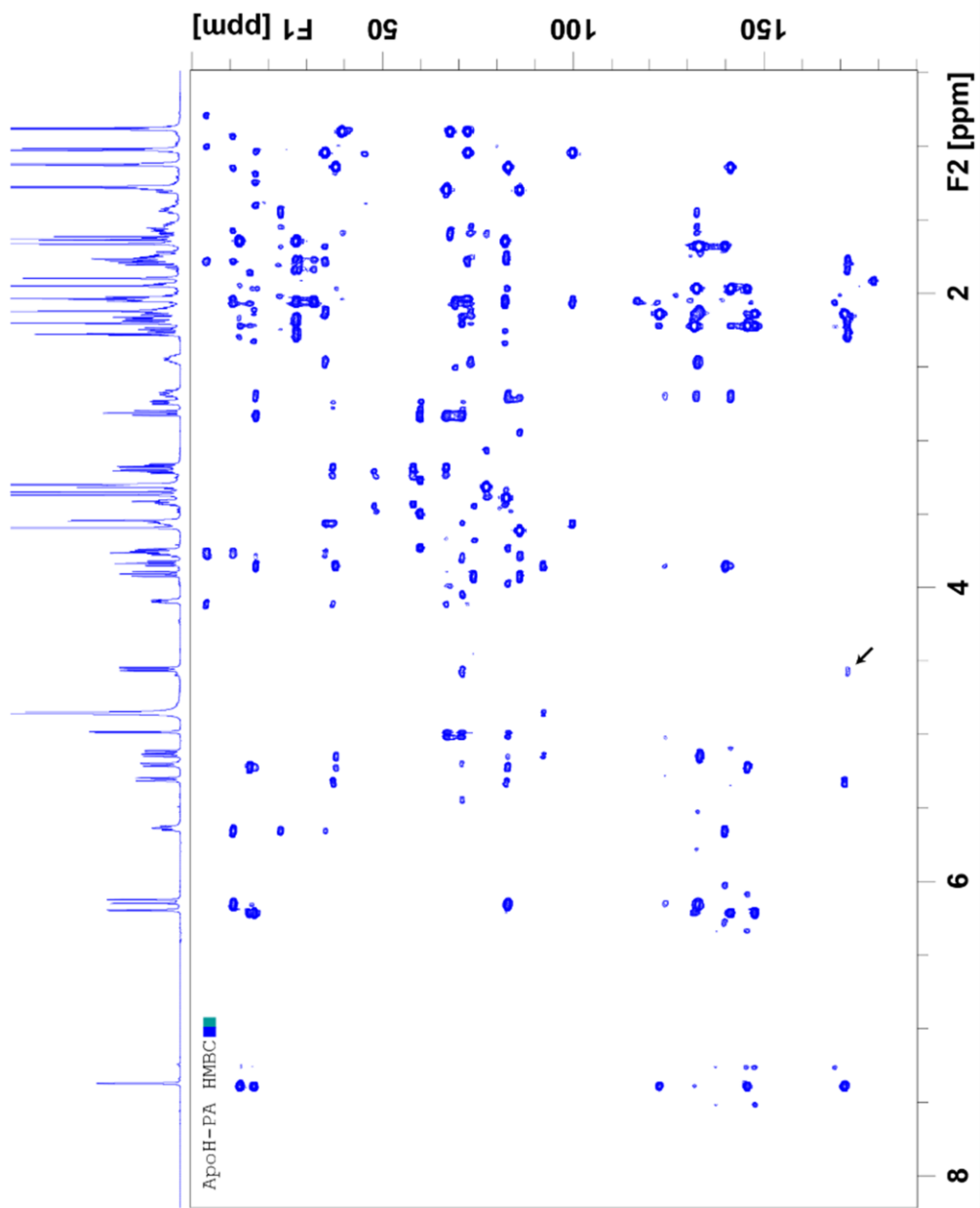
Spectrum 2.4. HMBC spectrum of Apoptolidin H PA (4) in MeOD at 600 MHz

Arrow denotes correlation from C2' to carbonyl of alkyl diazerine

Table 2.4. NMR validation of Ammocidin A PA (6)

HMBC Correlations
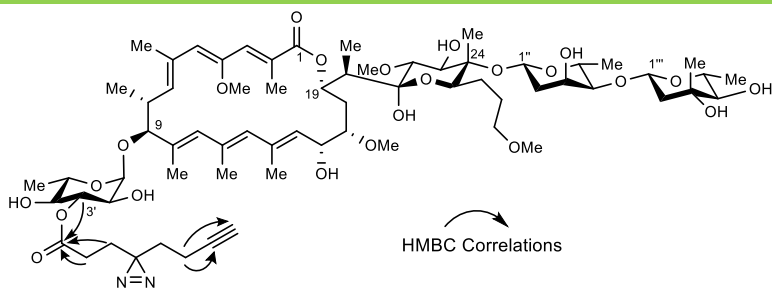
Position	δ_C	δ_H	Position	δ_C	δ_H
		Ammocidin A PA-Alkyne (6)			
1	171.2		1'	95.6	4.7
2	125.4		2'	71.6	3.58
3	138.2	7	3'	76.8	5.2
4	153.6		4'	87.1	3.15
5	134.2	5.79	5'	68.7	3.86
6	131.8		6'	18.1	1.29
7	142	5.35			
8	36.8	2.88	1"	92.6	5.11
9	87.9	3.85	2"	38.9	1.97, 1.76
10	134.8		3"	68.3	4.28
11	136.3	5.94	4"	83.3	3.31
12	134.1		5"	69.5	3.92
13	133.5	5.61	6"	18.3	1.27
14	136.2				
15	129.4	5.25	1'''	101.8	4.72
16	67.9	4.83	2'''	46.6	1.97, 1.74
17	82.8	2.7	3'''	72.3	
18	35.8	1.93, 1.67	4'''	80.2	3.13
19	72.3	5.54	5'''	72.6	3.41
20	44.9	2.07	6'''	19	1.3
21	99.9		3'''-Me	20.4	1.27
22	81.9	3.08			
23	76.8	3.95			
24	82.4				
25	73.9	3.66	1*	174	
26	25.8	1.60, 1.24	2*	29.4	2.27
27	27.8	1.53, 1.34	3*	29	1.78
28	73.9	3.3	4*	-	
2-Me	13.8	2.12	5*	33.2	1.65
6-Me	13.1	2.09	6*	13.7	2.05
8-Me	18.2	1.2	7*	83.1	
10-Me	12	1.62	8*	70.7	2.27
12-Me	18.1	1.91			
14-Me	17.6	1.76			
20-Me	9.3	1.14			
24-Me	10.7	1.16			
4-OMe	61.4	3.54			
17-OMe	57.6	3.38			
22-OMe	61.4	3.57			
28-OMe	58.7	3.27			

Data recorded in CD$_3$OD at 600 Hz

128
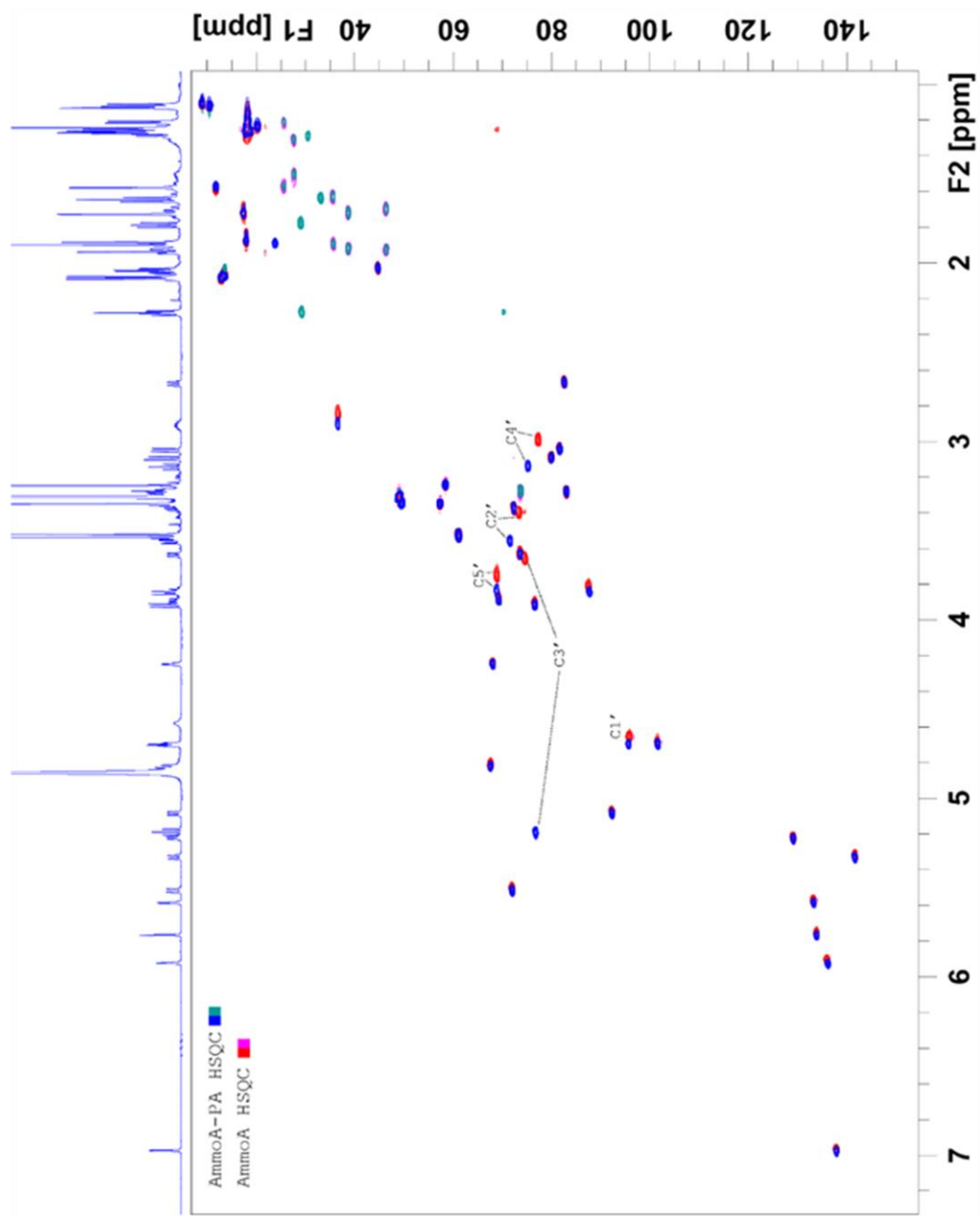
Spectrum 2.5. HSQC spectrum of Ammocidin A PA (6) in MeOD at 600 MHz

Overlaid on HSQC spectrum of Ammocidin A in MeOD (red/pink)
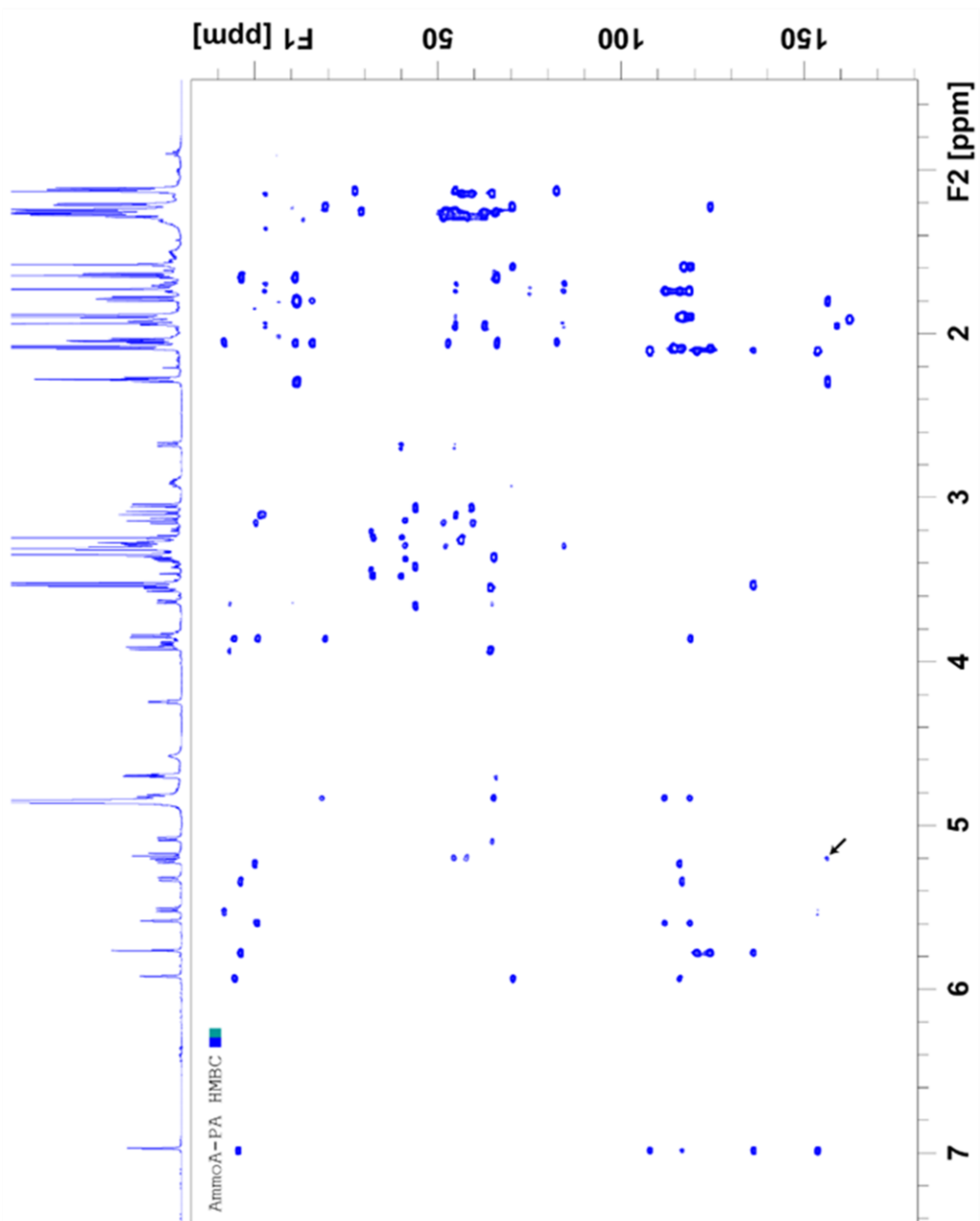
Spectrum 2.6. HMBC spectrum of Ammocidin A PA (6) in MeOD at 600 MHz

Arrow denotes correlation from C2' to carbonyl of alkyl diazerine

2.5 References

7.   D. Hanahan, R. A. Weinberg, Hallmarks of cancer: the next generation. *Cell* **144**, 646-674 (2011).

29.   R. M. Smith, University of Wisconsin--Madison, (1953).

34.   J. P. Abrahams, A. G. Leslie, R. Lutter, J. E. Walker, Structure at 2.8 A resolution of F1-ATPase from bovine heart mitochondria. *Nature* **370**, 621-628 (1994).

37.   J. Symersky, D. Osowski, D. E. Walters, D. M. Mueller, Oligomycin frames a common drug-binding site in the ATP synthase. *Proc Natl Acad Sci U S A* **109**, 13961-13965 (2012).

52.   C. Baldwin, Biological and chemical properties of aurovertin, a metabolic product of Calcarisporium abuscula. *Lloydia* **27**, 88-95 (1964).

61.   R. L. Cross, W. E. Kohlbrenner, The mode of inhibition of oxidative phosphorylation by efrapeptin (A23871). Evidence for an alternating site mechanism for ATP synthesis. *J Biol Chem* **253**, 4865-4873 (1978).

64.   S. B. Krasnoff, S. Gupta, Identification and directed biosynthesis of efrapeptins in the fungusTolypocladium geodes gams (Deuteromycotina: Hyphomycetes). *J Chem Ecol* **17**, 1953-1962 (1991).

67.   J. R. Gledhill, J. E. Walker, Inhibitors of the catalytic domain of mitochondrial ATP synthase. *Biochemical Society transactions* **34**, 989-992 (2006).

69.   R. J. DeBerardinis, N. S. Chandel, We need to talk about the Warburg effect. *Nat Metab* **2**, 127-129 (2020).

71.   I. Martinez-Reyes *et al.*, Mitochondrial ubiquinol oxidation is necessary for tumour growth. *Nature* **585**, 288-292 (2020).

73.   J. R. Molina *et al.*, An inhibitor of oxidative phosphorylation exploits cancer vulnerability. *Nat Med* **24**, 1036-1046 (2018).

74.   T. M. Ashton, W. G. McKenna, L. A. Kunz-Schughart, G. S. Higgins, Oxidative Phosphorylation as an Emerging Target in Cancer Therapy. *Clin Cancer Res* **24**, 2482-2490 (2018).

76.   Y. Xu, D. Xue, A. Bankhead, 3rd, N. Neamati, Why All the Fuss about Oxidative Phosphorylation (OXPHOS)? *J Med Chem* **63**, 14276-14307 (2020).

87.   C. H. Arrowsmith *et al.*, The promise and peril of chemical probes. *Nat Chem Biol* **11**, 536-541 (2015).

98.   J. W. Kim, H. Adachi, K. Shin-ya, Y. Hayakawa, H. Seto, Apoptolidin, a new apoptosis inducer in transformed cells from Nocardiopsis sp. *J Antibiot (Tokyo)* **50**, 628-630 (1997).

99.   Y. Hayakawa *et al.*, Structure of Apoptolidin, a Specific Apoptosis Inducer in Transformed Cells. *J Am Chem Soc* **120**, 3524-3525 (1998).

101.   P. A. Wender *et al.*, Correlation of F0F1-ATPase inhibition and antiproliferative activity of apoptolidin analogues. *Org Lett* **8**, 589-592 (2006).

102.   P. A. Wender, K. E. Longcore, Isolation, structure determination, and anti-cancer activity of apoptolidin D. *Org Lett* **9**, 691-694 (2007).

103.   P. A. Wender, K. E. Longcore, Apoptolidins E and F, new glycosylated macrolactones isolated from Nocardiopsis sp. *Org Lett* **11**, 5474-5477 (2009).

104.   B. O. Bachmann *et al.*, Light-induced isomerization of apoptolidin a leads to inversion of C2-C3 double bond geometry. *Org Lett* **12**, 2944-2947 (2010).

105. Y. Du *et al.*, Biosynthesis of the Apoptolidins in Nocardiopsis sp. FU 40. *Tetrahedron* **67**, 6568-6575 (2011).

107. J. D. Pennington, H. J. Williams, A. R. Salomon, G. A. Sulikowski, Toward a stable apoptolidin derivative: identification of isoapoptolidin and selective deglycosylation of apoptolidin. *Org Lett* **4**, 3823-3825 (2002).

108. P. A. Wender, A. V. Gulledge, O. D. Jankowski, H. Seto, Isoapoptolidin: structure and activity of the ring-expanded isomer of apoptolidin. *Org Lett* **4**, 3819-3822 (2002).

109. R. Murakami *et al.*, Ammocidin, a new apoptosis inducer in Ras-dependent cells from Saccharothrix sp. I. Production, isolation and biological activity. *J Antibiot (Tokyo)* **54**, 710-713 (2001).

111. R. Murakami *et al.*, Ammocidin, a new apoptosis inducer in ras-dependent cells from Saccharothrix sp. II. Physico-chemical properties and structure elucidation. *J Antibiot (Tokyo)* **54**, 714-717 (2001).

112. S. T. Chau, Y. Hayakawa, G. A. Sulikowski, 18O assisted analysis of a gamma,delta-epoxyketone cyclization: synthesis of the C16-C28 fragment of ammocidin D. *Org Lett* **13**, 756-759 (2011).

113. R. Murakami *et al.*, Ammocidins B, C and D, new cytotoxic 20-membered macrolides from Saccharothrix sp. AJ9571. *J Antibiot (Tokyo)* **62**, 123-127 (2009).

114. Z. G. Khalil *et al.*, Amycolatopsins A-C: antimycobacterial glycosylated polyketide macrolides from the Australian soil *Amycolatopsis* sp. MST-108494. *J Antibiot (Tokyo)* **70**, 1097-1103 (2017).

115. A. R. Salomon, D. W. Voehringer, L. A. Herzenberg, C. Khosla, Apoptolidin, a selective cytotoxic agent, is an inhibitor of F_0F_1-ATPase. *Chem Biol* **8**, 71-80 (2001).

117. A. R. Salomon, Y. Zhang, H. Seto, C. Khosla, Structure-activity relationships within a family of selectively cytotoxic macrolide natural products. *Org Lett* **3**, 57-59 (2001).

118. A. R. Salomon, D. W. Voehringer, L. A. Herzenberg, C. Khosla, Understanding and exploiting the mechanistic basis for selectivity of polyketide inhibitors of F(0)F(1)-ATPase. *Proc Natl Acad Sci U S A* **97**, 14766-14771 (2000).

119. V. P. Ghidu *et al.*, Synthesis and evaluation of the cytotoxicity of apoptolidinones A and D. *J Org Chem* **73**, 4949-4955 (2008).

120. M. T. Crimmins, H. S. Christie, A. Long, K. Chaudhary, Total synthesis of apoptolidin A. *Org Lett* **11**, 831-834 (2009).

124. P. A. Wender, O. D. Jankowski, E. A. Tabet, H. Seto, Toward a structure-activity relationship for apoptolidin: selective functionalization of the hydroxyl group array. *Org Lett* **5**, 487-490 (2003).

129. S. M. DeGuire *et al.*, Fluorescent probes of the apoptolidins and their utility in cellular localization studies. *Angew Chem, Int Ed* **54**, 961-964 (2015).

131. Y. Akimov, T. Aittokallio, Re-defining synthetic lethality by phenotypic profiling for precision oncology. *Cell Chem Biol* **28**, 246-256 (2021).

132. N. N. Pavlova, C. B. Thompson, The Emerging Hallmarks of Cancer Metabolism. *Cell Metab* **23**, 27-47 (2016).

133. B. Faubert *et al.*, Lactate Metabolism in Human Lung Tumors. *Cell* **171**, 358-371 e359 (2017).

134. C. L. Jones, A. Inguva, C. T. Jordan, Targeting Energy Metabolism in Cancer Stem Cells: Progress and Challenges in Leukemia and Solid Tumors. *Cell Stem Cell* **28**, 378-393 (2021).

135. J. L. Carter *et al.*, Targeting mitochondrial respiration for the treatment of acute myeloid leukemia. *Biochem Pharmacol* **182**, 114253 (2020).

136. E. D. Lagadinou *et al.*, BCL-2 inhibition targets oxidative phosphorylation and selectively eradicates quiescent human leukemia stem cells. *Cell Stem Cell* **12**, 329-341 (2013).

137. S. Pei *et al.*, Monocytic Subclones Confer Resistance to Venetoclax-Based Therapy in Patients with Acute Myeloid Leukemia. *Cancer Discov* **10**, 536-551 (2020).

138. F. Wang *et al.*, Targeted inhibition of mutant IDH2 in leukemia cells induces cellular differentiation. *Science* **340**, 622-626 (2013).

139. V. P. Ghidu *et al.*, Combined chemical and biosynthetic route to access a new apoptolidin congener. *Org Lett* **11**, 3032-3034 (2009).

140. J. D. Serrill *et al.*, Apoptolidins A and C activate AMPK in metabolically sensitive cell types and are mechanistically distinct from oligomycin A. *Biochem Pharmacol* **93**, 251-265 (2015).

141. A. L. Mackinnon, J. Taunton, Target Identification by Diazirine Photo-Cross-linking and Click Chemistry. *Curr Protoc Chem Biol* **1**, 55-73 (2009).

142. Z. Li *et al.*, Design and synthesis of minimalist terminal alkyne-containing diazirine photo-crosslinkers and their incorporation into kinase inhibitors for cell- and tissue-based proteome profiling. *Angew Chem, Int Ed* **52**, 8551-8556 (2013).

143. H. Guo, J. L. Rubinstein, Cryo-EM of ATP synthases. *Curr Opin Struct Biol* **52**, 71-79 (2018).

144. C. Woo *et al.*, Labeling Preferences of Diazirines with Protein Biomolecules. *ChemRxiv*, (2020).

145. M. Tantama, J. R. Martinez-Francois, R. Mongeon, G. Yellen, Imaging energy status in live cells with a fluorescent biosensor of the intracellular ATP-to-ADP ratio. *Nat Commun* **4**, 2550 (2013).

146. J. R. Gledhill, M. G. Montgomery, A. G. Leslie, J. E. Walker, How the regulatory protein, IF(1), inhibits F(1)-ATPase from bovine mitochondria. *Proc Natl Acad Sci U S A* **104**, 15671-15676 (2007).

147. F. A. Ran *et al.*, Genome engineering using the CRISPR-Cas9 system. *Nat Protoc* **8**, 2281-2308 (2013).

148. K. A. Matreyek, J. J. Stephany, M. A. Chiasson, N. Hasle, D. M. Fowler, An improved platform for functional assessment of large protein libraries in mammalian cells. *Nucleic Acids Res* **48**, e1 (2020).

149. E. E. Wrenbeck *et al.*, Plasmid-based one-pot saturation mutagenesis. *Nat Methods* **13**, 928-930 (2016).

150. H. E. Ramsey *et al.*, A Novel MCL1 Inhibitor Combined with Venetoclax Rescues Venetoclax-Resistant Acute Myelogenous Leukemia. *Cancer Discov* **8**, 1566-1581 (2018).

151. I. Baccelli *et al.*, Mubritinib Targets the Electron Transport Chain Complex I and Reveals the Landscape of OXPHOS Dependency in Acute Myeloid Leukemia. *Cancer Cell* **36**, 84-99 e88 (2019).

152. C. L. Jones *et al.*, Inhibition of Amino Acid Metabolism Selectively Targets Human Leukemia Stem Cells. *Cancer Cell* **34**, 724-740 e724 (2018).

153. D. A. Pollyea *et al.*, Venetoclax with azacitidine disrupts energy metabolism and targets leukemia stem cells in patients with acute myeloid leukemia. *Nat Med* **24**, 1859-1866 (2018).

154. D. Sharon *et al.*, Inhibition of mitochondrial translation overcomes venetoclax resistance in AML through activation of the integrated stress response. *Sci Transl Med* **11**, eaax2863 (2019).

155. E. Gatza *et al.*, Manipulating the bioenergetics of alloreactive T cells causes their selective apoptosis and arrests graft-versus-host disease. *Sci Transl Med* **3**, 67ra68 (2011).

156. H. Guo *et al.*, Structure of mycobacterial ATP synthase bound to the tuberculosis drug bedaquiline. *Nature* **589**, 143-147 (2021).

157. R. Guieze *et al.*, Mitochondrial Reprogramming Underlies Resistance to BCL-2 Inhibition in Lymphoid Malignancies. *Cancer Cell* **36**, 369-384 e313 (2019).

158. M. R. Savona, J. C. Rathmell, Mitochondrial Homeostasis in AML and Gasping for Response in Resistance to BCL2 Blockade. *Cancer Discov* **9**, 831-833 (2019).

159. D. J. Newman, G. M. Cragg, Natural Products as Sources of New Drugs from 1981 to 2014. *J Nat Prod* **79**, 629-661 (2016).

160. J. R. Thomas *et al.*, in *Proteomics for Drug Discovery*. (Springer New York, 2017), pp. 1-18.

161. R. Paxman *et al.*, Pharmacologic ATF6 activating compounds are metabolically activated to selectively modify endoplasmic reticulum proteins. *Elife* **7**, e37168 (2018).

162. M. J. Moulton, A. Letsou, Modeling congenital disease and inborn errors of development in Drosophila melanogaster. *Dis Model Mech* **9**, 253-269 (2016).

163. W. Huber, A. von Heydebreck, H. Sultmann, A. Poustka, M. Vingron, Variance stabilization applied to microarray data calibration and to the quantification of differential expression. *Bioinformatics* **18 Suppl 1**, S96-104 (2002).

164. M. E. Ritchie *et al.*, limma powers differential expression analyses for RNA-sequencing and microarray studies. *Nucleic Acids Res* **43**, e47 (2015).

165. C. Ritz, F. Baty, J. C. Streibig, D. Gerhard, Dose-Response Analysis Using R. *PloS One* **10**, e0146021 (2015).

166. E. A. Orellana, A. L. Kasinski, Sulforhodamine B (SRB) Assay in Cell Culture to Investigate Cell Proliferation. *Bio Protoc* **6**, (2016).

167. V. Kabaleeswaran, N. Puri, J. E. Walker, A. G. Leslie, D. M. Mueller, Novel features of the rotary catalytic mechanism revealed in the structure of yeast F1 ATPase. *EMBO J* **25**, 5433-5442 (2006).

168. J. L. Rubinstein, V. K. Dickson, M. J. Runswick, J. E. Walker, ATP synthase from Saccharomyces cerevisiae: location of subunit h in the peripheral stalk region. *J Mol Biol* **345**, 513-520 (2005).

169. D. M. Mueller *et al.*, Ni-chelate-affinity purification and crystallization of the yeast mitochondrial F1-ATPase. *Protein Expr Purif* **37**, 479-485 (2004).

170. C. R. Marr, S. Benlekbir, J. L. Rubinstein, Fabrication of carbon films with approximately 500nm holes for cryo-EM with a direct detector device. *J Struct Biol* **185**, 42-47 (2014).

171. J. R. Meyerson *et al.*, Self-assembled monolayers improve protein distribution on holey carbon cryo-EM supports. *Sci Rep* **4**, 7084 (2014).

172. C. J. Russo, L. A. Passmore, Electron microscopy: Ultrastable gold substrates for electron cryomicroscopy. *Science* **346**, 1377-1380 (2014).

173. W. F. Tivol, A. Briegel, G. J. Jensen, An improved cryogen for plunge freezing. *Microsc Microanal* **14**, 375-379 (2008).

174. A. Punjani, J. L. Rubinstein, D. J. Fleet, M. A. Brubaker, cryoSPARC: algorithms for rapid unsupervised cryo-EM structure determination. *Nat Methods* **14**, 290-296 (2017).

175. S. Q. Zheng *et al.*, MotionCor2: anisotropic correction of beam-induced motion for improved cryo-electron microscopy. *Nat Methods* **14**, 331-332 (2017).

176. A. Punjani, H. Zhang, D. J. Fleet, Non-uniform refinement: adaptive regularization improves single-particle cryo-EM reconstruction. *Nat Methods* **17**, 1214-1221 (2020).

177. J. Zivanov *et al.*, New tools for automated high-resolution cryo-EM structure determination in RELION-3. *Elife* **7**, (2018).

178. D. Asarnow, E. Palovcak, Y. Cheng, UCSF pyem v0. 5. *Zenodo* **3576630**, (2019).

179. J. Zivanov, T. Nakane, S. H. W. Scheres, A Bayesian approach to beam-induced motion correction in cryo-EM single-particle analysis. *IUCrJ* **6**, 5-17 (2019).

180. M. A. Cianfrocco, M. Wong-Barnum, C. Youn, R. Wagner, A. Leschziner, in *Proceedings of the Practice and Experience in Advanced Research Computing 2017 on Sustainability, Success and Impact*. (ACM, 2017).

181. R. Sanchez-Garcia *et al.*, DeepEMhacer: a deep learning solution for cryo-EM volume post-processing. (2020).

182. E. F. Pettersen *et al.*, UCSF Chimera--a visualization system for exploratory research and analysis. *J Comput Chem* **25**, 1605-1612 (2004).

183. P. Emsley, K. Cowtan, Coot: model-building tools for molecular graphics. *Acta Crystallogr D Biol Crystallogr* **60**, 2126-2132 (2004).

184. T. I. Croll, ISOLDE: a physically realistic environment for model building into low-resolution electron-density maps. *Acta Crystallogr D Struct Biol* **74**, 519-530 (2018).

185. P. D. Adams *et al.*, PHENIX: a comprehensive Python-based system for macromolecular structure solution. *Acta Crystallogr D Biol Crystallogr* **66**, 213-221 (2010).

186. T. D. Goddard *et al.*, UCSF ChimeraX: Meeting modern challenges in visualization and analysis. *Protein Sci* **27**, 14-25 (2018).

187. C. Frezza, S. Cipolat, L. Scorrano, Organelle isolation: functional mitochondria from mouse liver, muscle and cultured fibroblasts. *Nat Protoc* **2**, 287-295 (2007).

188. G. Gouspillou *et al.*, Accurate determination of the oxidative phosphorylation affinity for ADP in isolated mitochondria. *PloS One* **6**, e20709 (2011).

189. A. Kornberg, W. E. Pricer, Jr., Enzymatic phosphorylation of adenosine and 2,6-diaminopurine riboside. *J Biol Chem* **193**, 481-495 (1951).

190. J. N. Gallant *et al.*, EGFR Kinase Domain Duplication (EGFR-KDD) Is a Novel Oncogenic Driver in Lung Cancer That Is Clinically Responsive to Afatinib. *Cancer Discov* **5**, 1155-1163 (2015).

191. A. M. Glazer *et al.*, High-Throughput Reclassification of SCN5A Variants. *Am J Hum Genet* **107**, 111-123 (2020).

192. A. V. Medina-Cucurella *et al.*, User-defined single pot mutagenesis using unamplified oligo pools. *Protein Eng Des Sel* **32**, 41-45 (2019).

193. K. A. Matreyek, J. J. Stephany, D. M. Fowler, A platform for functional assessment of large variant libraries in mammalian cells. *Nucleic Acids Res* **45**, e102 (2017).

194. H. Li, Aligning sequence reads, clone sequences and assembly contigs with BWA-MEM. *arXiv* **1303.3997**, (2013).
195. G. A. Van der Auwera *et al.*, From FastQ data to high confidence variant calls: the Genome Analysis Toolkit best practices pipeline. *Curr Protoc Bioinformatics* **43**, 11 10 11-11 10 33 (2013).
196. J. H. Boyce, B. J. Reisman, B. O. Bachmann, J. A. Porco, Jr., Synthesis and Multiplexed Activity Profiling of Synthetic Acylphloroglucinol Scaffolds. *Angew Chem, Int Ed* **60**, 1263-1272 (2021).

5

CHAPTER 3 – TRANSLATIONAL DEVELOPMENT OF APOPTOLIDIN FAMILY GLYOCOMACROLIDES

3.1 Defining a path from chemical probe to drug

At the outset of my thesis research, I set out to define the mechanism of action of both the apoptolidin and ciromicin family of glycosylated polyketides. The mechanism of action for selective cytotoxicity was divided into two separate aims: Aim 1 – The cellular basis of selective cytotoxicity, Aim 2 – the molecular basis of selective cytotoxicity. Chapter 2 summarizes our efforts on Aim 2 which resulted in identification and validation of the apoptolidin target and binding site, establishing the catalytic portion of ATP synthase as the mechanistic target of apoptolidin family glycomacrolides. With these molecular insights in hand, we can return to Aim 1 which can be recast as "Why are some cancer cells sensitive to ATP synthase inhibition by apoptolidin?" In this chapter I summarize the extensive literature on OXPHOS dependence in cancer with a focus on leukemia, and our studies to validate the role of these mechanism in the selective cytotoxicity of apoptolidin family glycomacrolides.

Based on the definitions of mechanism, chemical probes, and drugs presented in chapter 1, I believe that the studies described in Chapter 2 justify classification of apoptolidin and ammocidin as validated chemical probes for ATP synthase. The key requirement for classification as a chemical probe is that a compound must act through a defined mechanism of action. In chapter 1, I presented three groups of evidence supporting a proposed mechanism of action: 1. Evidence of expected cellular phenotype; 2. Evidence of target engagement *in vivo* and *in vitro*; and 3. Evidence of genetic dependency on the target in the form of resistance mutations. In Chapter 2, I presented all three classes of evidence which provide strong support for our proposed mechanism. While chemical probes must operate via a defined mechanism of action,

for a compound to be considered a drug it must be demonstrated to be safe and effective in humans. Fundamentally, this can only be demonstrated via randomized clinical trial, a rigorous, costly, and time-consuming process. In the United States, a compound must demonstrate safety and efficacy in three phases of clinical trials which can costs upwards of $1 billion from

5   initiation of the project to FDA approval – an endeavor which is outside the scope of dissertation. Prior to the initiation of a clinical trial, a company must submit an investigational new drug (IND) application which also requires substantial investment and approval by the FDA. Here I summarize preliminary data supporting the therapeutic application of ammocidin family ATP synthase inhibitors to address OXPHOS dependent cancers. This data was collected in a

10   non GLP/GMP setting which is often required for an IND, though my hope is that this preliminary data will provide justification for larger institutional or outside investment necessary to bring ammocidin to the clinic.

Specifically, I will address: the scientific rationale for using OXPHOS inhibitors for cancer, rationale and evidence supporting patient selection for preclinical development and

15   clinical trials, pharmacodynamic markers which can be used to monitor target engagement in preclinical and clinical settings, pharmacokinetic characterization of ammocidin in rodents and methods to enable therapeutic drug monitoring via mass-spectrometry, and the development of optimized, novel analogs of ammocidin which can be used to establish intellectual property rights and optimized formulations.

20   **3.2 OXPHOS as a therapeutic target in Leukemia**

Thought cancer metabolism is usually thought of in the context of glycolytic 'Warburg' metabolism, there is increasing evidence that OXPHOS is a functional dependency in many cancers (75, 76). The most prominent recent study describing the therapeutic application of an

OXPHOS inhibitor was Molina et al.'s description of IACS-010759, a synthetic inhibitor of mitochondrial complex I (73). Within the framework of mechanism of action validation, IACS-010759 was demonstrated to inhibit cell proliferation when cells were grown with complex I substrates (pyruvate, malate) but not with complex II substrates (succinate). Furthermore, ectopic expression of S. cerevisiae NDI1 – the yeast ortholog of complex I, conferred resistance to IACS-010759 inhibition and spontaneous resistance mutations in complex I were identified (though they could not be validated by orthogonal genome editing). The binding site of IACS-010759 was identified as located on the ND1 subunit of complex I by photoaffinity labeling (197). In their original report, Molina et al. evaluated IACS-010759 in the context of enolase deficient (ENO1) cell line models which were artificially rendered glycolysis deficient in cell culture and xenograft models and it has since shown efficacy in other tumor models including SWI/SNF mutated lung cancer (198), mantel cell lymphoma (199), and in phase I clinical trials for myeloid malignancies and solid tumors (200). Mubritinib has also been proposed as a complex I inhibitor with therapeutic potential in OXPHOS dependent cancers (151), thought it was originally developed as a ERBB2 kinase inhibitor which casts doubt on its specificity.

Outside of inhibitors which directly target the electron transport chain, there is evidence that inhibition of other mitochondrial targets can indirectly inhibit OXPHOS. The eukaryotic mitochondria are thought to be have originated from specialized bacteria which became endosymbionts. Most mitochondrial genes have migrated to the nucleus though key portions of complexes I, III, IV, and V remain encoded by the mitochondrial genome. Mitochondria also encode genes for the mitochondrial ribosome and tRNAs for mitochondrially synthesized proteins. As the mitochondrial ribosome is bacterial in origin, it is vulnerable to antibiotics which target the bacterial ribosome. One study demonstrated that the antibiotic tigecycline was able to

suppress leukemia ([201](#)), by inhibiting mitochondrial translation resulting in suppression of OXPHOS at complex I and IV, with less suppression at II which is nuclear encoded. More recent studies have shown that targeting mitochondrial translation ([154](#)) or mitochondrial structure ([202](#)) can sensitize AML cells to BCL-2 inhibition.

5   As discussed in the introduction, one of the major advances in leukemia treatment over the past decade was the development of BCL-2 inhibitors leading to the approval of venetoclax. This is noteworthy in the context of translational development of new leukemia therapeutics as the existence of effective treatment for leukemia make it unethical to conduct a placebo-controlled trial, especially in newly diagnosed patients. The most likely path towards a clinical

10   trial for ammocidin would involve comparison of new therapy + standard of care vs standard of care alone, with venetoclax being a likely candidate for the combination therapy. Another path would involve a clinical trial in relapsed/refractory AML with or without combination therapy, though these patient's cancers would have already demonstrated resistance to all other front-line therapies which may make the new therapy less likely to succeed.

15   Though venetoclax was developed as an apoptosis inducing inhibitor of BCL-2, there is increasing evidence that venetoclax and combination therapies that include venetoclax may achieve some of their efficacy by inhibition of OXPHOS. At the time of this writing, it is not clear if these effects are due to on-target inhibition of BCL-2 and an as of yet underappreciated role of BCL-2 in bioenergetics or due to off-target activity against other mitochondrial targets.

20   Research by Craig Jordan's group demonstrated that 'leukemic stem cells' exhibit low levels of reactive oxygen species, high expression of BCL-2, and sensitivity to BCL-2 inhibition which manifested as decreased OXPHOS ([136](#)). From these data, they proposed that BCL-2 inhibitors target OXPHOS in LSCs but not in healthy cells. They later provided evidence that LSCs from

patients treated with venetoclax + 5-azacytadine (Ven/Aza) had evidence of disrupted mitochondrial metabolism and in particular complex II, leading them to propose that Ven/Aza achieves its efficacy via disruption of OXPHOS (153). This model was extended by proposing that Ven/Aza inhibits metabolism by disrupting amino acid metabolism and resistance to

5 Ven/Aza is mediated by upregulation of fatty acid oxidation (152). Alternatively, resistance to Ven/Aza may be mediated by differentiation dependent differences in BCL-2 expression, with more Ven/Aza resistant monocytic AMLs exhibiting upregulated MCL-1 as opposed to BCL-2 (137). Interestingly, in their study combining mitochondrial translation inhibitors with venetoclax, Sharon et al. noted that venetoclax appeared to inhibit OXPHOS in cell lines which

10 are resistant to the pro-apoptotic effects of venetoclax (154). Additionally, venetoclax appeared to inhibit the activity of purified bovine complex I when it was partially purified, but not after full purification (two distinct chromatography steps), suggesting that the factor which conferred venetoclax sensitivity to complex I could be lost (154). It is tempting to speculate whether this missing factor is BCL-2 or another, as of yet uncharacterized venetoclax target.

15   Beyond the direct effects of venetoclax on OXPHOS, there is also growing evidence that OXPHOS inhibitors exhibit synergy with venetoclax and/or are able to overcome venetoclax resistance. Loss of OXPHOS complexes appear to be a recurring 'hit' in genetic screens for venetoclax combination therapies including in AML(154, 158, 203) and CLL(157, 204), though interestingly papers often do not focus on validating the top hit (OXPHOS) and choose to focus

20 the second or third hits, perhaps due to a lack of safe and effective OXPHOS inhibitors.

3.3 OXPHOS in cancer beyond ATP

      OXPHOS targeted therapies are usually thought to achieve their efficacy by targeting bioenergetics, thought there is increasing evidence that the non-ATP generating roles of

141

OXPHOS may be just as relevant. Flux through the TCA cycle and electron transport chain is essential for generating precursors for amino acid and DNA synthesis. Flux through the electron transport chain is required to drive dihydroorate dehydrogenase (DHODH) which catalyzes the first step of *de novo* pyrimidine biosynthesis. Multiple studies have demonstrated that DHODH inhibition may play a role in cancers which exhibit OXPHOS dependence (71, 205-207). In one particularly elegant study, Bajzikova et al. expressed an alternative oxidase (AOX), a bacterial ortholog of complex III/IV which was able to restore DHODH activity in cells which lacked mitochondrial genomes and restored tumorigenic potential to the cells. Interestingly, to rule out the bioenergetic contribution of the ETC, they also evaluated cells which in which the β subunit was knocked out and observed that DHODH activity and tumorigenic potential remained (207). This is in contrast to the evidence presented in Chapter 2 which suggested that ATP synthase activity is required in ammocidin sensitive cell lines. There is also evidence that the OXPHOS plays an essential role in supplying aspartate to enable cell proliferation (208), which can also be leveraged as a pharmacodynamic biomarker for OXPHOS inhibitors (209).

Thus far we have largely addressed OXPHOS inhibitors in cancer as a single class, but in reality OXPHOS involves five distinct complexes with multiple possible targets. The question of which OXPHOS complex is best to target in which context is a worthy one but cannot be fully addressed here. Briefly, complex I and II are attractive targets in that either complex alone can provide electrons and pump protons which potentially opens a therapeutic index if cancer cells are more dependent on one complex than the other. However, this also provides an opportunity for resistance as cells can sustain ETC with complex I or II alone. One recent study examined the patterns of spontaneous mitochondrial mutations in various tumors and looked for recurrent patterns of loss of function mutation in the mitochondrially encoded complexes I, III, IV, and V

(210). Surprisingly they observed that cancers had a high frequency of truncating mutations in complex I, a moderate frequency of truncating mutations in complex III and IV, and a lower-than-expected frequency of truncating mutations in complex V (210). These data suggest that loss of complex I may impart a fitness benefit for some cancers, while loss of complex V is nearly universally detrimental (210).

3.4 IDH Mutations and Oxidative Phosphorylation

Isocitrate dehydrogenases 1 and 2 (IDH1, IDH2) are frequently mutated in acute myeloid leukemia as well as glioma (IDH1). Isocitrate dehydrogenase catalyzes the conversion of isocitrate to 2-oxoglutarate in the TCA cycle. Most of the IDH activity involved in the TCA cycle is driven by IDH3, but IDH2 is also present in the mitochondria while IDH1 is present in the cytosol. In AML and glioma, IDH1/2 mutations impart a gain of function which shunts isocitrate to the 'onco-metabolite' 2-hydroxyglutarate (2HG), which acts as competitive inhibitor of alpha-ketoglutarate dependent enzymes including HIF1α and TET2. TET2 catalyzes the first step in demethylation of DNA, and direct loss of TET2 or functional loss of TET2 via mIDH leads to hypermethylation and a block in differentiation which contributes to leukemogenesis. Based on the effects of apoptolidin on HIF1α signaling (140), we hypothesized that mIDH AMLs may be more or less sensitive to OXPHOS inhibition than WT cells.

TF1 WT or TF1 cells expressing IDH2-R140Q introduced by CRISPR/Cas9 (both from ATCC) cells were treated with apoptolidin A, apoptolidin A azide, or oligomycin for 16 hrs and assayed using multiplexed activity profiling (see Chapter 6), using pS6 [Ser235/236] as an readout of AMPK activation. Surprisingly, the IDH2-R140Q expressing cells were ~10 fold more sensitive to OXPHOS inhibition by apoptolidin A or oligomycin than their wildtype controls (Figure 3.1). This experiment was carried out early on in our studies on the apoptolidins

143

before we had accessed ammocidin and was not followed up once we began our studies, though

it does provide a starting point for further studies on OXPHOS inhibitors in mIDH AML. Since

this data was collected, an independent group also noted the potential for synergy between

OXPHOS and IDH inhibitors (209). IDH mutant leukemias were noted to exhibit high levels of

5   OXPHOS, which appears to be driven by 2HG mediated inhibition of CEBPα which normally

represses fatty acid oxidation (209). High levels of 2HG were associated with increased fatty

acid oxidation and OXPHOS (209). Interestingly, IDH inhibitors lowered 2HG levels, but cells

retained high levels of OXPHOS perhaps via downregulation of AKT. The same found that the

OXPHOS inhibition with IACS-010759 synergized with IDH inhibitors in PDX models of

10   mIDH leukemia (209).
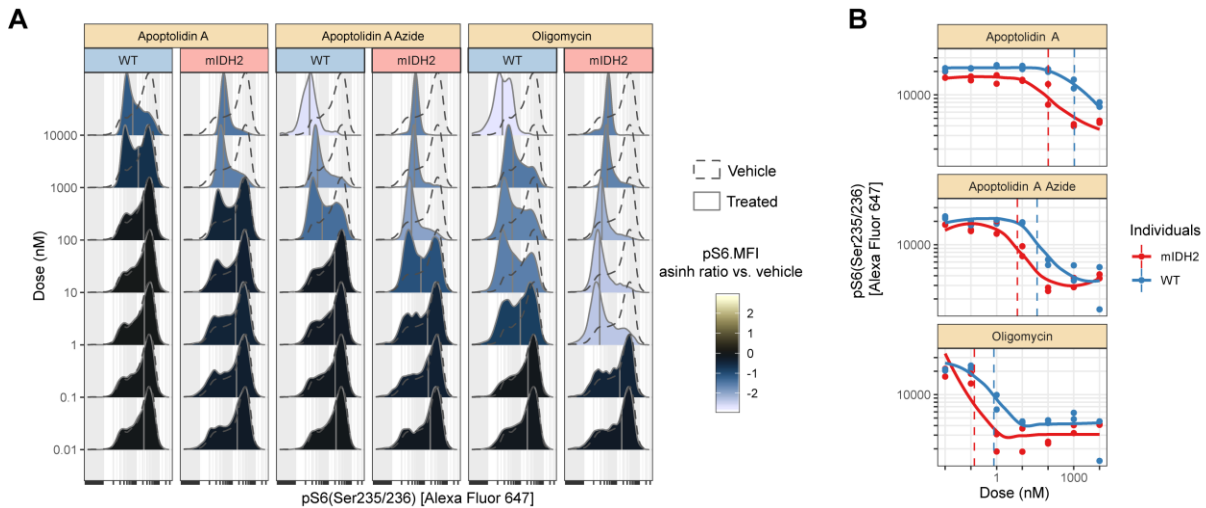
Figure 3.1. IDH2-R140Q sensitizes AML to OXPHOS inhibition

3.5 Mass cytometry reveals Cell Subset Targeting by Apoptolidin in Human Primary AML samples

        One of the observations from our multiplexed activity metabolomics paper was that

15   glycosylated macrolides produced by Nocardiopsis FU-40 appeared to target distinct subsets of

cells in human primary samples as evaluated by mass cytometry (CyTOF). Early in the project,

we evaluated whether this phenomenon was generalizable and whether it was dose dependent.

AML047 bone marrow cells were treated for 48 hrs with various doses of apoptolidin and

evaluated by Pd barcoded mass cytometry using 24 surface markers and 10 intracellular markers.

5   The most notable effect of apoptolidin was an apparent depletion of more primitive myeloid cells

with a shift towards a more monocytic phenotype (Figure 3.2). In particular, increased

expression of CD25 was noted alongside slightly increased expression of CD184 and CD123 and

decreased expression of CD13. The significance of these shifts is not entirely clear. One

possibility is that apoptolidin treatment alters the immunophenotype of AML blasts to account

10 for the observed shifts. Another possibility is that apoptolidin is toxic to primitive cells and

spares cells with high expression of CD25. Further *ex vivo* profiling using patient samples would

be worthwhile to ascertain which subsets of patient cells are most sensitive to OXPHOS

inhibition.
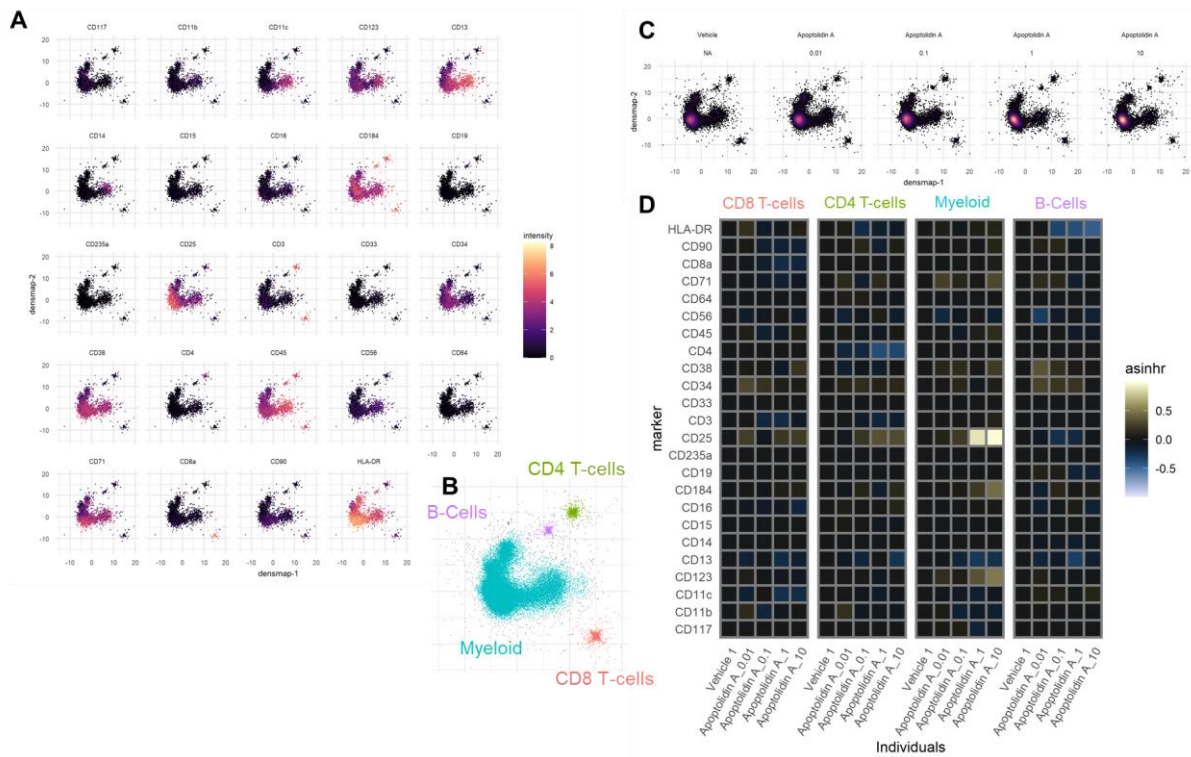
Figure 3.2. Apoptolidin selects for monocytic cells in primary AML patient cells

After a 48hr treatment with apoptolidin at the indicated dose (μM), a shift towards a more mature phenotype was noted. **A,** shows marker expression across cell subsets embedded using densmap; **B,** Shows clusters identified using HDBSCAN and labeled using expert knowledge; **C,** cell embeddings for each untreated cells and cells treated with apoptolidin at 4 different doses; **D,** shift in immunophenotype for each cluster after treatment with apoptolidin A, the most notable changes are increases in CD25, CD184, and CD123, and decreased CD13.

3.6 Galactose growth media sensitizes cells to OXPHOS inhibition by apoptolidin family glycomacrolides

One of the challenges of assaying the apoptolidin family compounds is the apparently

5   high variability in sensitivity from assay to assay. In our hands, MV-4-11 and K562s leukemia

cells lines were consistently sensitive to OXPHOS inhibition which led to their selection as the

primary model system for our target ID studies. Prior to our studies, H292 lung cancer cell lines

were the most widely used cell line, thought they were not always sensitive to apoptolidin. In

146

Sean Deguire's studies, he found apoptolidin sensitivity was dependent on cell density, with

higher cell densities (10K+ per well) being associated with greater sensitivity to apoptolidin.

Lars Plate suggested to us that replacing glucose with galactose in the growth medium may

sensitize otherwise insensitive cells to OXPHOS inhibition, as cells must metabolize galactose

via the Leloir pathway which provides less ATP from glycolysis then glucose (211-213). Indeed,

replacing 5 mM glucose with 10 mM galactose increased the maximal effect of both apoptolidin

and oligomycin as assayed using a 48 hr MTT assay (Figure 3.3).
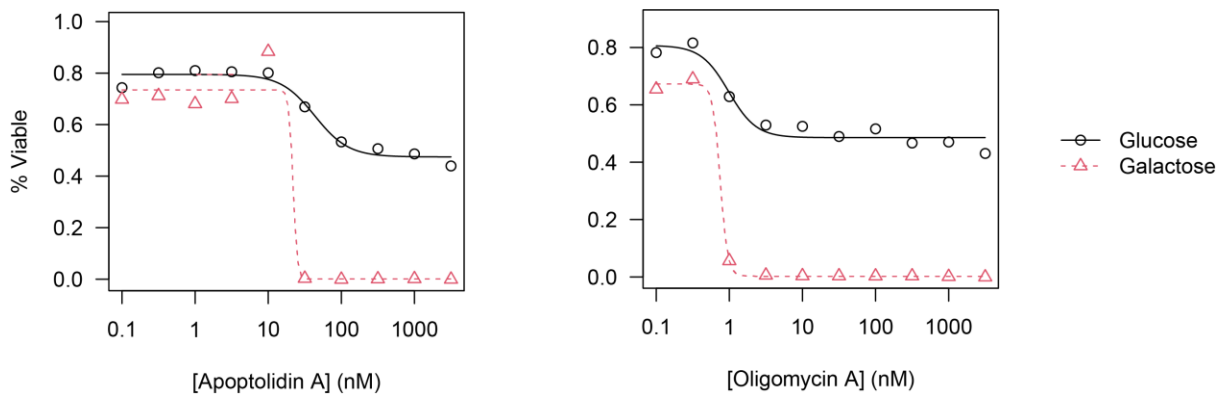
Figure 3.3. Galactose growth media sensitizes cells to OXPHOS inhibition

The use of galactose as a non-fermentable carbon source to sensitize cells to OXPHOS

inhibition is a valuable tool for the assaying apoptolidin family glycomacrolides. It provides a

method to sensitize cells to apoptolidin/ammocidin which are otherwise insensitive to them and

increases the robustness of assays on moderately sensitive cell lines. Additionally, it prevents

cells from surviving on glycolysis alone which is useful when studying glycomacrolide

resistance.

3.7 Analysis of Spontaneous Resistance Mutations in H292 cells treated with glycomacrolides

147

One of the goals of this dissertation was to obtain genetic validation of the apoptolidin target by identifying one or more mutations which confer resistance to the target. Various approaches were considered to achieve this goal before attempting the deep mutational scanning approach outlined in Chapter 2. The simplest approach for identifying resistant mutants is to

5   simply expose sensitive cells to increasing doses of the drug to select for naturally occurring resistance mutations that may arise. This approach was adopted by both Lin et al.(91) and Molina et al. (73). One concern is that cells may simply adapt to survive on glycolysis alone, and so this screen was carried out using glucose free RPMI supplemented with Galactose. H292 cells were grown till confluent on 10cm dishes and then treated with 3 nM ammocidin A or

10   apoptolidin A (close to the EC$_{50}$). This resulted in the death of the majority the cells, though some survived. Cells were passaged in 3 nM apoptolidin/ammocidin media for 3 weeks, followed by 3 weeks with 10 nM apoptolidin/ammocidin media, followed by 30 nM apoptolidin/ammocidin for 3 weeks. Resistant clones were isolated using glass cloning rings and expanded in galactose containing media without any drugs. Each clone was assayed for

15   sensitivity to apoptolidin, ammocidin, and oligomycin using the sulforhodamine B (SRB) assay. Colonies 05, 08, 10, and 13 were selected for whole exome sequencing (WES) alongside the parental line.
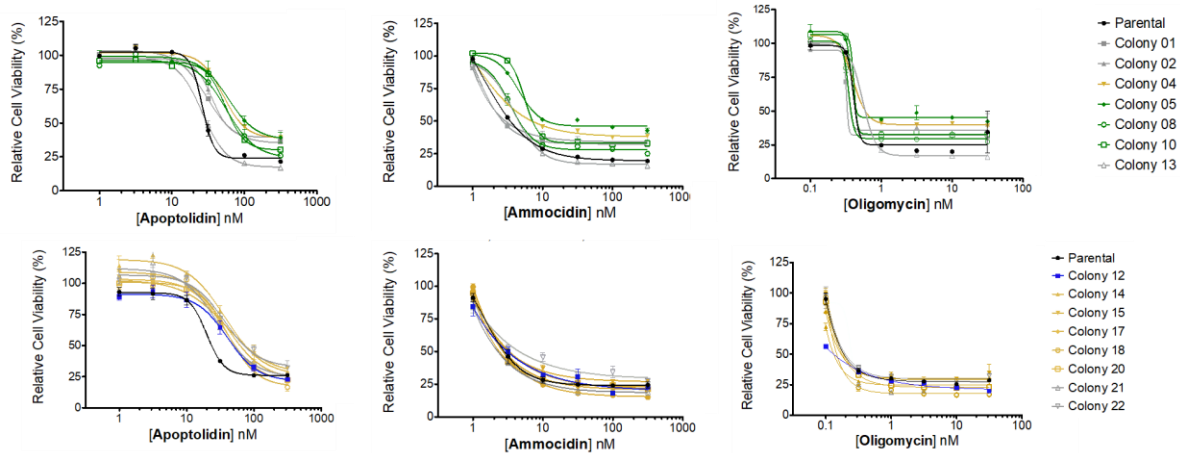
Figure 3.4. Sensitivity analysis of Glycomacrolide resistant H292 clones

WES was carried out at the VANTAGE sequencing core using the Twist biosciences library preparation kit and sequenced using the Illumina Novaseq 6000 (PE150) platform. VANTAGE also provided analysis services in the form of alignment and variant calling. The results of the WES are summarized in Table 3.1. New variants were defined as those not present in the parental line, and non-synonymous variants in coding regions with a variant allele frequency > 0.4 were selected for further analysis. No mutations were noted in any genes coding for ATP synthase. One gene coding for a protein identified in our proteomics experiment was identified as mutated in 2 colonies (*FDFT1*). Focusing on mitochondrial proteins, all colonies 05, 08, and 10 had missense mutations in adenylate kinase 2 (*AK2)* but at sub heterozygous variant

allele frequencies (~0.2).

Table 3.1. Summary of Whole Exome Sequencing Results on Apoptolidin Resistant H292 Colonies

Cell Line	#Variants	#New Variants	#Non-synonymous	#VAF>0.4	#Genes
H292-Parental	33090				
H292-ApoR05	33130	606	226	85	63
H292-ApoR08	33093	629	234	71	52
H292-ApoR10	32885	799	275	118	86
H292-ApoR13	33156	721	281	105	78

The most notable mutation was *ATAD3A* which had acquired multiple frameshift and missense variants in Exon 8 in all four resistant colonies at a VAF of ~1.0, consistent with biallelic loss. *ATAD3A* codes for ATPase family AAA domain-containing protein 3A (ATAD3A) and is involved in various mitochondrial processes and is involved in cholesterol channeling between the inner and outer mitochondrial membrane ([214](#)). Additionally, ATAD3A is thought to play a key role in maintaining OXPHOS in hematopoietic progenitors ([215](#)) and has been implicated in chemotherapy resistance ([216](#)), though this has been more often observed as overexpression rather than loss of ATAD3A. The role of ATAD3A in the transport or mechanism of action of apoptolidin family glycomacrolides is unclear. As mutations in ATP synthase would be necessary to demonstrate genetic dependence of the target, validation of the ATAD3A finding was not prioritized for follow-up, though it is my hope that others will investigate this result by independent introduction of the Exon 8 truncation and/or genetic complementation of ATAD3A in the resistant H292s.

3.8 Biomarkers of apoptolidin family glycomacrolide on-target activity

The on-target (ATP synthase) activity of apoptolidin A and ammocidin A was validated by multiple orthogonal approaches to exclude any additional targets which should be sufficient to conclude that any observed effects of apoptolidin or ammocidin *in vivo* are due to inhibition of ATP synthase. Nevertheless, it could be valuable to identify and validate biomarkers for target engagement that can be used in preclinical models and clinical trials. ATP and ADP sensors or assays are a logical choice, however, the potentially short half-life of ammocidin *in vivo* and the transient nature of metabolism make direct measurement of ATP a poor candidate for a robust biomarker. The on-target activity of IACS-010759 was validated by assessment of serum aspartate, gene expression, phospho-histone H3 and CCasp3 ([217](#)) and these biomarkers may be suitable for ammocidin as well. Serrill et al. demonstrated that apoptolidins A and C activate AMPK, a mitochondrial sensor of ADP/ATP, which he assayed by multiple phosphoproteins including the S6 kinase ([140](#)), which phosphorylates S6 at Ser235/236 (pS6). pS6 is one of the validated biomarkers on our multiplexed activity profiling (Chapter 6) panel and the D57.2.2E clone is an excellent antibody with cross reactivity across both mouse and human.

To determine whether pS6 would be a suitable biomarker for on-target ammocidin activity, MV-4-11 cells were treated with varying concentrations of ammocidin or apoptolidin and assayed for cytotoxicity at 48 hrs (MTT assay Figure 3.5A) and pS6 at 16 hrs (using MAP Figure 3.5B). Reponses were comparable between the two experiments with the exception of apoptolidin which exhibited a response to pS6 at a lower dose than cytotoxicity was observed, likely due to the longer timeframe of the cytotoxicity assessment leading to isomerization of apoptolidin but not ammocidin. A reverse time-course experiment with ammocidin and IACS-010759 was consistent with pS6 inhibition though it is notable that IACS-010759 appeared to suppress pS6 within 30 min, whereas the ammocidin response only began after 2 hrs and was

maximized at 8 hrs (Figure 3.5C). This difference is notable and may reflect a more nuanced

mechanism involving transport or uncompetitive inhibition in which partial inhibition of ATP

synthase would result in increased ADP and a positive feedback loop which would cause

increased ATP synthase inhibition over time. A schematic showing the pathway from

5 apoptolidin A inhibition of ATP synthase to pS6 is shown in Figure 3.5D.
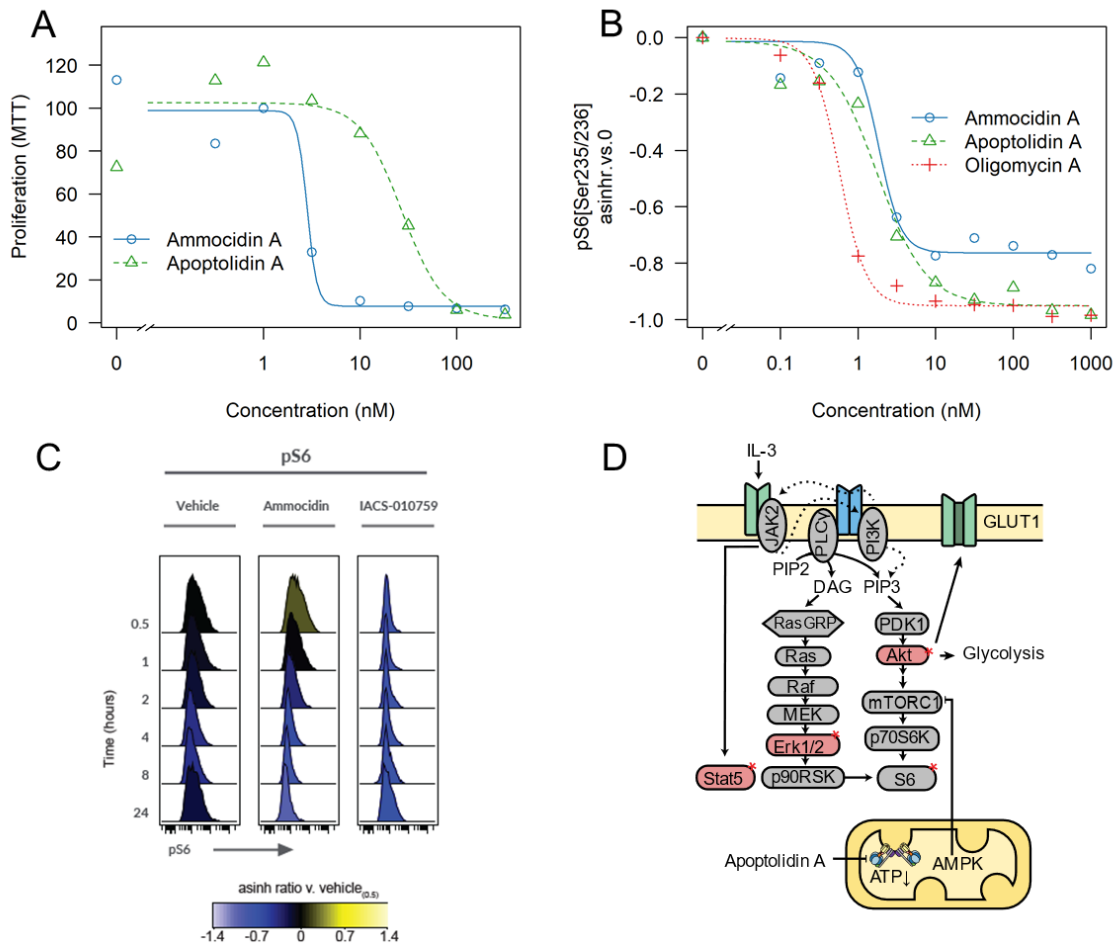
Figure 3.5: Validation of pS6 as a biomarker for ATP Synthase Inhibition.

A, Cytotoxicity of compounds in MV-4-11 at 48 hrs using MTT assay; **B,** pS6 suppression in MV-4-11 at 16 hrs using flow cytometry against pS6; **C,** Time course of ammocidin and IACS-010759 pS6 responses in MV-4-11 at 100 nM; **D,** Pathways leading to phosphorylation of pS6 at Ser235/236 and modulation by AMPK sensing of ATP/ADP ratio.

153

3.9 Novel analogs of apoptolidin and ammocidin

The previously described analogs of apoptolidin and ammocidin are detailed in Chapter 1. Here I describe novel analogs of both compound classes obtained via fermentation of the producing strains, genetically modified strains, and via semi-synthesis.

3.9.1 Apoptolidin I

In the course of isolating apoptolidin A from the culture filtrates of wildtype *Nocardiopsis Sp.* FU-40 I isolated a novel apoptolidin, denoted apoptolidin I. Apoptolidin I[5] was slightly less hydrophobic than apoptolidin A with a retention time of ~8 min vs 9-10 min for apoptolidin A. The mass of the Na+ adduct was determined to have an m/z = 1137.6185, corresponding to a molecular formula of $C_{57}H_{94}O_{21}$, consistent with the loss of a methyl group relative to apoptolidin A. Comparing the HSQC spectra of apoptolidin I to apoptolidin A (Spectrum 3.1), the only protons which had shifted were those on the terminal L-oleandrose and the 3''' O-Me was completely missing, suggesting that L-olivose (desmethyl-L-oleandrose) had been added. The structure of apoptolidin I was assigned as depicted in Figure 3.6. Surprisingly, apoptolidin I was found to be ~6 fold less active (28 nM vs 5.3 nM) in MV-4-11 cells.
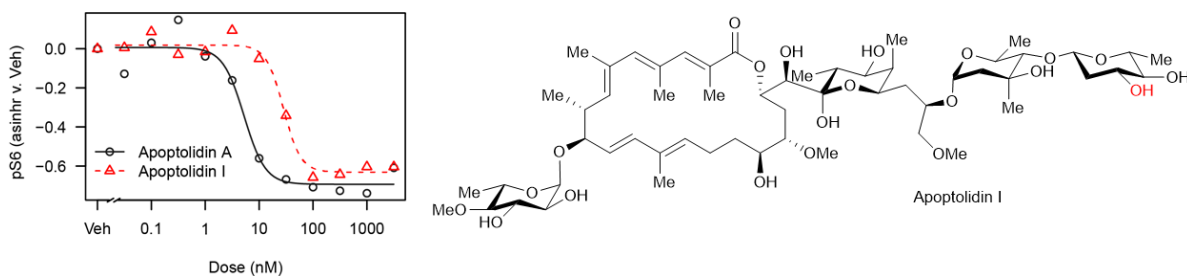
Figure 3.6. Structure and bioactivity assessment of apoptolidin I

[5] Some of the original data from Jan 2019 for apoptolidin I (prior to its elucidation) is labeled as apoptolidin X.
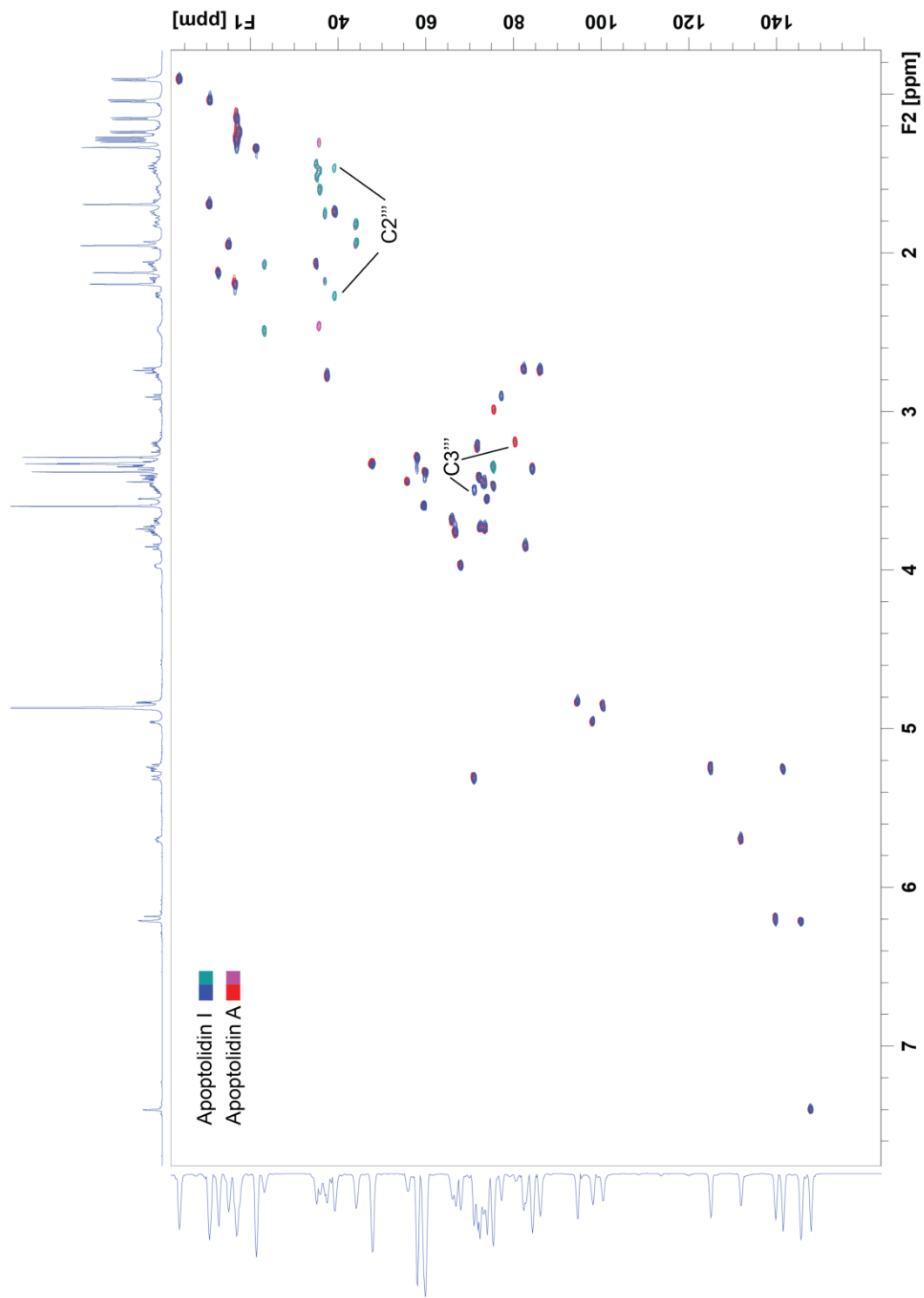
Spectrum 3.1. HSQC spectrum of Apoptolidin I in MeOD at 600 mHz

3.9.2 <u>Apoptolidin J</u>

Our group had previously identified and validated the biosynthetic gene cluster for apoptolidin A in *Nocardiopsis sp. FU-40 (*105*)* and generated knockouts of multiple biosynthetic genes including the cytochrome P450 monooxygenase ApoP. In his thesis work, David Earl isolated a shunt product from *ΔApoP* which lacked a hydroxyl group at C16, suggesting that ApoP was responsible for oxidizing that position (218). To follow-up on Earl's efforts, I attempted to reisolate ApoP in sufficient quantities for bioactivity characterization.

The ethyl acetate extract from a 10L fermentation of N. FU-40 ΔApoP yielded many apoptolidins, though the product missing only a single hydroxyl was not prominent in the crude extract (Figure 3.7). Apoptolidins C and E were isolated in a yield of ~30 mg/10L. Peaks corresponding to apoptolidin J were identified (M+NH$_4^+$ = *m/z* 1130) and prioritized for isolation via repeated preparative HPLC to yield apoptolidin J (Figure 3.8). Unlike Earl's 16-deoxyapoptolidin, the apoptolidin J isolated was found to lack the C20 hydroxyl group. Comparison of the chemical shifts of apoptolidin J to Earl's dexoyapoptolidin reveals that the two compounds are distinct, and both appear be assigned correctly. Of note, a second peak (RT = ~14 min) with the same *m/z* was observed but could not be isolated in sufficient yield for characterization; it is possible that this second deoxyapoptolidin peak is Earl's 16-deoxy product. Though I was unsuccessful at reproducing Earl's *ΔApoP* product, this study provides a clue to as to the role of *ApoP*. The apoptolidin gene cluster also contains a Riskee dioxygenase (*ApoD1/D2/D3*). We hypothesize that *ApoP* and *ApoD1/D2/D3* are responsible for installing the C16 and C20 hydroxyl groups on apoptolidin A, but it is unclear which one adds which. This study demonstrates that the *ΔApoP* strain produces Apoptolidins C and E, which lack both

hydroxyl groups, in large quantities. These shunt products should be useful for *in vitro* turnover

assays with purified ApoP and ApoD1/D2/D3 for determining the role of these two enzymes.
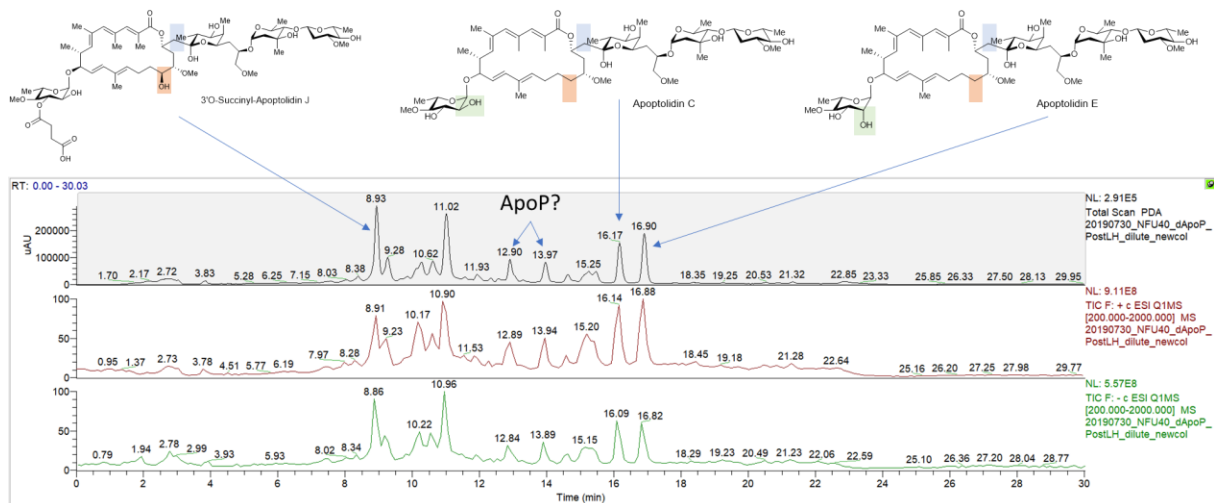
Figure 3.7. Apoptolidins identified in EtOAc extract of *Nocardiopsis sp.* FU-40 *ΔApoP*

16-deoxyapoptolidin (Earl 2018)
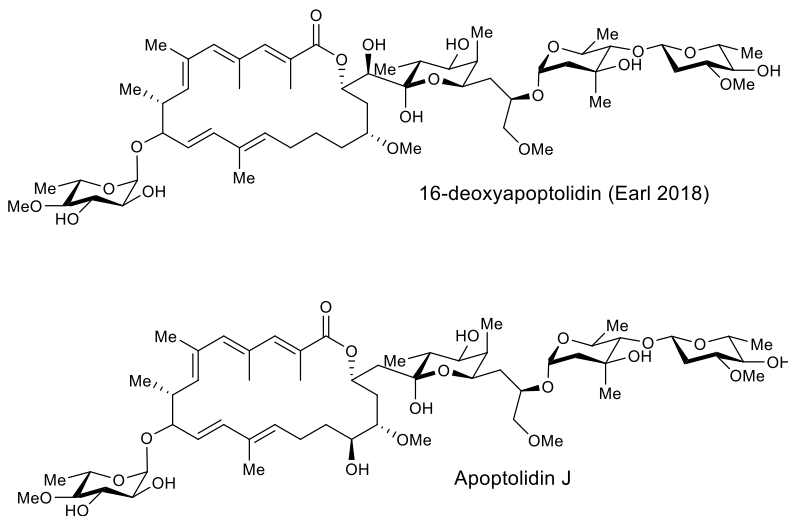
Apoptolidin J

Figure 3.8. Proposed structures of deoxyapopotlidins.

5

Spectrum 3.2. HSQC spectrum of Apoptolidin J in MeOD at 600 mHz

Apoptolidin J
Apoptolidin A

20190904_NFU40dApoP_P27_P13_P27 3 1 "C:\Users\benja\OneDrive\Vanderbilt\Bachmann Lab\Notebook\2019\09_Sept

3.9.3 Ammocidin C9 acyl analogs

The bioassay and structural studies presented in Chapter 2 demonstrate that the C9 6-deoxyglucose of ammocidin A can tolerate modification without significantly impacting its activity. Interestingly acylation at C9 on ammocidin favor addition at C3' rather than C2' as was seen with apoptolidin. We speculate this may be due the steric effect of the C4' OMe on apoptolidin which favors addition at C2'. Our pharmacokinetic studies on ammocidin A suggest it has a relatively short apparent half-life, which may necessitate frequent dosing. We sought to develop analogs based of addition to the C9 sugar which exhibit longer half-lives which may be better candidates for therapeutic development. However, extremely long half-lives may not be desirable as toxicity from the prolonged metabolic insult may increase toxicity.

Four new ammocidin A analogs were synthesized (with the help of rotation student Scott Brenner) using the reaction conditions described in Chapter 2, shown in Figure 3.9. Ammocidin A BDP was synthesized as a potential imaging probe for live cell imaging. Ammocidin A 4-fluorvaleric acid (4FVA) and trifluoropentanoic acid (TFPA) were designed to be more hydrophobic than ammocidin A which would favor albumin binding and would extend its biological half-life. Ammocidin A Bis FPA was a side-product from the reaction which generated ammocidin A TFPA. Pharmacokinetic assessments of these analogs are in progress and will be reported before this thesis is finalized.

159
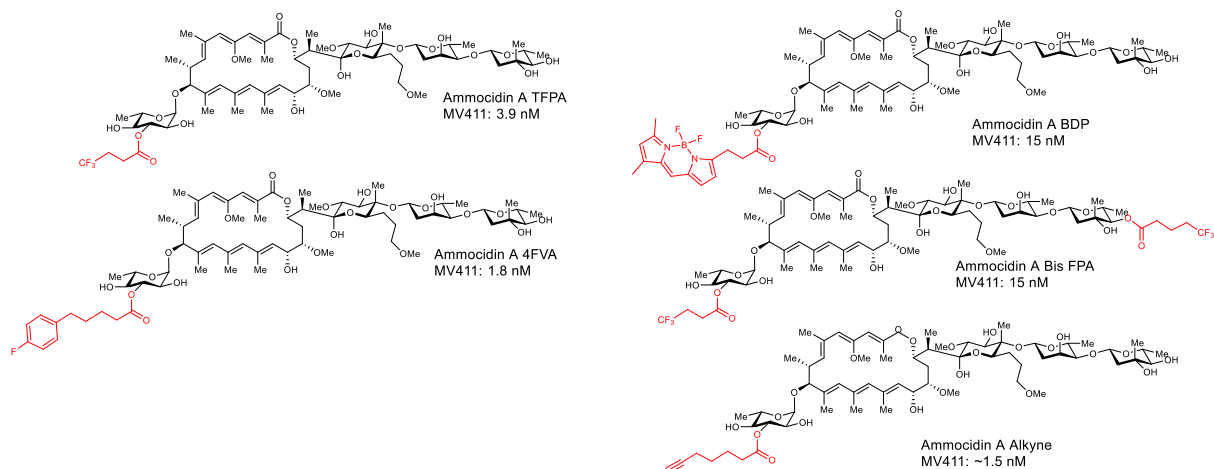
Figure 3.9. Semi-synthetic ammocidin analogs

3.10 Pharmacokinetic assays for therapeutic monitoring of ammocidin A

A thorough understanding of a potential drug's pharmacokinetic properties is essential for guiding dosing and PK/PD modeling. The current state of the art assay for therapeutic drug monitoring is electrospray mass spectrometery (ESI-MS). Typically, serum or plasma metabolites are separated from serum or plasma proteins by protein precipitation or extraction (liquid/liquid or solid phase SPE) and analyzed on a mass-spectrometer. With appropriate controls and internal standards, the observed response can be correlated to the concentration of the metabolite in the sample. For increased specificity and improved signal-to-noise, metabolites are often monitored as fragments of a particular parent ion, called selective reaction monitoring (SRM or MRM or PRM). Even if there are unrelated serum components which have the same m/z of the metabolite of interest they are unlikely to fragment in the same manner.

At the outset of our *in vivo* experiments, we set-out to develop an MS based pharmacokinetic assay. One of the challenges of developing a sufficiently sensitive assay is that ammocidin is quite potent (~1-10 nM), which necessitates a very low lower limit of quantitation

160

(LLOQ), ideally below 1 nM (~1 ng/mL). Additionally, ammocidin is relatively large (~1100 Da) for ESI-MS and neutral which results in less-than-optimal ionization. Various extraction and detection schemes were attempted, and the results are summarized here. Protein precipitation is one of the most robust sample preparation methods which involves merely adding 3 volumes of

5   acetonitrile to the sample, vortexing, and removing the insoluble proteins by high-speed centrifugation. Unfortunately, it also dilutes the sample by a factor of 3 and results in a sample which contains many serum/plasma components which could reduce sensitivity via matrix effects. Liquid/liquid extraction using 2 volumes of ethyl acetate was selected as the sample preparation method, based on its utility in extracting ammocidin/apoptolidin from the culture

10   filtrate. In order to account for sample losses during liquid handling and injection to injection variability at the mass-spectrometer an internal standard was added to each sample prior to extraction. The ideal internal standard would be isotopically labeled ammocidin, though this was not readily available. Instead apoptolidin was selected as an internal standard for ammocidin quantification due to its similar chromatographic properties – with apoptolidin A used in our

15   early experiments and apoptolidin C used in later experiments due to its improved stability. After addition of the internal standard and liquid/liquid extraction, the samples were centrifuged and the organic layer transferred to a fresh tube, dried using a Genevac HT-6, and resuspended in methanol (~50 μL).

       Chromatography was carried out on 50 x 2.1 mm C18 columns using various buffer

20   systems at 0.25-0.30 mL/min. Acidic buffers including formic acid and acetic acid were found to favor formation of single precursor ions in ESI+ mode. For quantification of ammocidin A, a 3 minute isocratic method using 62/38 water/acetonitrile with 0.1% formic acid was found to provide good separation. For C9 acylated analogs (see next section), gradient methods were

necessary, ramping for 62/38 water/acetonitrile to 20/80 water acetonitrile. Later experiments

used 0.2% acetic acid as a buffer for compatibility with our ammonium acetate buffered

chromatography system. Ammocidin A and analogs were observed to form positive ions with

loss or gain of water (-17, +19) and negative ions with loss of a proton. Fragmentation was

5   optimized on both our Thermo TSQ Quantum Access Max system and the Q Exactive Orbitrap

system at the mass spectrometry core (MSRC). The most prominent positive fragment

consistently observed was 209.1172 (209.12 on the TSQ), which correspond to $C_{12}H_{17}O_3$. A

proposed fragmentation scheme is shown in Figure 3.10. Supporting this assignment,

apoptolidins A and C form a fragment of 193.1224 which matches the C1-C8 fragment of

10   apoptolidin. Of note, the apoptolidin tends to ionize by gaining water (+18), while ammocidin

strongly favors loss of water. This may reflect the distinct stereochemistry of ammocidin A and

apoptolidin A at the C16 hydroxyl which is theorized for ammocidin A though not confirmed.
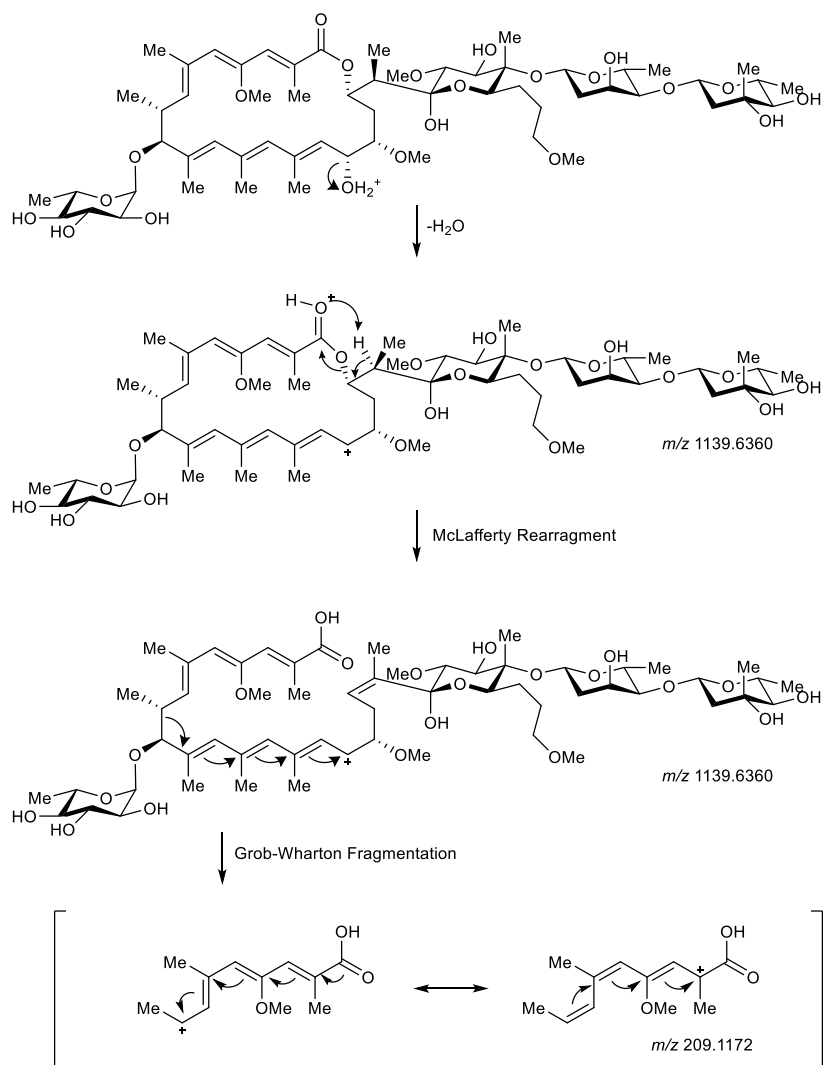
Figure 3.10. Proposed Fragmentation of Ammocidin A in ESI+ MS/MS

3.11 Conclusions and Future Directions

The findings described in Chapter 2 are the product of years of work by our group and others to probe the SAR of the apoptolidin family of glycomacrolides and understand their mechanism of action. The details of the molecular specificity of these remarkably selective glycomacrolides have now come into light. One of the surprising findings of this dissertation was that ammocidin A exhibits favorable bioavailability (including oral bioavailability) and tolerability in mice and was effective at suppressing leukemia growth *in vivo*. Though the molecular details of the mechanism are noteworthy, apoptolidin was thought to be an ATP synthase inhibitor at the outset of these studies which raises the question, "why weren't apoptolidin family glycomacrolides advanced into mouse models?"

At the time when the early mechanistic studies on apoptolidin were taking place, the prevailing view was that cancer was a disorder associated with glycolysis, not OXPHOS. Furthermore, ATP synthase is thought to be an 'essential' protein in all cells, and so one might expect an ATP synthase inhibitor to exhibit excessive toxicity. Indeed, Ajinomoto Co. Inc. had access to the producing strain for ammocidin for decades but did not develop it further as they thought the target was also present in healthy cells (110). Fortunately, my studies were taking place during a renaissance of cancer metabolism with increasing recognition of the importance of OXPHOS in leukemia and other cancers, and the therapeutic potential of OXPHOS inhibitors. It is my hope that the preliminary data and references presented here will present a convincing case for continued development of the apoptolidin family of glycomacrolides to address OXPHOS dependent cancers.

3.12 References

71.   I. Martinez-Reyes *et al.*, Mitochondrial ubiquinol oxidation is necessary for tumour growth. *Nature* **585**, 288-292 (2020).

73.   J. R. Molina *et al.*, An inhibitor of oxidative phosphorylation exploits cancer vulnerability. *Nat Med* **24**, 1036-1046 (2018).

75.   V. Sica, J. M. Bravo-San Pedro, G. Stoll, G. Kroemer, Oxidative phosphorylation as a potential therapeutic target for cancer therapy. *Int J Cancer* **146**, 10-17 (2020).

76.   Y. Xu, D. Xue, A. Bankhead, 3rd, N. Neamati, Why All the Fuss about Oxidative Phosphorylation (OXPHOS)? *J Med Chem* **63**, 14276-14307 (2020).

91.   A. Lin *et al.*, Off-target toxicity is a common mechanism of action of cancer drugs undergoing clinical trials. *Sci Transl Med* **11**, eaaw8412 (2019).

105.   Y. Du *et al.*, Biosynthesis of the Apoptolidins in Nocardiopsis sp. FU 40. *Tetrahedron* **67**, 6568-6575 (2011).

110.   R. Murakami, T. Kajiura, B. J. Reisman, B. O. Bachmann, Eds. (2021).

136.   E. D. Lagadinou *et al.*, BCL-2 inhibition targets oxidative phosphorylation and selectively eradicates quiescent human leukemia stem cells. *Cell Stem Cell* **12**, 329-341 (2013).

137.   S. Pei *et al.*, Monocytic Subclones Confer Resistance to Venetoclax-Based Therapy in Patients with Acute Myeloid Leukemia. *Cancer Discov* **10**, 536-551 (2020).

140.   J. D. Serrill *et al.*, Apoptolidins A and C activate AMPK in metabolically sensitive cell types and are mechanistically distinct from oligomycin A. *Biochem Pharmacol* **93**, 251-265 (2015).

151.   I. Baccelli *et al.*, Mubritinib Targets the Electron Transport Chain Complex I and Reveals the Landscape of OXPHOS Dependency in Acute Myeloid Leukemia. *Cancer Cell* **36**, 84-99 e88 (2019).

152.   C. L. Jones *et al.*, Inhibition of Amino Acid Metabolism Selectively Targets Human Leukemia Stem Cells. *Cancer Cell* **34**, 724-740 e724 (2018).

153.   D. A. Pollyea *et al.*, Venetoclax with azacitidine disrupts energy metabolism and targets leukemia stem cells in patients with acute myeloid leukemia. *Nat Med* **24**, 1859-1866 (2018).

154.   D. Sharon *et al.*, Inhibition of mitochondrial translation overcomes venetoclax resistance in AML through activation of the integrated stress response. *Sci Transl Med* **11**, eaax2863 (2019).

157.   R. Guieze *et al.*, Mitochondrial Reprogramming Underlies Resistance to BCL-2 Inhibition in Lymphoid Malignancies. *Cancer Cell* **36**, 369-384 e313 (2019).

158.   M. R. Savona, J. C. Rathmell, Mitochondrial Homeostasis in AML and Gasping for Response in Resistance to BCL2 Blockade. *Cancer Discov* **9**, 831-833 (2019).

197.   A. Tsuji, T. Akao, T. Masuya, M. Murai, H. Miyoshi, IACS-010759, a potent inhibitor of glycolysis-deficient hypoxic tumor cells, inhibits mitochondrial respiratory complex I through a unique mechanism. *J Biol Chem* **295**, 7481-7491 (2020).

198.   Y. Lissanu Deribe *et al.*, Mutations in the SWI/SNF complex induce a targetable dependence on oxidative phosphorylation in lung cancer. *Nat Med* **24**, 1047-1057 (2018).

199.   L. Zhang *et al.*, Metabolic reprogramming toward oxidative phosphorylation identifies a therapeutic target for mantle cell lymphoma. *Sci Transl Med* **11**, eaau1167 (2019).

200.   T. A. Yap *et al.* (American Society of Clinical Oncology, 2019).

201. M. Skrtic *et al.*, Inhibition of mitochondrial translation as a therapeutic strategy for human acute myeloid leukemia. *Cancer Cell* **20**, 674-688 (2011).
202. X. Chen *et al.*, Targeting Mitochondrial Structure Sensitizes Acute Myeloid Leukemia to Venetoclax Treatment. *Cancer Discov* **9**, 890-909 (2019).
203. K. H. Lin *et al.*, Systematic Dissection of the Metabolic-Apoptotic Interface in AML Reveals Heme Biosynthesis to Be a Regulator of Drug Sensitivity. *Cell Metab* **29**, 1217-1231 e1217 (2019).
204. D. Y. Yosifov *et al.*, Oxidative stress as candidate therapeutic target to overcome microenvironmental protection of CLL. *Leukemia* **34**, 115-127 (2020).
205. S. Christian *et al.*, The novel dihydroorotate dehydrogenase (DHODH) inhibitor BAY 2402234 triggers differentiation and is effective in the treatment of myeloid malignancies. *Leukemia* **33**, 2403-2415 (2019).
206. D. B. Sykes *et al.*, Inhibition of Dihydroorotate Dehydrogenase Overcomes Differentiation Blockade in Acute Myeloid Leukemia. *Cell* **167**, 171-186 e115 (2016).
207. M. Bajzikova *et al.*, Reactivation of Dihydroorotate Dehydrogenase-Driven Pyrimidine Biosynthesis Restores Tumor Growth of Respiration-Deficient Cancer Cells. *Cell Metab* **29**, 399-416 e310 (2019).
208. K. Birsoy *et al.*, An Essential Role of the Mitochondrial Electron Transport Chain in Cell Proliferation Is to Enable Aspartate Synthesis. *Cell* **162**, 540-551 (2015).
209. L. Stuani *et al.*, Mitochondrial metabolism supports resistance to IDH mutant inhibitors in acute myeloid leukemia. *J Exp Med* **218**, (2021).
210. A. N. Gorelick *et al.*, Respiratory complex and tissue lineage drive recurrent mutations in tumour mtDNA. *Nat Metab* **3**, 558-570 (2021).
211. P. A. Frey, The Leloir pathway: a mechanistic imperative for three enzymes to change the stereochemical configuration of a single carbon in galactose. *FASEB J* **10**, 461-470 (1996).
212. L. D. Marroquin, J. Hynes, J. A. Dykens, J. D. Jamieson, Y. Will, Circumventing the Crabtree effect: replacing media glucose with galactose increases susceptibility of HepG2 cells to mitochondrial toxicants. *Toxicol Sci* **97**, 539-547 (2007).
213. S. Valle *et al.*, Exploiting oxidative phosphorylation to promote the stem and immunoevasive properties of pancreatic cancer stem cells. *Nat Commun* **11**, 5265 (2020).
214. B. Gilquin *et al.*, The AAA+ ATPase ATAD3A controls mitochondrial dynamics at the interface of the inner and outer membranes. *Mol Cell Biol* **30**, 1984-1996 (2010).
215. G. Jin *et al.*, Atad3a suppresses Pink1-dependent mitophagy to maintain homeostasis of hematopoietic progenitor cells. *Nat Immunol* **19**, 29-40 (2018).
216. K. H. Huang, K. C. Chow, H. W. Chang, T. Y. Lin, M. C. Lee, ATPase family AAA domain containing 3A is an anti-apoptotic factor and a secretion regulator of PSA in prostate cancer. *Int J Mol Med* **28**, 9-15 (2011).
217. B. M. Hover *et al.*, Culture-independent discovery of the malacidins as calcium-dependent antibiotics with activity against multidrug-resistant Gram-positive pathogens. *Nat Microbiol* **3**, 415-422 (2018).
218. D. Earl, Vanderbilt University, Nashville, TN (2018).

CHAPTER 4 – STUDIES ON THE CIROMICIN FAMILY OF GLYCOSOYLATED MACROLACTAMS

4.1 The discovery of the ciromicins and related macrolactams

In our laboratory's efforts to elucidate the biosynthesis of apoptolidin in *Nocardiopsis sp.* FU-40 (FU-40), Jacques Ravel assisted Yu 'Sunny' Du with sequencing and assembling the FU-40 genome using Roche 454 sequencing at 30x coverage. The putative apoptolidin gene cluster was identified by searching for a type-I polyketide synthases (PKS) and finding one with 14 PKS modules (28-carbon backbone) and appropriate tailoring enzymes (105). At the time, a second type-I PKS gene cluster was noted containing fewer modules (~8) and no deoxysugar biosynthetic genes.

In a separate project, Dagmara K. Derewacz (Kasia) began experimenting with co-culture as a technique for eliciting the production of new natural products. Though humans are largely interested in natural products for their medicinal properties, microbes evolved to produce natural products in order to gain a competitive advantage in their environmental niche. We hypothesize that the 'purpose' of natural products is to mediate intergenic microbial interactions to facilitate cooperation or competition between microbes trying to survive with limited resources. While some natural products are produced under standard culture conditions, we hypothesized that other gene clusters are only activated in response to stressful stimuli such as nutrient depravation, antibiotic stress, toxin exposure, or co-culture. Moreover, it is tempting to speculate that natural products produced only in response to narrow stimuli are responding directly to that stimuli to affect a specific biological 'goal.'

Kasia examined the metabolome of FU-40 ΔApoS8 (ΔS8) under various co-culture conditions and observed that a small set of metabolites were upregulated by co-culture with

167

various competitors, particularly *Tsukamurella Pulmonis* (TP) and *Rhodococcus wratislaviensis* (RW) ([219](#)). Of note, both of these competitors produce mycolic acid which has been noted to stimulate natural production in other streptomyces ([220](#)). The ΔS8 FU-40 strain was selected due to its inability to make apoptolidin as the ApoS8 loading model had been knocked out by

5   replacement with an apramycin resistance gene ([105](#)). One of the metabolites prioritized for isolation was a polyene with a m/z of 515.275 and a characteristic chromophore with a UV$_{\lambda max}$ of 290 nm. Using HP-20 resin, size exclusion chromatography, and preparative HPLC, isolated this compound and used multidimensional NMR to identify it as a novel metabolite, ciromicin A (Figure 4.1), named after the latin 'ciro' meaning war/cite/disturb/invoke.
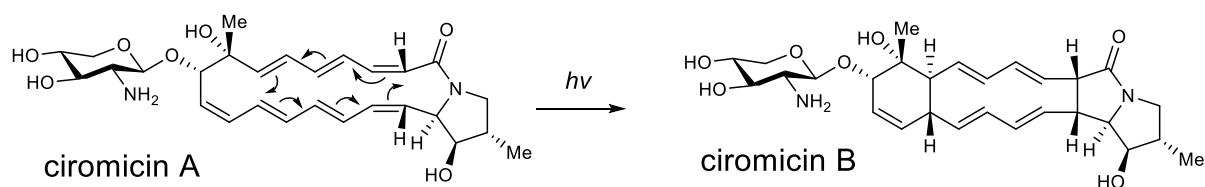
Figure 4.1. Ciromicins A & B

10

        As Kasia worked to isolate and determine the structure of ciromicin A, she found that a minor side product with the same mass but lacking the 290 nm chromophore would repeatedly form over time under ambient conditions in methanol. After experimenting with various possible environmental variables (temperature, pH, etc…) Kasia discovered that exposure to visible light

15   was necessary to initiate conversion. By exposing ciromicin A to ambient sunlight (windowsill) for 2 hrs, she was able to obtain enough of the new metabolite to elucidate its structure as ciromicin B (Figure 4.1). Kasia proposed that ciromicin B forms from ciromicin A via a photochemical 12π electron rearrangement similar to (though larger than any previously described), the 8π previously observed for other natural products ([221](#)).

The core of ciromicin A is composed of a 21-carbon polyketide synthesize by the 10 PKS

domains with a unique amino starter unit which is eventually joined the terminal carboxylic acid

to form the macrolactam. An amino sugar is attached to C9. This places ciromicin A in the larger

class of polyketide macrolactams including vicenistatin (222), icedinine (223), heronamides

5   (224-226), and macrotermycins (227), which have diverse structures and activities.
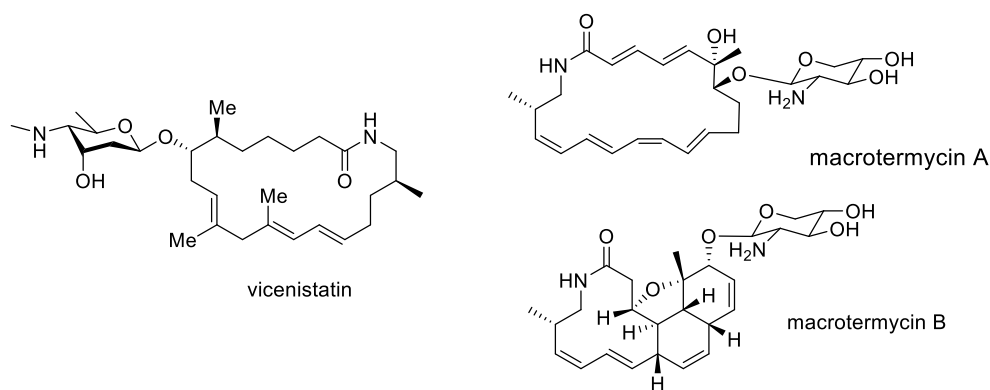
Figure 4.2. Glycosylated Macrolactams

4.2   Ciromicin A and B exhibit divergent cell subset targeting in AML

In David Earl's demonstration of multiplexed activity metabolomics (228), he analyzed

the cell subset targeting of crude extracts FU-40 (WT), and observed that the fractions

10   corresponding to apoptolidin appear to target lymphocytes while the fractions corresponding to

ciromicins A and B appeared to target myeloid cells with ciromicin A targeting leukemia blasts

while ciromicin B targets more monocytic myeloid cells. To expand upon this finding, Earl

applied ciromicins A and B to primary AML patient samples and assessed the immunophenotype

and signaling of the cells that remained after 48 hrs using mass cytometry (CyTOF).

15   Surprisingly, he observed that ciromicin A and B appeared to deplete distinct subsets of cells,

with ciromicin B targeting immunophenotypically defined (C34+/CD38-) leukemic stem cells

and smaller blast subsets while ciromicin A targeted the largest subset of blasts. As was the case

with the apoptolidin cell subset targeting CyTOF data, this could be due to selective depletion of

the missing cell subset or by causing the cells to alter their immunophenotype. This surprising

finding led to my thesis proposal to determine the basis of the 'differenatiation dependent'

targeting of glycosylated polyketides in clonal hematopoietic disorders.

4.3 Approach

The path towards identifying the mechanistic basis of differential subset targeting of the

ciromicins could follow a similar path as that followed for the apoptolidins in chapter 2, however

the two projects began at two very different points. Whereas apoptolidin was accessible in large

quantities, had well characterized SAR, and exhibited nanomolar activity in immortalized cell

lines, none of these prerequisites were in place for the ciromicins. Ciromicin A is accessible in

quantities of 1-2 mg/L in co-culture with ΔS8 and TP and the existing purification approach

required the use of HP-20 resin which was not amenable to large scale extractions (10 L).

Ciromicin B was even harder to access as the photoconversion of A to B also generated side

products which reduced the yield considerably. Ciromicin A+B also contains an amine on the C9

sugar which would form an amide bond more readily than any of the hydroxyl groups, and the

relative reactivity of each position was unknown. Furthermore, ciromicin A and B were only

shown to be active in primary patient samples, not in cell lines, which would make it more

difficult to assay potential analogs and identify their molecular target. Herein I will describe our

progress towards 'derisking' the prospect of studying the mechanism of action of the ciromicins.

4.4 **Novel ciromicins from** *Nocardiopsis FU-40*

In the course of my efforts to isolate sufficient material for biological assays, I isolated a number of new ciromicins which provide valuable insights in the biosynthesis of this class and their SAR in leukemia.

4.4.1 Ciromicin C

In one round of shake flask fermentation of ΔS8 + TP, we observed a peak with the same *m/z* as ciromicin A (515) but with a shorter retention time (8 vs 9 min) and a distinct chromophore. This peak is also present, but much smaller, in previous datasets. This novel ciromicin, ciromicin C, was isolated by preparative HPLC and structure determined by multidimensional NMR.
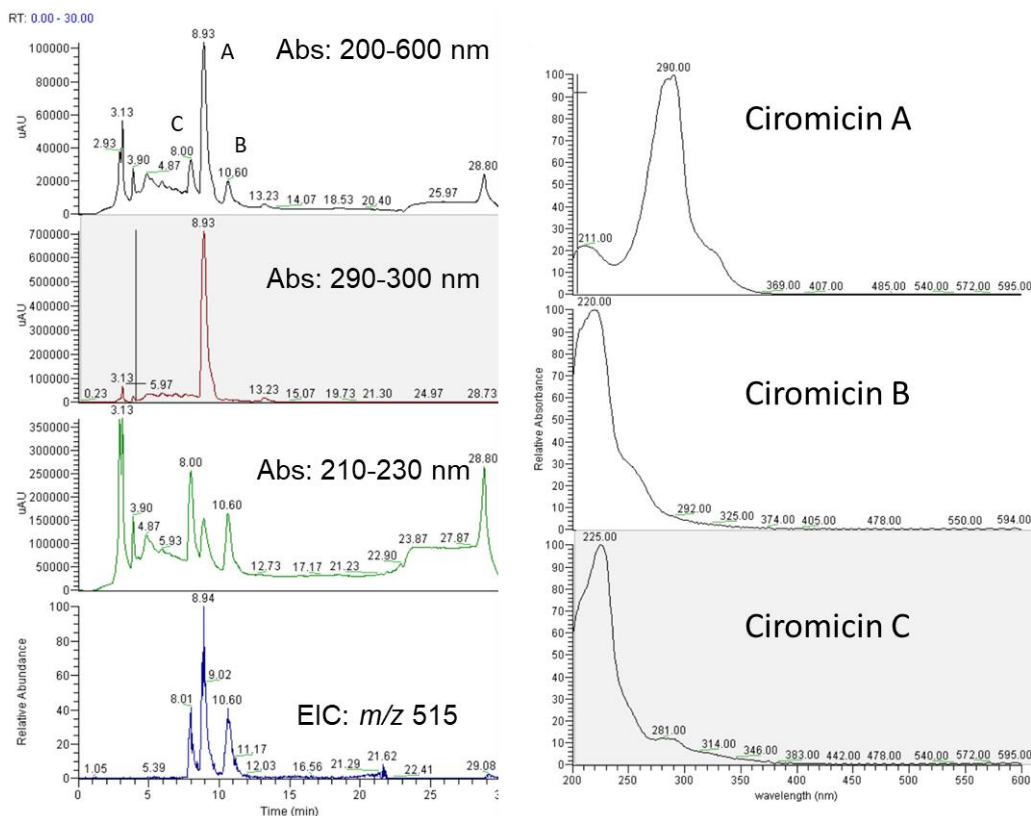
Figure 4.3. Identification of ciromicin C in ΔS8 crude extract

171

Unlike ciromicin A, which had two separate COSY spin systems (C1-C8 and C9-C21), ciromicin C had one large COSY spin system with a new correlation between C3/C14 in addition to C2/C17 (Figure 4.4). The relative stereochemistry of C2, C3, and C17 were determined by NOESY correlations and consistent with a 4+2 Diels-alder cycloaddition. One point of ambiguity is the cis/trans isomerization of C6/C7 which may be trans rather than cis as drawn.

Figure 4.4. Key NMR correlations for elucidating ciromicin C

The origin of ciromicin C is not entirely clear, though it thought to arise via an internal, Diels-alder rearrangement from ciromicin C. Interestingly, in our limited experience, we have been unable to generate ciromicin C from purified ciromicin A and it does not appear to form spontaneously or on exposure to light. Ken Houk's group examined similar 4+2 and 6+4 cycloadditions in the case of the heronamides, and using computational modeling to propose that the 6+4 product formed via cope rearrangement of the 4+2 product (Figure 4.5), which would

172

suggest that ciromicin C can rearrange to form ciromicin B. However, when ciromicin C was

exposed to sunlight for 1 hr, no conversion was observed, though the small residual amount of

ciromicin A did degrade, suggesting that ciromicin C does not convert to ciromicin B.
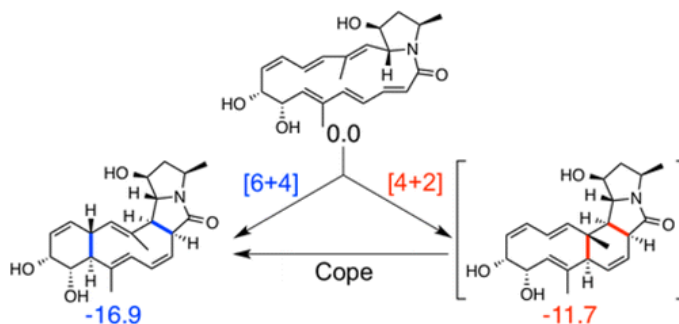
Figure 4.5. Houk's proposed mechanism for heronamide A formation from Yu P, et al. JACS, 2015
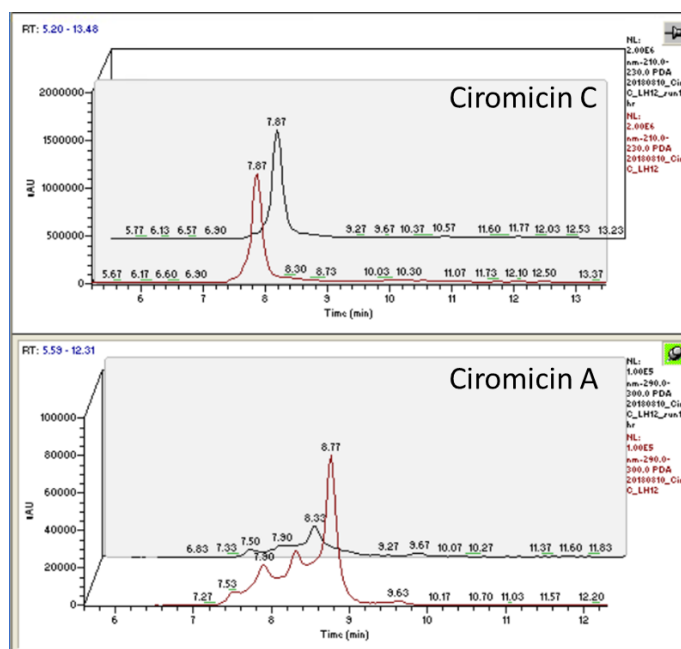
Figure 4.6. Ciromicin C is photostable

Ciromicin C was resuspended in methanol and kept in the dark (red) or exposed to sunlight

for 1 hr (black). No conversion of ciromicin C was observed though the residual ciromicin A

did degrade.

5

4.4.2 <u>Ciromicins B$_2$ and B$_3$</u>

      In the course of attempting generate sufficient ciromicin B for biological studies, two new ciromicins were isolated, designated ciromicin B2 and B3. Ciromicin A resuspended in MeOH was exposed to sunlight for 1 hr and purified by preparative HPLC. In addition to

5   ciromicin B in fraction 12 (now ciromicin B$_1$), two additional minor products were isolated in fractions 15 and 16, designated ciromicins B$_2$ and B$_3$, with distinct ^{1}H NMR spectra (Spectrum 4.1).
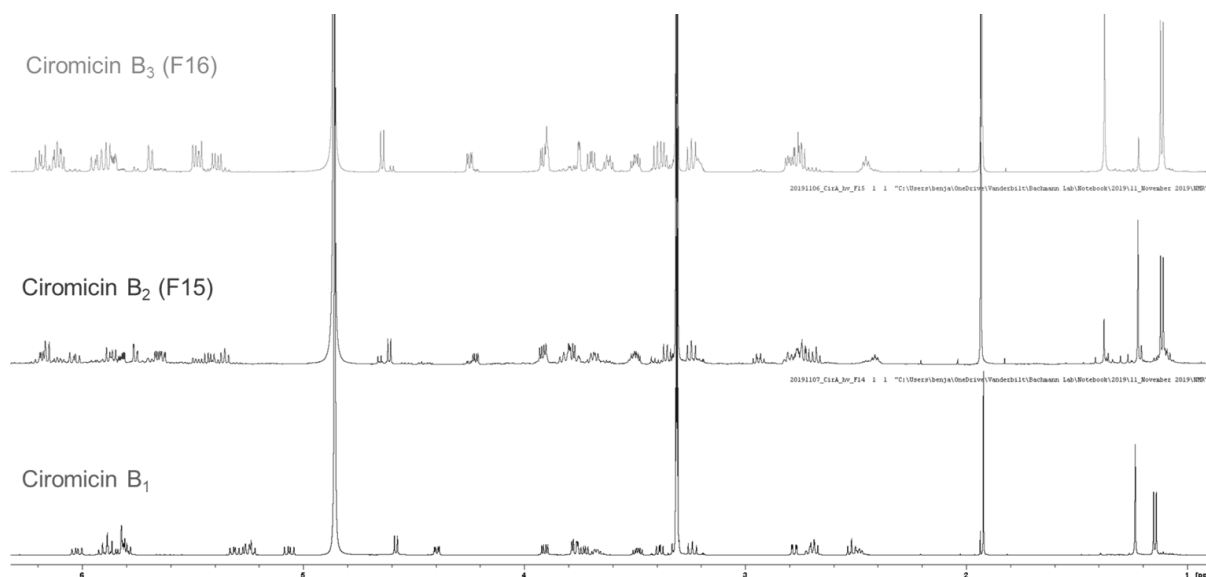
Spectrum 4.1. Proton NMRs of Ciromicins B1, B2, B3 in MeOD at 600 mHz

      After careful analysis of COSY and HMBC correlations, ciromicins B$_2$ and B$_3$ were

10   determined to have the same 2D connectivity as ciromicin B$_{(1)}$, hence my proposal to designate them as B$_2$ and B$_3$ rather than ciromicins D and E. The HSQC assignments for the new ciromicins are shown in Figure 4.7.
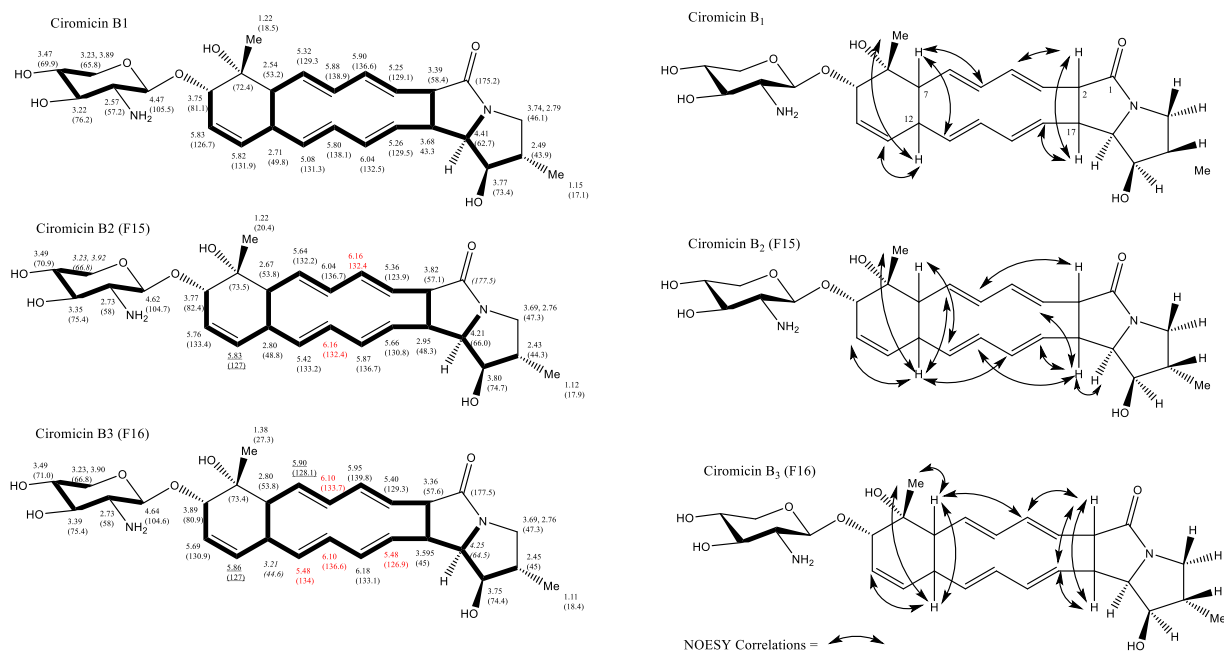
Figure 4.7. NMR assignments of Ciromicins B1, B2, B3 in MeOD

Positions labeled in red are potentially ambiguous but were assigned based on the best available evidence.

NOESY analysis of ciromicins B1, B2, and B3 revealed that ciromicins B1, B2, and B3 differ in their assigned stereochemistry at C2, C7, C12, and C17, leading to the final assignments. One point of ambiguity is again the cis/trans assignment of C3/4, C5/6, C13/14, C15/16 which were tentatively assigned as identical to ciromicin B$_1$. Additional heteronuclear decoupling experiment may be necessary to extract coupling constants for these protons which could lead to more confident assignments at these positions. Reviewing older data, ciromicins B2 and B3 are often seen as side products when attempting to generate ciromicin B1, though it is likely that they were not isolable in sufficient quantities in previous, smaller scale reactions. One of the challenges to obtaining ciromicin B$_1$ is the poor yield of the ciromicin A to B conversion. By elucidating the structures of these secondary products, it may be possible to propose a

mechanism for their formation and devise reaction conditions which favor formation of one or more products, similar to the chemistry devised by Jonathan Boyce and John Porco in Chapter 6. Additionally, if these secondary products can be obtained in sufficient quantities, they may serve as valuable negative controls for target ID studies on ciromicin B, with identical 2D connectivity but distinct 3D structures. The complete set of ciromicins currently identified are summarized in Figure 4.8.
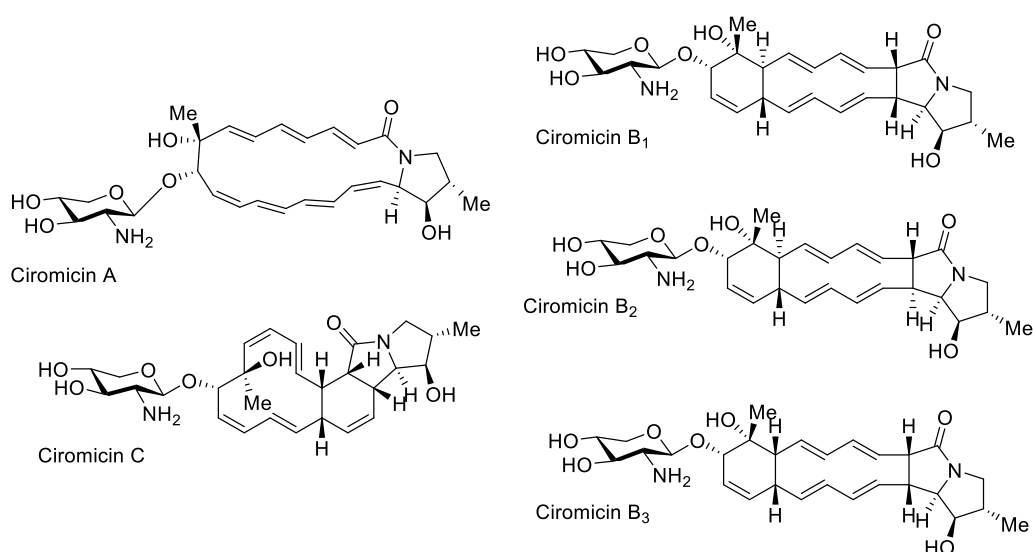
Figure 4.8. Proposed structures of Ciromicins A, B₁, B₂, B₃, and C

4.5 Large scale production and isolation of ciromicins

One strategy for obtaining larger quantities of ciromicin is to simply grow the producing strain on a larger scale. This was facilitated by the addition of a Bioflo 3000 bioreactor to the laboratory which included both 1L and 10L fermentation vessels. The fermentation was carried out nearly identically to the conditions used for shake flasks except for a much larger scale: a 2% seed culture of ΔS8 was added to 10L of production media (same as apoptolidin media) followed by a 2% inoculum of TP which was started at the same time as the production culture. Various

176

parameters were monitored over the course of the fermentation including pH and DO which provided readback on the state of the fermentation. Ciromicin A levels were quantified daily beginning on day 4 by removing aliquots via the sampling port and analysis by HPLC (λ=290 nm). The culture was harvested on day 12 based on plateauing levels of ciromicin A and

5   increasing pH indicative of cell death.

Rather than using HP-20 and solid phase extraction, we sought a compatible liquid/liquid extraction which was more amenable to large scale isolation. Unfortunately, a pilot experiment revealed that ethyl acetate extraction only yielded 14% recovery compared to 60% recovery for HP-20. In order to increase partitioning, a 'salting out' strategy was trialed using various salts as

10   described in the literature ([229](#)). Dibasic potassium phosphate (K_2HPO_4) was found to be the most favorable, with 77% recovery of ciromicin A by addition of K_2HPO_4 at a final concentration of 1M. Using this approach, 30 mg of ciromicin A was isolated from a single 10 L fermentation.

4.6 CyTOF profiling of ciromicin cell subset targeting in AML

15   In David's initial work on cell subset targeting of the ciromicins, the diverging effects of ciromicin A and B were only apparent in primary AML samples. A variety of leukemia cell lines were tested for evaluated for ciromicin sensitivity including HL-60, MV-4-11, K562, KG1, KG1a, and Jurkat, without notable activity below 10 μM. In order to confirm that the ciromicins A and B I had isolated were still active, we repeated David's experiment with a new patient

20   sample at the same 48 hr timepoint with different concentrations of ciromicin A, B(1), and C and are shown in Figure 4.9. (Note this as part of the same experiment described in Chapter 3).
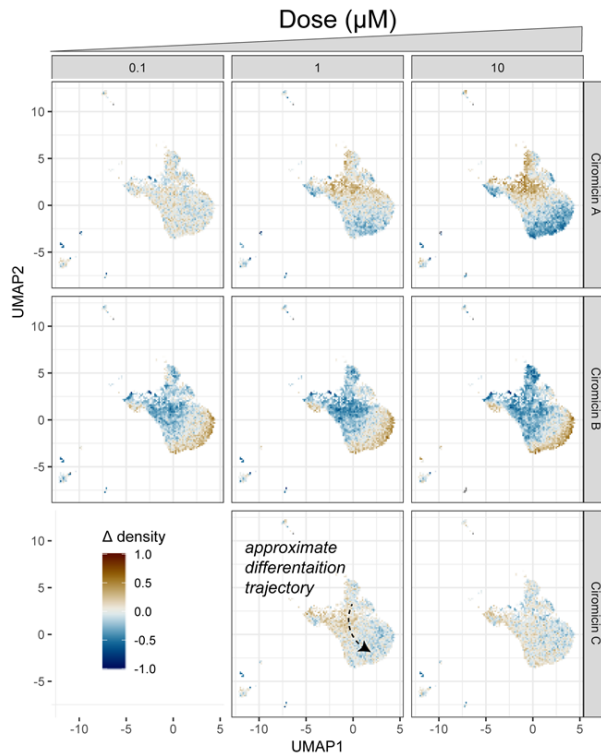
Figure 4.9. CyTOF dose-response analysis of ciromicins in AML

Thought ciromicins A, B, and C showed no activity in AML cell lines, ciromicin A and B exhibited notable, opposing, bioactivities in AML047, just as was seen in Earl 2018. Rather than comparing each map to vehicle treated cells side-by-side, I plotted the change in local density
5   around each cell, computed based on the average distance to each cells 15 nearest neighbors in each map. On this plot (Figure 4.9), areas of the map which lose cells are highlighted in blue, areas which gain cells are marked in red, and areas which saw no change are depicted in white, examining the marker expression on the largest cluster of cells (blasts), several changes are apparent, ciromicin A appeared to select for loss of CD25, CD71, CD123, HLA-DR, and a slight
10   increase in CD117, while ciromicin B selected for increased CD25, CD184, and loss of CD13. Ciromicin C did not appear active and could serve as a useful negative control.
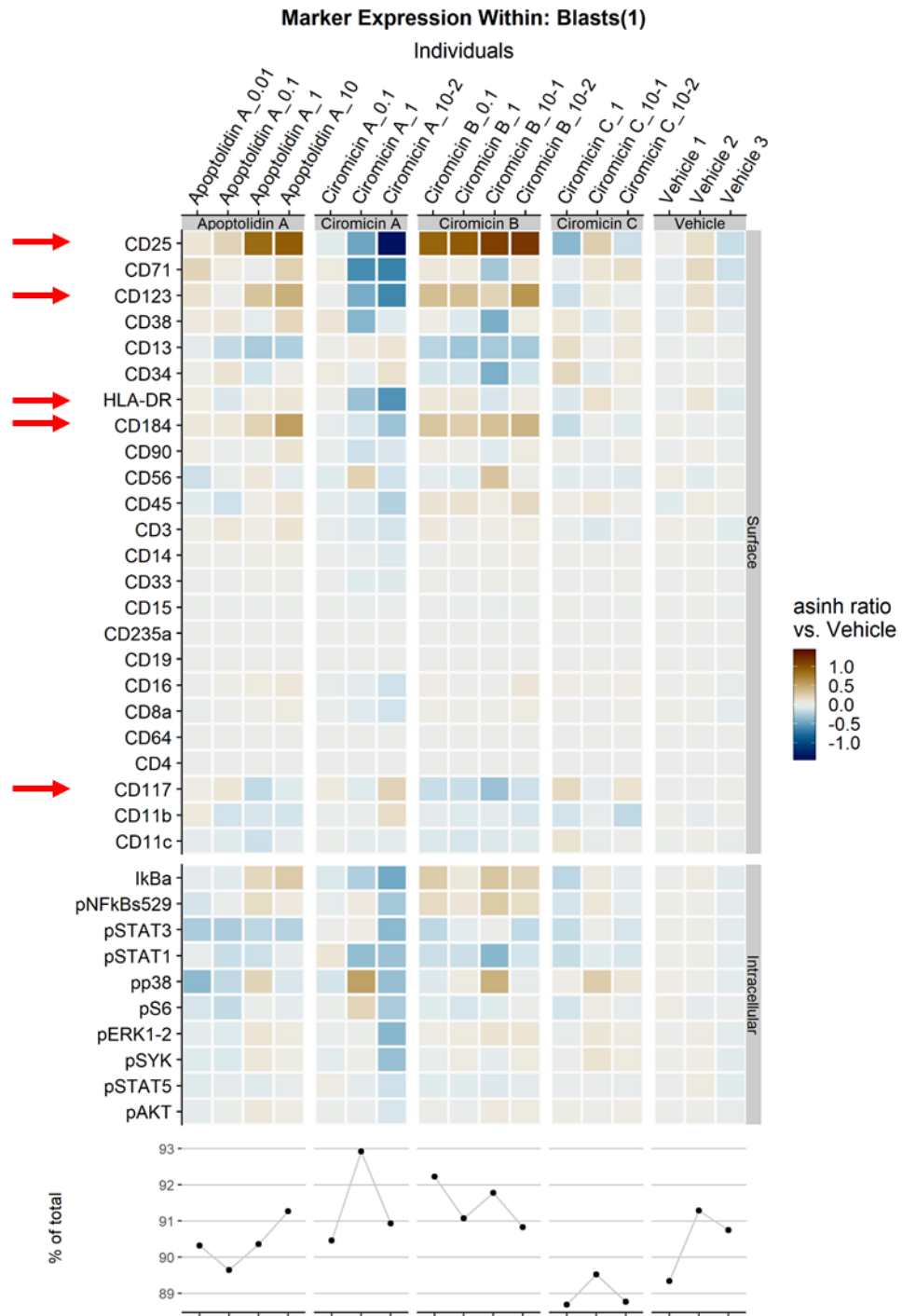
Figure 4.10. CyTOF analysis of leukemia blast immunophenotypes after ciromicin treatment

179

4.7 Ciromicin B suppresses cell differentiation in mobilized human progenitors

While the results from primary samples are intriguing, primary patient samples are not a suitable biological system for target identification studies as the cell subsets of interest represent a subpopulation of cells within each sample and the results may different between different

5   patient samples. We hypothesized that healthy human hematopoietic progenitors, particularly peripherally collected 'mobilized progenitors' may be a suitable model system for studying the ciromicins. To test if the ciromicins were influencing hemopoietic differentiation, we evaluated them in a methylcellulose colony forming assay, treating ~30K progenitors per plate in duplicate with vehicle or ciromicins A, B, or C at 10 µM for 14 days. Consistent with the David's CyTOF

10   data and the data presented in the previous section, ciromicin B appeared to suppress erythroid and monocytic differentiation without a notable effect on megakaryocyte or granulocyte colony formation.
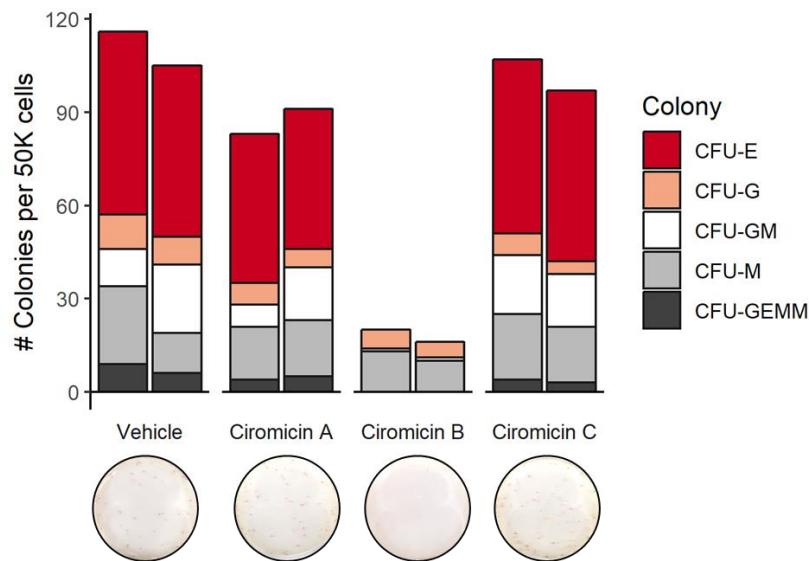
Figure 4.11. Ciromicin B suppresses myeloid differentiation in human progenitors

4.8 Ciromicin B suppresses OXPHOS

The ciromicins were evaluated alongside the apoptolidins and ammocidins in each of the experiments described above. One observation was that ciromicin B and apoptolidin/ammocidin appeared to target similar cell subsets when evaluated by CyTOF on treated primary samples. In the course of our *in vitro* assessments of ATP synthase inhibition by apoptolidin family glycomacrolides in isolated mouse liver mitochondria, I choose to assay ciromicin B as well. Surprisingly, ciromicin B appeared to inhibit ATP synthesis in isolated mouse liver mitochondria (Figure 4.12). Notably, this assay requires complexes II-V to be fully functional, so ciromicin B may be inhibiting any part of the electron transport chain or regulatory machinery and there is no evidence that the activity seen in this *in vitro* context is responsible for the differentiation dependent targeting seen by CyTOF.
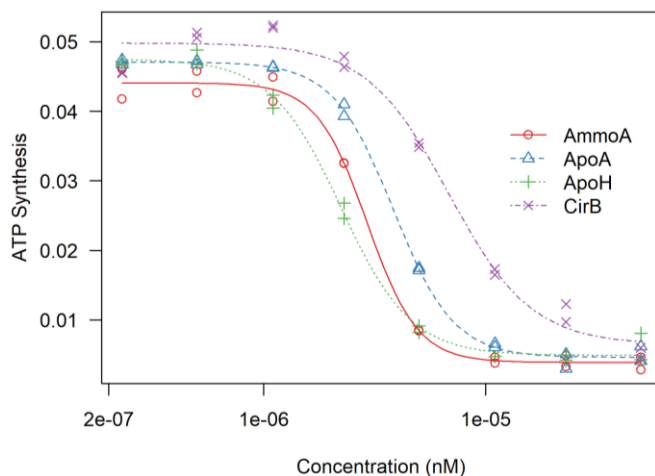
Figure 4.12. Ciromicin B inhibits OXPHOS in isolated mouse liver mitochondria

4.9 Conclusions and future directions

Though my thesis proposal included target ID efforts for both the apoptolidins and ciromicins, the work on the ciromicins did not progress nearly to the same extent. The data

presented here will hopefully provide a starting point for future trainees or scientists seeking to

elucidate the mechanism of action of the ciromicins. Confirming the results of Earl's 2018 study,

we observed dose-dependent cell subset targeting in primary AML samples. It is tempting to

speculate that ciromicin A and B engage identical or similar targets in distinct manners to trigger

5   mutually exclusive differentiation programs, and thus, target ID efforts on the ciromicins may

shed light on the mechanisms controlling hematopoietic differentiation. The methods described

here for isolating ciromicins in large quantities may also be useful in the future. Beyond the

human biology applications of the ciromicins, the mechanisms underlying the pericyclic

reactions which yield ciromicins B1, B2, B3, and C are unusual and interesting. It is my hope

10   that the structural elucidation efforts described here for ciromicins B2, B3, an C can be combined

with computational modeling to more fully understand how these compounds form and perhaps

guide more selective reaction conditions to yield fewer products.

4.10 References

105.   Y. Du *et al.*, Biosynthesis of the Apoptolidins in Nocardiopsis sp. FU 40. *Tetrahedron* **67**, 6568-6575 (2011).

219.   D. K. Derewacz, B. C. Covington, J. A. McLean, B. O. Bachmann, Mapping Microbial Response Metabolomes for Induced Natural Product Discovery. *ACS Chem Biol* **10**, 1998-2006 (2015).

220.   H. Onaka, Y. Mori, Y. Igarashi, T. Furumai, Mycolic acid-containing bacteria induce natural-product biosynthesis in Streptomyces species. *Appl Environ Microbiol* **77**, 400-406 (2011).

221.   C. M. Beaudry, J. P. Malerich, D. Trauner, Biosynthetic and Biomimetic Electrocyclizations. *Chem Rev (Washington, DC, U S)* **105**, 4757-4778 (2005).

222.   K. Shindo, M. Kamishohara, A. Odagawa, M. Matsuoka, H. Kawai, Vicenistatin, a novel 20-membered macrocyclic lactam antitumor antibiotic. *J Antibiot (Tokyo)* **46**, 1076-1081 (1993).

223.   Y. Futamura *et al.*, Discovery of incednine as a potent modulator of the anti-apoptotic function of Bcl-xL from microbial origin. *J Am Chem Soc* **130**, 1822-1823 (2008).

224.   W. Zhang *et al.*, Heronamides D-F, polyketide macrolactams from the deep-sea-derived Streptomyces sp. SCSIO 03032. *J Nat Prod* **77**, 388-391 (2014).

225.   P. Yu, A. Patel, K. N. Houk, Transannular [6 + 4] and Ambimodal Cycloaddition in the Biosynthesis of Heronamide A. *J Am Chem Soc* **137**, 13518-13523 (2015).

226. T. J. Booth, S. Alt, R. J. Capon, B. Wilkinson, Synchronous intramolecular cycloadditions of the polyene macrolactam polyketide heronamide C. *Chem Commun (Camb)* **52**, 6383-6386 (2016).

227. C. Beemelmanns *et al.*, Macrotermycins A-D, Glycosylated Macrolactams from a Termite-Associated Amycolatopsis sp. M39. *Org Lett* **19**, 1000-1003 (2017).

228. D. C. Earl *et al.*, Discovery of human cell selective effector molecules using single cell multiplexed activity metabolomics. *Nat Commun* **9**, 39 (2018).

229. A. M. Hyde *et al.*, General Principles and Strategies for Salting-Out Informed by the Hofmeister Series. *Organic Process Research & Development* **21**, 1355-1370 (2017).

CHAPTER 5 – DEVELOPMENT OF FLUORESCENT CELL BARCODING METHODS TO ACCELERATE NATURAL PRODUCTS DISCOVERY

Note: This work has been accepted for publication at Cytometry Part A and is in press at the time of this writing. B. J. Reisman, S. M. Barone, B. O. Bachmann, J. M. Irish, DebarcodeR

5   Increases Fluorescent Cell Barcoding Capacity and Accuracy. *Cytometry, Part A*, (2021).

5.1 Introduction

Fluorescent cell barcoding (FCB) is a technique for applying sample barcoding to fluorescence flow cytometry by using amine-reactive dyes which react with cellular proteins to covalently label cells ([230](#), [231](#)), or in some applications using fluorescently labeled antibodies

10   against common targets ([232](#)). Once each sample is stained with a unique barcode or combination of barcodes, they can be pooled, processed, and analyzed as a single sample which reduces reagent consumption, increases sample throughput, and improves data robustness. This principle has also been adapted to mass-cytometry in the form of palladium mass-tag cell barcoding (MCB) where it is paired with a computational algorithm for debarcoding the pooled

15   data into separate datasets for each sample ([233](#)). Unlike MCB, in which each barcoding channel is used to denote a bit of information (barcode positive or negative, 2 levels per channel), applications of FCB typically use multiple concentrations or 'levels' of barcoding dye on a single channel (e.g., 6 or 8 levels of barcoding per channel, as in examples here).

In FCB and MCB, the process of determining the original sample identity of barcoded

20   cells is variously referred to as demultiplexing, deconvolution, and debarcoding. Existing tools for mass cytometry barcoding are impractical for debarcoding dense FCB barcoding schemes with complex cell types. Human expert debarcoding can effectively address complex samples, but requires significant prior knowledge. Algorithmic debarcoding may be fast and accurate with

simple FCB designs, but struggles to accurately assign barcodes when cells are comprised of mixtures of cell types or otherwise reflect changes in features that impact dye uptake, such as morphology and viability. Therefore, early published implementations of FCB generally relied on manual debarcoding with user drawn biaxial gates in a process called "forward

5   deconvolution" (231). This manual process is a substantial bottleneck to the use of FCB in high-throughput settings, with more complex barcode schemes, and with cell mixtures.

Computational debarcoding has the potential to remove the requirement of manual biaxial gating, which would eliminate operator bias and increase assay throughput and reproducibility. A successful debarcoding algorithm should assign as many cells as possible

10   (yield) with a minimal number of misassignments (accuracy). Critically, the algorithm must be unbiased with regards to assignment or mis-assignment, with the probability of assignment being independent of the biological features of the cell. In the absence of this criterion, certain cell subsets of interest may be lost during debarcoding, or worse yet, systematically misassigned to the wrong sample. Ideally the algorithm should require minimal user intervention and should

15   interface with other widely used analysis pipelines. When fully implemented, an automated debarcoding approach can also permit the use of optimized barcoding schemes that increase sample multiplexing capacity beyond that which would be practical for manual biaxial gating.

Previous approaches to computational deconvolution aimed to automate biaxial gating (234). Though this approach decreases analysis time and improves reproducibility, the sample

20   multiplexing capacity remains limited to ~24 samples using two barcoding dyes, a scheme designed for manual gating by a human expert. One of the limitations of gating-based approaches to automated debarcoding is sample cell heterogeneity. This is because mixed cell types can have highly variable (>5-fold) differences in barcode intensity within the same

185

barcoding level. As NHS-ester dyes react with cellular proteins, larger cells with more protein

will tend to stain brighter than smaller cells. One approach for overcoming this is to use

additional cell type markers to gate populations of interest that might variably uptake dye prior to

deconvolution (234-236). A limitation of this approach is that it requires prior knowledge and

5   thus can introduce bias, especially in high dimensional schemes. Prior work has debarcoded

primary human cells with manual gating based on scatter and barcoding dyes prior to cell type

gating (237). However, this approach requires a less efficient spacing of the barcoding levels in

order to avoid confusing sample well assignments.

One of the applications with the most pressing need for computational debarcoding is

10   high-throughput screening (HTS) in which thousands of chemical or biological perturbations are

screened for their ability to induce a phenotype of interest. Non-FCB flow cytometry HTS assays

generally use fluorescent dyes or genetically encoded reporters as phenotypic readouts as

antibody-based assays are costly and require multiple wash steps which are not compatible with

automated liquid handling. Furthermore, in most HTS settings, a small fraction (<5%) of

15   samples are positive for the desired phenotype ('hits'), which necessitates screening thousands of

inactive perturbations to find small subset that are active. FCB allows perturbed cells to be

pooled together prior to antibody staining, enabling high dimensional assessments of the induced

phenotype at a scale that would not otherwise be possible for applications such as identification

of bioactive microbial metabolites (228) or screening synthetic compound libraries (196, 238).

20   To overcome these limitations, we describe herein 'DebarcodeR,' an approach to

debarcoding that leverages computational modeling of dye-uptake across cellular space and does

not require pre-gating for specific populations in heterogeneous samples. DebarcodeR reliably

demultiplexed complex FCB samples into separate FCS files according to user-defined tolerance

settings for misassignment. Unlike previous approaches, which aimed to define gates around each barcoded population in high dimensional space, DebarcodeR estimated the probability of cluster membership for each cell. This approach allowed DebarcodeR to accurately assign 99.8% of cells in a 48-sample well pool, even for challenging sample types. By including

5 additional experimental controls designed to improve model estimates, DebarcodeR thus permitted a high degree of multiplexing while leaving free many channels for quantifying cell type and function.

5.2 Materials and Methods

5.2.1 <u>Experimental methods</u>

10 Jurkat Cells were obtained from ATCC and maintained in RPMI 1640 medium supplemented with 10% heat inactivated FBS and 1% penicillin/streptomycin (10,000 U/mL). Peripheral blood mononuclear cells (PBMCs) were obtained in accordance with the Declaration of Helsinki following protocols approved by the Vanderbilt University Medical Center Institutional Review Board. Cells were fixed with paraformaldehyde at a final concentration of

15 1.6% w/v for 10 min at room temperature and permeabilized with ice cold methanol for 30 min at -20 °C. Cells were centrifuged at 800 g x 5 min, methanol was removed by decanting, and resuspended by pipetting in 200 μL PBS. Barcoding plates were prepared with 5 μL of each dye concentration at 40x the final concentration in DMSO in 96 well plates (see Supplementary Protocols 4 and 5). Samples of 185 μL of cell suspensions (typically 250-1,000 cells/μL) were

20 transferred to the barcoding plate to stain for 30 min at room temperature protected from ambient light, and the reaction was quenched by addition of 70 μL of 1% BSA in PBS. The plate was centrifuged at 800 g x 5 min, decanted, and all cells were pooled into a single FACS tube in 1%

PBS/BSA for further processing. For CD45 staining, PE anti-human CD45 antibody [HI30] and APC anti-mouse CD45 antibody [I3/2.3], (Biolegend, Inc, San Diego, CA) were used.

5.2.2 Description of Datasets

Three datasets are introduced to benchmark the applicability of this approach. The gating
5 schemes for selecting intact, single cells, are depicted in Figure 5.1. All non-scatter channels were transformed using asinh transformations with appropriate co-factors. **Dataset 1: Cytobank Barcoding Example:** Peripheral blood mononuclear cells (PBMCs) barcoded 2x Alexa 750, 3x Pacific Orange, available at community.cytobank.org (Experiment 8938); **2: Jurkat Separate Tubes:** Fixed and permeabilized Jurkat cells barcoded 8x Pacific Blue, 6x Pacific Orange, 1x
10 Alexa 750, where each well was acquired separately at the cytometer and the events concatenated *in silico,* resampling 5,000 events per well with replacement, (FlowRepository: FR-FCM-Z368); **3. Human + Mouse Checkerboard:** Human PBMCs and mouse splenocytes were fixed and permeabilized, distributed across 48 wells in a checkerboard pattern, barcoded 8x Pacific Blue, 6x Pacific Orange, 1x Alexa 750, and stained for human and mouse CD45
15 (FlowRepository: FR-FCM-Z369). As an added example of DebarcodeR applied to published dataset, an analysis of the U397 dataset from Krutzik *et al*., 2006 (231) obtained from the supplementary data published in Knijnenburg *et al.* 2011 (239) is included in Figure 3.5. Dataset 2 is included with the DebarcodeR R package to facilitate reproducibility in different computing environments.
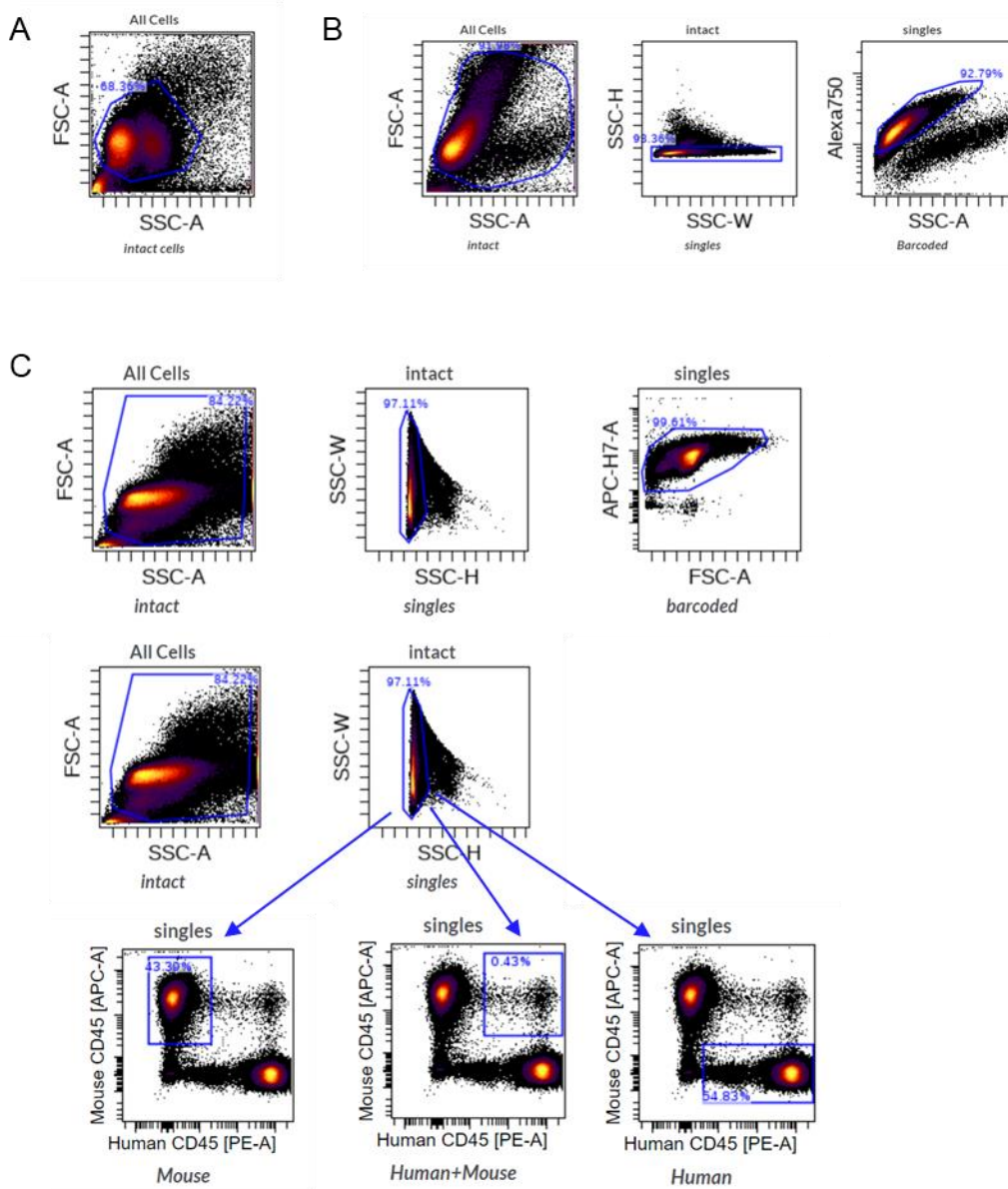
Figure 5.1. Gating Scheme for Datasets 1-3:

A, Dataset 1 – Cytobank Barcoding Demonstration, gating on intact cells; **B,** Dataset 2 – Jurkat separate tubes, gating on barcoded, single, intact cells; **C,** Dataset 3 – human/mouse checkerboard, barcoded population was used for debarcoding, human and mouse CD45+ gates shown below (not used for debarcoding).

5.2.3 The DebarcodeR framework for debarcoding

The DebarcodeR pipeline, as illustrated in Figure 5.2, consists of three individual steps which are applied sequentially to each barcoding channel: 1) de-skewing, 2) population modeling, and 3) assignment. In the de-skewing step, linear regression is first (1a) used to model dye uptake across a continuous range of cell subsets, ideally using a sample which is stained with a single concentration of the barcoding dye (external standard). In the second step of de-skewing (1b), the uptake model from step 1a is used to predict dye uptake for each cell in the barcoded dataset, and corrected values are generated by subtracting the observed and predicted dye uptake. The resulting distributions have a greatly reduced variance compared to the original uncorrected barcoding channels, which allows the modeling step (2) to estimate assignment probability using parametric (Gaussian mixture modeling, GMM (240)) or non-parametric (Jenks natural breaks (241)) methods. If multiple dyes are used, the probabilities for each individual sample can be refined by using a multivariate GMM to estimate the probabilities of each sample rather than each barcoding level. Using the probabilities predicted by population modeling step, individual cells are assigned to each well in step 3 by assigning cells to the most probable level and discarding cells with unacceptable probabilities of originating from more than one level or those in the tails of the fitted distribution.
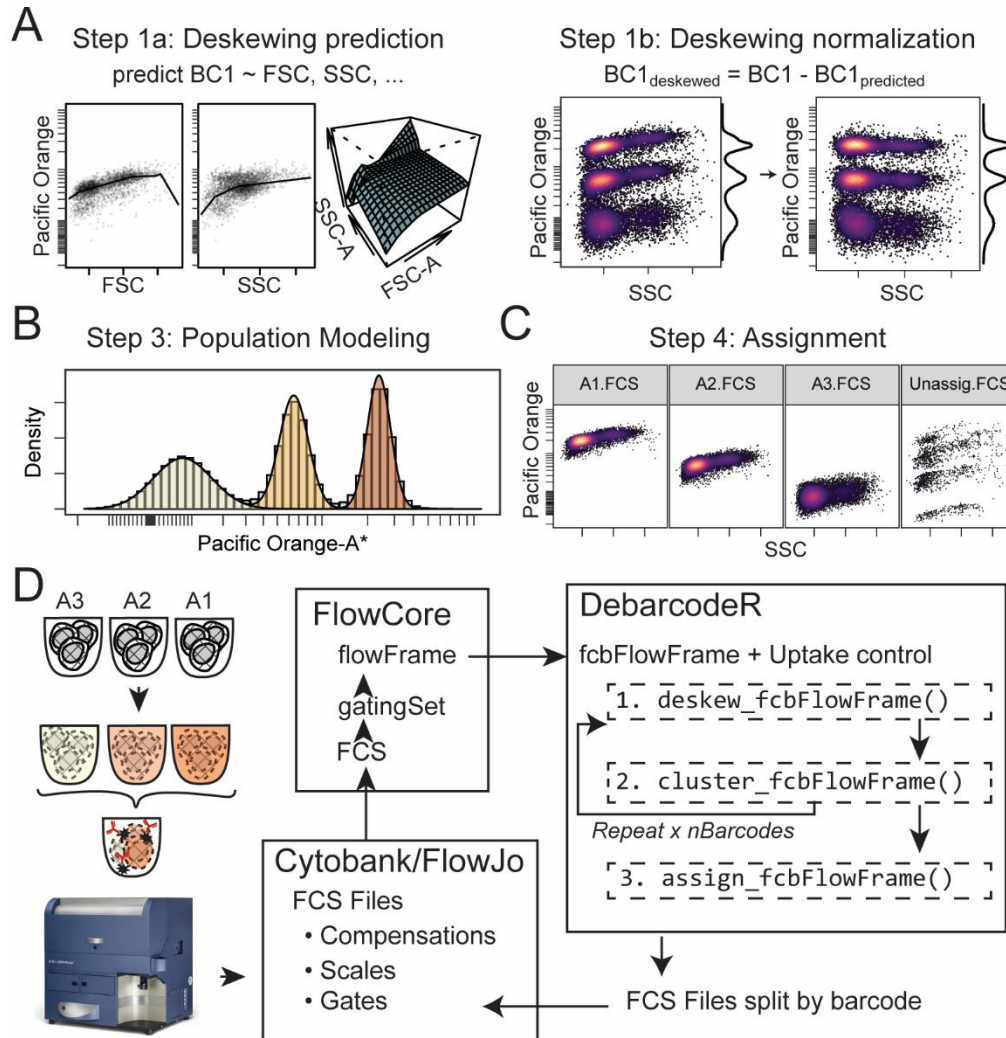
Figure 5.2. DebarcodeR assigns cells to samples without using biaxial gates

A, In step 1, the external standard is used to build a model of dye uptake based on non-barcoding channels that is used to deskew the barcoding channels to correct for differential dye uptake; **B,** Gaussian mixture modeling is applied to the deskewed barcoding intensities to estimate barcoding level probabilities; **C,** Cells are assigned to samples and written to new FCS files. **D,** User facing workflow: cells in samples are barcoded, pooled, and acquired, preprocessed using available software packages and imported to R using the CytoML package. Each group of files to be barcoded is de-skewed, clustered, and assigned to specific well based on a user defined well-plate layout.

5.2.4 <u>Computational and experimental approaches account for differential dye uptake</u>

One approach to modeling dye uptake was demonstrated by Knijnenburg et al. ([239]) using a constrained regression modeling approach to model fluorescence intensity as a function of forward scatter (FSC - a measurement of cell size) and side scatter (SSC - a measurement of cell granularity). Applied to FCB deconvolution, constrained regression modeling improved the separation between populations and led to improved clustering using k-means or Gaussian mixture modeling. Though this approach worked well on some datasets, it performed poorly in several common real-world scenarios. One limitation was revealed when one or more samples differ in the distribution of cell subsets present, which can occur when cells are exposed to cytotoxic conditions or multiplexing multiple patient samples or cell lines. Since the regression model is trained on the same dataset that is being demultiplexed, it attempts to minimize the total variation across all levels under the assumption of a single Gaussian distribution, rather than the variation within each barcoded level represented by a set of k Gaussian distributions, one for each level.

5.2.5 <u>Additional experimental controls improve modeling of dye uptake</u>

In order improve the model of dye uptake and avoid overfitting, it is essential to have a separate control for dye uptake – the 'external standard' – one which is biologically identical to the fully barcoded sample but is stained with a single concentration of each barcoding dye. In cases where this control is not available, the compensation control used to set-up the instrument can also fulfill this role. By training the regression model on this external standard, dye uptake can be precisely predicted based on the non-barcoding parameters including FSC and SSC. Using a separate external standard also removes the need for constraints on the regression model, which are otherwise needed to avoid spurious fitting in sparse areas of cellular space and allows

more flexible predictive models to be applied to model dye uptake. Multivariate adaptive regression splines (MARS) ([242]), a regression modeling approach that dynamically models non-linear interactions between predictors, was found to perform well when an uptake control was present, and the 'earth' implementation of MARS ([243]) was selected as the default regression modeling approach in the DebarcodeR pipeline.

5.2.6 Direct measurement of dye uptake using an internal standard

The number of distinct dye levels which can be resolved by DebarcodeR is determined by width (variance) of the Gaussian distributions after de-skewing, which is determined by what fraction of the variance in dye uptake can be accounted for by the uptake model (R^2). Whereas previous approaches to morphology correction rely on scatter to indirectly measure dye uptake ([239]), we sought to directly measure dye uptake using additional barcoding dyes as an 'internal standard'. This internal standard is specific to each cell, rather than each sample. In addition to providing a direct measurement of dye uptake for each cell, the internal standard can also be used to account for any variation between samples introduced by liquid handling errors, which provides added robustness for high-throughput applications. Additionally, the inclusion of the internal standard has the potential to reduce barcode heteroskedasticity - uneven variation in predicted dye uptake across cell states - which could contribute to uneven loss of cell subsets.

5.2.7 Estimation of sample origin probabilities by Gaussian mixture modeling

Whereas a direct approach to modeling barcode populations must separate clusters in high dimensional space ([244]), the 'de-skewing' step in DebarcodeR removes the influence of the non-barcoding channels on barcode dye uptake making them amenable to univariate clustering. Rather than cluster the cells directly, DebarcodeR uses Gaussian mixture modeling (GMM) to estimate the probability that each cell originated from each level. Each barcoding channel is

initially modeled independently by fitting independent univariate models. Theoretically this approach should yield optimal assignments if each well in a level has been barcoded uniformly, though in practice liquid handling variation can cause individual wells to drift slightly from a perfect grid. To account for this drift, a multivariate GMM is fitted initializing on the univariate

5   population assignments via an E-M algorithm implemented by mclust ([240]), yielding a probabilistic model of each well in the barcode.

5.2.8 Defining metrics for confident barcode assignments

The output of the Gaussian mixture modeling step is a matrix consisting of rows for each cell and columns for each modeled population with estimates of the likelihood of originating

10 from each population. In order to interface with other flow cytometry analysis pipelines, each cell must be assigned to a discrete sample. Rather than simply assign each cell to its most likely well of origin, DebarcodeR includes two user defined thresholds to account for uncertainty and potential misassignments – ambiguity and relative likelihood. The ambiguity cutoff culls cells between populations by normalizing likelihood across samples (by row) such that cells that have

15 an unacceptable probability (default, $> 5\%$) of originating from a different sample are left unassigned. The relative likelihood cutoff culls cells from areas of low density by normalizing likelihood across cells (by column) such that cells that are less than $1/x$ (default, $x = 8$) likelihood relative to the most likely cell are left unassigned. The resulting assignments are returned as a logical filter, allowing the samples to be split into separate files using existing computational

20 pipelines (Figure 5.2B) ([245]).

5.3 Results

5.3.1 <u>Incorporation of an internal standard improved uptake modeling</u>

   The first step of DebarcodeR pipeline is modeling of dye uptake and correction for cell

intrinsic factors which influence barcode staining. DebarcodeR was applied to Dataset 2,

5   consisting of 48 barcoded well which were each acquired separately to provide ground truth

labels for well of origin. The prior gold standard (Model 2, Figure 5.3A), using Forward Scatter

(FSC) and Side Scatter (SSC) ([239](#)), was compared to the new DebarcodeR approach with the

addition of an internal standard (Model 3, Figure 5.3A). The more flexible regression modelling

approach used by DebarcodeR allowed for the inclusion of additional covariates including

10   Height and Width of both Forward Scatter and Side Scatter (Model 4, Figure 5.3A) and the

addition of the internal standard (Model 5, Figure 5.3A) decreased the estimated variance of each

peak further, allowing for 50% more levels per log-decade using a conventional fluorescent flow

cytometer (Figure 5.3A).
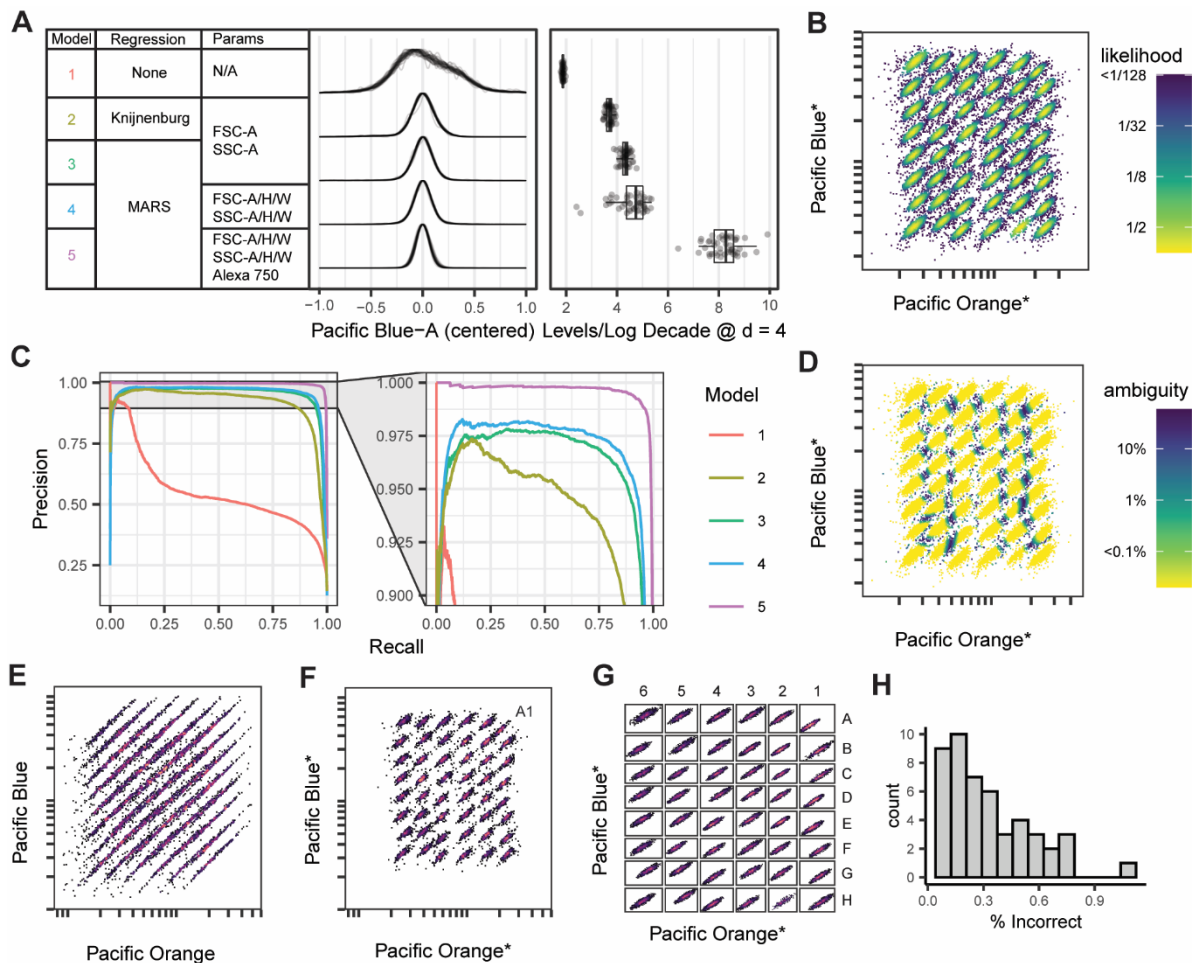
Figure 5.3. DebarcodeR with an internal standard outperforms pervious approaches to debarcoding

A, Comparison of different uptake correction approaches on 48 separately run wells showing reduced population variation and theoretical barcoding capacity assuming separation of each population by 4σ; **B,** Visualization of the relatively likelihood parameter used to eliminate cells from low density areas. **(C)** Precision recall curves for each of the five models after concatenation and debarcoding, using well as ground truth; **D,** Visualization of the ambiguity parameter used to eliminate cells likely to have originated from neighboring wells; **E** Original barcoding channels prior to morphology correction; **F,** Barcoding channels after morphology correction using model 5, well A1 highlighted; **G,** Barcoding channels are plotted on each assigned well after Gaussian mixture modeling and assignment; **H,** Misassignment rate for each well defined as % of cells not originating from the true well (Mean 99.8%, 95%CI = [99.3-100%]).

5.3.2 <u>Populations after 'de-skewing' were accurately modeled by GMM</u>

The parametric modeling approach used by DebarcodeR provides control over yield and misassignments, as demonstrated in Figure 5.3C, which shows precision recall curves for each of the different uptake models at different tolerances for misassignment. Two user-defined cutoffs can be specified to control misassignments: relative likelihood (Figure 5.3B) and ambiguity (Figure 5.3D). The output of the complete pipeline using model 5 is illustrated in Figure 5.3E-H on a Dataset 2. Overall, 92% of cells were assigned to wells and of those, 99.7% were assigned correctly with a range of 98.9 – 100% of accuracy across all 48 wells (Figure 5.3G).

5.3.3 <u>DebarcodeR outperforms manual gating for heterogenous samples</u>

To test the ability of DebarcodeR to analyze datasets consisting of heterogenous samples, mouse splenocytes and human PBMCs were fixed, permeabilized, and distributed into alternating wells of a 48 well barcoding plate in a checkerboard pattern (Dataset 3, Fig 3A). The cells were pooled, stained with antibodies against human and mouse CD45, and analyzed. Intact, single, barcoded cells were selected for debarcoding (Figure 5.1C) and all debarcoding steps were done without referencing the CD45 markers. The debarcoding process is depicted in Figure 5.4B, with initial assignments provided by independently assigning each barcoding channel, and final assignments determined using a multivariate GMM initialized by the univariate assignments. Though ground truth cannot be firmly established for this dataset, each well should consist of cells from a single species, and cells from the opposite species are assumed to be misassigned. Using this standard, the pipeline successfully assigned 88% of cells with a misassignment rate of 0.8% (Figure 5.4C-D). Though this panel did not include markers for specific cell subsets, three populations are evident on the FSC vs. SSC plot (Figure 5.4E), which we denote as lysed cells, lymphocytes, and monocytes. The fraction of cells from each of these

197
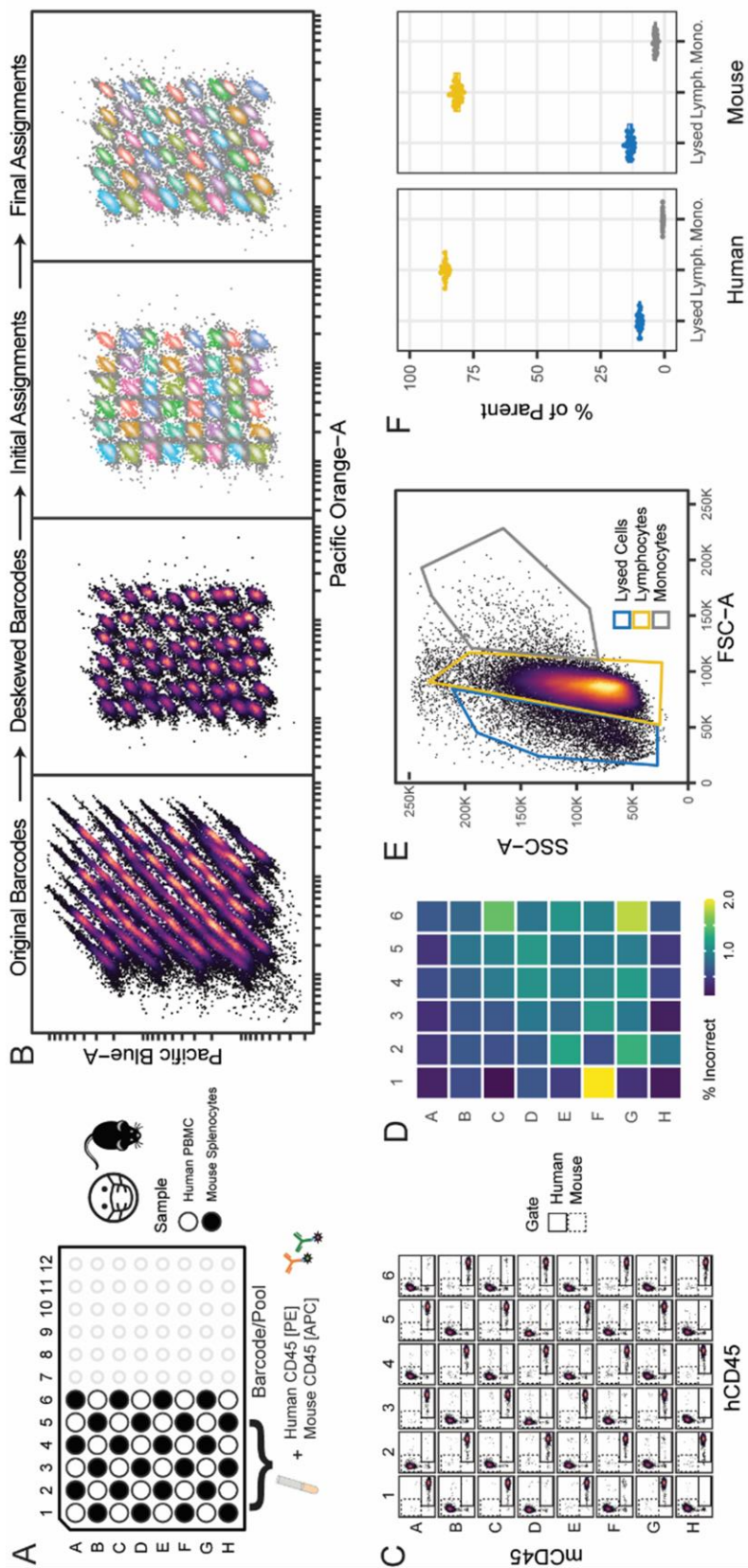
Figure 5.4. DebarcodeR accurately assigns subpopulations within heterogeneous samples.

A, Human PBMCs and mouse splenocytes were fixed and permeabilized and distributed into alternating barcoding wells as depicted. Cells were pooled, Fc blocked, and stained for human and mouse CD45; **B,** Illustration of the debarcoding processes showing initial assignments with 5% ambiguity tolerance, likelihood tolerance of 1/12, (18% unassigned) and final assignments after multivariate EM optimization (10% unassigned); **C,** Biaxial plots for each assigned well, demonstrating that each well consists of cells from a single species; **D,** Quantification of cells from the opposite species in each well; average misassignment rate of 0.8%; **E,** Gating scheme for sub-populations present in each sample which should be preserved; **F,** Sub-population composition from each assigned well showing uniform assignment of populations across wells.

198

population estimated via back-gating was comparable across all wells (Figure 3F), demonstrating that heterogenous samples can be reliably debarcoded without the need for gating each population prior to debarcoding.

5.4 Discussion

5   The changes to barcoding described here significantly improved barcoding accuracy and scalability by improving elements of both the bench experimental steps and the computational analysis. Some users of DebarcodeR may wish to apply the algorithm to older data. In this case, the experimental components, the internal and external standard, are unlikely to be available. However, the pipeline can still be applied using included implementations of the constrained

10   regression modeling approach described by other investigators (Figure 3.5, adapted from (239)). For investigators who aim to most effectively use FCB, inclusion of these additional controls greatly facilitated the debarcoding process here and this is highly recommended going forward.

Compared to the original gating based forward deconvolution strategy (231), the DebarcodeR approach provides higher cell recovery, fewer mis-assignments, and reduced

15   analysis time to minutes. Though the addition of the internal standard requires the use of a fluorescence channel which could otherwise be used for a biological marker or barcoding channel, the value of additional markers or multiplexing capacity is limited if cells are not accurately assigned to samples. The external standard is critical for accurately modeling dye uptake by DebarcodeR and the protocols included make use of cells which would otherwise be

20   discarded during the staining steps.
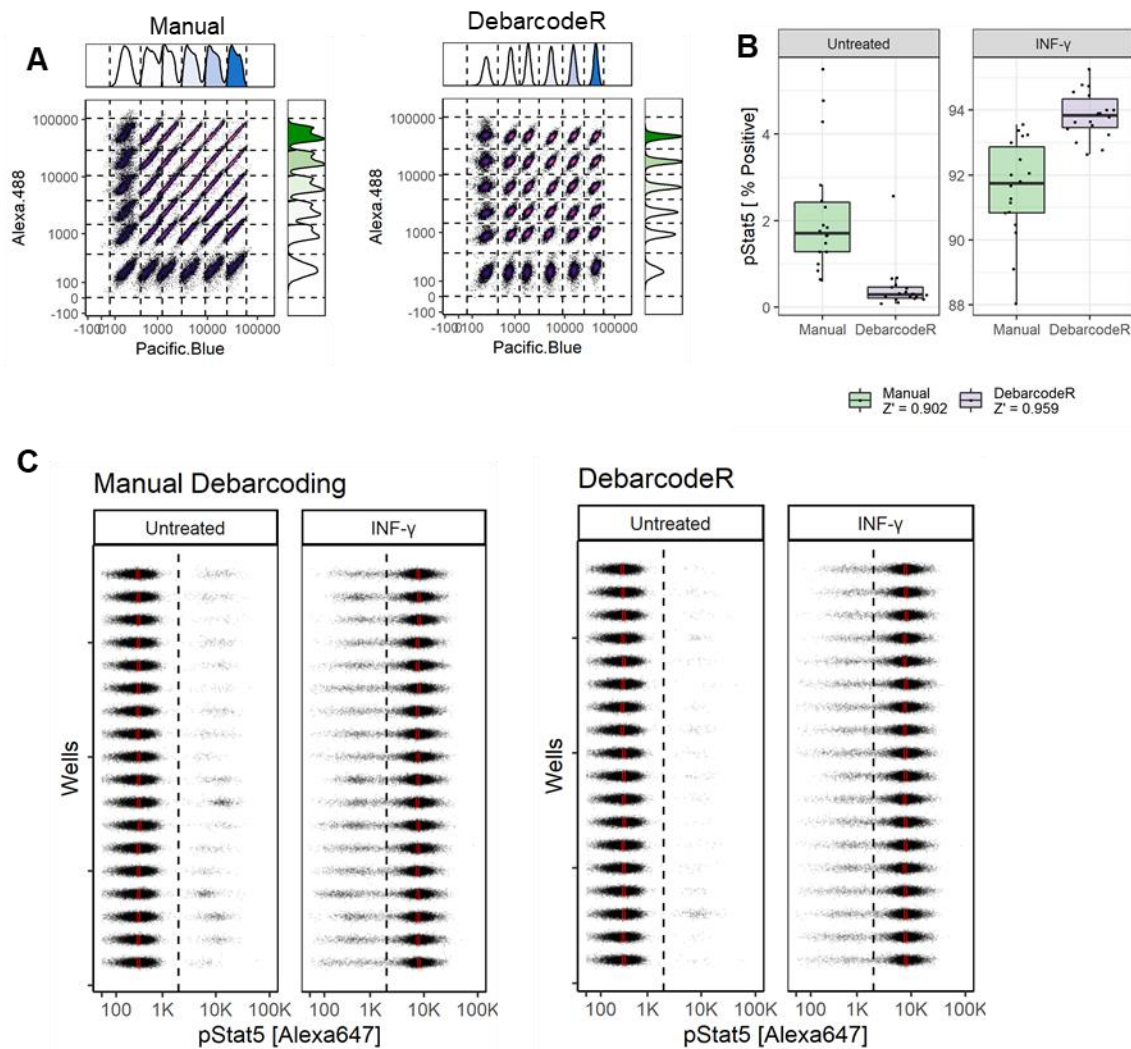
Figure 5.5. Application of DebarcodeR to Knijnenburg TA, 2011 / Krutzik PO, 2006 Dataset

This figure demonstrates the DebarcodeR implementation of the Knijnenburg regression based morphology correction approach originally written in MATLAB and is comparable to Figure 4 and Supplement 7 from Knijnenburg TA, 2011 and Figure 3 from Krutzik P, 2006. Data were obtained from the supplement of Knijnenburg TA and consist of U937 cells labeled stimulated in alternating wells with IFN-γ (10 μg/mL for 10 min) barcoded in with six concentrations of Pacific Blue and six concentrations of Alexa 488; **A,** Comparison between traditional debarcoding (Jenks natural breaks classification on original channels) and DebarcodeR after morphology correction; **B,** Comparison between manual debarcoding and DebarcodeR on the basis of pStat5 positivity with or without simulation; **C,** Jittered dot plot of cells from individual wells demonstrating reduced pStat5 in the untreated wells.

The three steps presented here (Figure 5.2A) are modular and can be replaced with differing algorithms. This type of modular framework is recommended for cytometry and has he potential to largely automate data analysis ([246], [247]). DebarcodeR fits into these workflows by providing a ready-to-use pipeline for debarcoding FCB data using MARS for uptake correction, GMM for

5 barcoded population modeling, and discrete assignment based on the modeled probabilities. Each of these steps can be modified or replaced to suit the task at hand, for example, omitting the step of assigning cells to individual FCS files and instead using the estimated cluster probabilities to estimate parameters of interest (MFI, percent positive, etc.) directly.

The principle underlying the 'de-skewing' step of DebarcodeR is that for a given cell,

10 staining intensity is directly proportional to dye concentration and independent of the specific dye used. For most purposes, these assumptions are true, but the exceptions provide valuable insights into the limitations of barcoding. It is tempting to expand the barcoding capacity of a single dye by adding additional dilutions or even a level with no dye at all. In practice, we find that two factors limit expanding barcoding by further dilution: first, fluorescent spillover from

15 other channels into the barcoding channel, and second, labeling with unquenched dye during the pooling step. The careful selection and titration of barcoding dyes and the application of new spectral unmixing technology has the potential to mitigate the first limitation and further extend barcoding capacity ([248-250]).

Another deviation from the concentration-dependent labeling assumption is found when

20 comparing dye uptake between barcoding channels and the internal standard. Different dye chemical structure types may react at different rates and uptake differentially in cells. For example, two cells which have equal uptake of Alexa Fluor 750, can have different uptake of Pacific Blue and Pacific Orange (Figure 3.6). In the case of Alexa Fluor 750, this may be due to

201

excitation with different laser lines and the difficulty of counting far-red photons. In the case of

Pacific Orange and Pacific Blue, the degree of correlation was much higher on average, though

dead cells often appear to take up less Pacific Orange than Pacific Blue (Figure 3.6). This

phenomenon has been observed in the case of live cell staining ([251]), though the exact cause is

5 unknown. It is likely that this limitation can be mitigated by using structurally related dyes for

both the internal standard and barcoding channels that are expected to have roughly equal

reactivity with proteins, such as a set of cyanine dyes or the Alexa Fluor family of sulfonated N-

Hydroxysuccinimide (NHS) ester dyes.

An alternative approach to expanding barcoding capacity is to reduce the spacing

10 between levels to accommodate more levels within the same range of fluorescence intensities. In

addition to the variance in fluorescence intensity for single sample, it is worthwhile to consider

the variation that may be introduced by pipetting and to expand the level spacing to

accommodate 5-10% drift between samples, though this could be further reduced by robotic

liquid handling. With manual liquid handling in 96 well plates, the cost benefits of barcoding

15 begin to diminish after pooling 48 samples, as plastic consumables become the cost-limiting

component and large cell counts necessitate larger antibody staining volumes ([230]). However,

compared to conventional flow cytometry using an automated plate loader, we estimate that

performing FCB with DebarcodeR for four 96 well plates uses ten-fold less cytometer time, is

three-fold faster than manual gating debarcoding, and has 48-fold reduced antibody and reagent

20 costs (Table S6).

The parametric nature of the DebarcodeR approach implemented here provides estimates

of assay reliability and robustness which may enable the application of fluorescent cell barcoding
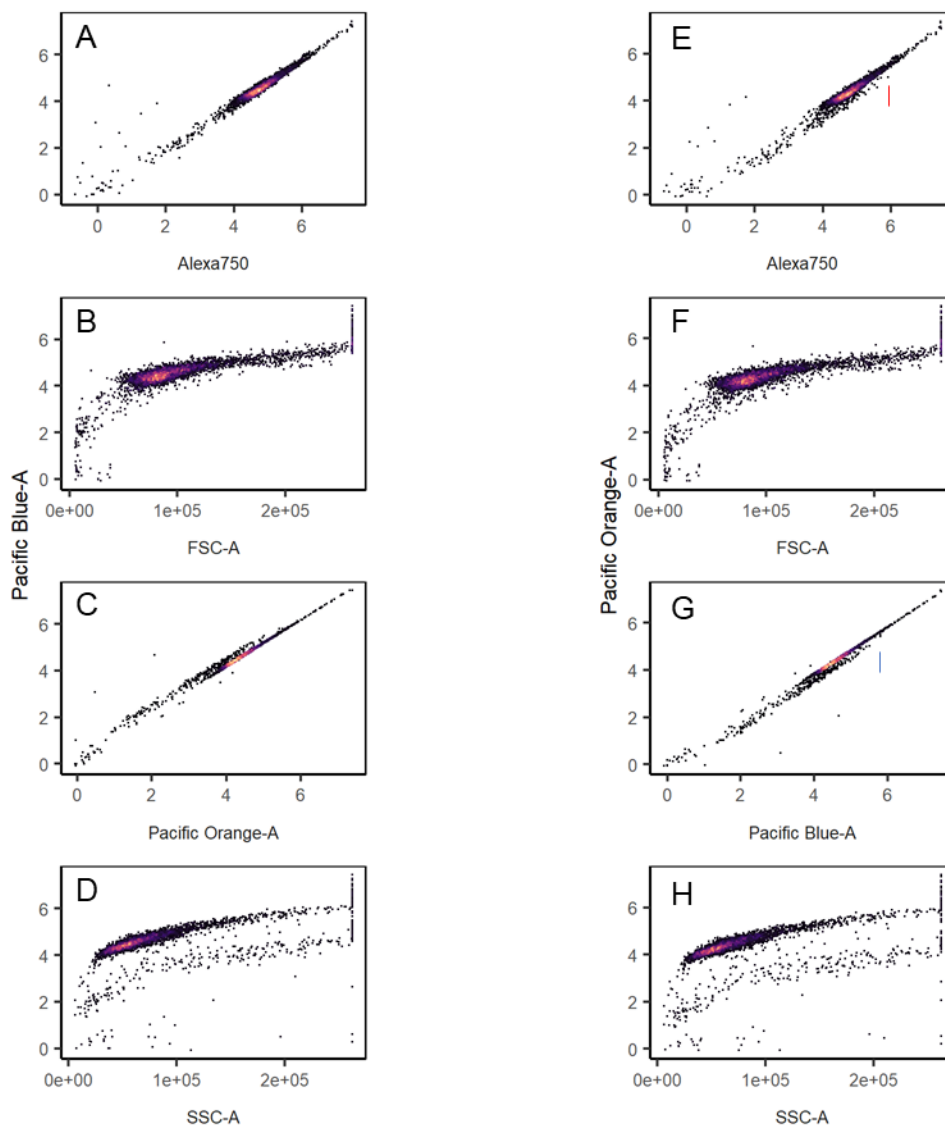
Figure 5.6. Differential dye uptake between Alexa Fluor 750, Pacific Orange, and Pacific Blue NHS esters.

Correlation between FSC, SSC, Alexa 750, and Pacific Orange / Pacific Blue vs Pacific Blue (A-D) and Pacific Orange (E-H). Comparing panel A to panel E, there are some cells in panel E which took up identical amounts of Alexa 750 but different amount of Pacific Orange (red line, panel E). Comparing panels C and G, there are cells which took up identical amounts of Pacific Blue, but differing amounts of Pacific Orange (blue line, panel G).

in more rigorous environments such as clinical research and clinical flow cytometry. Sample

level multiplexing has the potential to reduce instrument use time, conserve valuable reagents,

and improve data robustness, but these benefits are only realized in practice if the multiplexed

data can be reliably and reproducibly demultiplexed. The DebarcodeR software package

5   implements an approach to convolution of FCB data that is designed to model the cell staining

process and accounts for variation introduced by differential dye uptake and pipetting error. The

pipeline can also be applied to existing FCB datasets, including those originally intended for

manual debarcoding with biaxial gates, as well as new barcoding schemes designed specifically

for DebarcodeR (see Protocols 4 and 5 in Supplementary Information).

10   While the immediate benefits of FCB and DebarcodeR may be realized in the form of

reduced reagents consumption and analysis time for existing experimental questions, these tools

enable the application of high dimensional cytometry to entirely new questions which are not

otherwise feasible. The original motivation for DebarcodeR was to enable large scale screening

of microbial extracts for modulators of cell signaling in Multiplexed Activity Metabolomics

15   (MAM) ([228](#)). This pipeline has since been generalized for screening synthetic compound

libraries as Multiplexed Activity Profiling (MAP), taking advantage of FCB multiplexing to

include biological controls within each barcoded sample to identify potential activity([196](#)). In a

typical workflow, cell lines are treated with 48 samples including controls and assayed for five

biological markers, yielding 240 individual immuno-assays per barcoded tube, and 1,920 assays

20   when four plates pooled into eight tubes are analyzed per hour at the cytometer. Beyond

expanding the number of unique chemical and biological perturbations, DebarcodeR has the

potential to be useful in other applications such as multiplexing timepoints and doses for

improved screening ([252](#)), screening for human immune monitoring in COVID-19 or cancer

immotherapy ([253](#)), screening antibody hybridoma ([254](#)) or CRISPR clones, or analyzing

genetically encoded fluorescent barcodes ([255](#), [256](#)).

5.5 References

196. J. H. Boyce, B. J. Reisman, B. O. Bachmann, J. A. Porco, Jr., Synthesis and Multiplexed Activity Profiling of Synthetic Acylphloroglucinol Scaffolds. *Angew Chem, Int Ed* **60**, 1263-1272 (2021).

228. D. C. Earl *et al.*, Discovery of human cell selective effector molecules using single cell multiplexed activity metabolomics. *Nat Commun* **9**, 39 (2018).

230. P. O. Krutzik, M. R. Clutter, A. Trejo, G. P. Nolan, Fluorescent cell barcoding for multiplex flow cytometry. *Curr Protoc Cytom* **Chapter 6**, Unit 6 31 (2011).

231. P. O. Krutzik, G. P. Nolan, Fluorescent cell barcoding in flow cytometry allows high-throughput drug screening and signaling profiling. *Nat Methods* **3**, 361-368 (2006).

232. B. Akkaya *et al.*, A Simple, Versatile Antibody-Based Barcoding Method for Flow Cytometry. *J Immunol* **197**, 2027-2038 (2016).

233. E. R. Zunder *et al.*, Palladium-based mass tag cell barcoding with a doublet-filtering scheme and single-cell deconvolution algorithm. *Nat Protoc* **10**, 316-333 (2015).

234. W. L. Tsai *et al.*, High throughput pSTAT signaling profiling by fluorescent cell barcoding and computational analysis. *J Immunol Methods* **477**, 112667 (2020).

235. J. W. Jacobberger, Increasing the power of cytometry. *Nat Methods* **3**, 343-344 (2006).

236. A. Cossarizza *et al.*, Guidelines for the use of flow cytometry and cell sorting in immunological studies. *Eur J Immunol* **47**, 1584-1797 (2017).

237. J. M. Irish *et al.*, B-cell signaling networks reveal a negative prognostic human lymphoma cell subset that emerges during tumor progression. *Proc Natl Acad Sci U S A* **107**, 12747-12754 (2010).

238. P. O. Krutzik, J. M. Crane, M. R. Clutter, G. P. Nolan, High-content single-cell drug screening with phosphospecific flow cytometry. *Nat Chem Biol* **4**, 132-142 (2008).

239. T. A. Knijnenburg *et al.*, A regression model approach to enable cell morphology correction in high-throughput flow cytometry. *Mol Syst Biol* **7**, 531 (2011).

240. C. Fraley, A. E. Raftery, T. B. Murphy, L. Scrucca. (2012).

241. G. F. Jenks, The data model concept in statistical mapping. *International yearbook of cartography* **7**, 186-190 (1967).

242. J. H. Friedman, Multivariate Adaptive Regression Splines. *Ann Stat*, 1-67 (1991).

243. S. Milborrow. (2011).

244. Y. Ge, S. C. Sealfon, flowPeaks: a fast unsupervised clustering for flow cytometry data via K-means and density peak finding. *Bioinformatics* **28**, 2052-2058 (2012).

245. F. Hahne *et al.*, flowCore: a Bioconductor package for high throughput flow cytometry. *BMC Bioinf* **10**, 106 (2009).

246. K. E. Diggins, P. B. Ferrell, Jr., J. M. Irish, Methods for discovery and characterization of cell subsets in high dimensional mass cytometry data. *Methods* **82**, 55-63 (2015).

247. Y. Saeys, S. Van Gassen, B. N. Lambrecht, Computational flow cytometry: helping to make sense of high-dimensional immunology data. *Nat Rev Immunol* **16**, 449-462 (2016).

248. J. P. Nolan, D. Condello, Spectral flow cytometry. *Curr Protoc Cytom* **Chapter 1**, Unit1 27 (2013).

249. J. P. Robinson, Spectral flow cytometry-Quo vadimus? *Cytometry, Part A* **95**, 823-824 (2019).

250. L. M. Park, J. Lannigan, M. C. Jaimes, OMIP-069: Forty-Color Full Spectrum Flow Cytometry Panel for Deep Immunophenotyping of Major Cell Subsets in Human Peripheral Blood. *Cytometry, Part A* **97**, 1044-1051 (2020).

251. L. D. Hughes, R. J. Rawle, S. G. Boxer, Choose your label wisely: water-soluble fluorophores often interact with lipid bilayers. *PloS One* **9**, e87649 (2014).

252. L. A. Harris *et al.*, An unbiased metric of antiproliferative drug effect in vitro. *Nat Methods* **13**, 497-500 (2016).

253. A. R. Greenplate, D. B. Johnson, P. B. Ferrell, Jr., J. M. Irish, Systems immune monitoring in cancer therapy. *Eur J Cancer* **61**, 77-84 (2016).

254. M. Lu, B. M. Chan, P. W. Schow, W. S. Chang, C. T. King, High-throughput screening of hybridoma supernatants using multiplexed fluorescent cell barcoding on live cells. *J Immunol Methods* **451**, 20-27 (2017).

255. T. Maetzig *et al.*, A Lentiviral Fluorescent Genetic Barcoding System for Flow Cytometry-Based Multiplex Tracking. *Mol Ther* **25**, 606-620 (2017).

256. D. Cai, K. B. Cohen, T. Luo, J. W. Lichtman, J. R. Sanes, Improved tools for the Brainbow toolbox. *Nat Methods* **10**, 540-547 (2013).

CHAPTER 6 – MULTIPLEXED ACTIVITY PROFILING OF SYNTHETIC ACYLPHLOROGLUCINOLS

Note: This work described in this chapter was the result of a collaboration between our group, and Dr. John Porco's group at the Boston University. Dr. Jonathan Boyce led the collaboration from Dr. Porco's group and performed all the synthesis and chemical characterization detailed in this chapter. My role in this project was to apply Multiplexed Activity Profiling (MAP) to characterize the bioactivity of Jonathan's compounds. This material in this chapter was published in Angewandte Chemie in 2021 ([196](#)) with Jonathan and me as co-authors. In this chapter, I have included all the data, figures, and tables from the main manuscript, as well as the supplementary material that pertains to my contributions to the paper. For cross-references to supplementary material that pertains to Jonathan's work, I have referenced our published manuscript.

6.1 Introduction

Polycyclic polyprenylated acylphloroglucinols (PPAPs) ([257](#)) have played an important role in chemical synthesis ([258-269](#)) and pharmacological studies due to their diverse biological activity profiles ([270-292](#)). PPAPs are classified as "type A" when the acyl group is at the bridgehead position (e.g. garcimultiflorone A (**1**)) and "type B" when the acyl group is at the α-position of the β-hydroxyenone [for example, isogarcinol (**2**), didehydroxyisogarcinol (**3**), and garcinol (**4**)] ([257](#)). With more than 500 members ([257](#)) discovered to date from a variety of plant species (e.g. *Hypericum henryi* and *Clusia congestiflora*) ([293-296](#)), most PPAPs are biosynthetically derived from a common dearomatized carbocation **5** involving a combination of enzyme-catalyzed prenylations and carbocation cyclizations (Figure 6.1a) ([257](#), [297-300](#)). However, despite synthetic efforts over the past 20 years ([258](#), [299](#), [301-312](#)), a synthesis

through such a cation was not realized ([304](#), [308](#), [312](#)) until it was found that formic acid uniformly promoted the C3-cyclization of substrate (−)-**6** to the clusianone core (−)-**8a** through the related carbocation (−)-**7a** (Figure 6.1b) ([309](#)). Alternatively, the type A PPAP core of nemorosone (−)-**8b** could be accessed from diastereomer (+)-**6** through photocyclization of (+)-

5   **7b** at C1 ([310](#)). To date, these biomimetic cyclizations provide the most concise route to type A and B PPAPs ([257](#), [258](#), [301-310](#), [313](#)).

     In comparison to other Brønsted acids, formic acid has inherent properties that may be responsible for promoting cyclization to the clusianone core ([308](#), [314-316](#)): 1) formic acid may stabilize carbocations by solvation effects as evidenced by formate adducts of 1,1-disubstituted

10   olefins ([315](#)); 2) formate adducts of strained bridgehead ketones may facilitate cyclizations that would otherwise be less feasible ([308](#), [314](#), [316](#)). In this study, diversity-oriented synthesis (DOS)
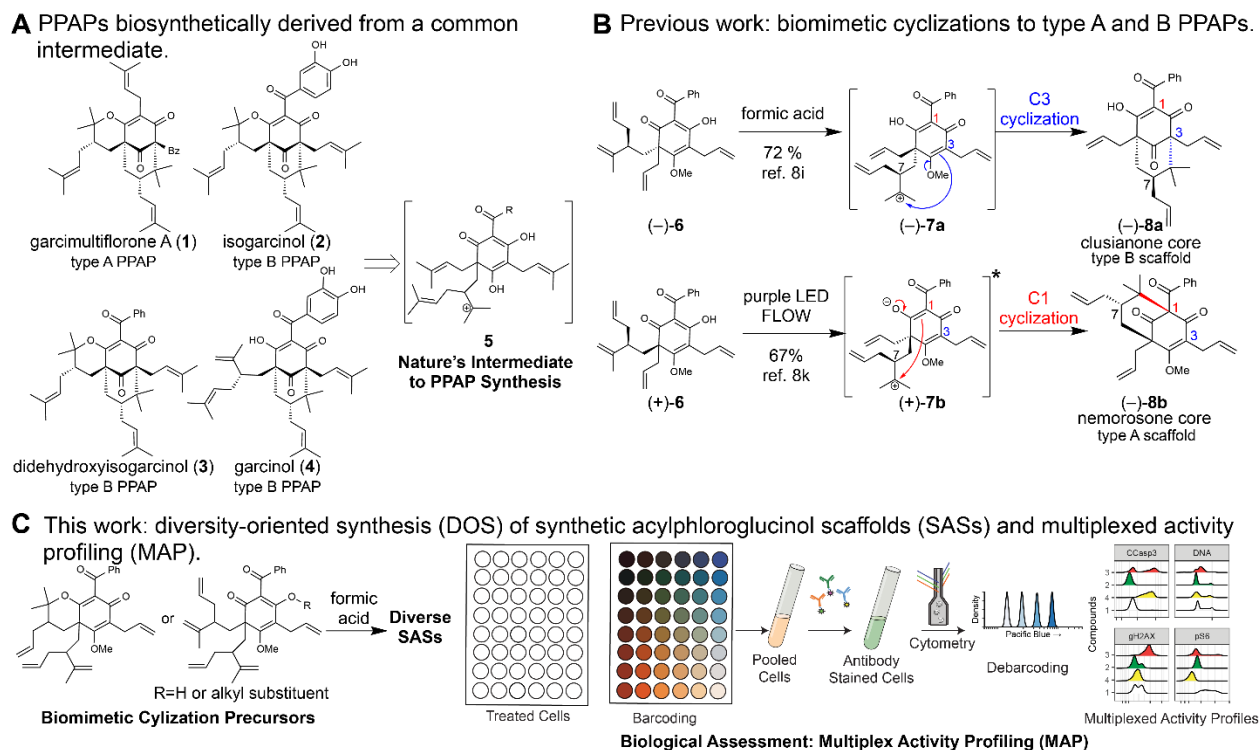
Figure 6.1. Synthesis and Multiplexed Activity Profiling of SASs

a) Representative PPAP natural products biosynthetically derived from a common carbocation; b) Previous work revealed that formic acid uniquely promoted biomimetic C3-cyclization to the clusianone core, and excited-state intramolecular proton transfer resulted in a biomimetic C1-cyclization to the nemorosone core; c) Biomimetic cyclizations lead to a small library of diverse SASs which were evaluated by MAP for biological activities.

(317-322) of synthetic acylphloroglucinol scaffolds (SASs) is described using formic acid in comparison to other Brønsted acids for promoting unique cyclizations and rearrangements, and multiplexed-activity profiling (MAP) is used to evaluate activities in diverse biological pathways (Figure 6.1c) (323).

5   MAP and other high-content assays (324-326) have advantages over traditional "single-target" in vitro screening assays (270) for evaluating compound libraries. In contrast to in vitro-targeted assays, the MAP approach utilizes multiplexed and orthogonal biological readouts to identify active compounds and provides insight into downstream effects on cell signaling and

homeostasis. Moreover, the MAP approach can be adapted to assess specific pathways and mechanistic targets using panels of antibody-based readouts. MAP also reduces the need for secondary counter-screens and allows for rapid identification of "true" hits by including mechanistically validated compound controls that identify nonspecific bioactivity and assay

5   interference. Finally, use of fluorescent cell barcoding (FCB) ([231](#)) for the multiplexed analysis of multiple biological samples reduces liquid handling error and consumption of costly fluorophore-conjugated antibodies.

PPAPs have antitumor ([275](#), [327](#)), antimicrobial ([278](#), [328](#), [329](#)), and immunosuppressive activities ([286](#), [288](#), [290](#), [330](#)), and their proposed molecular targets include histone

10   acetyltransferase (HAT) enzymes (e.g. PCAF and CBP/P300) ([278](#), [280](#), [331](#), [332](#)) and calcineurin ([290](#)). However, recent studies suggest that many of these bioactivities, identified with in vitro assays at low-to-mid micromolar concentrations, may be the result of assay interference rather than true target inhibition.[21] Herein, MAP is used to distinguish genuine activity from assay interference for a diverse collection of SASs produced largely from formic-

15   acid-mediated rearrangements (Figure 6.1c). Previously, we showed that this scalable, flow cytometry-based phenotypic screening system can be applied to fractionated metabolites from extracts for natural product discovery, which is known as multiplexed activity metabolomics (MAM) ([228](#)).

6.2 Results and Discussion

6.2.1 SASs are Produced by Unique Rearrangements in Formic Acid

At the outset of our investigation, we discovered that formic-acid-promoted rearrangement of pyranodienone substrate (±)-**9** ([333]) led to production of the fused lactones (±)-**10**, (±)-**11**, (±)-**12**, (±)-**13**, and (±)-**14** (Table 6.1, entry 1), four of which had notable activity (*vide infra*). Table 6.1 shows a selection of conditions from an extensive reaction screen to optimize product selectivity for active compounds. All rearrangement products (**10** – **14**) deriving from (±)-**9** could be obtained in formic acid over 72 h (Table 6.1, entry 1). After extensive experimentation, we discovered that treatment of (±)-**9** with formic acid at 80°C for 1 h selectively provided the fused lactone (±)-**11** in 33% yield without significant formation of byproducts (Table 6.1, entry 2). Rearrangement of (±)-**9** did not proceed in neat TFA but worked well in TFA mixtures with formic acid (Table 6.1, entries 3–4), suggesting that formic acid may be important for rearrangement. Unexpectedly, lactone (±)-**12**, the most active compound in this study (IC$_{50}$=0.95 μM), could be selectively obtained in 39% yield by reaction of (±)-**9** with TFA (20 equiv) in cyclohexane (Table 6.1, entry 5), in which case the reaction could be facilitated by trace amounts of water at elevated temperatures. However, all other solvents investigated with TFA and formic acid including ether, acetonitrile, acetic acid, DMF, water, and CH$_2$Cl$_2$ did not provide improved yields of rearrangement products. The diversity of products (**10**–**14**) obtained via formic-acid-mediated rearrangement of (±)-**9** provided insight into the proposed mechanism (Figure 6.2a). C-cyclization and oxonium-induced ring
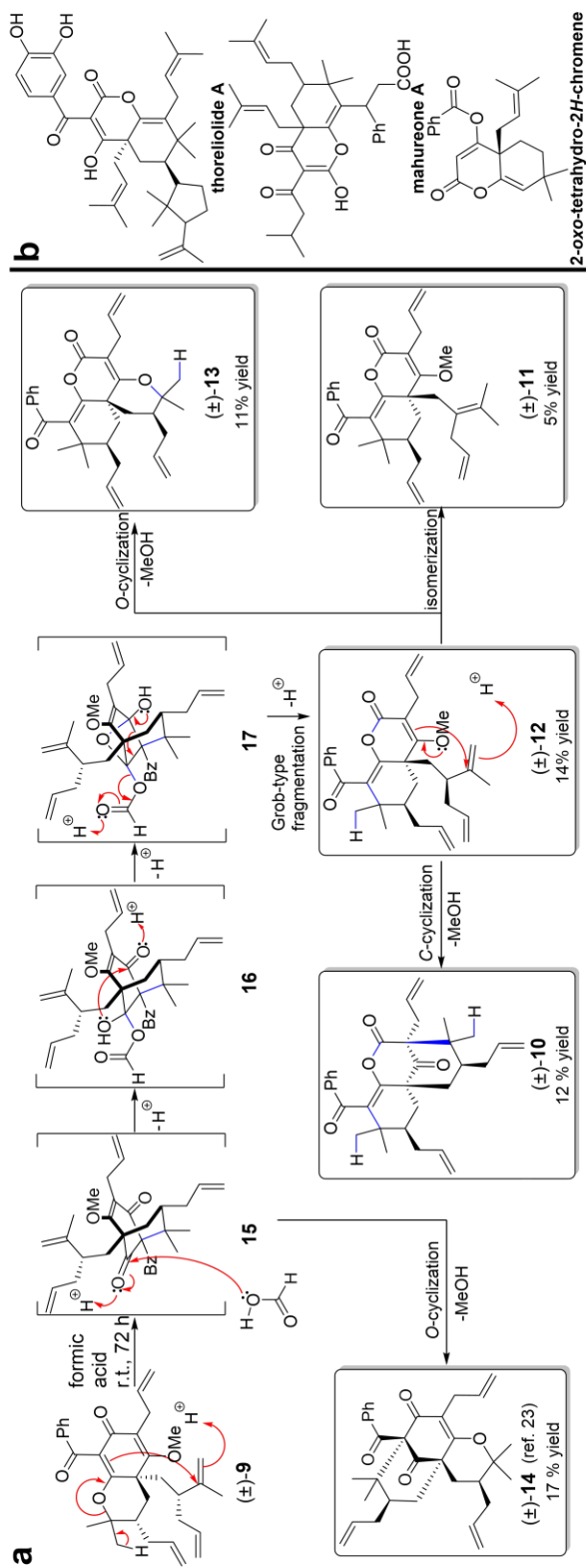
Figure 6.2. Formic Acid Catalyzed Rearrangments of (±)-9

a) Proposed mechanism for rearrangement of (±)-9 in formic acid. b) PPAP natural products and a reported synthetic derivative that possess the 2-oxo-tetrahydro-2H-chromene core found in scaffolds 10, 11, 12, and 13.

Table 6.1. Rearrangement of (±)-9 and optimization of selectivity to favor bioactive products (±)-11 and (±)-12.

(±)-**9** → formic acid, r.t., 72 h → (±)-**10** + (±)-**11** + (±)-**12** + (±)-**13** + (±)-**14** (ref. 23)

Entry	Brønsted Acid	Solvent	Temp/Time	Yield[a]
1	formic acid[b]	neat	r.t., 72 h	12% (±)-**10** + 5% (±)-**11** + 14% (±)-**12** 11% (±)-**13** + 17% (±)-**14**
2	formic acid[b]	neat	80 °C, 1 h	33% (±)-**11**
3	formic acid[b]/TFA (5:1)	neat	r.t., 72 h	18% (±)-**10** + 17% (±)-**11** + 11% (±)-**13** + 10% (±)-**14**
4	formic acid[b]/TFA (1:1)	neat	10 °C, 72 h	11% (±)-**10** + 21% (±)-**11** + 8% (±)-**14**
5	TFA (20 equiv)	CyH	60 °C, 24 h	39% (±)-**12**

213

opening of the pyran to intermediate is supported by the isolation of type A scaffold (±)-**14** from

the reaction mixture. We propose that addition of formic acid to the strained bridgehead ketone

of **15** may lead to formation of hemiketal **16** ([308](#), [314](#), [316](#)). Following cyclization to the

bridged oxetane **17**, Grob-type fragmentation ([334](#), [335](#)) may provide product **12**. A concerted or

5 stepwise Grob-type fragmentation process is supported by DFT calculations (see ([196](#)) Figure

S2). Lactone **12** may also be an intermediate to (±)-**10**, (±)-**11**, and (±)-**13**. The 2-*oxo*-tetrahydro-

2*H*-chromene core present in **10**--**13** is also found in PPAP natural products (e.g. theoliolides A

and B; mahureones A–E) and a synthetic derivative (Figure 6.2b) ([293](#), [294](#), [296](#)).

We also found that (+)-**18** ([333](#)), a diastereomer of **9**, underwent a similar rearrangement

10 in formic acid providing the bioactive [3.3.1]-bicyclic lactone (−)-**19** (a diastereomer of **10**) in

9% yield (Table 6.2, entry 1); its relative stereochemistry was unambiguously confirmed by X-

ray crystal structure analysis (*336*). Relative to its diastereomer **9**, the product diversity resulting

from rearrangement of **18** is significantly decreased. Based on our proposed mechanism, it was

not surprising that the rearrangement did not proceed in TFA or HCl (Table 6.2, entries 4 and 6).

15 Mixtures of formic acid in TFA (1:1) provided SAS (−)-**19** in similar yields (Table 6.2, entries 2

and 3), strongly supporting that formic acid may facilitate its formation. Surprisingly, lactone

(−)-**19** was obtained in 16% yield from TFA in wet HFIP at 60 °C, in which case the reaction

may be facilitated by water at elevated temperatures. We have previously noted that cyclizations

of compounds **9** and **18** to [3.3.1]-bicyclic scaffolds do not proceed in dry TFA ([333](#)). However,

20 such cyclizations could be achieved in the presence of 1% water which may serve as an

appropriate nucleophile for hemiketal formation or contribute to enhanced stability of cationic

intermediates leading to these products. The results described in

Table 6.2. Select conditions from a Brønsted acid screen for rearrangement of (+)-18 to the bioactive SAS (–)-19.
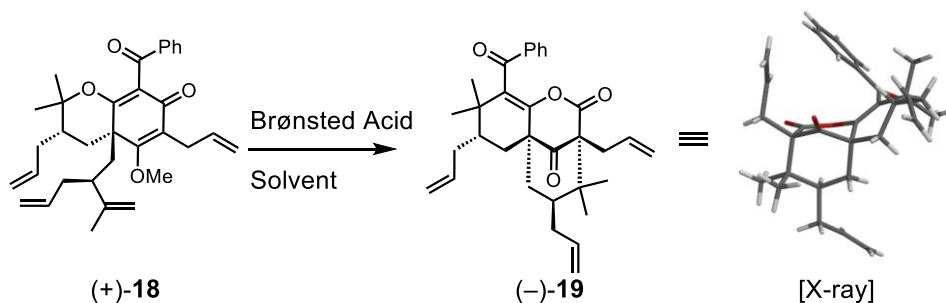
Entry	Brønsted Acid	Solvent	Temp/Time	Yield[b]
1	formic acid[c]	neat	75 °C, 5.5 h	9 %
2	TFA/formic acid[c] (1:1)	neat,	65 °C, 3 h	10 %
3	TFA/formic acid[c] (1:1)	neat	r.t., 4 d	11 %
4	TFA	neat	r.t., 8 h	not isolated[d]
5	TFA (9 equiv)	HFIP[e]	60 °C, 8 h	16 %
6	HCl (4 M)	1,4-dioxane	r.t., 3.5 h	decomp

a] Type B scaffold (+)-**36** and *O*-cyclization product (+)-**38** were also produced (see supporting information, page S10). [b] Isolated yields after purification. [c] 98 % formic acid. [d] Rearrangment not observed. [e] 0.015 M.

stereochemical and DFT-optimized, orbital-alignment analysis (Figures S1–S4).

6.2.2 Cyclization of Substrates Lacking a C3-Allyl Group

We also investigated formic-acid-mediated rearrangements of the corresponding desallyl, dearomatized substrates *meso*-**20a**, (±)-**20b**, and *meso*-**20c** to determine how the C3-allyl group affects cyclization (Figure 6.3) ([333](#)). Diastereomer *meso*-**20a** rearranged to bicyclic lactone (±)-**21** in 38% yield (Figure 6.3a) through a mechanism similar to that described in Figure 6.2a; its structure and relative stereochemistry was unambiguously confirmed by X-ray crystal structure analysis (*337*). Formic-acid-mediated cyclizations of (±)-**20b** and *meso*-**20c** resulted in the type B scaffolds (±)-**22**, (±)-**23**, and (±)-**24** (Figure 6.3b and c). Notably, formic acid provided the highest yield of the less thermodynamically stable 7-*epi* isomer (±)-**23**. Formation of the latter compound may be suppressed by steric interactions in the transition state resulting from an axially-orientated allyl group directed on the concave face of the molecule (see ([196](#)) Figure S4). Relative to the compounds shown in Tables 1 and 2, the absence of a C3-allyl group (Figure 6.3) may reduce the transition state energy for C-cyclization leading to improved yields of the desallyl-PPAP analogues **21**–**24**.

6.2.3 *O*-Allyl and *O*-Homoallyl Groups Facilitate Rearrangement to a Type A Scaffold at Elevated Temperatures in Formic Acid.

For *O*-alkylated derivatives of **20**, the products of formic acid-promoted rearrangements were influenced by the *O*-alkyl group. For example, rearrangement to the type A scaffold **26** required an *O*-allyl or a *O*-homoallyl alkene (Table 6.3). This may be attributed to stabilization of an oxonium intermediate through π-π* donation (e.g. **32**, Figure 6.4). Moreover, product **26** was only formed in formic acid at elevated temperatures suggesting that the solvent may also have a stabilizing effect on intermediate cations of 1,1-disubstituted olefins (e.g. **33** and **34**,

Figure 6.4) ([308](#), [314-316](#)). Indeed, cyclization of the *O*-homoallyl substrate (+)-**25** in formic

acid provided (−)-**26** as a single diastereomer in 42% yield (Table 6.3, entry 1); the relative

stereochemistry was unambiguously confirmed by X-ray crystal structure analysis (*338*). The

related *O*-homoallyl substrate (±)-**28b** led to improved rearrangement yields (60%, Table 6.3,

entry6).
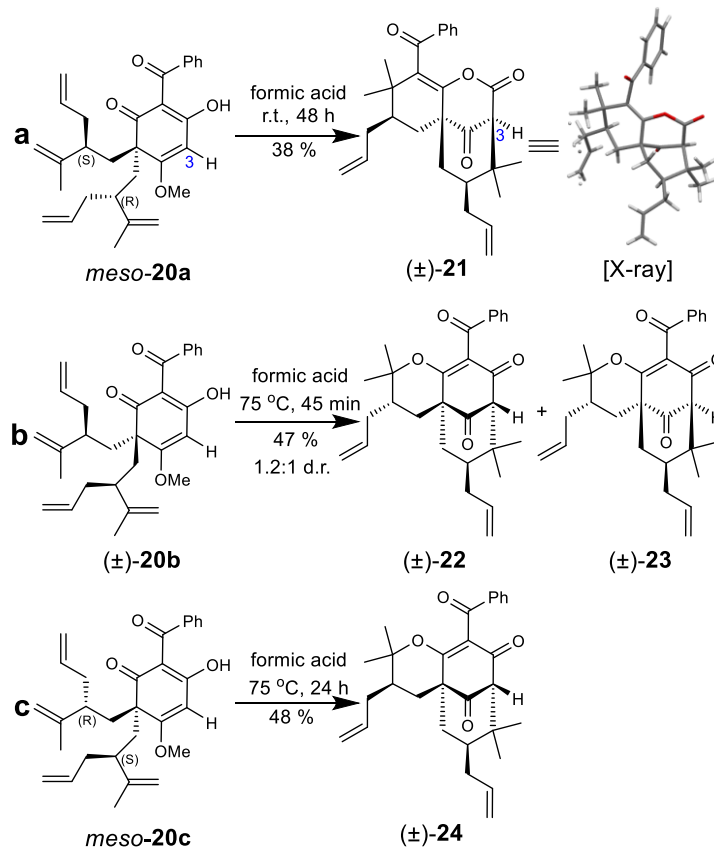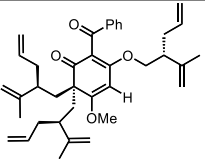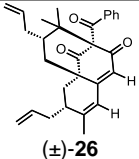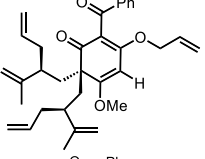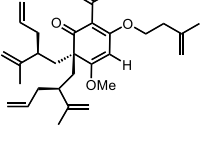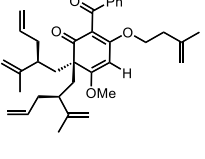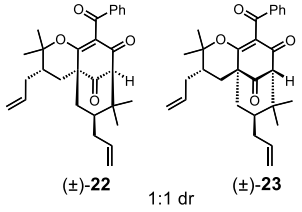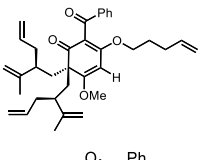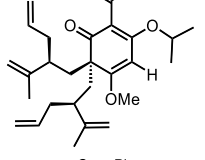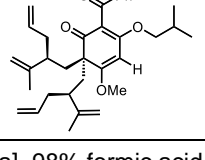
Figure 6.3. Cyclizations of meso-20 a, (±)-20 b, and meso-20 c in formic acid.

Table 6.3. Cyclization of *O*-alkylated, dearomatized acylphloroglucinols.

Entry	Substrate		Conditions[a]	Product	Yield[b]
1		(+)-**25**	formic acid, 75 °C, 1 h	(±)-**26**	42
2		(+)-**27**	formic acid, 75 °C, 45 min	(±)-**26**	16
3		(±)-**28b**	formic acid, 75 °C, 1.5 h	(±)-**26**	60
4		(±)-**28b**	TFA, 75 °C, 1.5 h	(±)-**22** 1:1 dr (±)-**23**	62
5		(±)-**29**	formic acid, 75 °C, 3 h	(±)-**22** + (±)-**23** 1.8:1 d.r.	34
6		(±)-**30**	formic acid, 75 °C, 45 min	(±)-**26**	10
7		(±)-**31**	formic acid, 75 °C, 45 min	(±)-**22** + (±)-**23** 1:1 d.r.	8

[a] 98% formic acid. [b] Isolated yields after purification by silica gel chromatography

Following protonation of **28b**, alkene π-π* donation may stabilize intermediate **32**, thereby enabling Prins cyclization to cation **33** (Figure 6.4) ([339](#)). In this scenario, premature hydrolysis of the *O*-alkyl group appears to be prevented allowing for alkene addition to form the proposed carbocation **34**, and isomerization of the α-stereocenter results in a more sterically favored conformation by directing the allyl group to the convex face of the molecule. Loss of

218

methanol and the pendant *O*-isopentenyl group would then afford the type A scaffold **26**. In contrast to the rearrangement of **28b** in formic acid, we found that TFA led to production of the type B products (±)-**22** and (±)-**23** in 62% yield (1:1.8 d.r. as determined by ^{1}H NMR analysis, Table 6.3, entry 4).
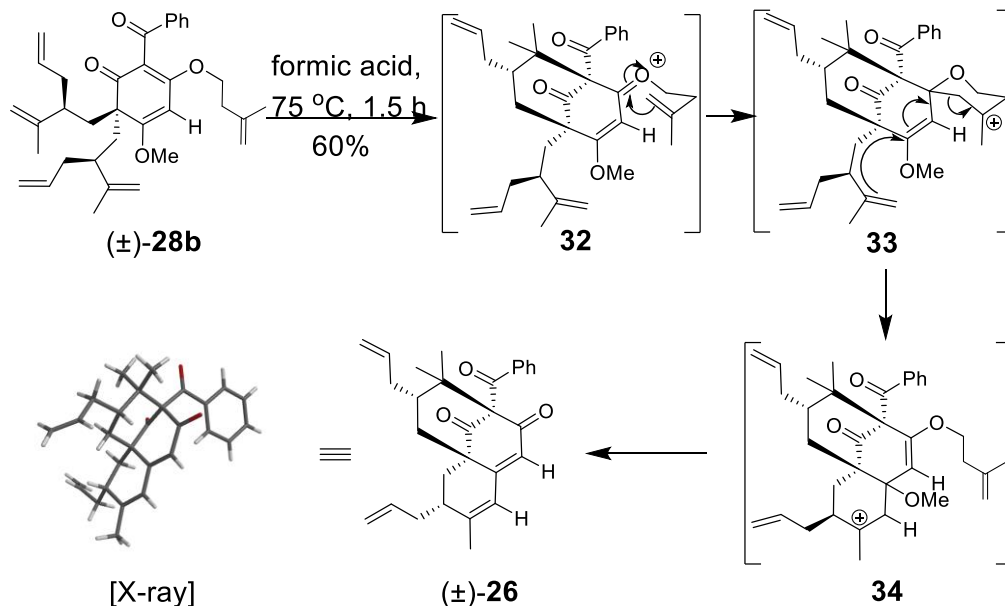
Figure 6.4. Proposed mechanism for formic acid rearrangement of ( )28b to type A scaffold ( )-26.

5

This result supports our hypothesis that formic acid may have a stabilizing effect on the charged intermediates leading to rearrangement product **26** (Figure 6.4) (308, 314-316). When *O*-allyl substrate (±)-**27** was heated in formic acid, (±)-**26** was only produced in 16% yield along with undesired *O*-cyclization products (Table 6.3, entry 2). Based on the proposed mechanism, a

10 lower rearrangement yield was expected as the terminal alkene of **27** may be less electron donating to the resulting oxonium intermediate relative to the 1,1-disubstituted alkene in **28b**. In

comparison, the *O*-pentenyl substrate (±)-**29** only provided type B scaffolds (Table 6.3, entry 5).

Substrates (±)-**30** and (±)-**31** (Table 6.3, entries 6 and 7) with *O*-alkyl groups that lack allyl or

homoallyl alkenes resulted in lower yields of (±)-**26** and largely afforded undesired type B and

O-cyclization products. Since **28b** provided the best yield of rearrangement product **26**, formic-

5   acid-promoted cyclizations of its diastereomers (*meso*-**28a** and *meso*-**28c**) were also investigated

(Figure 6.5). Type A product (±)-**26** was obtained in 40% yield from *meso*-**28a** by a mechanism

similar to that proposed in Figure 6.4. Cyclization of *meso*-**28c** provided the type B scaffold (±)-

24 along with the oxycyclization product (±)-**35**. It was not surprising that rearrangement to **26**

did not occur for the case of *meso*-**28c** as the transition state would experience unfavorable steric

10   interactions from the axially oriented C7-allyl group directed on its concave face (as shown for

the formation of (±)-**10** in (196) Figure S4b). Taken together, these transformations resulted in

diverse SASs with unexplored biological activities through novel cyclization and rearrangement

pathways.
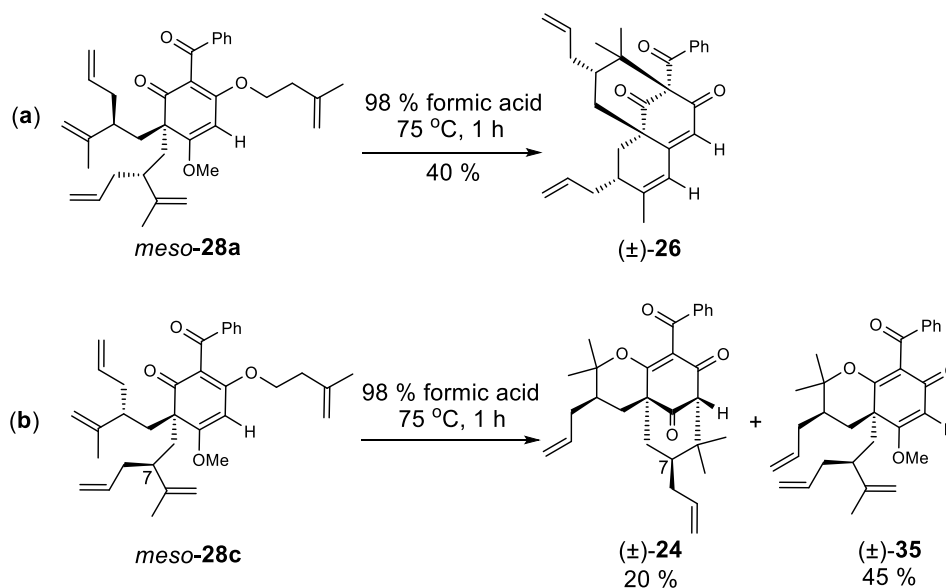
Figure 6.5. Cyclizations of meso-28 a and meso-28c in formic acid.

6.2.4 <u>MAP Captures Known Mechanisms of Model Compounds</u>

Due to the interesting activities of isogarcinol (**2**) and garcinol (**4**), the diverse SASs from this study merited a broad and unbiased investigation of their potential biological activities ([308](#), [333](#)). We utilized MAP to perform comparative assays of these compounds in the context of reported activities for **2** and **4.** MAP is multiplexed in two distinct ways: 1) multiple biological readouts are assessed simultaneously at single-cell resolution using panels of fluorophore-conjugated antibodies, and 2) the assay utilizes fluorescent cell barcoding (FCB) ([231](#)) to enable robust large-scale screening of multiple treatment conditions, including different compounds, doses, or timepoints. For biological evaluation of the novel SASs produced, the primary panel included markers for apoptosis and homeostasis, such as cleaved caspase 3 (CCasp3) ([340](#)), DNA damage (γH2AX) ([77](#)), ERK/mTOR signaling [phopsho-S6, (pS6)] ([341](#), [342](#)), and cell cycle progression (DNA content and phospho-histone H3) ([343](#)). To address one of the most frequently reported mechanisms proposed for PPAP bioactivity, we also assessed HAT inhibition using acetyl histone-specific antibodies against H3K9Ac and H3K18Ac as representative substrates of PCAF and CBP/P300, respectively, in combination with a readout for total histone H3 content ([344](#)). Unless otherwise stated, compounds were tested in Jurkat cells (human T-cell leukemia) for 16 h at both 1 and 10 μM to establish dose-dependent bioactivity and prioritize compounds for EC_{50} analysis.
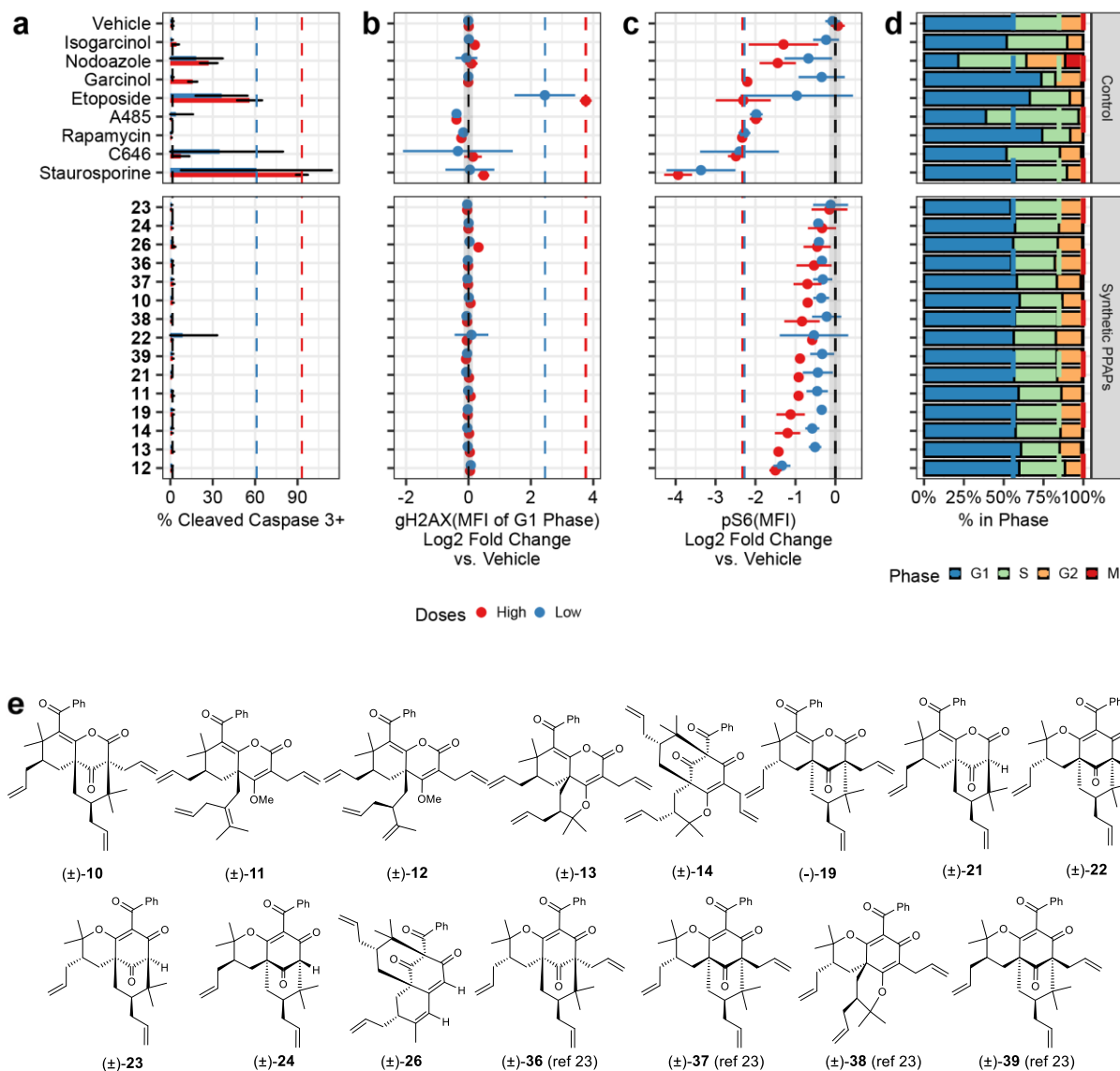
Figure 6.6. Multiplexed Bioactivity Assessment of the SAS library with Reference Compounds

Jurkat cells were treated for 16 h at two doses (high - 10 μM, low - 1 μM), with the exception of rapamycin (10 nM and 1 nM) and staurosporine (1 μM and 100 nM). Each panel represents an average of 3 replicates of a single marker [channel]: a) Casp3 as a marker of apoptosis [PE]; b) γH2AX as a marker of DNA damage [PerCPCy5.5], c) pS6 [Ser235/236] as a marker of mTOR/ERK signaling [Alexa Fluor 647]; and d) Cell cycle distribution, assessed using biaxial gating on DNA content [YO-PRO-1] and phospho-histone H3 (Ser28) [PE-Cy7]. Median fluorescence intensity (MFI) of γH2AX and pS6 were normalized to the average of the two vehicle-treated wells. The error bars represent the 95% confidence interval for each point estimate. The dashed lines in panels A-C show the vehicle-treated wells (*black*) and the reference compounds for each channel at the high (red) and low (blue) doses. e) SASs evaluated.

222

Eight control compounds were included in the screening panel alongside the synthetic SAS library to provide internal biological validation of the assay. Four of these controls were selected to maximally perturb the chosen activity markers. Additional controls included two PPAPs (isogarcinol (**2**) and garcinol (**4**), Figure 6.1a) for comparison to the structurally related SASs and two synthetic HAT inhibitors (C646 (345) and A485 (346)). Phenotypes induced by these control compounds (Figure 6.6) were consistent with their established mechanistic targets and uses as chemical probes. For example, staurosporine effectively induced apoptosis in ≈90% of the cells, etoposide increased relative γH2AX via induction of double-stranded breaks, rapamycin reduced S6 phosphorylation via inhibition of mTOR, and nocodazole led to an accumulation of cells in G2/M phase.

Although markers were selected to evaluate orthogonal biological pathways, the phenotypes induced by control compounds revealed both known and novel crosstalk that could otherwise confound interpretation of individual markers if assessed in isolation. For example, DNA replication stress is known to induce a DNA damage response in cycling cells, which leads to a relative increase in median γH2AX for both S and G2 phase cells over G1 phase cells (347). This crosstalk is evident in cells treated with compounds that perturb cell cycle progression. Specifically, nocodazole increased γH2AX, while G1 arresting compounds paradoxically decrease γH2AX relative to vehicle-treated cells (Figure 6.7). To account for this phenomenon, γH2AX intensity was normalized to vehicle treated cells in each phase of the cell cycle. This result suggested that etoposide, consistent with its reported mechanism, was the only DNA-damaging compound in our library at the tested doses, while the SASs did not exhibit notable DNA damage activity.

223
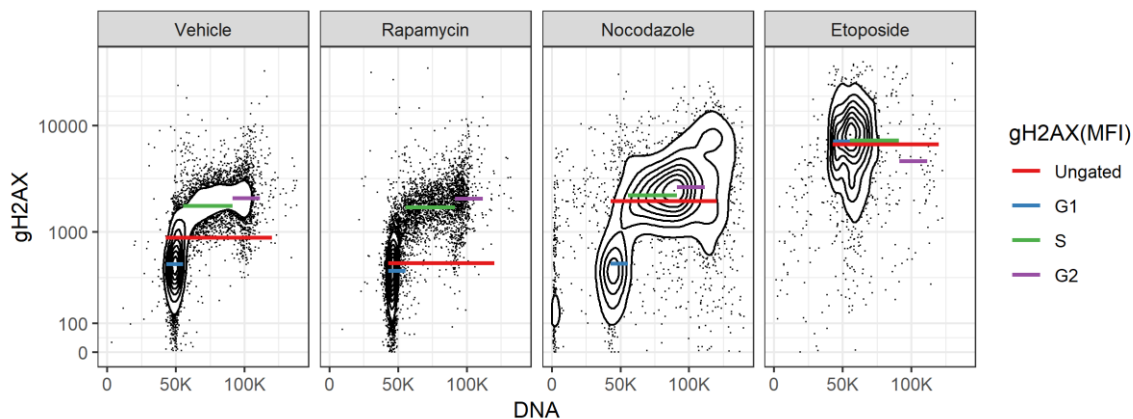
Figure 6.7. γH2AX interpretation is confounded by cell cycle progression.

In cycling cells, γH2AX increases over the course of the cell cycle, from G1, to S, to G2 phase. This phenomenon must be accounted for by normalizing γH2AX to baseline γH2AX for each phase of the cell cycle. In the absence of this correction (red line) compounds which perturb cell cycle progression can appear to be inducing DNA damage (nocodazole) or even 'decreasing' DNA damage (rapamycin) compared to vehicle treated wells.

6.2.5 SASs Induce Selective Suppression of pS6

Consistent with previous reports (275, 327), garcinol (**4**) exhibited modest antiproliferative cytotoxicity at 10μM: ≈20% of cells were positive for the apoptosis marker CCasp3 (Figure 6.6a) and the fraction of cells in G1 phase increased (Figure 6.6d), which is consistent with cell cycle arrest. In addition, isogarcinol (**2**) and garcinol (**4**) also decreased basal pS6 at Ser235/236, which indicates inhibition of mTOR/ERK signaling (341, 342). These results are consistent with their reported immunosuppressive activities (286). Although the bioactivities exhibited by **2** and **4** were dose-dependent (Figure 6.6), the perturbation was not specific to any one phenotypic marker, suggesting that their bioactivities are relatively non-specific. Five rearrangement products (**11**–**14** and **19**) selectively exhibited the pS6 suppression phenotype

with minimal cytotoxicity relative to garcinol (**4**). This phenotype was not specific to the Jurkat model system, as the same effect was observed in KG-1 (acute myeloid leukemia) cells treated in a similar manner (Figure 6.8)**.** The antibody used the pS6 readout specific for Ser235/236 phosphorylation, which is downstream of both the mitogenic mTOR and ERK pathways (Figure 6.8). To determine whether mTOR or ERK was responsible for the observed phenotype, a subset of the SAS library was assayed for suppression of pS6 at Ser240/244, a site that is downstream of mTOR, but not ERK ([342](#)). This secondary panel revealed pS6 was suppressed at both Ser235/236 and Ser240/244, suggesting that suppression of mTOR signaling is a component of the phenotype induced by SASs (Figure 6.6 and Figure 6.8).

The compounds depicted in Figure 6.6a–d are ordered from least to most active in the measured suppression of pS6 (Ser235/236) at 10μM. The compound library was not designed for an exhaustive study of SAS structure–activity relationships (SAR), but some general SAR trends are readily evident from MAP data. Notably, compounds **12** [IC_{50}=0.95μM] and **13** [IC_{50}=1.0μM] bearing the 2-*oxo*-tetrahydro-*2H*-chromene core (*cf.* Figure 6.2) were more active than isogarcinol (**2**) [IC_{50}=12 μM] but lack the [3.3.1]-bicyclic core that is characteristic of many PPAPs (Figure 6.9). Four of the five active compounds (**11**–**13** and **19**, Figure 6.6e) have fused 6-6 lactone ring systems, and compound **14** is a type A scaffold. More importantly, all of the active SASs in this study (**11**–**14** and **19**) resulted from the same formic-acid-promoted rearrangement pathway described in Figure 6.2a originating from pyranodienones **9** and **18**.

In contrast to isogarcinol (**2**) and garcinol (**4**), SASs lack catecholic hydroxy groups, which have been linked to their cytotoxicity ([280](#)). Additionally, catechols are known "pan-assay interference" (PAINS) ([78](#))functional groups that contribute to nonspecific hits in screening assays. Consistent with this model, **2** and **4** exhibited cytotoxicity relative to vehicle-treated

wells (Figure 6.6), while the catechol-lacking SASs showed minimal cytotoxicity at the tested doses.
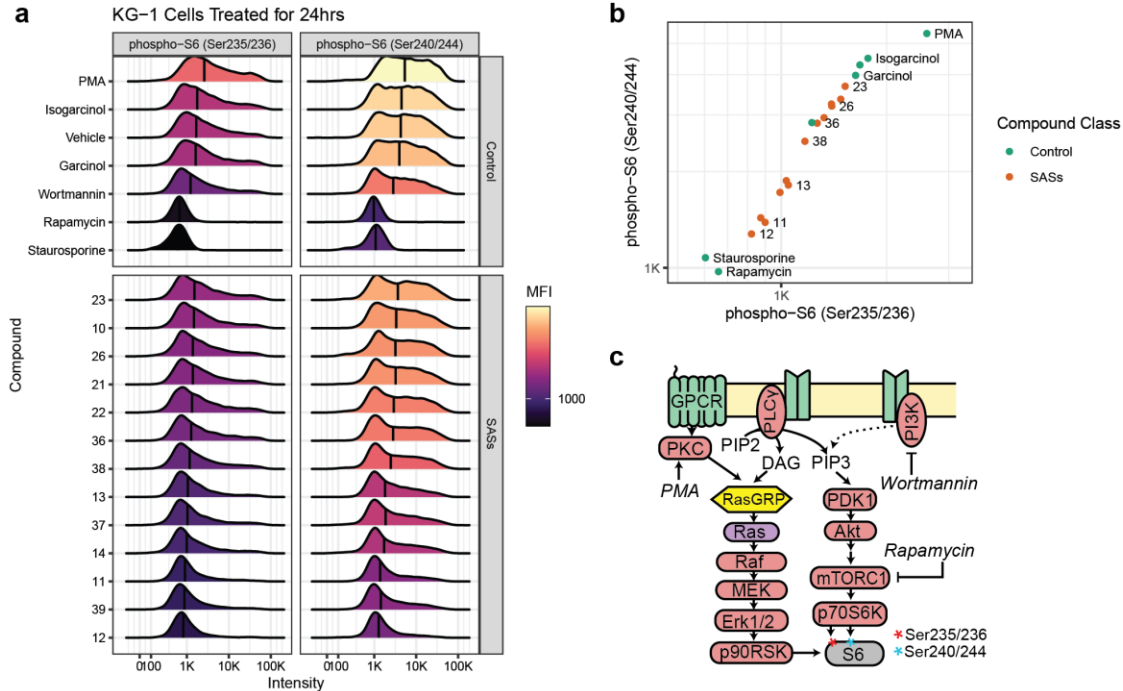
Figure 6.8. Synthetic acylphloroglucinol scaffolds (SASs) suppress pS6 at sites consistent with mTOR inhibition.

a) KG-1 myeloid leukemia cells were treated with 10 μM of synthetic compounds or optimized dose of control compounds for 24hrs and stained with antibodies against phospho-S6 (Ser235/236) [Alexa Fluor 647] and phosho-S6 (Ser240/244) [Alexa Fluor 488]; **b)** Median Fluoresence Intensity (MFI) of phospho-S6 (Ser235/236) vs phospho-S6 (Ser240/244) showing correlation between the two sets phosphorylation sets indicative of mTOR driven pS6 phosphorylation compared to PMA which preferentially results in phosphorylation of phospho-S6 (Ser235/236) over (Ser240/244). **c)** diagram of pathways leading to phosphorylation of S6 ribosomal subunit at Ser235/236 and Ser240/244 with treatments depicted in italics.
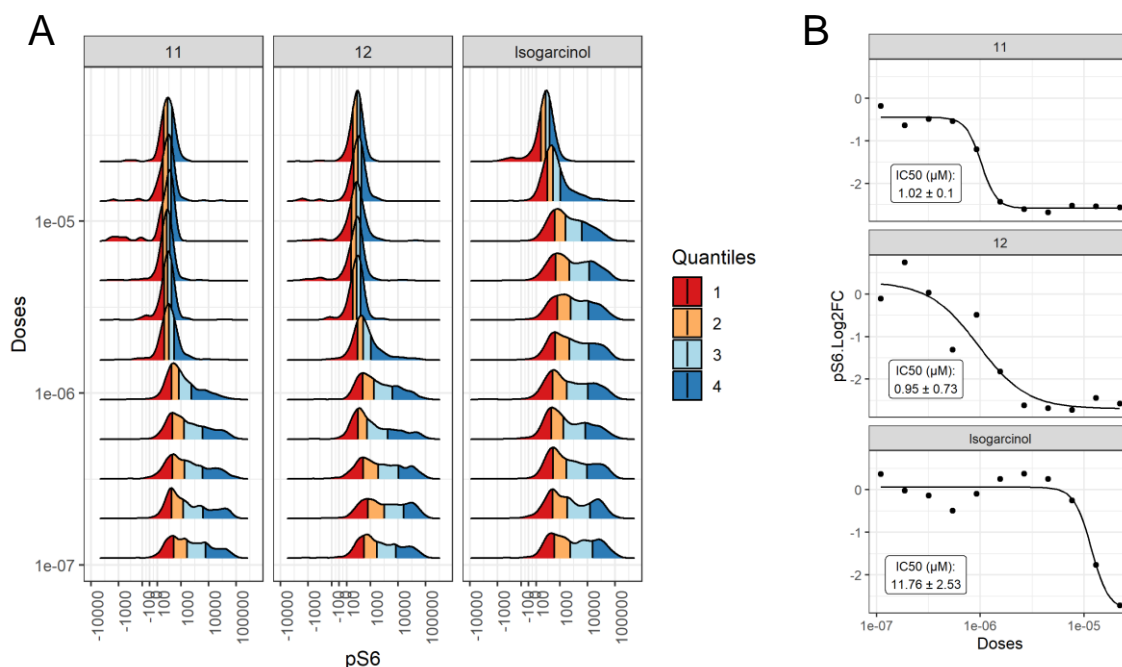
Figure 6.9. Concentration response curves for lead compounds in comparison to isogarcinol.

Jurkat cells treated for 24 h with compounds **11, 12,** or isogarcinol, stained for pS6(Ser235/236) **A,** histogram showing raw data at tested doses; **B,** IC50 curves fitted based on a four-component log-logistic model.

6.2.6 PPAPs are Nonspecific HAT Modulators

Garcinol (**4**) and C646 were originally identified as HAT inhibitors in in vitro assays using recombinant HATs ([348](#)). However, recent reports suggest that the activity of these compounds may represent assay interference rather than targeted inhibition ([349](#)). To test this hypothesis, cells exposed to compounds were also stained for antibodies against acetyl-histone (H3K9Ac, H3K18Ac) and total histone (H3) content (Figure 4.11)**.** Examining each marker separately, we found that isogarcinol (**2**), garcinol (**4**), C646, and A485 suppressed H3K9 and H3K18 acetyl content while the SASs did not appear to influence histone acetylation. However, the cytotoxic compounds etoposide and staurosporine, which are not thought to act directly on HATs, suppressed histone acetylation to an equal or greater extent compared to C646 and **4**. In

227

an attempt to account for this discrepancy, cells were stained for total histone H3, which should

not be influenced by HAT inhibition. When H3K9Ac/H3K18Ac is compared to total histone H3

content, we observe the loss of acetyl-histone H3 accompanied by a proportional loss of total

histone H3. One exception to this pattern is A485, a selective p300/CBP inhibitor (346) that

5   suppresses H3K18Ac without significantly affecting total H3 or H3K9Ac content (Figure 4.11).

The correlation between acetyl and total histone for cytotoxic compounds is consistent with a

nonspecific loss of histone epitopes rather than a specific loss of one histone mark and

emphasizes the importance of considering total histone content when assessing specific histone

epitopes (350). Though the mechanism of this non-specific histone loss is unknown, the

10   observed loss of total and acetyl-histone content with cytotoxic compound treatment suggests

that apoptosis leads to loss of histones (351), or otherwise alters the accessibility of histone

epitopes in a manner that confounds antibody-based detection of histone marks. This leads us to

conclude, in agreement with recent reports (349), that the tested PPAPs and SASs, including

isogarcinol (**2**) and garcinol (**4**), are not direct inhibitors of HAT-induced acetylation at

15   concentrations below 10 μM.
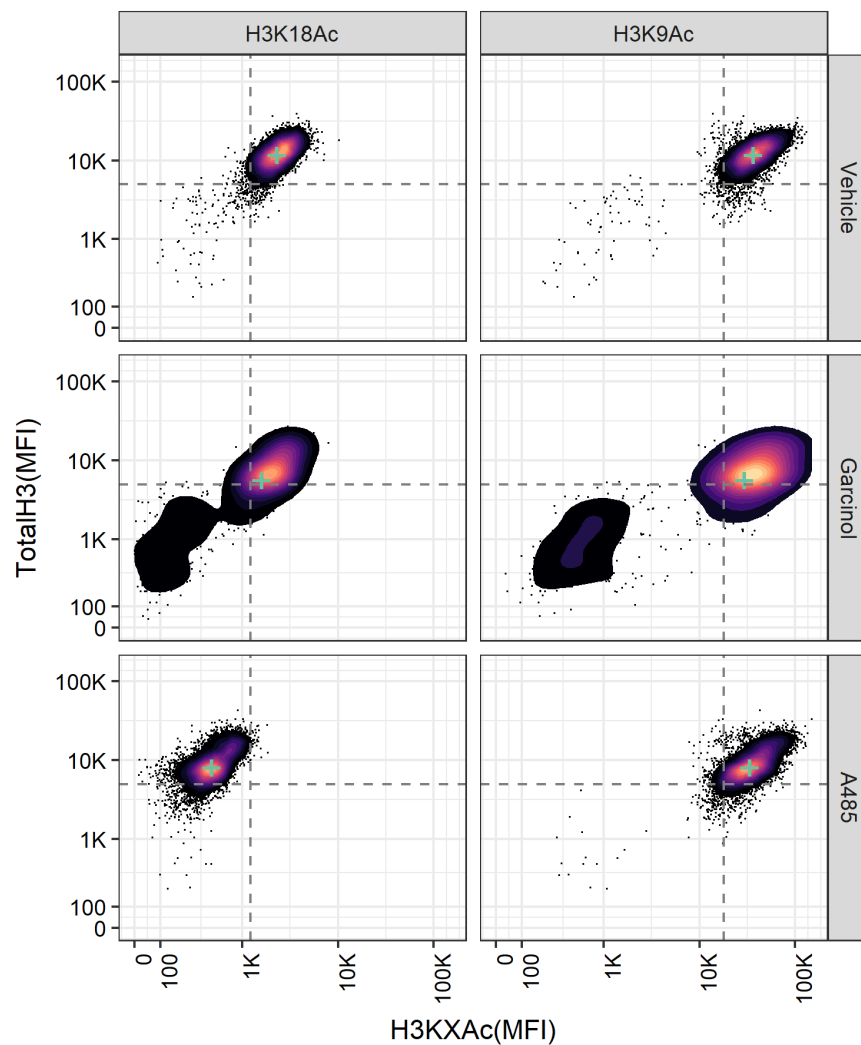
Figure 6.10. Validation of acetyl-H3 markers.

Selected biaxial contour plots from a single replicate for Vehicle, garcinol (10 μM) and A485 (10 μM), the green "+" represent the Median Fluorescence Intensity (MFI) for each marker as plotted in Figure 7 of manuscript. The dashed lines represent the 5th percentile for the vehicle treated well.
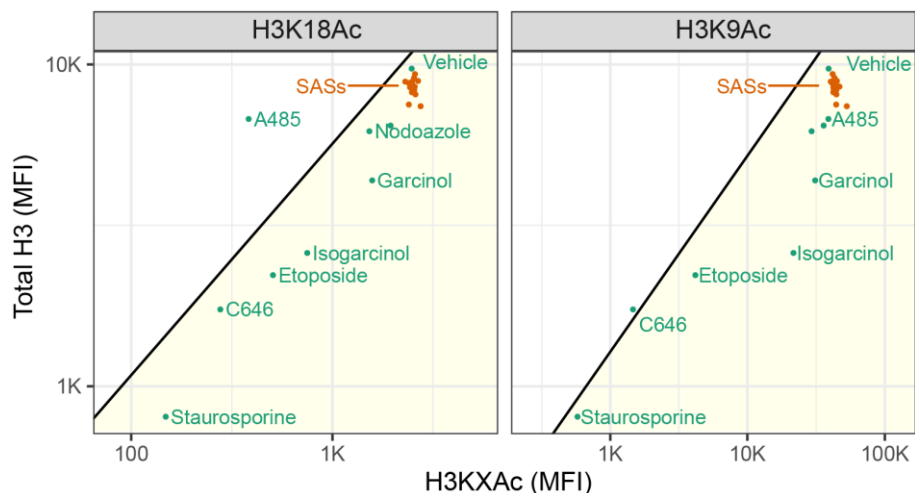
Figure 6.11. Assessment of histone acetylation in SAS treated Jurkat cells.
Assessment of histone acetylation in treated Jurkat cells. Jurkat cell treated as in
Figure 6.6, stained with antibodies against total H3 (PE), H3K9Ac (Alexa Fluor
488), or H3K18Ac (Alexa Fluor 647). Median fluorescence intensity (MFI) for each
channel was calculated and averaged over three replicates which were plotted as
points, with reference compounds in green and SASs in orange. Compounds below
the diagonal exhibited a loss of total H3 greater than or equal to the loss of acetyl-
histone H3, indicative of non-specific histone loss.

6.2.7 Conclusion

      Formic-acid-promoted rearrangements of dearomatized acylphloroglucinol substrates

resulted in a diverse collection of synthetic acylphloroglucinol scaffolds (SASs) which were

evaluated for activities in diverse biological pathways using multiplexed activity profiling

(MAP). MAP evaluates several markers of cell signaling to distinguish genuine activity from

assay interference that is commonly associated with PPAPs. Rearrangements described in this

work were facilitated by formic acid which has an inherent ability to stabilize carbocations in

solution and form adducts with strained carbonyls (308, 314-316). Formic-acid-mediated

rearrangements of **9**, **18**, and *meso*-**20c** produced a diverse group of SASs, five of which (**11**–**14**

230

and **19**) displayed notable biological activity. The absence of a C3-allyl group reduced product diversity but improved rearrangement and cyclization yields. Furthermore, we discovered that a pendant *O*-homoallyl group was critical for rearrangement to the type A scaffold (±)-**26** which may result from oxonium stabilization by alkene π-π* donation. The most active analogues in this study derived from a single formic-acid-promoted rearrangement pathway, and two of these compounds (**12** and **13**) were more active than the natural product isogarcinol (Figure 6.6) ([333](#)).

MAP was effectively used as an unbiased platform to assess the bioactivities of SASs which revealed that **11**–**14** and **19** suppressed pS6 (Ser235/236) with minimal cytotoxicity relative to garcinol (**4**). As pathways leading to pS6 are central to the adaptive immune response, metabolism, and the mTOR signaling pathway, further study of SASs in target-identification campaigns and as immunosuppressants is warranted. We found that isogarcinol (**2**) and garcinol (**4**) resulted in nonspecific inhibition of HAT activity *in vivo* but did induce nonspecific changes in measured histone and acetyl-histone content, which could account for previous reports of HAT activity. Our study highlights the combination of controlled synthetic diversity with multiplexed activity analysis across a broad panel of cell status markers to facilitate thorough exploration of the potential chemical activity space around both privileged and novel scaffolds. Further studies to employ diversity-oriented synthesis/reaction discovery approaches to produce novel scaffolds for evaluation by MAP are currently in progress and will be reported in due course.

6.3 Materials and Methods

^{1}H NMR spectra were recorded at 400 MHz or 500 MHz at ambient temperature with $CDCl_3$, MeOD, or CD_3CN (Cambridge Isotope Laboratories, Inc.) as solvents unless otherwise stated. Data for ^{1}H NMR are reported as follows: chemical shift, integration, multiplicity (app = apparent, br = broad, par obsc = partially obscure, ovrlp = overlapping, s = singlet, d = doublet, t = triplet, q = quartet, m = multiplet) and coupling constants. ^{13}C NMR were recorded at 100 MHz or 125.0 MHz at ambient temperature with the same solvents unless otherwise stated. Chemical shifts are reported in parts per million relative to $CDCl_3$ (^{1}H, δ 7.26; ^{13}C, δ 77.0), C_6D_6 (^{1}H, δ 7.16), DMSO-D_6 (^{1}H, δ 2.50; [13]C δ 39.4), or CD_3OD (^{1}H, δ 3.31, 4.78; ^{13}C, δ 49.3). All ^{13}C NMR spectra were recorded with complete proton decoupling. Infrared spectra were recorded on a Nicolet Nexus 670 FT-IR spectrophotometer. High-resolution mass spectra were obtained in the Boston University Chemical Instrumentation Center using a Waters Q-TOF mass spectrometer. Melting points were recorded on a Mel-temp (Laboratory Devices). Analytical thin layer chromatography was performed using 200-400 mesh silica gel (Scientific Absorbents, Inc.). Yields refer to chromatographically and spectroscopically pure materials, unless otherwise stated. All reactions were carried out in oven-dried glassware under an argon atmosphere unless otherwise noted. Analytical LC-MS experiments were performed using a Waters Acquity UPLC (Ultra Performance Liquid Chromatography) with a Binary solvent manager, SQ mass spectrometer, Water 2996 PDA (PhotoDiode Array) detector, and Evaporative Light Scattering Detector (ELSD). An Acquity UPLC BEH C18 1.7 μm column was used for analytical UPLC-MS. Preparative HPLC purification was performed on a Gilson PLC 2020 Personal Purification System. Optical rotations were recorded on an AUTOPUL III digital polarimeter at 589 nm and are recorded as $[\alpha]_D^{22}$ (concentration in grams/100 mL solvent). A CHIRALPAK® AD-H [Chiral Technologies Inc., 150

x 4.60 mm (L x I.D.)] column was used for enantiomeric excess determination. The Scilligence Electronic Laboratory Notebook (ELN) was used for experimental procedure planning. HPLC grade tetrahydrofuran, methylene chloride, diethyl ether, toluene, acetonitrile, and benzene were purchased from Fisher and VWR and were purified and dried by passing through a PURE SOLV® solvent purification system (Innovative Technology, Inc.). Other ACS grade solvents for chromatography were purchased from Clean Harbors. All other reagents and relevant catalysts were purchased from Sigma-Aldrich, Acros, Alfa Aesar, and Strem Chemicals. American Chemical Society (ACS) grade formic acid (98%) was purchased from EMD Millipore in 1L plastic bottles. Antibodies and flow cytometric reagents were obtained from suppliers listed in Table S4.

Cell Culture: Jurkat (E6-1, ATCC Cat # TIB-512) and KG-1 (ATCC Cat # CCL-246) cells were obtained in April 2017, and last confirmed to be mycoplasma free. Cells were maintained under sterile conditions in a humidified 37 °C incubator under 5% CO_2 atmosphere in RPMI 1640 media (Gibco) supplemented with 10% (v/v) Fetal Bovine Serum (Gibco), and 1% (v/v) Penicillin-Streptomycin (10,000U/mL, Sigma). Cells were maintained at a density of between 2 x 10^5 and 1 x 10^6 cells/mL of culture media.

Drug Treatment and Sample Preparation: All compounds were resuspended in DMSO at a concentration of 10 mM in multiple aliquots to generate the working stocks. Compounds not generated by the authors were obtained commercially (see table). Each compound was diluted in DMSO to at 200x the desired concentration and 1 μL of the 200x stock or vehicle was added to wells of a 96-well tissue culture treated plate. Cells in suspensions (199 μL) were added to each well using a multichannel pipette to achieve the final concentration of the desired drug and 0.5% (v/v) DMSO. The vehicle control was 0.5% (v/v) DMSO.

233

The cell samples (wells) were processed using the protocol developed previously ([228]) and described here. At 30 minutes prior to the end of the experiment, 20 µL of a 10x Alexa Fluor 700 in phosphate buffered saline (PBS) was added (final conc: 0.04 µg/mL) as a viability stain per a published protocol ([352]). Cells were then transferred to a polypropylene v-bottom 96-well plate containing 25 µL of 16% paraformaldehyde (PFA, Alfa Aesar) and allowed to fix (final concentration: 1.6% PFA v/v) for 10 minutes at room temperature protected from ambient light. Cells were then centrifuged at 800g x 5 min at 4 °C and the supernatant decanted by inverting the plate. The cell pellets were vigorously vortexed for 20 seconds to resuspend the pellet, 200 µL of -20 °C methanol was added to each well, and the cells were stored at -20 °C for at least 30 minutes to permeabilize the cells.

To barcode the cells, the plate containing the cells in methanol was centrifuged at 800 g x 5 minutes at 4 °C, decanted, and resuspended in 200 µL of PBS (Gibco). A volume of 185 µL from each well of this fixed and permeabilized cell plate was added to each well of a prepared dye gradient barcoding plate (described below) containing 5 µL of a 40x stock of each barcoding dye (total of 15 µL), to achieve a total volume of precisely 200 µL pipetting gently to mix. The cells were allowed to react with the barcoding dye for 30 minutes at room temperature protected from ambient light, at which point 70 µL of 1% (v/v) PBS/BSA (bovine serum albumin) was added to each well to quench the unreacted dye. The cells were then centrifuged at 800 g x 5 minutes at 4 °C, supernatant decanted, and then resuspended in a total of 1.2 mL of PBS/BSA, combining all 48 wells into a single 5 mL FACS tube.

Cell Staining: Each barcoded sample was split three ways: A FCB control comprising 10% of the pooled barcoded sample, not stained with antibodies (see intrinsic fluorescence supplement); a sample comprising 45% of the pooled wells stained with Panel 1; and a sample

234

comprising 45% of the pooled wells stained with Panel 2. All staining was carried out in a staining volume of 100 μL of PBS/BSA.

Panel 1: A master mix containing all four antibodies (see below) was prepared and added to the cells in a total volume of 100 μL and allowed to stain for 30 minutes at 4 °C. The cells were washed twice to remove unbound antibodies by centrifugation at 800 g x 5 minutes at 4 °C, resuspended in excess PBS/BSA (1 mL), and further resuspended to a final volume of 475 μL. Yo-Pro-1 (Invitrogen, Y3603) staining solution (25 μL of a 20x stock solution in 1% BSA in PBS containing RNase A) was added to each well to achieve a final YoPro-1 concentration of 50 nM and a final RNase A concentration of 200 μg/mL.

Panel 2: The unconjugated rabbit anti-H3K18Ac antibody was added to barcoded cells in a total volume of 100 μL and allowed to bind for 30 minutes at 4 °C. The cells were washed twice to remove unbound antibodies by centrifugation at 800 g x 5 minutes at 4 °C and resuspended in excess PBS/BSA (1 mL). In a similar manner, the cells were incubated with an anti-rabbit Ax647 secondary FAB fragment, followed by binding with the fluorophore conjugated antibodies, with 2x PBS/BSA washes between each round of staining to remove unbound antibodies. Validation experiments (data not shown) verified that that the fluorophore conjugated antibodies did not cause retention of the secondary antibody in the absence of the H3K18Ac primary antibody.

Flow cytometry and analysis: All samples were run on a BD LSRFortessa flow cytometer, the configuration of which is shown below. Gating and compensation were carried out using Cytobank (Beckman.com) and exported as csv files for further analysis in R version 4.0.0 (R Core Team (2017). R: A language and environment for statistical computing. R Foundation for Statistical Computing, Vienna, Austria. URL http://www.R-project.org/). Barcoded samples were

235

demultiplexed using a custom script (see supplement) to yield separate FCS files for each well, which were then analyzed using an R script (see code supplement).

Categorical markers (Caspase, cell cycle phase) were analyzed as follows. The caspase positive (CCasp3+) gate was placed using vehicle and Staurosporine treated wells as a reference, and % CCasp3+ was calculated by dividing the number of CCasp3+ cells by the total number of cells in each well. Cell cycle gates were placed using vehicle and nocodazole treated cells to define the G1, S, and G2/M phase cells, and G2/M was further divided into G2 and M phase using the marker phospho-Histone H3.

Continuously variable markers (phospho-S6, γH2AX) were analyzed as follows: The median fluorescence intensity of each marker under each condition was calculated. Fold change was calculated by normalizing the MFI to the vehicle treated well. For γH2AX, the MFI was calculated and normalized on a per well, per cell cycle phase basis to account for the relationship between cell cycle progression and γH2AX.

The following R packages(353) were used to supplement the analysis: ggplot2 (354), dplyr (355), tidyr (356), ggridges (357), cowplot (358). All code used in the analysis and generation of figures is included in the supplementary material.

Fluorescence Cell Barcoding:

The fluorescence cell barcoding protocol was adapted from the original FCB protocol (231) and the 48 well barcoding scheme previously published by our group (228). Barcoding dyes were plated onto polypropylene plates with 5 µL of each dye at 40x the final concentration (below).

Table S1: Final concentrations of each dye in barcoding plates after addition of cells.

	Pacific Blue (final µg/mL)
Row A	0.384
Row B	0.218
Row C	0.124
Row D	0.07
Row E	0.04
Row F	0.023
Row G	0.013
Row H	0.007

	Pacific Orange (final µg/mL)
Column 1	1.05
Column 2	0.618
Column 3	0.363
Column 4	0.214
Column 5	0.126
Column 6	0.074

	Alexa 750 (final µg/mL)
All wells	0.15

5

Drug	Supplier	Catalog#	High Concentration (µM)	Low Concentration (µM)
Staurosporine	LKT Labs	S7600	1	0.1
Etoposide	LC Labs	E-448	20	2
Rapamycin	LC Labs	R-5000	0.01	0.001
Nocodazole	Acros	358240100	10	1
Garcinol	Enzo	BML-GR343-0010	10	1
Isogarcinol	Cayman Chemical	21164	10	1
C646	Calbiochem	382113-10MG	10	1
A485	SGC		10	1

Table S3. Flow Cytometer Settings
BD LSRFortessa

Excitation	Channel	Filter
405 nm	Pacific Blue	450/40
	Pacific Orange	560/40
488 nm	Side Scatter (SSC)	488/10
	Yo-Pro-1/Alexa 488	525/50
	PerCP-Cy5.5	710/50
561nm	PE	582/15
	PE-Cy7	780/60
633nm	Alexa 647	670/14
	Alexa 700	730/40
	Alexa 750	780/60

Table S4: Antibodies Used in this Study.

Panel 1

Marker	Epitope	Supplier	Clone	Dye	Dilution
CCasp3		BD	C92-605	PE	1:10
gH2AX	pS139	BD	N1-431	PerCP-Cy5.5	1:40
pS6	pS235/236	CST	D57.2.2E	Ax647	1:200
pHistone H3	pS28	Biolegend	HTA28	PE-Cy7	1:400
DNA		Invitrogen	Y3603	YoPro-1	50nM

Panel 2

Marker	Epitope	Supplier	Clone	Dye	Dilution
Acetyl-H3	K18	CST	D8Z5H	Unconjugated	1:4000
	Anti-rabbit-IgG FAB	CST	4414S	Alexa 647	1:4000
Total H3		CST	D1H2	PE	1:400
Acetyl-H3	K9	CST		Ax488	1:200

Abbreviation	Supplier
CST	Cell Signaling Technologies
BD	Becton Dickinson
Invitrogen	Invitrogen (Thermofisher Scientific)
Biolegend	Biolegend

6.4 References

77.   E. P. Rogakou, W. Nieves-Neira, C. Boon, Y. Pommier, W. M. Bonner, Initiation of DNA fragmentation during apoptosis induces phosphorylation of H2AX histone at serine 139. *J Biol Chem* **275**, 9390-9395 (2000).

78.   J. B. Baell, G. A. Holloway, New substructure filters for removal of pan assay interference compounds (PAINS) from screening libraries and for their exclusion in bioassays. *J Med Chem* **53**, 2719-2740 (2010).

196.   J. H. Boyce, B. J. Reisman, B. O. Bachmann, J. A. Porco, Jr., Synthesis and Multiplexed Activity Profiling of Synthetic Acylphloroglucinol Scaffolds. *Angew Chem, Int Ed* **60**, 1263-1272 (2021).

228.   D. C. Earl *et al.*, Discovery of human cell selective effector molecules using single cell multiplexed activity metabolomics. *Nat Commun* **9**, 39 (2018).

231.   P. O. Krutzik, G. P. Nolan, Fluorescent cell barcoding in flow cytometry allows high-throughput drug screening and signaling profiling. *Nat Methods* **3**, 361-368 (2006).

257.   X. W. Yang, R. B. Grossman, G. Xu, Research Progress of Polycyclic Polyprenylated Acylphloroglucinols. *Chem Rev* **118**, 3508-3558 (2018).

258.   N. Simpkins, J. Taylor, M. Weller, C. Hayes, Synthesis of Nemorosone via a Difficult Bridgehead Substitution Reaction. *Synlett* **2010**, 639-643 (2010).

259.   M. R. Garnsey, D. Lim, J. M. Yost, D. M. Coltart, Development of a strategy for the asymmetric synthesis of polycyclic polyprenylated acylphloroglucinols via N-amino cyclic carbamate hydrazones: application to the total synthesis of (+)-clusianone. *Org Lett* **12**, 5234-5237 (2010).

260.   N. Biber, K. Mows, B. Plietker, The total synthesis of hyperpapuanone, hyperibone L, epi-clusianone and oblongifolin A. *Nature chemistry* **3**, 938-942 (2011).

261.   M. Uwamori, A. Saito, M. Nakada, Stereoselective total synthesis of nemorosone. *J Org Chem* **77**, 5098-5107 (2012).

262.   B. A. Sparling, D. C. Moebius, M. D. Shair, Enantioselective total synthesis of hyperforin. *J Am Chem Soc* **135**, 644-647 (2013).

263.   K. Lindermayr, B. Plietker, The bidirectional total synthesis of sampsonione P and hyperibone I. *Angew Chem, Int Ed* **52**, 12183-12186 (2013).

264.   F. Horeischi, N. Biber, B. Plietker, The total syntheses of guttiferone A and 6-epi-guttiferone A. *J Am Chem Soc* **136**, 4026-4030 (2014).

265.   G. Bellavance, L. Barriault, Total syntheses of hyperforin and papuaforins A-C, and formal synthesis of nemorosone through a gold(I)-catalyzed carbocyclization. *Angew Chem, Int Ed* **53**, 6701-6704 (2014).

266.   C. P. Ting, T. J. Maimone, Total Synthesis of Hyperforin. *J Am Chem Soc* **137**, 10516-10519 (2015).

267.   G. Bellavance, L. Barriault, Modular Total Syntheses of Hyperforin, Papuaforins A, B, and C via Gold(I)-Catalyzed Carbocyclization. *J Org Chem* **83**, 7215-7230 (2018).

268.   L. Wang *et al.*, Me2AlSEt-Promoted Domino Dieckmann Cyclization Enables the Total Synthesis of Polycyclic Polyprenylated Acylphloroglucinols. *Org Lett* **21**, 8075-8079 (2019).

269.   X. Shen, C. P. Ting, G. Xu, T. J. Maimone, Programmable meroterpene synthesis. *Nat Commun* **11**, 508 (2020).

270. F. Dal Piaz *et al.*, The identification of a novel natural activator of p300 histone acetyltranferase provides new insights into the modulation mechanism of this enzyme. *ChemBioChem* **11**, 818-827 (2010).

271. L. Zhu *et al.*, Identification of a novel polyprenylated acylphloroglucinolderived SIRT1 inhibitor with cancerspecific anti-proliferative and invasion-suppressing activities. *Int J Oncol* **45**, 2128-2136 (2014).

272. K. C. Ravindra *et al.*, Inhibition of lysine acetyltransferase KAT3B/p300 activity by a naturally occurring hydroxynaphthoquinone, plumbagin. *J Biol Chem* **284**, 24453-24464 (2009).

273. T. S. Sell, T. Belkacemi, V. Flockerzi, A. Beck, Protonophore properties of hyperforin are essential for its pharmacological activity. *Sci Rep* **4**, 7500 (2014).

274. H. Zhang *et al.*, Cytotoxic and anti-inflammatory prenylated benzoylphloroglucinols and xanthones from the twigs of Garcinia esculenta. *J Nat Prod* **77**, 1700-1707 (2014).

275. K. Matsumoto *et al.*, Cytotoxic benzophenone derivatives from Garcinia species display a strong apoptosis-inducing effect against human leukemia cell lines. *Biol Pharm Bull* **26**, 569-571 (2003).

276. J. Hong *et al.*, Effects of garcinol and its derivatives on intestinal cell growth: Inhibitory effects and autoxidation-dependent growth-stimulatory effects. *Free Radic Biol Med* **42**, 1211-1221 (2007).

277. V. Sarli, A. Giannis, Selective inhibition of CBP/p300 HAT. *Chem Biol* **14**, 605-606 (2007).

278. K. Mantelingu *et al.*, Specific inhibition of p300-HAT alters global gene expression and represses HIV replication. *Chem Biol* **14**, 645-657 (2007).

279. G. Marti *et al.*, Antiplasmodial benzophenones from the trunk latex of Moronobea coccinea (Clusiaceae). *Phytochemistry* **70**, 75-85 (2009).

280. M. Arif *et al.*, Mechanism of p300 specific histone acetyltransferase inhibition by small molecules. *J Med Chem* **52**, 267-277 (2009).

281. G. Marti, V. Eparvier, M. Litaudon, P. Grellier, F. Gueritte, A new xanthone from the bark extract of Rheedia acuminata and antiplasmodial activity of its major compounds. *Molecules* **15**, 7106-7114 (2010).

282. Z. Tian *et al.*, Cambogin is preferentially cytotoxic to cells expressing PDGFR. *PloS One* **6**, e21370 (2011).

283. M. S. Baliga, H. P. Bhat, R. J. Pai, R. Boloor, P. L. Palatty, The chemistry and medicinal uses of the underutilized Indian fruit tree Garcinia indica Choisy (kokum): A review. *Food Res Int* **44**, 1790-1799 (2011).

284. P. D. Tchakam *et al.*, Antimicrobial and antioxidant activities of the extracts and compounds from the leaves of Psorospermum aurantiacum Engl. and Hypericum lanceolatum Lam. *BMC Complement Altern Med* **12**, 136 (2012).

285. S. Cao, J. Cen. (China, 2013), vol. CN 103275048 A.

286. J. Cen *et al.*, Isogarcinol is a new immunosuppressant. *PloS One* **8**, e66503 (2013).

287. V. Kuete *et al.*, Cytotoxicity and modes of action of four naturally occuring benzophenones: 2,2',5,6'-tetrahydroxybenzophenone, guttiferone E, isogarcinol and isoxanthochymol. *Phytomedicine* **20**, 528-536 (2013).

288. Y. Fu, H. Zhou, M. Wang, J. Cen, Q. Wei, Immune regulation and anti-inflammatory effects of isogarcinol extracted from Garcinia mangostana L. against collagen-induced arthritis. *J Agric Food Chem* **62**, 4127-4134 (2014).

240

289. X. Hongxi, S. Kaikai, D. Zhijie, Z. Hong. (2014), vol. CN103536588A.

290. J. Cen *et al.*, The new immunosuppressant, isogarcinol, binds directly to its target enzyme calcineurin, unlike cyclosporin A and tacrolimus. *Biochimie* **111**, 119-124 (2015).

291. G. Park *et al.*, Regulation of Histone Acetylation by Autophagy in Parkinson Disease. *J Biol Chem* **291**, 3531-3540 (2016).

292. H. Bridi, G. C. Meirelles, G. L. von Poser, Structural diversity and biological activities of phloroglucinol derivatives from Hypericum species. *Phytochemistry* **155**, 203-232 (2018).

293. K. Mows, M. Schurmann, H. Preut, B. Plietker, 7,7-Dimethyl-4a-(3-methyl-2-buten-yl)-2-oxo-4a,5,6,7-tetra-hydro-2H-chromen-4-yl benzoate. *Acta Crystallogr Sect E Struct Rep Online* **65**, o2139 (2009).

294. B. A. Sparling, J. K. Tucker, D. C. Moebius, M. D. Shair, Total Synthesis of (-)-Nemorosone and (+)-Secohyperforin. *Org Lett* **17**, 3398-3401 (2015).

295. X. W. Yang *et al.*, Polycyclic Polyprenylated Acylphloroglucinol Congeners Possessing Diverse Structures from Hypericum henryi. *J Nat Prod* **78**, 885-895 (2015).

296. L.-T. T. Nguyen *et al.*, Thoreliolides A and B, two polyisoprenylated benzoylphloroglucinol derivatives with a new carbon skeleton from the fruits of Calophyllum thorelii. *Tetrahedron Lett* **57**, 2737-2741 (2016).

297. A. V. R. Rao, G. Venkatswamy, A. D. Pendse, Camboginol and Cambogin. *Tetrahedron Lett* **21**, 1975-1978 (1980).

298. G. L. Pardo-Andreu *et al.*, The anti-cancer agent nemorosone is a new potent protonophoric mitochondrial uncoupler. *Mitochondrion* **11**, 255-263 (2011).

299. S. B. Raikar, P. Nuhant, B. Delpech, C. Marazano, Synthesis of Polyprenylated Benzoylphloroglucinols by Regioselective Prenylation of Phloroglucinol in an Aqueous Medium. *Eur J Org Chem* **2008**, 1358-1369 (2008).

300. K. Zhou, C. Wunsch, J. Dai, S. M. Li, gem-Diprenylation of Acylphloroglucinols by a Fungal Prenyltransferase of the Dimethylallyltryptophan Synthase Superfamily. *Org Lett* **19**, 388-391 (2017).

301. C. Tsukano, D. R. Siegel, S. J. Danishefsky, Differentiation of nonconventional "carbanions"-the total synthesis of nemorosone and clusianone. *Angew Chem, Int Ed* **46**, 8840-8844 (2007).

302. J. Qi, J. A. Porco, Jr., Rapid access to polyprenylated phloroglucinols via alkylative dearomatization-annulation: total synthesis of (+/-)-clusianone(1). *J Am Chem Soc* **129**, 12682-12683 (2007).

303. Q. Zhang, B. Mitasev, J. Qi, J. A. Porco, Jr., Total synthesis of plukenetione A. *J Am Chem Soc* **132**, 14212-14215 (2010).

304. J. Qi, A. B. Beeler, Q. Zhang, J. A. Porco, Jr., Catalytic enantioselective alkylative dearomatization-annulation: total synthesis and absolute configuration assignment of hyperibone K. *J Am Chem Soc* **132**, 13642-13644 (2010).

305. Q. Zhang, J. A. Porco, Jr., Total synthesis of (+/-)-7-epi-nemorosone. *Org Lett* **14**, 1796-1799 (2012).

306. J. H. George, M. D. Hesse, J. E. Baldwin, R. M. Adlington, Biomimetic synthesis of polycyclic polyprenylated acylphloroglucinol natural products isolated from Hypericum papuanum. *Org Lett* **12**, 3532-3535 (2010).

307. H. P. Pepper, H. C. Lam, W. M. Bloch, J. H. George, Biomimetic total synthesis of (+/-)-garcibracteatone. *Org Lett* **14**, 5162-5164 (2012).

308. J. H. Boyce, J. A. Porco, Jr., Asymmetric, stereodivergent synthesis of (-)-clusianone utilizing a biomimetic cationic cyclization. *Angew Chem, Int Ed* **53**, 7832-7837 (2014).

309. H. P. Pepper, S. J. Tulip, Y. Nakano, J. H. George, Biomimetic total synthesis of (+/-)-doitunggarcinone A and (+)-garcibracteatone. *J Org Chem* **79**, 2564-2573 (2014).

310. S. Wen, J. H. Boyce, S. K. Kandappa, J. Sivaguru, J. A. Porco, Jr., Regiodivergent Photocyclization of Dearomatized Acylphloroglucinols: Asymmetric Syntheses of (-)-Nemorosone and (-)-6-epi-Garcimultiflorone A. *J Am Chem Soc* **141**, 11315-11321 (2019).

311. B. Mitasev, J. A. Porco, Jr., Manganese(III)-mediated transformations of phloroglucinols: a formal oxidative [4 + 2] cycloaddition leading to bicyclo[2.2.2]octadiones. *Org Lett* **11**, 2285-2288 (2009).

312. E. A. Couladouros, M. Dakanali, K. D. Demadis, V. P. Vidali, A short biomimetic approach to the fully functionalized bicyclic framework of type A acylphloroglucinols. *Org Lett* **11**, 4430-4433 (2009).

313. N. S. Simpkins, M. D. Weller, Expedient synthesis of ialibinones A and B by manganese(III)-mediated oxidative free radical cyclisation. *Tetrahedron Lett* **51**, 4823-4826 (2010).

314. J. P. Schaefer, The Peroxidation of Bicyclo [2.2.1]heptadiene. *J Am Chem Soc* **82**, 4091-4094 (2002).

315. H. W. Gibson, Chemistry of formic acid and its simple derivatives. *Chem Rev (Washington, DC, U S)* **69**, 673-692 (2002).

316. D. M. Pawar, D. Cain-Davis, E. A. Noe, Conformational equilibria in formic acid and the adduct of formic acid and hexafluoroacetone, HCO2C(CF3)2OH. *J Org Chem* **72**, 2003-2007 (2007).

317. S. L. Schreiber, Target-oriented and diversity-oriented organic synthesis in drug discovery. *Science* **287**, 1964-1969 (2000).

318. W. R. Galloway, A. Isidro-Llobet, D. R. Spring, Diversity-oriented synthesis as a tool for the discovery of novel biologically active small molecules. *Nat Commun* **1**, 80 (2010).

319. O. C. CJ, H. S. Beckmann, D. R. Spring, Diversity-oriented synthesis: producing chemical tools for dissecting biology. *Chem Soc Rev* **41**, 4444-4456 (2012).

320. S. Yi, B. V. Varun, Y. Choi, S. B. Park, A Brief Overview of Two Major Strategies in Diversity-Oriented Synthesis: Build/Couple/Pair and Ring-Distortion. *Front Chem* **6**, 507 (2018).

321. I. Pavlinov, E. M. Gerlach, L. N. Aldrich, Next generation diversity-oriented synthesis: a paradigm shift from chemical diversity to biological diversity. *Org Biomol Chem* **17**, 1608-1623 (2019).

322. C. J. Gerry, S. L. Schreiber, Recent achievements and current trajectories of diversity-oriented synthesis. *Curr Opin Chem Biol* **56**, 1-9 (2020).

323. X. Lin *et al.*, Synthesis of novel guttiferone E and xanthochymol derivatives with cytotoxicities by inducing cell apoptosis and arresting the cell cycle phase. *Eur J Med Chem* **162**, 765-780 (2019).

324. Y. Feng, T. J. Mitchison, A. Bender, D. W. Young, J. A. Tallarico, Multi-parameter phenotypic profiling: using cellular effects to characterize small-molecule compounds. *Nat Rev Drug Discov* **8**, 567-578 (2009).

325. K. L. Kurita, E. Glassey, R. G. Linington, Integration of high-content screening and untargeted metabolomics for comprehensive functional annotation of natural product libraries. *Proc Natl Acad Sci U S A* **112**, 11999-12004 (2015).

326. B. Melillo *et al.*, Synergistic Effects of Stereochemistry and Appendages on the Performance Diversity of a Collection of Synthetic Compounds. *J Am Chem Soc* **140**, 11784-11790 (2018).

327. M. H. Pan, W. L. Chang, S. Y. Lin-Shiau, C. T. Ho, J. K. Lin, Induction of apoptosis by garcinol and curcumin through cytochrome c release and activation of caspases in human leukemia HL-60 cells. *J Agric Food Chem* **49**, 1464-1474 (2001).

328. V. Jeffers *et al.*, Garcinol Inhibits GCN5-Mediated Lysine Acetyltransferase Activity and Prevents Replication of the Parasite Toxoplasma gondii. *Antimicrob Agents Chemother* **60**, 2164-2170 (2016).

329. C. Guttroff *et al.*, Polycyclic Polyprenylated Acylphloroglucinols: An Emerging Class of Non-Peptide-Based MRSA- and VRE-Active Antibiotics. *Angew Chem, Int Ed* **56**, 15852-15856 (2017).

330. A. Koeberle, H. Northoff, O. Werz, Identification of 5-lipoxygenase and microsomal prostaglandin E2 synthase-1 as functional targets of the anti-inflammatory and anti-carcinogenic garcinol. *Biochem Pharmacol* **77**, 1513-1521 (2009).

331. T. Nishino *et al.*, Ex vivo expansion of human hematopoietic stem cells by garcinol, a potent inhibitor of histone acetyltransferase. *PloS One* **6**, e24298 (2011).

332. H. M. Collins *et al.*, Differential effects of garcinol and curcumin on histone and p53 modifications in tumour cells. *BMC Cancer* **13**, 37 (2013).

333. J. H. Boyce, V. Eschenbrenner-Lux, J. A. Porco, Jr., Syntheses of (+)-30-epi-, (-)-6-epi-, (+/-)-6,30-epi-13,14-Didehydroxyisogarcinol and (+/-)-6,30-epi-Garcimultiflorone A Utilizing Highly Diastereoselective, Lewis Acid-Controlled Cyclizations. *J Am Chem Soc* **138**, 14789-14797 (2016).

334. C. A. Grob, W. Baumann, Die 1,4-Eliminierung unter Fragmentierung. *Helv Chim Acta* **38**, 594-610 (1955).

335. K. Prantz, J. Mulzer, Synthetic applications of the carbonyl generating Grob fragmentation. *Chem Rev* **110**, 3741-3766 (2010).

339. B. B. Snider, D. J. Rodini, J. Van Straten, Lewis acid induced conjugate addition of alkenes to .alpha.,.beta.-unsaturated ketones or aldehydes. *J Am Chem Soc* **102**, 5872-5880 (2002).

340. D. W. Nicholson *et al.*, Identification and inhibition of the ICE/CED-3 protease necessary for mammalian apoptosis. *Nature* **376**, 37-43 (1995).

341. S. Ferrari, H. R. Bandi, J. Hofsteenge, B. M. Bussian, G. Thomas, Mitogen-activated 70K S6 kinase. Identification of in vitro 40 S ribosomal S6 phosphorylation sites. *J Biol Chem* **266**, 22770-22775 (1991).

342. M. Pende *et al.*, S6K1(-/-)/S6K2(-/-) mice exhibit perinatal lethality and rapamycin-sensitive 5'-terminal oligopyrimidine mRNA translation and reveal a mitogen-activated protein kinase-dependent S6 kinase pathway. *Mol Cell Biol* **24**, 3112-3124 (2004).

343. H. Goto *et al.*, Identification of a novel phosphorylation site on histone H3 coupled with mitotic chromosome condensation. *J Biol Chem* **274**, 25543-25549 (1999).

344. Q. Jin *et al.*, Distinct roles of GCN5/PCAF-mediated H3K9ac and CBP/p300-mediated H3K18/27ac in nuclear receptor transactivation. *EMBO J* **30**, 249-262 (2011).

345. E. M. Bowers *et al.*, Virtual ligand screening of the p300/CBP histone acetyltransferase: identification of a selective small molecule inhibitor. *Chem Biol* **17**, 471-482 (2010).

346. L. M. Lasko *et al.*, Discovery of a selective catalytic p300/CBP inhibitor that targets lineage-specific tumours. *Nature* **550**, 128-132 (2017).

347. S. H. MacPhail, J. P. Banath, Y. Yu, E. Chu, P. L. Olive, Cell cycle-dependent expression of phosphorylated histone H2AX: reduced expression in unirradiated but not X-irradiated G1-phase cells. *Radiat Res* **159**, 759-767 (2003).

348. K. Balasubramanyam *et al.*, Polyisoprenylated benzophenone, garcinol, a natural histone acetyltransferase inhibitor, represses chromatin transcription and alters global gene expression. *J Biol Chem* **279**, 33716-33726 (2004).

349. J. L. Dahlin *et al.*, Assay interference and off-target liabilities of reported histone acetyltransferase inhibitors. *Nat Commun* **8**, 1527 (2017).

350. P. Cheung *et al.*, Single-Cell Chromatin Modification Profiling Reveals Increased Epigenetic Variations with Aging. *Cell* **173**, 1385-1397 e1314 (2018).

351. D. Wu *et al.*, Apoptotic release of histones from nucleosomes. *J Biol Chem* **277**, 12001-12008 (2002).

352. J. M. Irish, D. B. Doxie, in *High-Dimensional Single Cell Analysis: Mass Cytometry, Multi-parametric Flow Cytometry and Bioinformatic Techniques,* H. G. Fienberg, G. P. Nolan, Eds. (Springer Berlin Heidelberg, Berlin, Heidelberg, 2014), pp. 1-21.

353. R. C. Team. (R Foundation for Statistical Computing, Vienna, Austria, 2018).

354. H. Wickham, *ggplot2: elegant graphics for data analysis*. (Springer, 2016).

355. H. Wickham, R. François, L. Henry, K. Müller. (2018).

356. H. Wickham, L. Henry. (2018).

357. C. O. Wilke. (2018).

358. C. O. Wilke. (2017).

CHAPTER 7 – FUTURE DIRECTIONS

At the outset of this project in 2018, it appeared that research on the apoptolidin family of glycosylated polyketides was tapering off. For the first decade after their discovery in the late 1990s, there was intense interest by multiple groups in accessing new apoptolidin analogs and understanding their mechanism of action. By 2010, interest (measured by publications) on apoptolidin had begun to fade. My impression is that part of this decline was due to the assumption that apoptolidin acted in a similar manner to oligomycin ([117](#)). For instance, in our discussions with structural biologists regarding attempting to solve the structure of apoptolidin or ammocidin bound to ATP synthase, one remarked that they actually had apoptolidin in their freezer but deprioritized determining its structure as it was thought to bind like oligomycin, to the F_O subunit. The work demonstrates that apoptolidin family glycomacrolides act through a distinct mechanism of action from oligomycin, targeting the F_1, rather than F_O portion of ATP synthase. Though these data establish the mechanism of action of apoptolidin at the molecular level, there are still many questions left unanswered and new questions arose in the course of this work. While some of these questions are of a more academic nature, the demonstration that ammocidin can be used *in vivo*, makes these questions ever more pressing. Outside of this work, oxidative phosphorylation (OXPHOS) has emerged as an important target in cancer and immunology, and it is my hope that apoptolidin, ammocidin, and analogs thereof, will be useful research tools to understand OXPHOS dependence and potentially therapeutics that can help patients suffering from cancer and other diseases. In order realize these goals, it will be important to address these questions.

7.1 How do apoptolidin family compounds cause cell death?

Apoptolidin and ammocidin are inhibitors of ATP synthase, an enzyme which catalyzes

the final step in OXPHOS – generating ATP from ADP and inorganic phosphate. Apoptolidin

was discovered in a screen for compounds which selectively induce apoptosis in transformed

cells, and it is tempting to draw a dashed mechanistic arrow from ATP depletion to apoptosis.

5   However, this simplified model does not explain the molecular events that lead from ATP

synthase inhibition to cell death. As touched in Chapter 3, OXPHOS has a much larger role in

cell survival and growth beyond generation of ATP. Flux through the TCA cycle provides

biosynthetic intermediates for DNA replication and cell growth (207). The balance between

proton flux between complex I-IV and complex V determine the state of the mitochondrial

10   membrane potential ($\Delta\psi$m), and loss of this membrane potential is intimately connected with

apoptosis (359) – both a potential precipitant and a consequence of apoptosis. Inhibition of

complex V would be expected to increase the mitochondrial membrane potential if the

mitochondria are well coupled, leading to a hyperpolarized state. One possible way to 'uncouple'

these interconnected processes would be to use low doses of uncouplers to restore ETC flux

15   while ATP synthase is inhibited to determine if ATP synthesis or ETC flux is driving cell death.

One caveat is that I suspect the results of these experiments would not be generalizable to all

cells – some cells may be more dependent on mitochondrial ATP synthesis than others.

Revisiting the original apoptolidin papers (98), apoptosis was defined on the basis of

chromatin condensation and DNA fragmentation. In the late 1990s, our conception of cell death

20   was largely dichotomized into necrosis into apoptosis. The field of cell death has grown

considerably over the last two decades with new forms of cell death including ferroptosis,

pyroptosis, and necroptosis (360). Additionally, there is increasing evidence that the mode of

programmed cell death can influence how the immune system response, as in immunogenic cell

death ([361](#)). These findings are of great importance in the age of immune-oncology and are of interest to the Laboratory for Biosynthetic Studies. It would be worthwhile to revisit mode of cell death induced by ammocidin and apoptolidin in different biological contexts.

7.2 Is ATP synthase inhibition by apoptolidin different from inhibition by oligomycin?

5   Though apoptolidin and oligomycin appear to target distinct subunits of ATP synthase, one might think that the ultimate effect of both drugs is the same – inhibition of ATP synthesis. Work by Serrill ([140](#)) and others have shown that this is not the case, oligomycin and apoptolidin have distinct effects on cell bioenergetics and AMPK signaling and some cell lines are more sensitive to OXPHOS inhibition by oligomycin but not apoptolidin. Furthermore, Serrill's work

10   showed that the IC50 of apoptolidin appeared to vary between 10-300 nM while the IC50 of oligomycin in sensitive cell lines was ~ 1 nM. If F_1 and F_O are well coupled, inhibition of F_1 should also stop F_O and vice versa. This is a question which deserves further experimental investigation, but our existing data does provide some starting points for speculation.

       One possibility is that there is something about the mode of inhibition of

15   apoptolidin/ammocidin that causes its IC50 to vary in different contexts. In my studies with isolated mouse liver ATP mitochondria apoptolidin appeared to act as an un-competitive inhibitor with respect to ADP; its K_i was dependent on ADP concentration. In the ATPase assay with isolated yeast F_1 ATPase apoptolidin and ammocidin exhibited similar mixed inhibition with a higher affinity in the presence of higher concentrations of ATP, though the double

20   reciprocal plots do suggest some affinity for F_1 in the absence of ATP as well. These assays are difficult to perform with nanomolar inhibitors, particularly the ATP synthesis assay which requires functional mitochondria and is further confounded the adenine nucleotide translocase (ANT) which can be rate limiting. A better assay would use inverted, coupled, sub-mitochondrial

particles (SMP, ETPH) ([39](#), [41](#)), which I attempted to prepare unsuccessfully. These inverted

SMPs have the ATP synthase facing out and the ETC pumps protons to an inner lumen,

bypassing the ANT. Literature protocols from the 1960s and 70s use rat and bovine heart

mitochondria as opposed to the yeast and mouse liver mitochondria I was able to access. These

5   assays would be useful to confirm the precise mode of inhibition of apoptolidin and ammocidin

with regards to ADP, ATP, and phosphate.

       If apoptolidin was an uncompetitive inhibitor, it would preferentially target cells with

high ADP concentrations and low ATP/ADP ratios. If a cell was running 'lean' with ADP

quickly converted to ATP, the ADP concentration would be low and cells would be resistant. A

10   cell running 'rich,' consuming large amounts of ATP to generate large amounts of ADP, would

be more sensitive. Cells also have mechanisms to restore ATP/ADP balance – they can

regenerate ATP using glycolysis or use adenylate kinase to convert $2ADP \rightarrow ATP + AMP$. Cells

which are deficient in glycolysis or adenylate kinase would be expected to have lower ATP/ADP

ratios which could make them more sensitive to OXPHOS inhibition by glycomacrolides.

15   Another consequence of this mechanism is that partial inhibition of ATP synthase would cause

ADP to accumulate and increase the degree of inhibition of an uncompetitive inhibitor in a

positive feedback loop – over time cells would become more sensitive to ATP synthase

inhibition. One piece of evidence that this may be playing a role is that AMPK activation by

apoptolidin as measured by pS6 (Figure 3.5) appears to evolve over time, reaching maximal

20   activation at 4 – 8 hrs. By comparison, the complex I inhibitor IACS-010759 appears to activate

AMPK within 30 min. Additional time course and concentration-response experiments may

provide further support for this hypothesis.

Another interesting possibility that connects back to how apoptolidin causes cell death is that ATP synthase has been speculated to be a component of the mitochondrial permeability transition pore (PTP) ([362](#)) which is responsible for permeabilization of inner mitochondrial membrane during apoptosis. One study observed that oligomycin, but not aurovertin, inhibited TNFα induced apoptosis ([363](#)), which suggests that there may be a more complex relationship between the bioenergetic and apoptotic roles of the mitochondria and ATP synthase.

7.3 How is inhibition of ATP synthase different from inhibiting other ETC complexes?

As discussed in Chapter 3, there is considerable interested in targeting OXPHOS in cancer and there are multiple OXPHOS inhibitors in clinical trials, mostly targeting complex I and II. *In vitro*, scientists studying metabolism use different metabolic inhibitors such as antimycin, FCCP, and oligomycin to dissect the state of each of the respiratory complexes. *In vivo*, many of these distinctions seems to break down and compounds are generally referred to as 'OXPHOS inhibitors.' However, there is good reason to suspect targeting different ETC complexes would have different effects on cell bioenergetics and survival. As discussed in Chapter 3, across cancers there is a high rate of truncating mutations in the mitochondrially encoded components of complex I and a very low rate of truncating mutations in complex V ([210](#)). This suggests that cancer cells have varying degrees of dependence on each of the various respiratory complexes. Furthermore, inhibiting different ETC complexes would be expected to have different effects on the mitochondrial membrane potential, TCA cycle flux, and generation of reactive oxygen species (ROS), which may influence the connection between ETC inhibition and cell death. It would be worthwhile to compare ammocidin directly to other OXPHOS inhibitors *in vivo* and *ex vivo* to survey the relative dependence of cells to each ETC complex.

The cases where cells are sensitive to one OXPHOS inhibitor, but not another, would be of particular interest.

7.4 Why aren't glycomacrolides more toxic?

The initial screening data on apoptolidin and ammocidin suggested that they would be cytotoxic towards cancer cells but not healthy cells. These findings were all in cell culture, where supraphysiologic levels of glucose can activate glycolysis and reduce sensitivity to OXPHOS inhibition, a phenomenon known as the Crabtree effect ([212](#), [364](#)). Moving ammocidin *in vivo*, there was some skepticism that it could be dosed at a level which would suppress tumor growth without excessive toxicity, one collaborator jokingly remarked 'cyanide is also an effective OXPHOS inhibitor.' Though high doses of ammocidin were indeed toxic (>0.5 mg/kg), lower dose (0.1-0.25 mg/kg) were tolerated surprisingly well, with only mild weight loss and a slight quantitative decrease in platelet counts noted. Though this is very good for ammocidin's prospects as a therapeutic candidate, the question remains – why isn't ammocidin more toxic?

Some theories as to why this might be have already been presented. Perhaps ammocidin is acting as an uncompetitive inhibitor and leukemia cells have lower spare respiratory capacity ([365](#)) and high ADP concentrations? Perhaps healthy cells are able to compensate with glycolysis while cancer cells are not? One factor which has not been discussed is the pharmacology of ammocidin. In our very preliminary non-GLP pharmacokinetic tests, ammocidin appears to be cleared from the plasma quiet quickly, in the order of 30 min – 2 hrs. For a kinase inhibitor, where the goal is to maximize the area under the curve (AUC), this might be undesirable, however, for a metabolism targeted agent this transient inhibition may contribute to its therapeutic index. Furthermore, the efficacy of ammocidin appears to be higher in the marrow than the spleen in the MV-4-11 NSGS xenograft model. Per our collaborators, this is not

uncommon and is not necessarily disqualifying for further development as splenic involvement is more often seen in murine models than human disease. However, this differential targeting of spleen vs marrow may also provide insights into ammocidin's therapeutic index. Perhaps ammocidin reaches higher concentrations in the marrow than the spleen? Perhaps the stromal cells in the marrow or spleen are altering the metabolic phenotype of the cancer cells? These are questions deserving of further study.

On the topic of pharmacologic properties, ammocidin theoretically has additional advantages over oligomycin which should be investigated further. Oligomycin is extremely lipophilic and poorly soluble, while apoptolidin and ammocidin are quite soluble in aqueous solution. This is consistent with their mechanism – with the oligomycin binding site lying in the membrane while the apoptolidin binding site is in the soluble F_1 portion of ATP synthase. This makes ammocidin and apoptolidin much easier to dose in mice and we have very preliminary evidence to suggest that ammocidin A is orally bioavailable. Additional studies on the pharmacological properties of ammocidin will be essential in order to advance it as a therapeutic candidate.

7.5 How does oncogenic transformation lead to OXPHOS dependence?

One of the unanswered questions regarding ammocidin and apoptolidin is why they arose as 'hits' in their original assays using isogeneic cell lines. RAS transformation has been widely studied with regards to metabolism, but curiously its usually associated with Warburg metabolism and increased glycolysis (366). Some studies have shown that HRas-G12V transformation upregulates mitochondrial metabolism, including OXPHOS (367, 368) which may provide a clue to how transformation mediates ammocidin sensitivity. Curiously, in the original apoptolidin manuscript, H-*ras* transformed cells were evaluated alongside E1A

transformed cells and found to be apoptolidin resistant. This suggests that different RAS

mutations in different contexts may mediate OXPHOS dependence differently.

Similarly, BCL-2 expression was observed to block the pro-apoptotic effects of

ammocidin A by Salomon et al. (115). Using FL5.12 cells overexpressing BCL-XL (369)

5 provided by Dr. Rathmell, I observed a similar loss of sensitivity with overexpression of BCL-

XL. Curiously, adenoviral E1B-19K encodes a homolog of BCL-2, but overexpression of E1B-

19K in rat glia or E1A fibroblasts failed to block apoptolidin induced apoptosis (98).

One discrepancy in the literature is that the metabolic profile of the cell can be measured

in many different ways: by OCR and ECAR using the seahorse platform, by transcriptional

10 profiles, or by sensitivity to inhibitors. Many of these assays are done *ex vivo* with homogenous

cells under non-physiologic conditions. Though there are many cases where these different

'metabolic profiles' may correlate, these assays do measure different things. A cell can

simultaneously exhibit high levels of lactate production and reliance on OXPHOS. Modern

studies on oncogenesis and metabolism need to (and indeed do) take tumor heterogeneity and *in*

15 *vivo* metabolism into account, and I hope that apoptolidin and ammocidin will be useful tool

compounds in this field.

7.6 Can ammocidin/apoptolidin be improved?

The studies described in Chapters 2 and 3 demonstrate that ammocidin A is a promising

therapeutic candidate with high specificity, potency, and acceptable toxicity, but the question

20 remains, can it be made even better? The studies described in the preceding chapters demonstrate

that the C9 sugar of apoptolidin and ammocidin can be modified with retention of nanomolar

activity. Additionally, the cryoEM structures of apoptolidin and ammocidin bound to the yeast

enzyme provide a blueprint for rationally designing improved analogs. One area of interest is

optimizing the clearance of ammocidin. Several medicinal chemistry experts have remarked that the short half-life of ammocidin is less than desirable. As addressed above, it may be that a short half-life is desirable, but this is a hypothesis that needs to be tested with a series of analogs. It is my hope that other will continue this work.

5   In our *in vivo* studies we decided to proceed with ammocidin A as our lead compounds as opposed to apoptolidin family compounds due to the tendency of apoptolidin family compounds to isomerize to isoapoptolidins. Given that isomerization of apoptolidin and clearance of ammocidin appear to occur on similar time scales, this may not be as much of a liability as first thought. Additionally, in conversations with other scientists working on mitochondrially targeted therapeutics, in seems that in some cases slow clearance and high stability contribute to excessive toxicity. It may be that apoptolidin is better candidate for lead development than ammocidin.

In regard to analogs, another question that arose is whether improved, novel, analogs can be obtained by genetic engineering of the producing strains. In chapter 3, I attempted to isolate deoxyapoptolidin from *Nocardopsis sp.* FU-40 *ΔApoP*, and isolated a compound lacking the C20 hydroxyl. When Earl attempted the same, he isolated a compound lacking the C16 hydroxyl. These results appear to be in conflict and raise the question as to the role of *ApoP*. One possibility is that either Earl or I misassigned our compounds. On my inspection of David's NMR data (218), our compounds have distinct HSQC spectra suggesting they are indeed different. Another possibility is that both David and I correctly assigned our compounds, but we were working with different strains. Further validation of the genotype of the strain labeled *ΔApoP* (nsf_7199) would be worthwhile. One orthogonal way to resolve this apparent conflict is to express and isolate ApoP and ApoD1/D2/D3 and assay for turnover assays with apoptolidin C

which lacks both the C16 and C20 hydroxyl groups. Sunny and David did clone both genes onto pET vectors for expression in *E. coli* but this would require additional expertise that is outside the scope of my thesis but well within the scope of the laboratory for biosynthetic studies.

7.7 What are other settings where apoptolidin family glycomacrolides would be useful?

5   Thus far we have mainly looked at ammocidin in the context of leukemia, but emerging evidence suggests that there are many other settings where complex V inhibition would be useful both as a research tool and as a therapeutic. Chapter 3 includes a discussion of specific cancers where OXPHOS dependence has been described and where ammocidin may be efficacious. Additionally, it would be useful to further study how ammocidin can be combined with other

10   clinically used compounds such as venetoclax and to study the clinicopathologic features which correlate with OXPHOS sensitivity including mutational status and FAB classification. These are areas of study are outside the scope of the laboratory for biosynthetic studies, but it is my hope that these studies will continue in collaboration with others with expertise in human leukemia and murine models.

15   **7.8 What are the mechanisms of action of the ciromicins?**

       When I first began outlining the target identification project as a NRSA fellowship proposal, my intention was to determine the mechanism of action of ciromicins A and B. As we developed the proposal, Dr. Bachmann encouraged me to include the apoptolidins in the proposal as the SAR had already been worked out and they were accessible in much larger

20   quantities. I am very grateful for his advice on this point. The ciromicins proved to be challenging to study, as they were accessible in at only 1-3 mg/L quantities and their bioactivity was much more difficult to assay in cell lines. Though we were close to triaging the project due to a lack of a reliably sensitive cell lines, we decided to test ciromicins A, B, and C in primary

patient samples and found them to be surprisingly active, below 1 µM. The divergence in cell

subset targeting by the ciromicin A and B is striking, and it is tempting to speculate that they

bind to a common target but perturb it in distinct ways to alter cell differentiation.

One of the pressing questions which remains unanswered about the ciromicins is whether

5   the pattern of cells that remain after 48 hr of treatment is due to selective cytotoxicity towards

the cells that are missing or due to altering the development of the cells such that they 'move to a

new spot on the map.' Future experiments with sorted cell populations may help answer this

question. The chemical ecology of these compounds is also an interesting topic for speculation.

Is ciromicin A or B (or C or B2 or B3) the 'active' form of ciromicin in the environment?

10   Unraveling its mechanism of action in its niche or in human hematopoiesis will likely provide

insights into the other. Unlike the glycomacrolides, the glycomacrolactams appear to be quite

diverse and I suspect do not have a unifying mechanism. I am very hopeful that future trainees in

the VLBS will be able to 'shed light' on their mechanism of action.

7.9 References

15   39.   R. E. Beyer, in *Oxidation and Phosphorylation*. (Academic Press, 1967), vol. 10, pp. 186-194.
41.   P. L. Pedersen *et al.*, in *Methods in Cell Biology Volume 20*. (Academic Press, 1978), vol. 20, pp. 411-481.
98.   J. W. Kim, H. Adachi, K. Shin-ya, Y. Hayakawa, H. Seto, Apoptolidin, a new apoptosis
20   inducer in transformed cells from Nocardiopsis sp. *J Antibiot (Tokyo)* **50**, 628-630 (1997).
115.   A. R. Salomon, D. W. Voehringer, L. A. Herzenberg, C. Khosla, Apoptolidin, a selective cytotoxic agent, is an inhibitor of F_0F_1-ATPase. *Chem Biol* **8**, 71-80 (2001).
117.   A. R. Salomon, Y. Zhang, H. Seto, C. Khosla, Structure-activity relationships within a
25   family of selectively cytotoxic macrolide natural products. *Org Lett* **3**, 57-59 (2001).
140.   J. D. Serrill *et al.*, Apoptolidins A and C activate AMPK in metabolically sensitive cell types and are mechanistically distinct from oligomycin A. *Biochem Pharmacol* **93**, 251-265 (2015).
207.   M. Bajzikova *et al.*, Reactivation of Dihydroorotate Dehydrogenase-Driven Pyrimidine
30   Biosynthesis Restores Tumor Growth of Respiration-Deficient Cancer Cells. *Cell Metab* **29**, 399-416 e310 (2019).

210. A. N. Gorelick *et al.*, Respiratory complex and tissue lineage drive recurrent mutations in tumour mtDNA. *Nat Metab* **3**, 558-570 (2021).

212. L. D. Marroquin, J. Hynes, J. A. Dykens, J. D. Jamieson, Y. Will, Circumventing the Crabtree effect: replacing media glucose with galactose increases susceptibility of HepG2 cells to mitochondrial toxicants. *Toxicol Sci* **97**, 539-547 (2007).

218. D. Earl, Vanderbilt University, Nashville, TN (2018).

359. J. D. Ly, D. R. Grubb, A. Lawen, The mitochondrial membrane potential (Δψm) in apoptosis; an update. *Apoptosis* **8**, 115-128 (2003).

360. D. Tang, R. Kang, T. V. Berghe, P. Vandenabeele, G. Kroemer, The molecular machinery of regulated cell death. *Cell Research* **29**, 347-364 (2019).

361. L. Galluzzi, A. Buque, O. Kepp, L. Zitvogel, G. Kroemer, Immunogenic cell death in cancer and infectious disease. *Nat Rev Immunol* **17**, 97-111 (2017).

362. G. Beutner, K. N. Alavian, E. A. Jonas, G. A. Porter, in *Handbook of Experimental Pharmacology*. (Springer International Publishing, 2016), pp. 21-46.

363. L. A. Shchepina *et al.*, Oligomycin, inhibitor of the F0 part of H+-ATP-synthase, suppresses the TNF-induced apoptosis. *Oncogene* **21**, 8149-8157 (2002).

364. I. Sussman, M. Erecińska, D. F. Wilson, Regulation of cellular energy metabolism. The Crabtree effect. *Biochimica et Biophysica Acta (BBA) - Bioenergetics* **591**, 209-223 (1980).

365. S. Sriskanthadevan *et al.*, AML cells have low spare reserve capacity in their respiratory chain that renders them susceptible to oxidative metabolic stress. *Blood* **125**, 2120-2130 (2015).

366. S. Mukhopadhyay, M. G. Vander Heiden, F. McCormick, The metabolic landscape of RAS-driven cancers from biology to therapy. *Nature Cancer* **2**, 271-283 (2021).

367. A. J. de Groof *et al.*, Increased OXPHOS activity precedes rise in glycolytic rate in H-RasV12/E1A transformed fibroblasts that develop a Warburg phenotype. *Mol Cancer* **8**, 54 (2009).

368. S. Telang, A. N. Lane, K. K. Nelson, S. Arumugam, J. Chesney, The oncoprotein H-RasV12 increases mitochondrial metabolism. *Mol Cancer* **6**, 77 (2007).

369. D. R. Plas, S. Talapatra, A. L. Edinger, J. C. Rathmell, C. B. Thompson, Akt and Bcl-xL Promote Growth Factor-independent Survival through Distinct Effects on Mitochondrial Physiology. *J Biol Chem* **276**, 12041-12048 (2001).